POLITECNICO DI MILANO
Dottorato di Ricerca in Bioingegneria
Ph.D. Degree in Bioengineering

Claudio Chiastra

Numerical modeling of hemodynamics in stented coronary arteries

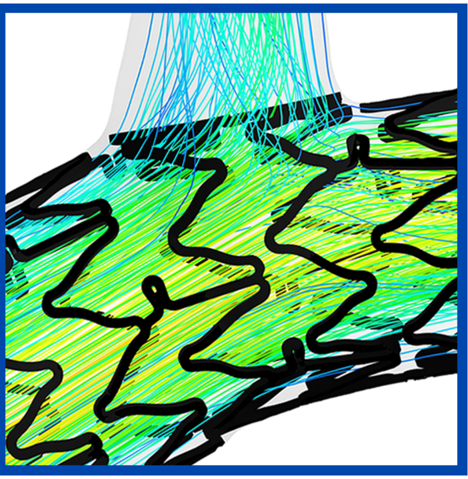

POLITECNICO DI MILANO
Dottorato di Ricerca in Bioingegneria
Ph.D. Degree in Bioengineering

Numerical modeling of hemodynamics in stented coronary arteries

Claudio Chiastra

Supervisor:
Prof. Francesco Migliavacca

PhD Coordinator:
Prof. Maria G. Signorini

XXVI Cicle
2011-2013

To Maria
and my parents.

Claudio

“*If you can dream it, you can do it.*”

Walt Disney

Acknowledgements

I would like to give very special thanks to my supervisor Prof. Francesco Migliavacca, always kind and available for suggestions, for guiding my work in the last three years. Thanks for believing in my capabilities and for constantly encouraging me to reach the final goal of each study.

I wish to acknowledge all the people who collaborated with me during the last years on several studies, for the most part presented in this thesis. In particular, I would like to thank: Prof. Mauro Malvè, for the great hospitality at Universitad de Zaragoza and for working with me on fluid-structure interaction modeling with great passion; Dr. Francesco Burzotta, Prof. Luca Mainardi, and especially Eros Montin, for the study on intravascular optical coherence tomography; Prof. Umberto Morbiducci, for his availability and for having introduced me to the concept of helicity, and Diego Gallo, Ignacio Larrabide, and Ruben Cárdenes, for the study of image-based stented coronary arteries; Prof. Paolo Zunino, Elena Cutrì, and Brandis Keller for the study of mass transport phenomena within stented coronary arteries; Prof. Gabriele Dubini and Prof. Giancarlo Pennati for their suggestions.
Special thanks go to Stefano Morlacchi, with whom I have worked closely during these years, sharing the study of the stented coronary arteries.

I wish to thank all the people at the Laboratory of Biological Structure Mechanics (LaBS), Politecnico di Milano, where I spent my PhD. You created a unique atmosphere in the laboratory.

Last, but definitely not least, I would like to thank my parents, Maria, Nice Try, and all my friends who have supported me during the last years at LaBS.

Claudio

Contents

Abbreviations

1D	One-dimensional
2D	Two-dimensional
3D	Three-dimensional
ALE	Arbitrary Lagrangian-Eulerian
awa-WSS	Area-weighted average wall shear stress
CABG	Coronary artery bypass grafting
CAD	Computer-aided design
CCA	Conventional coronary angiography
CFD	Computational fluid dynamics
CHD	Coronary heart disease
CoCr	Cobalt-chromium
CPU	Central processing unit
CT	Computed tomography
CTA	Computed tomography angiography
DES	Drug eluting stent
FCM	Fuzzy C-means
FKB	Final kissing balloon
FSI	Fluid-structure interaction
FSP	Flow separation parameter
HDL	High-density lipoproteins
ICAM-1	Intercellular adhesion molecule-1
ISR	In-stent restenosis
IVUS	Intravascular ultrasound
LAD	Left anterior descending coronary artery
LCX	Left circumflex artery
LDL	Low-density lipoproteins
LMCA	Left main coronary artery
LNH	Local normalized helicity
MB	Main branch

MET	Mean exposure time
micro-CT	Micro-computed tomography
MRI	Magnetic resonance imaging
NH	Neointimal hyperplasia
NURBS	Non-uniform rational B-Spline
OCT	Optical coherence tomography
OSI	Oscillatory shear index
PCI	Percutaneous coronary intervention
PIV	Particle image velocimetry
PLLA	Poly-L-lactide
PSB	Provisional side branch
RCA	Right coronary artery
RGB	Red, green, and blue
ROI	Region of interest
RRT	Relative residence time
SAM	Surface-adherent monocyte
SB	Side branch
TAWSS	Time-averaged wall shear stress
TIM	Tissue-infiltrating monocyte
VCAM-1	Vascular cell adhesion molecule-1
WSS	Wall shear stress
WSSG	Wall shear stress gradient

Summary

Chapter 1 - Introduction

Coronary heart disease (CHD) is one of the major causes of death and premature disability in developed societies. According to the American Heart Association estimates 15.4 million adults are affected by CHD in the USA alone (Go et al., 2013). CHD is caused by atherosclerotic lesions that reduce arterial lumen size through plaque formation and arterial thickening, decreasing blood flow to the heart and frequently leading to severe complications like myocardial infarction or angina pectoris.
PCI, which consists in balloon angioplasty usually followed by stenting, is the most commonly performed procedure for the treatment of CHD (Go et al., 2013). This procedure is still associated to serious clinical complications such as in-stent restenosis (ISR) (Park et al., 2012), which is the reduction of the lumen size as a result of neointimal hyperplasia (NH), an excessive growth of tissue inside the stented vessel. The phenomenon of ISR has been partially attenuated by the introduction in 2004 of drug eluting stents, which are able to release antiproliferative drugs with programmed pharmacokinetics into the arterial wall. However, restenosis rate remains higher than 10 % when complex lesions (e.g. bifurcation lesions) are treated (Mauri et al., 2008; Zahn et al., 2005).
The mechanisms and the causes of ISR are not fully understood. In addition to vascular injury caused by device implantation and foreign-body reactions, hemodynamic alterations induced by the stent presence can be associated with NH (Wentzel et al., 2008). Therefore, the study of the fluid dynamics of stented coronary arteries is of extreme importance for a better comprehension of the mechanisms involved in ISR.
In this context, the present thesis is focused on the numerical modeling of hemodynamics in stented coronary artery geometries. Indeed, computational

fluid dynamics (CFD) allows the investigation of local hemodynamics at a level of detail not always accessible with experimental techniques, calculating fluid flow variables that can be used as indicators to predict sites where NH is excessive.
The specific aims of the present work are the following:

- the study of the effect of wall compliance of stented coronary artery models on hemodynamic quantities;
- the comparison, from the fluid dynamic perspective, of different stenting procedures for the treatment of bifurcation lesions;
- the study of the hemodynamics of image-based stented coronaries.

The contents of the thesis are presented according to the following chapters.

Chapter 2 - Coronary arteries: anatomy and physiology, atherosclerosis and its treatments

In this chapter a general introduction to coronary arteries is given. Firstly, elements of anatomy and physiology of coronary arteries are presented. Coronary circulation is characterized by a system of repeated bifurcations via a stepwise adaptation of vessel diameter down to the capillary level that allows the spatial distribution of blood flow throughout the myocardium. Several theories based on the principle of energetic efficiency are presented in order to define a mathematical relationship between the mother-vessel and daughter-vessels of each coronary bifurcation.
Secondly, the atherosclerosis, which is a disease of the large and intermediate-sized arteries, principally coronary arteries, is discussed. Atherosclerosis consists in the development of fatty lesions (i.e. atheromatous plaques) on the inside surfaces of the arterial walls. Many risk factors contribute to the formation of atherosclerotic plaques. The most important one is the high plasma concentration of cholesterol in the form of low density lipoproteins. Other risk factors are ageing, physical inactivity and obesity, diabetes mellitus, hypertension, hyperlipidemia, and cigarette smoking. Atherosclerosis can be also caused by a genetic disorder called familial hypercholesterolemia.
Thirdly, the main revascularization procedures for the treatment of atherosclerotic lesions are introduced, focusing on PCI. Particular attention is paid to the treatment of coronary bifurcations which nowadays remains a challenging area in interventional cardiology with a lower rate of procedural success and higher

rate of restenosis compared to non-bifurcation interventions. No single strategy exists for the treatment of atherosclerotic lesions because of the variability of bifurcations in anatomy (plaque burden, location of plaque, angle between branches, diameter of branches, bifurcation site) and in the dynamic changes in anatomy during treatment (plaque shift, dissection). Many stenting techniques that involve the implantation of one or two stents, conventional or dedicated to bifurcation, have been proposed in the literature. However, each technique is associated with some limitations that make uncertain the choice of the best-fitting treatment.
Lastly, ISR, which is one of the main clinical complications of stent implantation, is discussed.

Chapter 3 - State-of-the-art of CFD models of stented coronary arteries[1]

The present chapter opens with an introduction to the most investigated hemodynamic quantities in this research field and their relation with ISR. These hemodynamic quantities can be classified in near-wall quantities (e.g. wall shear stress - WSS, oscillatory shear index - OSI, relative residence time - RRT), flow stasis quantities (e.g. mean exposure time - MET, flow separation parameter - FSP), and bulk flow quantities (e.g. local normalized helicity - LNH).
The-state-of-the-art of the CFD models of stented coronary arteries is then presented. In the recent years numerous CFD studies have been proposed in the literature. Initially, the models were characterized by two-dimensional, highly simplified geometries. With the gradual increase of the computational resources, the analysis of three-dimensional (3D) stented geometries became possible. Complex models with or without bifurcations and with the presence of multiple stents were investigated.
The CFD models which are reviewed in this chapter are classified in two categories: (1) idealized models of stented coronary arteries, considering in particular the coronary bifurcations; (2) models based on geometries reconstructed through imaging techniques. The models that belong to the second category are further subdivided in three categories according to the origin of the images used for the creation of the fluid domain: *in vitro* model, animal

[1] The contents within this chapter can be found in Chiastra C. and Migliavacca F., *Modelling of blood flow in stented coronary arteries*. In Becker, S. and Kuznetsov, A., editors. Heat transfer and fluid flow in biological processes, Elsevier (accepted for publication).

model or patient images.
The studies are reported in a chronological order, highlighting the novelties introduced by the recent works. A description of the methods adopted in each study and the main results is provided. The most significant limitations of the reviewed studies are also discussed, including the absence of the cardiac motion, the assumption of rigid wall for the arterial wall and the stents, the lack of use of patient-specific boundary conditions in image-based studies, the creation of image-based stented geometries which are not completely obtained from imaging data (the arterial wall is reconstructed from images while the stent is created by using a computer-aided design (CAD) software), and the difficulties of the validation of these models. In the end, the potential future developments are presented.

Chapter 4 - On the necessity of modeling FSI for stented coronary arteries[2]

In the fluid dynamic studies of stented coronary arteries the arterial wall and the stents are assumed to be rigid and fixed. This assumption might produce different local hemodynamic results. In this chapter a FSI model of an idealized straight stented coronary artery was compared to the corresponding rigid-wall model in order to understand the effects of the wall compliance and the blood pressure on the hemodynamic quantities, focusing in particular on the analysis of the WSS distribution.
A geometrical model of a straight coronary artery and a typical open-cell stent were created using a CAD software. In order to obtain the geometrical model of a stented artery which is not based only on geometrical assumptions buy also takes into account the deformation of the vessel caused by stent deployment, the device was expanded inside the vessel through a structural simulation following the method proposed in (Gastaldi et al., 2010). The final geometrical configuration was used to create the fluid and solid domains for the subsequent FSI and CFD analyses.
The arterial wall was modeled as a hyperelastic incompressible isotropic and homogenous material using the Demiray model (Demiray, 1972) with strain energy function parameters obtained from human coronary artery experimental

[2] The contents within this chapter have been submitted to Chiastra, C., Migliavacca, F., Martínez, M.A., and Malvè, M. On the necessity of modelling fluid-structure interaction for stented coronary arteries. *Journal of the Mechanical Behavior of Biomedical Materials* (accepted for publication).

tests (Carmines et al., 1991). The stent material was considered linear elastic, isotropic and homogeneous. Two different cases were analyzed maintaining the same geometry: cobalt-chromium (CoCr) and poly-L-lactide (PLLA) stent. The blood was modeled as an incompressible Newtonian fluid.
The extremities of the solid model were constrained by preventing axial and transaxial motion. The artery was initially pressurized by applying at the inlet cross-section a ramp of velocity from 0 m/s to 0.138 m/s and, at the outlet, a ramp of pressure from 0 mmHg to 80 mmHg. Then, velocity and pressure tracings which are representative a human left anterior descending coronary artery (LAD) (Davies et al., 2006) were imposed at the inlet and the outlet, respectively. The no-slip boundary condition was applied to the fluid-structure interface. Numerical simulations were carried using the commercial software ADINA (ADINA R&D, Inc., Watertown, MA, USA). In order to obtain a more realistic comparison between FSI and rigid-wall simulations, the geometries of the CoCr and PLLA cases, pressurized at 80 mmHg, were considered for the rigid-wall models.
The results showed similar trends in terms of instantaneous WSS and TAWSS between compliant and rigid-wall cases. In particular, the difference of percentage area exposed to TAWSS lower than 0.4 Pa between the CoCr FSI and the rigid-wall cases was ~ 1.5 % while between the PLLA cases ~ 1.0 %. The comparison between compliant and rigid-wall cases showed similar results in terms of WSS although CoCr and PLLA FSI models deformed differently during the cardiac cycle, with higher values of displacement in the stented region for the PLLA FSI case.
The results indicate that, for idealized models of a stented coronary artery, the rigid-wall assumption for fluid dynamic simulations is adequate when the aim of the study is the analysis of near-wall quantities like WSS.

Chapter 5 - Hybrid meshing method for stented coronary artery CFD models[3]

CFD analyses have been frequently performed to study the influence of stent implantation on blood flow. However, due to the complexity of the geometry of stented arteries, the high computational cost required for this

[3] The contents within this chapter have been published in Chiastra, C., Morlacchi, S., Pereira, S., Dubini, G., and Migliavacca, F. (2012). Computational fluid dynamics of stented coronary bifurcations studied with a hybrid discretization method. *European Journal of Mechanics B/Fluids*, 35: 76-84.

kind of simulations have strongly limited their use both in the clinical and industrial field. Hence, the present study focuses on the development of an efficient volume meshing method, which allowed us to obtain accurate results on 3D complex geometries in a short time compatible with the available computational resources. A hybrid meshing method was chosen, using both tetrahedral and hexahedral elements. Hexahedral elements should be preferred because of their higher accuracy and reduced number of elements necessary to discretize a certain volume resulting in better performances in terms of computational speed. On the other hand, producing fully hexahedral elements for highly complex geometrical structures, i.e. intersection zones between stent struts and the arterial wall, is not practical.

The new meshing strategy was developed on a straight real-dimensioned coronary artery model with one repeating unit of a typical open-cell stent. This model was initially meshed with only tetrahedral elements using ANSYS ICEM CFD (Ansys Inc., Canonsburg, Pa, USA). A more refined mesh was created in the vicinity of the stent struts. In order to assure accurate results in the stented region (i.e. the portion of arterial wall close to the stent), an appropriate grid independence analysis was conducted. Four tetrahedral meshes were considered, from a coarser to a finer: (A) 192000, (B) 367000, (C) 433000, (D) 778000 elements. Steady-state CFD simulations were performed by means of the commercial software ANSYS Fluent (Ansys Inc., Canonsburg, Pa, USA) applying a constant paraboloid-shaped velocity profile (mean velocity = 0.3 m/s) at the inlet and reference zero pressure at the outlet. The no-slip condition was imposed at the arterial wall and at the stent. Blood was defined as an incompressible non-Newtonian fluid using the Carreau model. Mesh C was chosen for creating the hybrid mesh because the percentage difference of area-weighted average WSS between this mesh and the finest one (mesh D) was lower than 0.25 % and the computational time was about 30 % lower than mesh D.

The main steps of the hybrid meshing method are the following: firstly, an internal cylinder along the whole vessel length and the corresponding hexahedral mesh are created; secondly, in the region between the internal cylinder and the arterial wall a tetrahedral mesh is generated; lastly, the two meshes were merged together. Tetrahedral mesh parameters were chosen in accordance with the previous grid independence analysis. Accordingly, the hexahedral mesh density was decided so that velocity fields and bulk flow quantities were not dependent on grid dimension.

The efficacy of this new meshing strategy was evaluated by comparing the hybrid mesh with a standard fully tetrahedral mesh. The hybrid mesh allowed

to halve the computational time required for a steady-state CFD simulation, obtaining at the same time similar results in terms of WSS and velocity field.
In conclusion, the hybrid meshing method appears to be a powerful tool to obtain correct fluid dynamic results in complex geometries like stented coronary arteries with a relatively low computational cost.

Chapter 6 - Hemodynamic assessment of stenting procedures for coronary bifurcations[4]

Stent implantation in coronary bifurcations is still a challenging area in interventional cardiology. A great number of stenting procedures has been proposed. However, each technique is associated with some limitations that make uncertain the choice of the treatment. Pulsatile CFD analyses on idealized stented coronary bifurcation models were performed using ANSYS Fluent in order to study the hemodynamic influence of different stenting techniques. The fluid domains were created starting from the final geometrical configuration obtained through structural simulations of stent deployment (Morlacchi et al., 2011a). The hybrid meshing method introduced in Chapter 4 was applied in order to reduce the computational time. Three case studies were investigated.

Provisional side branch approach: final kissing balloon inflation

Provisional side branch (PSB) approach is the current preferred strategy for the treatment of coronary bifurcation lesions (Mylotte et al., 2013). It implies the stenting of the main branch (MB) and an optional treatment of the side branch (SB). Frequently, PSB approach is concluded by the final kissing balloon (FKB) procedure, which consist in the simultaneous expansion of two balloons in both branches of the bifurcation. Fluid dynamic simulations were performed in order to examine hemodynamic forces on the intimal layer of the vessel before and after the FKB procedure, enlightening both its benefits and drawbacks. Furthermore, a new tapered balloon dedicated to bifurcations was proposed to enhance the WSS pattern at the intimal layer of the bifurcation.

[4] The contents within this chapter have been published in:
Morlacchi, S., Chiastra, C., Gastaldi, D., Pennati, G., Dubini, G., and Migliavacca, F. (2011). Sequential structural and fluid dynamic numerical simulations of a stented bifurcated coronary artery. *Journal of Biomechanical Engineering*, 133, art.no. 121010.
Chiastra, C., Morlacchi, S., Pereira, S., Dubini, G., and Migliavacca, F. (2012). Computational fluid dynamics of stented coronary bifurcations studied with a hybrid discretization method. *European Journal of Mechanics B/Fluids*, 35: 76-84.

The results of the CFD simulations highlighted the advantages of FKB inflation in terms of better flow pattern and access to the SB, but also its drawbacks in terms of overexpansion of the proximal part of the MB. In particular, FKB provoked a wider region characterized by low and oscillating WSS, which is associated to the risk of ISR. In the end, this work showed that the use of a tapered balloon deployed in the SB during FKB might reduce the main drawbacks of this procedure.

Provisional side branch approach: proximal or distal access to side branch?

Several kinds of accesses to the SB (e.g. proximal or distal access) can be used to perform FKB within the PSB approach, resulting in different final geometrical configuration of both artery and implanted stent and, consequently, altered hemodynamic scenarios.
In order to compare the different hemodynamic scenarios provoked by a FKB procedure performed with a proximal or a distal access to the SB, CFD simulations were performed.
The results of these simulations in terms of WSS distribution along the arterial wall, velocity and the helicity field showed that, from a fluid dynamic perspective, the distal access is better than the proximal one. Therefore, fluid dynamic simulations provided a valid tool to quantitatively support the clinical experience that suggests to perform the distal access instead the proximal one when the PSB approach is chosen.

Culotte technique: conventional or dedicated stents?

The culotte technique is one of the most commonly applied double stenting procedures. Main advantages of the this technique are the good coverage of the whole bifurcation and the suitability for all the bifurcation angles. However, this procedure provokes a high concentration of metal in the proximal part of the MB due to the overlap of the devices that could lead to ISR and thrombosis. Specific stents dedicated to bifurcations, such as the Tryton™ stent, which is characterized by few struts in its proximal part, have been designed to overcome the main drawbacks of the culotte technique.
CFD simulations were performed in order to study this double stenting procedure, comparing the behavior of the Tryton™ stent with a conventional one (Multi-Link Vision® stent).
The use of the Tryton™ stent allowed to reduce the amount of these layers, resulting in a lower metal-to-artery ratio with respect to the Multi-Link Vision®. Furthermore, the design of the dedicated stent markedly reduced the

areas with low TAWSS and high RRT, especially in the proximal MB. These results indicate that the use of the dedicated stent within culotte technique might improve the hemodynamics, thus reducing the regions associated to the risk of ISR.

Chapter 7 - CFD analyses of image-based stented coronary bifurcation models[5]

In this chapter the study of the hemodynamics of image-based stented coronary artery models which replicate the complete clinical procedure of stenting implantation is presented. Two cases (case A and B) of human LAD with their bifurcations treated at the University Hospital Doctor Peset (Valencia, Spain) are investigated. The vessel were reconstructed using the pre-operative computed tomography angiography and conventional coronary angiography images (Cárdenes et al., 2013). Then, the fluid domains were obtained from structural simulations which replicate the stenting procedures followed by the clinicians who performed the interventions (Morlacchi et al., 2013). A hybrid discretization was performed according to the meshing method introduced in Chapter 4.
Pulsatile CFD simulations were carried out by means of ANSYS Fluent. At the inlet cross-section a flow tracing which is representative of a human LAD (Davies et al., 2006) was applied as a paraboloid-shaped velocity profile. At the outlets flow splits were imposed according to a relation proposed by van der Giessen et al. (2011) which is based on data of human coronary bifurcations. The no-slip condition was applied to all the surfaces representing the arterial wall and the stents. Blood was defined as an incompressible non-Newtonian fluid using the Carreau model.
Both near-wall and bulk flow quantities were investigated, thus providing a complete study of the hemodynamics of the two analyzed cases. Results of TAWSS and RRT showed that the wall regions more prone to the risk of restenosis were located next to stent struts, to the bifurcations and to the stent overlapping zone for both investigated cases. Quantitatively, the percentage area exposed to values of TAWSS lower than 0.4 Pa, which are strongly correlated with endothelial permeability and, consequently, with NH, was

[5] The contents within this chapter have been published in Chiastra, C., Morlacchi, S., Gallo, D., Morbiducci, U., Cárdenes, R., Larrabide, I., and Migliavacca, F. (2013). Computational fluid dynamic simulations of image-based stented coronary bifurcation models. *Journal of the Royal Society of Interface*, 10(84), art.no. 20130193.

significant: 35.0 % for case A and 38.4 % for case B. Considering a bulk flow analysis, helical flow structures were generated by the curvature of the zone upstream from the stent and by the bifurcation regions. Helical recirculating microstructures were also visible downstream from the stent struts.
This study demonstrates the feasibility to virtually investigate the hemodynamics of image-based coronary bifurcation geometries.

Chapter 8 - From OCT to CFD simulations: a preliminary study

Intravascular OCT is a catheter-based imaging technique that performs optical cross-sectional images of a coronary artery. Compared to the other imaging techniques that are used in clinical practice for diagnosis of coronary artery disease, i.e. coronary angiography, computed tomography, magnetic resonance imaging, and intravascular ultrasound, OCT is characterized by higher resolution and the possibility to detect both vessel lumen and stent (Ferrante et al., 2013). These advantages allow the OCT to be successfully applied in the assessment of atherosclerotic plaque, stent apposition, and tissue coverage. Moreover, thanks to these two characteristics, OCT seems to be a useful tool to reconstruct 3D geometries of stented coronary arteries.
In this chapter reconstruction methods of stented coronary artery models for CFD simulations based on OCT images are presented. In particular, a reconstruction method was initially developed for an *in vitro* model of a stented coronary bifurcation and the obtained geometry was used to perform CFD simulations. Subsequently, the reconstruction method was adapted for an *in vivo* case.
OCT gives information about the vessel lumen contour and the position of the stent struts in each cross-sectional image. However, the spatial orientation of the vessel and the stent is not provided by this imaging technique. Coronary angiography can be used to obtain this information. As a consequence, in the *in vivo* case the centerline of the vessel was extracted from two angiographic projections using the open-source software 3D IVUS ANGIO Tool (Informatics and Telematics Institute, Thermi-Thessaloniki, Greece). The OCT images were processed in MATLAB (MathWorks Inc., Natick, MA, USA). After a pre-processing step, separate algorithms for the detection of the lumen contour and the stent struts were applied. Then, all the detected vessel contours and stent struts were registered orthogonal to the vessel centerline using the centroid of each lumen contour. In the last step of the reconstruction method,

the lumen contours and the struts were imported as a point cloud in a CAD software for the creation of the final 3D geometrical model of the stented coronary artery.
The works presented in this chapter are preliminary. However, they represent a first step towards the semi-automatic creation of stented coronary artery models for CFD simulations that are purely based on clinical images. Thus, the main limit of the current image-based geometrical models, in which only the vessel is reconstructed from patient-specific images while the stent is drawn inside the artery using CAD operations (Ellwein et al., 2011; Gundert et al., 2011) or deployed through structural simulations that replicate the complete clinical stenting procedure of stenting implantation (Chiastra et al., 2013), is overcome.

Chapter 9 - Final remarks

The main achievements of this thesis work are the following: (1) the implementation of a FSI model of a stented coronary artery; (2) the development of a hybrid meshing strategy for reducing computational costs of fluid dynamic simulations; (3) the fluid dynamic assessment of different stenting procedures for the treatment of coronary bifurcations; (4) the hemodynamic analysis of image-based models of stented coronary artery models which replicate a real stenting procedure; (5) the development of reconstruction methods of *in vitro* and *in vivo* stented coronary artery models from OCT images.
In conclusion, the results of CFD simulations are very useful for studying the ISR phenomenon and comparing different stenting techniques. However, they should be integrated with other modeling information as ISR is not driven only by hemodynamic factors. Structural simulations of stent deployment for the calculation of the stress state in the arterial wall and in the stent, and mass transport simulations accounting for the drug release should be considered as well.

Chapter 1

Introduction

1.1 Clinical problem

CORONARY heart disease (CHD) is one of the major causes of death and premature disability in developed societies. According to the American Heart Association estimates 15.4 million adults are affected by CHD in the USA alone (Go et al., 2013).
CHD is caused by atherosclerotic lesions that reduce arterial lumen size through plaque formation and arterial thickening, decreasing blood flow to the heart and frequently leading to severe complications like myocardial infarction or angina pectoris (Go et al., 2013; Libby, 2008). CHD treatments can be medical or surgical, including percutaneous coronary intervention (PCI) or coronary artery bypass grafting.
PCI consists in balloon angioplasty usually followed by stenting: the lumen of the diseased vessel is restored by balloon inflation and, subsequently, wire mesh tubular structures, known as stents, are deployed in order to hold open the newly expanded artery. PCI is performed under local anesthesia and requires only a short hospitalization, decreasing recovery time and costs compared to coronary bypass surgery. Since PCI introduction in the late '70s, the use of this minimally invasive procedure for coronary revascularization has rapidly expanded (Frye et al., 1996). Today, about 1 million procedures are performed annually in the USA, representing twice the annual number of coronary bypass operations (Go et al., 2013).
Although PCI with stenting is the most widely performed procedure for the treatment of CHD, it is still associated to serious clinical complications such as in-stent restenosis (ISR) (Park et al., 2012). ISR is the reduction of the lumen size as a result of neointimal hyperplasia (NH), an excessive growth of tissue inside the stented vessel. The phenomenon of ISR has been partially attenuated by the introduction in 2004 of drug eluting stents (DES), which are able to release antiproliferative drugs with programmed pharmacokinetics into the arterial wall. Restenosis rate after DES implantation have fallen below 10 % in several randomized clinical trials (Dangas et al., 2010). However, this rate increases when complex lesions are treated (Lemos et al., 2004; Mauri et al., 2008; Zahn et al., 2005), such as bifurcation lesions. The treatment of these lesions is a clinical challenge for interventional cardiologists because the success rates remain considerably lower than those in simple lesions (Mylotte et al., 2013). Moreover, both clinical and histologic studies on DES have demonstrated evidence of continuous neointimal growth during long-term follow-up (Grube et al., 2009; Nakazawa et al., 2011).
The mechanisms and causes of ISR are not fully understood. In addition to vas-

cular injury caused by device implantation and foreign-body reactions, hemodynamic alterations induced by stent presence can be associated with NH (Wentzel et al., 2008). Therefore, the study of the fluid dynamics of stented coronary arteries is of extreme importance for a better comprehension of the mechanisms involved in ISR.

1.2 Aims and objectives

The present thesis is focused on the numerical modeling of hemodynamics in stented coronary arteries. Indeed, computational fluid dynamics (CFD) allows the investigation of local hemodynamics at a level of detail not always accessible with experimental techniques, calculating fluid flow variables (e.g. wall shear stress - WSS) that can be used as indicators to predict sites where NH is excessive (Wentzel et al., 2008). The main aims and objectives of the present work are the following:

- *the study of the effect of wall compliance of stented coronary artery models on hemodynamic quantities*. In the literature studies on stented coronary arteries, the arterial wall and the stents are assumed to be rigid and fixed. In order to understand the validity of this assumption, the results of fluid-structure interaction (FSI) and rigid-wall fluid dynamic simulations are compared.

- *the comparison, from the fluid dynamic perspective, of different stenting procedures for the treatment of bifurcation lesions*. CFD simulations on idealized coronary bifurcation models are performed. A new meshing strategy is also developed in order to reduce the computational resources needed to solve these models.

- *the study of the hemodynamics of image-based stented coronaries*. Geometrical models reconstructed from computed tomography angiography (CTA) and conventional coronary angiography (CCA) are investigated. Moreover, reconstruction methods of stented coronary artery models for CFD simulations are developed starting from optical coherence tomography (OCT) images.

1.3 Outline

The present thesis starts with an introduction to coronary arteries, provided in Chapter 2. In this chapter elements of anatomy and physiology of coronary

arteries, the process of atherosclerosis with its causes and consequences, the treatment of coronary artery disease with PCI, and its possible drawbacks are discussed.
In Chapter 3 the state-of-the-art of CFD models of stented coronary arteries is given. Firstly, the mathematical definitions of the most investigated hemodynamic quantities in this research field and their relation with ISR are introduced (Section 3.1). Secondly, the fluid dynamic models of idealized stented coronary arteries are discussed, focusing on coronary bifurcations (Section 3.2). Thirdly, the fluid dynamic models based on geometries reconstructed through imaging techniques are presented (Section 3.3). Lastly, the most significant limitations of the studies reviewed in the previous sections are discussed (Section 3.4).
In Chapter 4 FSI analyses of a stented coronary artery are presented with the aim of understanding the effects of the wall compliance on the hemodynamic quantities. Two different materials are considered for the stent: cobalt-chromium (CoCr) and poly-L-lactide (PLLA). The results of the FSI and the corresponding rigid-wall models are compared.
In Chapter 5 a hybrid meshing strategy, which uses both tetrahedral and hexahedral elements, is proposed in order to obtain accurate results on three-dimensional (3D) complex geometries in a short time compatible with the available computational resources. Indeed, the high computational resources needed to solve fluid dynamic simulations of stented arteries, which are due to the complexity of the geometries, are a problem that limits the use of these simulations both in the clinical and industrial fields.
Chapter 6 is focused on the treatment of coronary bifurcation lesions, which is considered a challenging area in interventional cardiology. CFD analyses of idealized stented coronary bifurcation models are performed in order to study the hemodynamic influence of different stenting techniques. Firstly, the final kissing balloon (FKB) inflation within provisional side branch (PSB) stenting approach, which is the current preferred strategy for the treatment of coronary bifurcations, is investigated (Section 6.1). A new tapered balloon dedicated to bifurcations is proposed to enhance WSS patterns. Secondly, the different hemodynamic scenarios provoked by a PSB procedure performed with a proximal or a distal access to the side branch (SB) are compared (Section 6.2). Lastly, the culotte technique, which is one of the most commonly applied double stenting procedures, is studied in order to compare the behavior of a dedicated device with a conventional one (Section 6.3).
In Chapter 7 the study of the hemodynamics of image-based stented coronary artery models which replicate the complete clinical procedure of stenting implantation is presented. Two cases of human left anterior descending coronary

artery (LAD) with their bifurcations, reconstructed from CTA and CCA, are investigated. A comprehensive study of the fluid dynamics is carried out by investigating both near-wall quantities and the bulk flow.
In Chapter 8 a preliminary reconstruction method of stented coronary artery models for CFD simulations based on OCT images is discussed. OCT is a promising tool to reconstruct 3D geometries, due to its high spatial resolution (10-20 μm) and the possibility to detect both the stent and the vessel wall. The reconstruction method was initially developed on an *in vitro* case and the obtained geometry was used to perform CFD simulations (Section 8.3). Subsequently the reconstruction method was adapted for an *in vivo* case (Section 8.4).
Finally, in Chapter 9, the main conclusions and the future perspectives are provided.

Chapter 2

Coronary arteries: anatomy and physiology, atherosclerosis and its treatments

In the present chapter an introduction to coronary arteries is given. In particular, elements of anatomy and physiology of coronary arteries are presented. The process of atherosclerosis, which consists in the development of atheromatous plaques on the internal surfaces of the arterial walls, is discussed, including its causes and consequences. The main revascularization procedures for the treatment of atherosclerotic lesions are introduced, focusing especially on PCI. This procedure consists of balloon angioplasty usually followed by stent deployment. Particular attention is paid to the treatment of coronary bifurcations which remains a challenging area in interventional cardiology with a lower rate of procedural success compared to non-bifurcation interventions. In the end, the ISR phenomenon, which is one of the main clinical complications of stent implantation, is presented.

2.1 Coronary circulation: elements of anatomy and physiology

2.1.1 Anatomy of coronary arteries

CORONARY arteries supply blood to the cardiac muscle. They originate as the right (RCA) and left main (LMCA) coronary arteries from the aortic sinuses in the initial portion of the ascending aorta (Fig 2.1) (Drake et al., 2012). The main coronary arteries lie on the surface of the heart and divide into gradually smaller arteries that penetrate from the surface into the cardiac muscle mass.

RCA passes between the pulmonary artery and the right auricular appendix. It then descends vertically between the right atrium and right ventricle in the coronary sulcus. Reaching the inferior margin of the heart, it turns posteriorly and continues in the sulcus onto the diaphragmatic surface and base of the heart. During this course, numerous branches arise. RCA supplies the right atrium and right ventricle, the electrical conduction system of the heart and a portion of the left ventricle.

LMCA, larger than the former, passes between the pulmonary artery and the left auricular appendix before entering the coronary sulcus. Posterior to the pulmonary trunk, the artery divides into two branches (Fig. 2.1) (Drake et al., 2012):

- the left anterior descending coronary artery (LAD), which continues around the left side of the pulmonary trunk and descends obliquely toward the apex of the heart in the anterior interventricular sulcus. During its course, one or two large diagonal branches may arise and descend diagonally across the anterior surface of the left ventricle;
- the left circumflex artery (LCX), which continues to the left in the coronary sulcus and onto the base/diaphragmatic surface of the heart. It usually ends before reaching the posterior interventricular sulcus.

LMCA supplies most of the left atrium and left ventricle, and most of the interventricular septum.

After the capillary bed, the returning venous blood passes through the cardiac veins, most of which empty into the coronary sinus, located in the coronary sulcus on the posterior face of the heart between the left atrium and left ventricle (Drake et al., 2012). The coronary sinus opens into the right atrium, at the coronary sinus orifice, between the inferior vena cava and the right atrioventricular orifice.

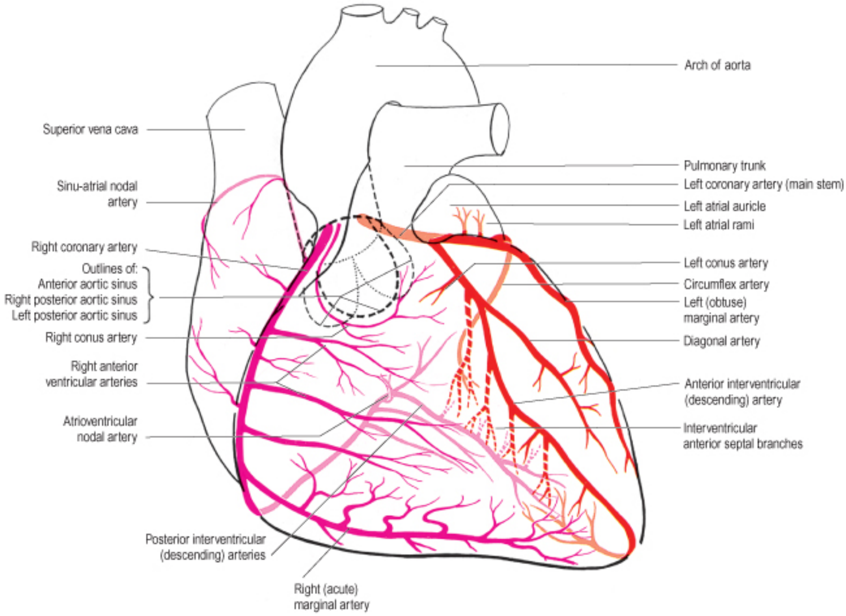

Figure 2.1: Normal coronary anatomy viewed from the diaphragmatic surface of the heart. Left coronary arteries are indicated in red, right coronary arteries in purple. *Reprinted from S. Standring (Ed.), Gray's Anatomy: The Anatomical Basis of Clinical Practice, 39th edition. ©(2005) Elsevier B.V.*

The distribution pattern of the coronary arteries described in this section is the most common one. It consists of the right-dominant coronary artery because RCA supplies a large portion of the left ventricle and LCX is relatively small. However, several variations in this basic distribution pattern can occur (Drake et al., 2012).

The proximal segments of the main coronary arteries are characterized by the following mean diameters: 3.0 ± 0.5 mm , 4.4 ± 0.4 mm, 3.0 ± 0.4 mm, 3.4 ± 0.5 mm, for RCA, LMCA, LAD, and LCX, respectively (Dodge Jr. et al., 1992).

2.1.2 Coronary bifurcations

The branching pattern of coronary arteries has been studying for many years. Coronary vasculature can be considered as an ”open” asymmetric tree in which

a parent vessel segment divides into two branches, then each of the branch segments divides into two branches, and so on (Fig. 2.2) (Zamir, 1999, 2001). The branching process at each step was found to be similar (i.e. dichotomous division) in 99 % of the coronary artery segments (Spaan, 1991). Only in about 1 % of the arteries, a proximal branch splits into three or more SB at the same location. Hence, from the point of view of the number of branches produced at each junction, the system has a fractal character (Zamir, 2001). This fractal character of the coronary tree is valid only in a rudimentary sense. In fact, the division of branches is the same as the division of parents but the properties of the branches vary considerably (high degree of variability in the diameters and lengths of vessel segments) from one level of the tree to the next as well as within each level (Zamir, 2001).
The system of repeated bifurcations via a stepwise adaptation of vessel diameter down to the capillary level allows to spatially distribute blood flow throughout the myocardium. This adaptation consists in a geometrical reduction probably driven by the principle of energetic efficiency (i.e. the energy required for blood circulation is minimized) (Finet et al., 2007, 2010). Several theories based on the principle of energetic efficiency have been formulated in order to understand what dictates the lumen dimension, defining a mathematical relationship between the mother-vessel and daughter-vessels of coronary bifurcations. Murray (1926) proposed a cost function defined as the sum of friction power loss and metabolic power dissipation proportional to blood volume. This minimum energy hypothesis results in Murray's law, which can be written as:

$$D_m^3 = D_{d1}^3 + D_{d2}^3 \tag{2.1}$$

where D_m is the diameter of the mother-vessel and D_{d1} and D_{d2} are the diameters of the daughter-vessels. Kassab and coworkers (Kassab, 2007; Zhou et al., 1999, 2002) showed that Murray's law is not valid in the whole tree as Murray's analysis considered each bifurcation in isolation rather than an integrated whole. The following relation (HK model) was introduced and validated (Huo and Kassab, 2009):

$$D_m^{7/3} = D_{d1}^{7/3} + D_{d2}^{7/3} \tag{2.2}$$

Finet et al. (2007) found a linear relation based on regression analysis of bifurcations with equal diameter for daughter-vessels (Y-tipe bifurcations):

$$D_m = 0.678\,(D_{d1} + D_{d2}) \tag{2.3}$$

where the value 0.678 expresses the ratio of mother diameter to the sum of daughter diameters. HK model gives rise to a ratio of 0.673 for the case of a

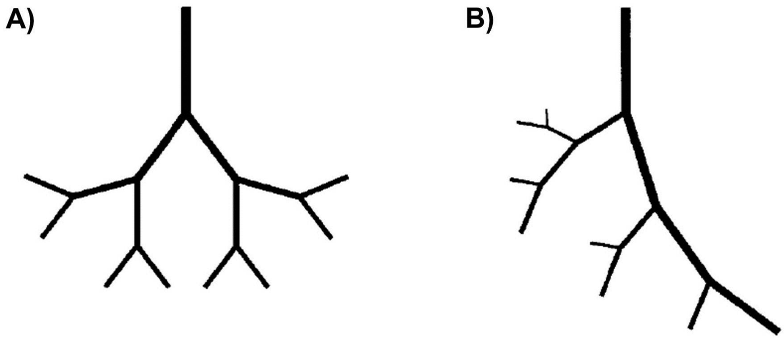

Figure 2.2: The distributive task of the vascular system is achieved mostly by repeated bifurcations. Vascular tree can be (a) symmetric, when the destinations and the needs for blood flow are uniformly distributed or, more generally, (b) asymmetric. Coronary tree is considered as an asymmetric tree. *Adapted with permission from Journal of Theoretical Biology, Vol.212(2): 183-190. M. Zamir, Fractal dimensions and multifractility in vascular branching ©(2001) Academic Press.*

Y-type bifurcations. Therefore, HK model is consistent with Finet's rule in case of Y-type bifurcation.

2.1.3 Coronary blood flow

The resting coronary blood flow in human being averages about 225 mL min^{-1} (0.7-0.8 mL min^{-1} g^{-1} of heart muscle), representing 4-5 % of the total cardiac output (Guyton and Hall, 2006; Ramanathan and Skinner, 2005). Arterial oxygen extraction in the heart is 70-80 %, compared with 25 % for the rest of the body. Therefore, increased oxygen consumption must primarily be met by an increase in coronary blood flow, which may increase fivefold during exercise (Ramanathan and Skinner, 2005).
Coronary blood flow is markedly affected by extravascular compression due to heart contraction (Fig. 2.3) (Guyton and Hall, 2006). During systole, blood flow falls to a low value because of the strong compression of the left ventricular muscle around the intramuscular vessels. During diastole, the cardiac muscle relaxes and does not obstruct blood flow through the left ventricular muscle capillaries, so that blood can rapidly flow. This phenomenon, particularly evident in the left coronary arteries, is less accentuated in the right coronary arteries because the force of contraction of the right ventricular muscle is far less than that of the left ventricular one.

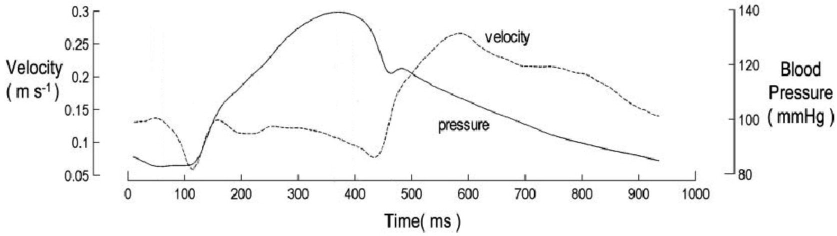

Figure 2.3: Simultaneous velocity and pressure waveforms measured in a human LCX. During systole (from about 120 to 400 ms) pressure increases while velocity, and hence blood flow, falls to a low value because of the strong compression of the left ventricular muscle around the intramuscular vessels. During diastole blood velocity increases because the cardiac muscle relaxes and does not obstruct blood flow through the coronary arteries. *Adapted with permission from Circulation, Vol.113(4): 1768-1778. J.E Davies et al., Evidence of a dominant backward-propagating "suction" wave responsible for diastolic coronary filling in humans, attenuated in left ventricular hypertrophy ©(2006) American Heart Association, Inc.*

2.2 Atherosclerosis

2.2.1 Atherogenesis

Atherosclerosis is a disease of the large and intermediate-sized arteries, principally coronary arteries, in which fatty lesions called atheromatous plaques develop on the inside surfaces of the arterial walls (Guyton and Hall, 2006). Atherosclerosis normally occurs over a period of many years, usually many decades. Growth of atheromatous plaques probably occurs discontinuously, with periods of relative quiescence and periods of rapid evolution. Not all manifestations of atherosclerosis result from stenotic, occlusive diseases (Libby, 2008).

The process of atherogenesis is schematized in Fig. 2.4. The formation of atheromatous plaques in the arterial walls (i.e. atherogenesis) starts with a dysfunction of the vascular endothelium. This dysfunction increases the expression of adhesion molecules such as the vascular cell adhesion molecule-1 (VCAM-1) and the intercellular adhesion molecule-1 (ICAM-1) on endothelial cells, and decreases their ability to release nitric oxide and other substances that help prevent adhesion of macromolecules, platelets and monocytes to the endothelium (Guyton and Hall, 2006; Libby, 2002; Yazdani et al., 2010). After damage to the endothelium occurs, lipids, mainly cholesterol in the form of low-density lipoproteins (LDL), and monocytes begin to accumulate at the site of injury (Fig. 2.4a). The monocytes migrate into the tunica intima of the vessel wall, and differentiate into macrophages. They ingest and oxidize LDL, assuming a foam-like appearance. Subsequently, smooth muscle cells begin migrating from the media, and the macrophage foam cells aggregate, creating a visible fatty streak (Davis, 2005; Guyton and Hall, 2006).

A fibrous cap consisting of smooth muscle cells and collagen forms. At the same time the macrophages and monocytes initially involved in the process begin to die resulting in the formation of a necrotic core covered by a fibrous cap. The plaque becomes larger and larger as leucocytes and lipid fragments continue to enter the lesion (Fig. 2.4b) (Davis, 2005). With the progress of atherogenesis, plaque can bulge into the vessel lumen, reducing the blood flow. Sometimes plaque can completely occlude the vessel (Davis, 2005; Guyton and Hall, 2006).

Atherosclerotic arteries become stiff and unyielding because of the extensive amounts of dense connective tissue deposited by the fibroblasts of the plaque and by calcium salts that often precipitate with the plaque lipids. Plaque rupture can occur, frequently leading to thrombus formation and finally to myocardial ischemia with or without necrosis (Guyton and Hall, 2006).

2.2.2 Causes of atherosclerosis

Many risk factors contribute to the dysfunction of the vascular endothelium and to the subsequent formation of atherosclerostic plaques (Table 2.1). The most important one is a high plasma concentration of LDL cholesterol. The plasma concentration of these molecules is increased by eating highly saturated fat and excess of cholesterol in daily diet, obesity and physical inactivity (Guyton and Hall, 2006).

The likelihood of developing atherosclerosis is higher if the concentration of high density lipoproteins (HDL) is low. Although the function of HDL is not completely established, it seems that these molecules protect against the formation of atherosclerotic plaques. In fact it is believed that these molecules can absorb cholesterol crystals to be deposited in the arterial walls.

Atherosclerosis develops also in people with perfectly normal levels of cholesterol and lipoproteins. In addition to ageing, risk factors contributing to atherosclerosis are physical inactivity and obesity, diabetes mellitus, hypertension, hyperlipidemia and cigarette smoking (Guyton and Hall, 2006; Libby, 2008).

In the end, atherosclerosis can be caused by a genetic disorder. Familial hypercholesterolemia is a genetic disease in which the level of LDL in the blood is higher than normal from birth. This is due to a defect in a gene for the forma-

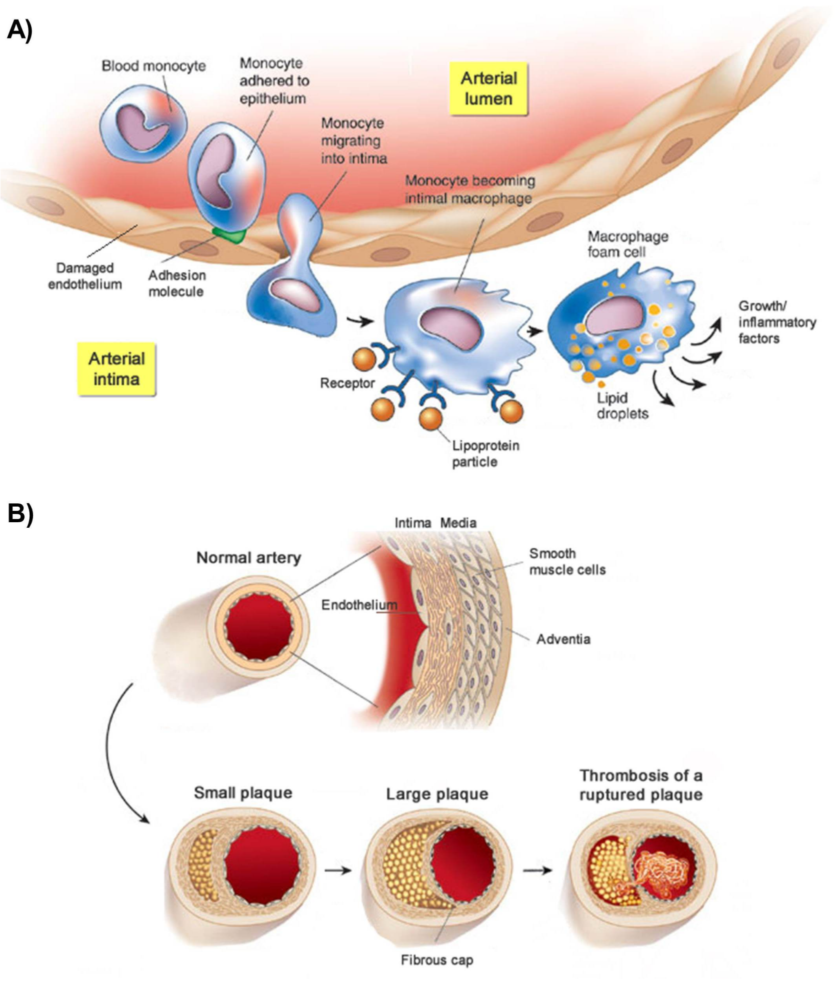

Figure 2.4: Development of atheromatous plaques: a) The monocyte attaches to an adhesion molecule on a damaged endothelial cell of the artery. The monocyte then migrates into the intimal layer of the arterial wall and differentiates into a macrophage. The macrophage ingests and oxidizes low-density lipoproteins (LDL), assuming a foam-like appearance. The foam cells release substances that cause inflammation and growth of the intimal layer. b) Additional accumulation of macrophages and lipid fragments causes the plaque to become larger and larger. With the progress of atherogenesis, the plaque might occlude the vessel, reducing the blood flow, and eventually rupture, leading to the formation of a thrombus. *Adapted with permission from from Nature, Vol.420: 868-874. P. Libby. Inflammation in atherosclerosis. ©(2002) Nature Publishing Group.*

Table 2.1: Major risk factors of atherosclerosis (Libby, 2008)

High LDL cholesterol concentration
Low HDL cholesterol concentration
Age (men $\geq$ 45 years; women $\geq$ 55 years)
Lifestyle risk factors: - Obesity - Cigarette smoking - Physical inactivity - Atherogenic diet
Diabetes mellitus
Hypertension
Family history of premature CHD: - CHD in male first-degree relative $<$ 55 years - CHD in female first-degree relative $<$ 65 years
Genetic disorder (familial hypercholesterolemia)
Emerging risk factors: - Homocysteine - Prothrombotic factors - Proinflammatory factors - Imparied fasting glucose - Subclinical atherogenesis

tion of LDL receptors on the membrane surface of body's cells. In absence of these receptors LDL cholesterol cannot be absorbed and its concentration into the plasma increases. Furthermore, many patients with familial hypercholesterolemia die before age 20 because of myocardial infarction (Guyton and Hall, 2006).

2.2.3 Consequences of atherosclerosis

In Fig. 2.5 the main consequences of atherosclerotic disease of coronary arteries are schematized. Atherosclerotic plaques cause partial or total stenosis of a coronary artery leading to ischemic heart disease, i.e. a condition in which there is an inadequate supply of blood and oxygen to a portion of the myocardium (Antman et al., 2008).
In case of partial stenosis, chronic diseases such as stable angina pectoris can develop due to myocardial ischemia. Stable angina pectoris consists of cardiac pain usually felt by the patient under the upper sternum over the heart or in

distant surface areas of the body like left arm, left shoulder, neck or even side of the face (Guyton and Hall, 2006). Most of the people with stable angina pectoris feel pain when they exercise or when they experience emotions that increase metabolism of the heart or temporarily constrict the coronary vessels because of sympathetic vasoconstrictor nerve signals. The pain usually lasts for only a few minutes.
Chronic coronary artery diseases are distinct from acute coronary syndromes such us unstable angina pectoris or myocardial infarction. Unstable angina pectoris is a form of acute coronary syndrome and consists of chest pain that occurs randomly or unpredictable, and is unrelated to physical exertion or emotional stress (Cannon and Braunwald, 2008). Acute myocardial infarction occurs when a coronary artery is completely occluded. Blood flow ceases in the coronary vessels beyond the occlusion causing necrosis of the myocardial tissue. This area of the heart, which is called infarcted area, cannot sustain cardiac muscle function.

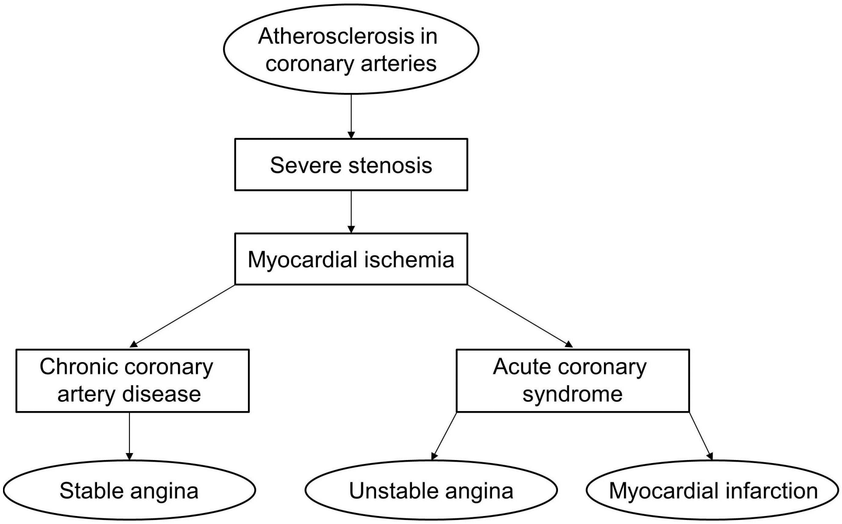

Figure 2.5: Scheme representing the main possible consequences of atherosclerosis in coronary arteries.

2.3 Percutaneous coronary intervention

2.3.1 Introduction to treatment techniques

Two main coronary revascularization procedures can be employed for the treatment of atherosclerotic lesions of coronary arteries: coronary artery bypass grafting (CABG) or PCI.

CABG is a surgical procedure in which the obstructive lesion is bypassed by a blood vessel graft (Fig. 2.6 a). In order to restore the normal blood flow to the heart, one or both of the internal mammary arteries, a radial artery or a segment of vein (usually the saphenous vein) are used to form a connection between the aorta and the coronary artery distal to the obstructive lesion (Antman et al., 2008). PCI is a non-surgical procedure that consists of balloon angioplasty usually followed by stent deployment (Fig. 2.6 b) (Antman et al., 2008). An inflatable balloon is threaded to the site of the atherosclerotic lesion on a catheter and inflated to open the narrowed coronary artery. In order to keep the

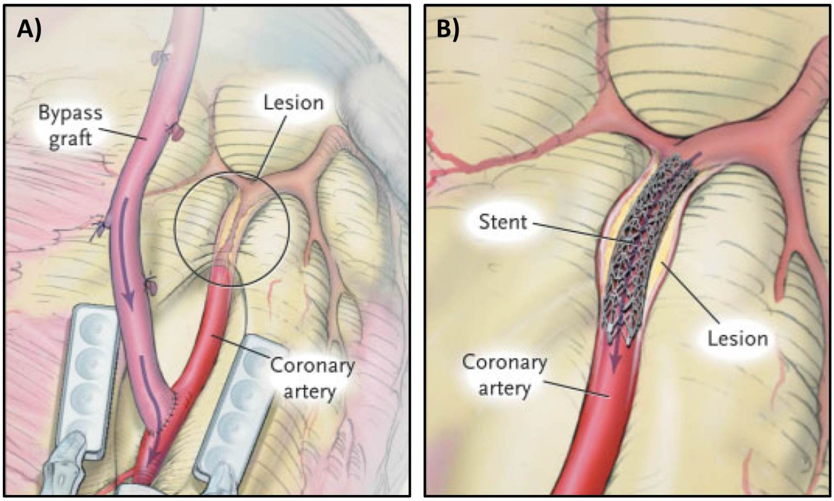

Figure 2.6: Different approaches for the treatment of atherosclerotic coronary lesions: a) CABG; b) PCI. Stenting procedure addresses the existing lesion but not future lesions, whereas bypass grafting is directed at the epicardial vessel proximal to the insertion of the artery/vein graft, including the existing lesion and also future lesions. *Adapted with permission from The New England Journal of Medicine, Vol.352(21): 2235-2237. B.J. Gersh and R.L. Frye. Methods of coronary revascularization - things may not be as they seem.* ©*(2005) Massachusetts Medical Society.*

vessel open, wire tubular structures, known as stents, are then expanded inside the artery. The main steps of stenting procedure are shown in Fig. 2.7. Firstly, the stent, mounted on a balloon catheter in a crimped (i.e. collapsed) state, is positioned where the narrowing occurs. Secondly, the stent is expanded by balloon inflation. Lastly, the balloon is deflated and the complete system is removed from the body except for the permanently deformed stent which remains in place, holding the artery open.
The majority of current coronary stents are fabricated in metallic alloys such as CoCr or 316-L stainless steel. They are coated with a drug carrier loading a pharmacologic agent that is known to interfere with the process of restenosis. These kind of devices are called DES. Fully biodegradable coronary stents, made of a polymer (e.g. PLLA) or degradable metals (e.g. magnesium alloys) that progressively degrade, are under development or clinical trial. Ideally, these devices should slowly degrade to provide mechanical support during the arterial remodeling period (6-12 months) before complete degradation within 12-24 months (Sammel et al., 2013; Sun et al., 2013).

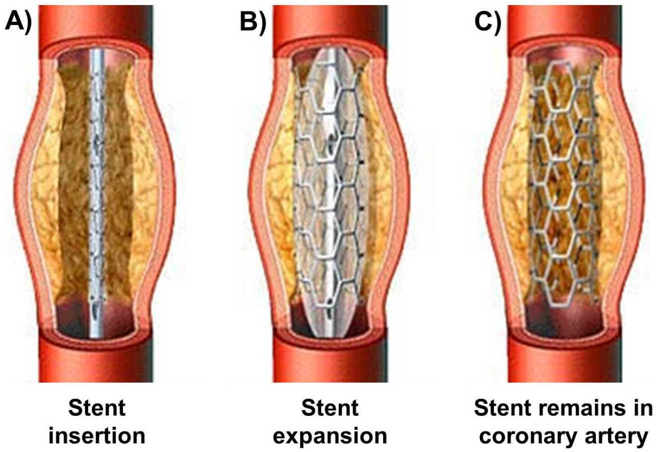

Figure 2.7: Main steps of stenting procedure: a) the stent, mounted on a balloon catheter in crimped state, is positioned where the narrowing occurs; b) the stent is expanded by balloon inflation; c) the balloon is deflated and the complete system is removed from the body except for the permanently deformed stent which remains in place, holding the artery open. *Adapted with permission from Journal of Materials Processing Technology, Vol.197: 174-181. V. Dehlaghi et al. Analysis of wall shear stress in stented coronary artery using 3D computational fluid dynamics modeling. ©(2008) Elsevier B.V.*

PCI with stent implantation firstly appeared in 1986 (Sigwart et al., 1987), becoming a valid alternative to CABG thanks to the following main advantage: coronary stenting is a minimally invasive technique which is performed under local anesthesia; it requires only a short (1-day) hospitalization, greatly decreasing recovery time and expense compared to CABG (Baim, 2008).
PCI is widely employed in patients with symptoms and evidence of ischemia due to stenosis of one or two vessels, and even in selected patients with three-vessel disease. CABG remains indicated in patients with stenosis of the LMCA and those with three-vessel distal disease, especially with diabetes and/or impaired left ventricle function (Antman et al., 2008).
Nowadays about 1 million of PCI are performed annually only in the USA, representing twice the annual number of CABG operations (Go et al., 2013).

2.3.2 Treatment of coronary bifurcations by PCI

The treatment of coronary bifurcation lesions is a challenging area in interventional cardiology because of a lower rate of procedural success and a higher rate of restenosis compared to non-bifurcation interventions (Louvard et al., 2008). It is estimated that the rate of lesions involving bifurcations is 15-20 % of all the PCI procedures (Sharma et al., 2010).
Bifurcations are characterized by recirculation and stagnation zones that cause low WSS, making these regions very prone to develop atherosclerosis. This was demonstrated by autopsy studies (Fox et al., 1982; Grottum et al., 1983; Nakazawa et al., 2010) in which it was found a higher prevalence of atherosclerotic plaques in the low WSS regions (e.g. the lateral walls) with respect to flow divider sites, characterized by high WSS (Fig. 2.8).
Bifurcations vary in anatomy (plaque burden, location of plaque, angle between branches, diameter of branches, bifurcation site) and in the dynamic changes in anatomy during treatment (plaque shift, dissection) (Yazdani et al., 2010). As a consequence, each bifurcation has its own peculiarities.
Medina's classification is the most commonly used tool for description of coronary bifurcation lesions (Medina et al., 2006). It indicates the location of significant stenoses (>50 %) in the bifurcation. As shown in Fig. 2.9, it is characterized by three numbers and two commas. The number before the first comma represents the proximal MB, the number between the two commas the distal MB, and the number after the second comma the SB. "1" accounts for the presence and "0" for the absence of a >50 % lesion. Medina's classification is very simple and it does not require memorization. However, it does not represent a complete description of the lesions (Louvard et al., 2010): no differentiation

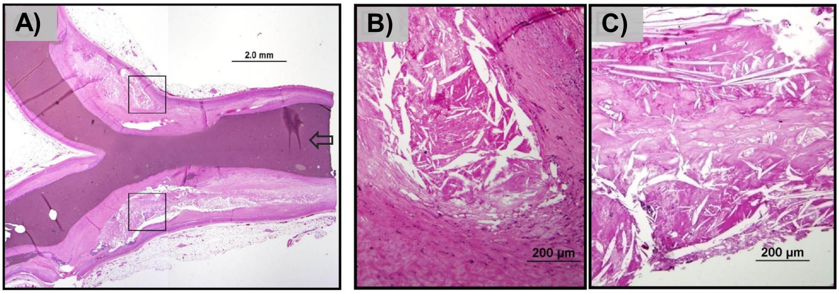

Figure 2.8: a) Histologic image of atherosclerotic plaques in the LCX/left obtuse bifurcation. The lateral walls show significantly greater prevalence of plaque as compared to flow divider region. b, c) Magnifications of the atherosclerotic plaques at the later walls. Necrotic core formation is visible. *Adapted with permission from Journal of the American College of Cardiology, Vol. 55 (16): 1679-1687. G. Nakazawa et al. Pathological Findings at Bifurcation Lesions. The Impact of Flow Distribution on Atherosclerosis and Arterial Healing After Stent Implantation. ©(2010) American College of Cardiology Foundation.*

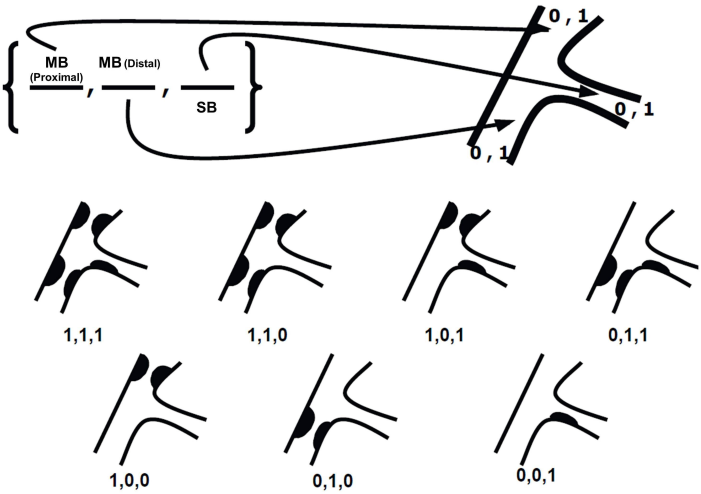

Figure 2.9: Medina's classification. *Reprinted with permission from EuroIntervention, Vol. 6 (Suppl J): J31-J35. Y. Louvard et al. Definition and classification of bifurcation lesions and treatments. ©(2010) Europa Digital & Publishing.*

is made between a lesion-free segment and a <50 % lesion, or between two lesions or a single lesion in the MB; calcifications are not identified; bifurcation angles are not indicated.

No single strategy exists for the treatment of atherosclerotic lesions because of the great variability of coronary bifurcations. Many stenting techniques, involving the implantation of one or two stents, have been proposed in the literature (Sheiban et al., 2009). However, each technique is associated with some limitations that make uncertain the choice of the best-fitting treatment.

In 2007 the European Bifurcation Club proposed a classification of bifurcation stenting strategies in order to facilitate their description and to allow comparisons between techniques in various anatomical and clinical settings (Louvard et al., 2008). This classification, called MADS classification, takes into account both final stent positioning and order of implantation, including the placement of the first stent and the potential implantation of additional stents according to the operator mind, the results and the difficulties encountered during the procedures (Louvard et al., 2010). Stenting strategies are subdivided in four classes (Fig. 2.10), which are identified by the letters of the acronym MADS: ”M” (main) indicates that the first stent is placed in the proximal MB; ”A” (across) that the stent is expanded in the MB through the SB; ”D” (double) that deployment of a single or two simultaneous stents is performed in two separated lumens, without the necessity to re-cross struts; ”S” (side branch first) that the first stent is implanted in the SB with or without protrusion in the MB. In each treatment class, the initial strategy may be completed by implantation of one or two additional stents.

Among the different stenting techniques schematized by MADS classification, PSB approach, which involves stent placement in the MB first with optional treatment of SB, is the gold standard strategy for the treatment of non-left main bifurcations (Brar et al., 2009). Several randomized trials comparing this strategy with double stenting techniques showed that the implantation of two stents is not associated with any benefits, regardless of the lesion type. Moreover, double stenting approach was related to a higher rate of periprocedural myocardial infarction and higher rate of stent thrombosis (Brar et al., 2009; Katritsis et al., 2009; Zhang et al., 2009).

Coronary bifurcations are usually treated with conventional stents, i.e. stents used in non-bifurcation lesions. The use of these devices can result in some problems occurring during the stenting procedure, such as the poor access to the SB (Latib and Colombo, 2008), and in high rates of restenosis, especially in the SB (Costa and Moussa, 2006). Moreover, current PCI techniques with conventional stents could be laborious and limited by the complexity of bifur-

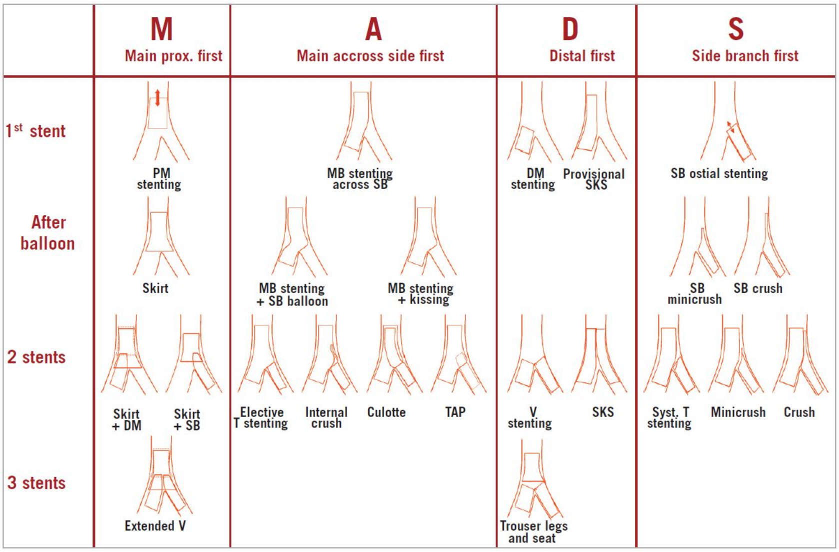

Figure 2.10: MADS classification of stenting techniques for coronary bifurcation lesions (straight techniques). *Reprinted with permission from EuroIntervention, Vol. 7(1): 160-163. Y. Louvard and T. Lefvre. Tools and Techniques: PCI in coronary bifurcations lesions. ©(2010) Europa Digital & Publishing.*

cation anatomy. In particular, double stenting procedures are associated with underexpansion or gap at the SB ostium, excessive metal-to-artery ratio at the carina, stent malapposition, and stent distortion (Collet et al., 2011). In order to overcome some of the main limitations associated with the use of conventional stents, several devices dedicated to coronary bifurcations were developed in the last years (Collet et al., 2011). These stents aim to simplify the stenting procedure, even in complex and challenging anatomies, improving the outcomes. Ideally, they should allow permanent access to SB during stenting procedure, provide optimal SB scaffolding, have enhanced deliverability and a modular design to make them applicable for different types of bifurcation lesions (Collet et al., 2011; Lefèvre et al., 2010a).
Dedicated stents can be classified in four groups (Collet et al., 2011; Lefèvre et al., 2010a):

- *Device treating MB with some degree of SB scaffolding.* These stents are implanted following PSB stenting approach, ensuring a more reliable scaffolding of the SB ostium compared to the classical PSB. Since the majority of these devices is characterized by asymmetric design, stent alignment during implantation is a key aspect. Three different categories of stents can be identified based on alignment requirement: self-alignment devices, as for example Multi-Link Frontier™, Pathfinder™, Xience SBA™ (Abbott Laboratories, Abbott Park, IL, USA) (Fig. 2.11 a), Taxus® Petal™ (Boston Scientific, Natick, MA, USA) and Nile CroCo® (Minvasys, Paris, France) stents; controlled alignment devices such as Antares® (TriReme Medical Inc., Pleasanton, CA, USA) and SideKick™ (Y-med Inc., San Diego, CA, USA) stents; devices that do not need alignment such as Stentys™ stent (Stentys S.A., Paris, France).

- *SB stents.* These devices are specifically designed to scaffold the SB and facilitate the stenting procedure. They should be used only for true bifurcation lesions (1,1,0), (1,0,0) or (0,1,0) according to Medina's classification. Sideguard® (Cappella Medical Devices Ltd, Galway, Ireland) and ™ (Tryton Medical Inc., Durham, NC, USA) (Fig. 2.11 b) stents belong to this category.

- *Proximal bifurcation stents.* These devices are designed for (1,0,0) lesions according to Medina's classification. They allow the scaffolding of the MB proximal to the bifurcation up to carina. An example of this kind of dedicated devices is Axxess™ stent (Biosensors International Technologies Pte Ltd, Singapore) (Fig. 2.11 c).

- *Bifurcated stents.* These devices, as for example Medtronic Bifurcation Y-Stent™ (Medtronic, Minneapolis, MN, USA) (Fig. 2.11 d), are characterized by two branches. This particular design results in less flexibility then a single branch stent. Moreover, the risk of wire wrap and misalignment is high because these stents need to be loaded on two wires.

The question whether to use or not dedicated stents is still opened (Secco and Di Mario, 2013). Current dedicated devices are far from being widely adopted in the clinical practice. These devices are associated with the following negative aspects (Lefèvre et al., 2010a): all stents require multi-step approaches, positioning of the stents is not easy because their specific design makes stent alignment delicate, and conformation to complex and various anatomies is not optimal. Clinical validation represents the major issue due to the lack of randomized studies comparing dedicated stents to PSB stenting.

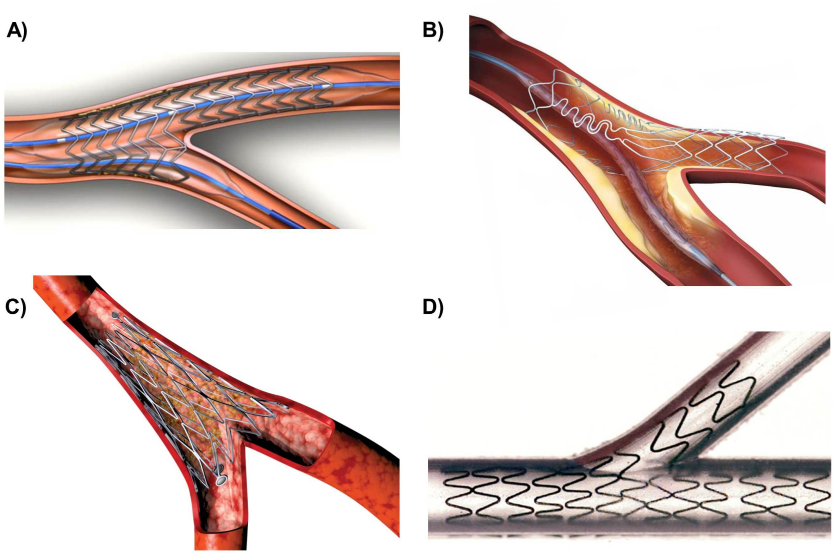

Figure 2.11: Examples of dedicated stents for coronary bifurcations: a) Xience SBA^{TM} (Abbott Laboratories, Abbott Park, IL, USA); b) Tryton^{TM} (Tryton Medical Inc., Durham, NC, USA); c) Axxess^{TM} (Biosensors International Technologies Pte Ltd, Singapore); d) Medtronic Bifurcation Y-Stent^{TM} (Medtronic, Minneapolis, MN, USA).

2.3.3 In-stent restenosis

Stent deployment for the treatment of coronary atherosclerotic lesions can result in two main clinical complications: ISR, which is the reduction in lumen size due to neointima formation within the first months of procedure, and stent thrombosis, which consists in the formation of a blood clot inside the stented artery. As previously exposed in Chapter 1, the present work considers only the ISR phenomenon.

Coronary stents were initially fabricated in a metallic alloy without the coating containing antiproliferative drugs (bare-metal stents). The rate of ISR caused by the implantation of these devices was clinically not negligible (15-20 %) (Baim, 2008). The use of DES, introduced in 2004, has resulted in significantly improved outcomes compared with bare-metal stents (Colombo et al., 2009; Thuesen et al., 2006). ISR rates after DES implantation have fallen below 10 % in several randomized clinical trials (Dangas et al., 2010). However, this rate increases when complex lesions are treated (Lemos et al., 2004; Mauri et al.,

2008; Zahn et al., 2005). Moreover, late restenosis and persistent neointimal growth after DES implantation has been reported (Aoki et al., 2005a,b; Grube et al., 2009; Nakazawa et al., 2011).
ISR is instigated and influenced by the following negative effects induced by stent presence in the coronary artery: structural injury during implantation, foreign-body reaction and local fluid dynamic alteration. Stent deployment results in a complex vascular response that is characterized by four phases, separated in time but partially interdependent (Fig. 2.12) (Edelman and Rogers, 1998; Murphy and Boyle, 2012, 2010b):

- *Thrombosis:* it represents the dominant physiological response in the first

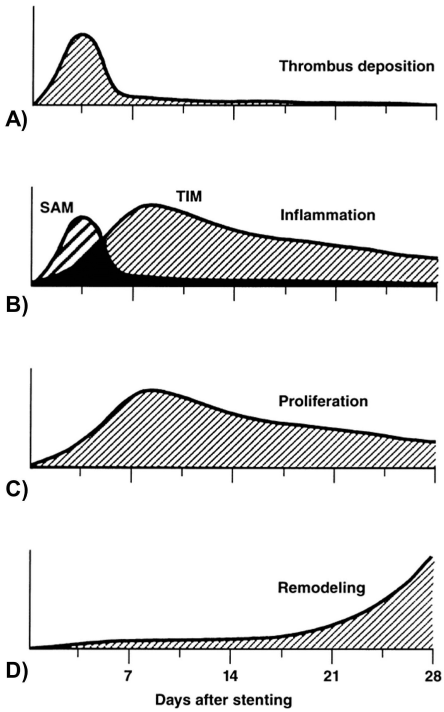

Figure 2.12: The four phases of vascular repair after stent deployment in terms of time after stenting: a) thrombosis; b) inflammation; c) proliferation; d) remodeling. SAM stands for surface-adherent monocyte while TIM for tissue-infiltrating monocyte. *Reprinted with permission from American Journal of Cardiology, Vol. 81(7A): 4E-6E. E.R. Edelman and C. Rogers. Pathobiologic responses to stenting. ©(1998) Excerpta Medica Inc.*

7 days after stent implantation with a peak at 3-4 days. During the implantation procedure, the stent and the balloon damage most of the endothelial cells on contact, exposing to the blood flow deeper wall structures as collagen fibers; moreover, the plaque is compressed and, in extreme cases, the inner arterial wall is dissected. These injuries provoked by stent implantation induce coagulation. Platelets present in the bloodstreams are activated by damaged endothelial cells, exposed collagen, and plaque. These platelets adhere to the damaged cells and release chemical attractants for other platelets. The coagulation cascade, which involves several coagulation factors (Van Dem-Mieras and Muller, 1986), leads to the formation of the fibrin around the platelets, binding them together into a thrombus. Thrombus formation is also caused by foreign-body reaction. Different blood-soluble proteins adsorb onto the stent surface and forms a thin film that controls the successive biological processes of the foreign-body response (Anderson et al., 2008). Fibrinogen, which is a pro-thrombotic protein, promoting activation and adhesion of platelets, is adsorbed preferentially over the other proteins.

- *Inflammation:* inflammatory reaction occurs immediately after stenting in the site where thrombus forms. Surface-adherent leukocytes are attracted to the injured site in order to prevent the propagation of the tissue damage and infection, and to aid in wound healing and tissue repair (McLaren and Kennedy, 2005). At 3-7 days after intervention, leukocytes migrate into the arterial wall as tissue-infiltrating monocytes (TIM) and remain there. These leukocytes infiltrate the injured site following a mechanism characterized by four steps (Fig. 2.13): tethering (i.e. initial contact), rolling and activation of the cell, firm adhesion, and lastly transmigration into the arterial wall.

- *Proliferation:* a new tissue (i.e. neointima) grows around the implanted stent as a result of foreign-body reaction and injury provoked by stent deployment. Smooth muscle cells migrate from the middle layer of the arterial wall towards the stent where they proliferate. These cells synthesize collagen creating the bulk of the new tissue that narrows the coronary artery. This phase coincides with the migration of inflammatory cells from vessel surface to the neointima 7 days after stent deployment. It can last up to 18 months after the intervention.
  NH occurs when the proliferation of smooth muscle cells with concomitant deposition of extracellular matrix molecules is uncontrolled, causing an excessive growth of neointima. This phenomenon represents the main

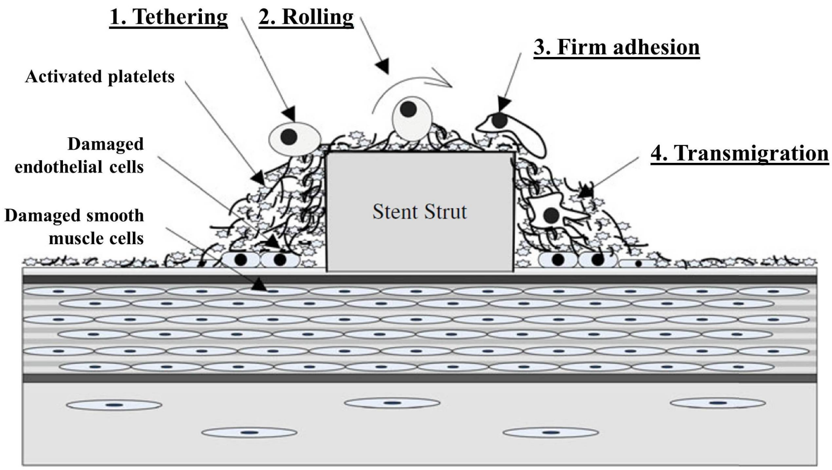

Figure 2.13: Diagram showing the four steps followed by leukocytes to infiltrate the injured site: (1) tethering (i.e. initial contact), (2) rolling and activation of the cell, (3) firm adhesion, and (4) transmigration into the arterial wall. *Reprinted with permission from Cardiovascular Engineering and Technology, Vol. 3(4): 353-373. E.A. Murphy and F.J. Boyle. Reducing in-Stent restenosis through novel stent flow field augmentation. ©(2012) Biomedical Engineering Society.*

cause of ISR. The degree of NH is greatly influenced by the degree of thrombosis and inflammation.

- *Remodeling:* coronary artery opposes the strain caused by stent strut by increasing collagen deposition, destruction of elastin, and persistent inflammation. From about 4 weeks after the stent implantation, collagen deposits in the adventitia and throughout the tunica media and neointima lead to shrinkage of the artery. This process increases the pressure on the device and may squeeze the arterial wall through the stent strut interstices from the outside.

Local hemodynamics play an important role in all the four phases that characterize the vascular response to stent implantation (Murphy and Boyle, 2012). In Section 3.1 the relation between local hemodynamic effects induced by the presence of a stent inside a coronary artery and the most commonly investigated hemodynamic variables is discussed.

Chapter 3

State-of-the-art of CFD models of stented coronary arteries

In the present chapter a review of the fluid dynamic studies on stented coronary arteries is given, focusing on CFD models. Indeed, CFD provides a useful tool for studying macro and micro aspects of blood flow through stented vessels and their influence on ISR.
The mathematical definitions of the most investigated hemodynamic quantities used in this research field and their relation with ISR are introduced. The fluid dynamic models of idealized stented coronary arteries are discussed, focusing on coronary bifurcations. The fluid dynamic models based on geometries reconstructed through imaging techniques are presented. In the end, the most significant limitations of the CFD studies are provided.

The contents within this chapter can be found in:
Chiastra C. and Migliavacca F., *Modelling of blood flow in stented coronary arteries*. In Becker, S. and Kuznetsov, A., editors. Heat transfer and fluid flow in biological processes, Elsevier (accepted for publication).

3.1 Hemodynamic quantities of interest

DISTURBED flow patterns, such as flow separation and reattachment, recirculation zones, significant secondary flow velocities, and stagnation point regions, play a key role in the onset and progression of atherosclerosis and NH (Archie Jr. et al., 2001). These altered flow patterns are due to the flow-input waveforms and to the geometrical features of the vessel (e.g. sudden expansions, sharp bends, bifurcations and the presence of the stent struts).

Several quantities are considered in the study of the disturbed flow, including the hemodynamic alterations induced by the stent presence, to identify sites in the coronary artery that might be prone to ISR. In this section, for each of the widely used quantities, the mathematical definition and the relation between them and the ISR is provided. The quantities are classified in near-wall quantities, quantities for the measure of flow stasis and flow separation, and bulk flow quantities.

3.1.1 Near-wall quantities

The main investigated quantity is the WSS which plays a fundamental role in the atherosclerotic processes (Chatzizisis et al., 2007). WSS is defined by the following relation:

$$\boldsymbol{\tau}_w = \boldsymbol{n} \cdot \boldsymbol{\tau}_{ij} \tag{3.1}$$

where $\boldsymbol{n}$ is the normal vector to the arterial wall surface and $\boldsymbol{\tau}_{ij}$ is the fluid viscous stress tensor. The magnitude of WSS vector is equal to the viscous stress on the surface and the direction of WSS is the direction of the viscous stress acting on the surface.

When time-dependent flows are studied, the time-averaged WSS (TAWSS) is introduced. It is calculated as:

$$TAWSS = \frac{1}{T} \int_0^T |\boldsymbol{\tau}_w| \, dt \tag{3.2}$$

where T is the duration of cardiac cycle.

From a biological standpoint, endothelial cell morphology and orientation are altered according to WSS. Endothelial cells subjected to WSS greater than 1 Pa have been shown to elongate and align themselves in the direction of flow, while those experiencing WSS lower than 0.4 Pa or oscillatory WSS were circular in shape, without showing any preferred alignment pattern (Fig. 3.1)(Malek et al., 1999). WSS changes may alter the endothelial cells in shape as well as

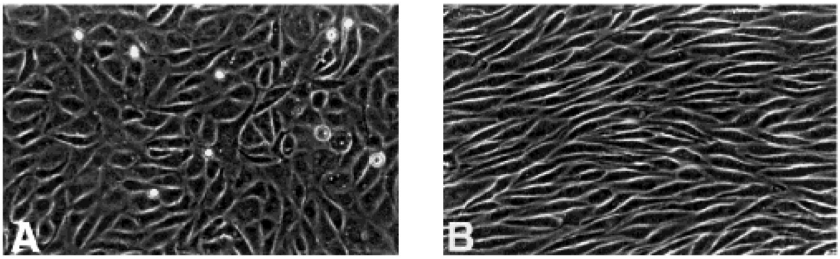

Figure 3.1: Phase contrast micrographs of bovine aortic endothelial cells: a) cells exposed to low WSS (< 0.4 Pa) for 24 hours do not elongate; b) cells exposed to physiologic WSS (> 1.5 Pa) align in the direction of blood flow. *Adapted with permission from Journal of Cell Science Vol.109(4): 713-726. A.M. Malek and S. Izumo Mechanism of endothelial cell shape change and cytoskeletal remodeling in response to fluid shear stress. ©(1996) Company of biologists.*

function. This alteration could increase cell permeability to serum substrates, either through the intercellular junction or by vesicular transport to the subendothelium, as in the case of atherosclerotic lesions (Gerlach et al., 1990; Okano and Yoshida, 1993). It has been also highlighted through animal experiments that tissue regrowth in a stented coronary artery is prominent at the sites of low WSS (LaDisa Jr. et al., 2005).
In the CFD studies on stented coronary arteries both thresholds of 0.4 Pa, e.g. Gundert et al. (2011) and Williams et al. (2010), and 0.5 Pa, e.g. Balossino et al. (2008) and Duraiswamy et al. (2009), are used to identify the low values of WSS that are associated with intimal thickening.
Analyses based only on the magnitude of WSS alone are not sufficient because variations in shear stress in both time and space have an influence on ISR phenomenon (Chatzizisis et al., 2007). The oscillatory nature of shear stress induced by pulsatile flow is quantified using the oscillatory shear index (OSI), which was defined by Ku et al. (1985) as:

$$OSI = \frac{1}{2}\left(1 - \frac{\left|\int_0^T \boldsymbol{\tau}_w dt\right|}{\int_0^T |\boldsymbol{\tau}_w|\, dt}\right) \tag{3.3}$$

where T is the period of the cardiac cycle, and $\boldsymbol{\tau}_w$ is the WSS vector. OSI values range between 0, when there is no oscillatory WSS, to 0.5 when there is the maximum oscillatory WSS. Regions characterized by high oscillatory WSS (OSI > 0.1, Williams et al. (2010)) have shown a greater risk of arterial narrowing (Zarins et al., 1983). High OSI have been associated to an increase of the endothelial permeability to blood borne particles (Himburg et al., 2004) and to

a greater production of the gene endothelin-1 mRNA which increases cell proliferation (Malek and Izumo, 1992). In addition, it has been shown that low and oscillatory WSS increase the expression of inflammatory markers, including the ICAM-1 and the VCAM-1 (Chatzizisis et al., 2007; Chiu and Chien, 2011), thus indicating cell activation. In the experimental study by Yin et al. (2011) it was found that cell surface ICAM-1 expression is significantly enhanced when coronary endothelial cells are exposed to low pulsatile shear stresses, indicating endothelial cell activation. These results, which are in agreement with the findings from other works (Dai et al., 2004; Dardik et al., 2005), suggested that this hemodynamic condition is atherogenic.
In order to combine the information provided by WSS and OSI, the relative residence time (RRT) was recently introduced (Himburg et al., 2004):

$$RRT = \frac{1}{(1 - 2 \cdot OSI) \cdot TAWSS} \tag{3.4}$$

High RRT is recognized as critical for the problem of atherogenesis and ISR (Hoi et al., 2011). RRT is also associated to the residence time of the particles near the wall (Himburg et al., 2004).
Another quantity of interest is the spatial wall shear stress gradient (WSSG). To mathematically define it, a local *m-n-l* coordinate system has to be introduced, where *m* is the WSS direction tangential to the endothelial surface (temporal mean WSS direction for pulsatile flows), *n* is the direction tangential to the surface and normal to *m*, and *l* is the endothelial surface normal direction. Using this coordinate system, the WSSG can be obtained calculating spatial derivatives of WSS, which results in a nine-component tensor:

$$\nabla \boldsymbol{\tau}_w = \begin{bmatrix} \frac{\partial \tau_{w,m}}{\partial m} & \frac{\partial \tau_{w,m}}{\partial n} & \frac{\partial \tau_{w,m}}{\partial l} \\ \frac{\partial \tau_{w,n}}{\partial m} & \frac{\partial \tau_{w,n}}{\partial n} & \frac{\partial \tau_{w,n}}{\partial l} \\ \frac{\partial \tau_{w,l}}{\partial m} & \frac{\partial \tau_{w,l}}{\partial n} & \frac{\partial \tau_{w,l}}{\partial l} \end{bmatrix} \tag{3.5}$$

where $\nabla = \left(\mathbf{m}\frac{\partial}{\partial m} + \mathbf{n}\frac{\partial}{\partial n} + \mathbf{l}\frac{\partial}{\partial l}\right)$ and $\mathbf{m}$, $\mathbf{n}$, and $\mathbf{l}$ are the unit vectors in their respective direction. As suggested by Lei et al. (1996), the components $\frac{\partial \tau_{w,m}}{\partial m}$ and $\frac{\partial \tau_{w,n}}{\partial n}$ are the most important ones for intimal thickening due to atherosclerosis or hyperplasia. In fact, these components generate intracellular tension, which causes widening and shrinking of the cellular gaps. Therefore, the WSSG can be written as:

$$WSSG = \left[\left(\frac{\partial \tau_{w,m}}{\partial m} \right)^2 + \left(\frac{\partial \tau_{w,n}}{\partial n} \right)^2 \right]^{1/2} \tag{3.6}$$

Results of *in vitro* and numerical studies (DePaola et al., 1992; Truskey et al., 1995) showed that large spatial WSSG induce morphological and functional changes in the endothelial cells, which contribute to increase the wall permeability, and hence possible atherosclerotic lesions. Endothelial cells have been shown to migrate downstream of an area with high WSSG (DePaola et al., 1992). This phenomenon could affect the process of growth of a new layer of endothelial cells after the damage provoked by stent implantation (Murphy and Boyle, 2010b). Moreover, regions that are susceptible to NH have been correlated with sites where WSSG has been predicted to exceed 200 N/m^3 in an end-to-side anastomosis model (Ojha, 1993) and a rabbic iliac model (LaDisa Jr. et al., 2005).

3.1.2 Flow stasis quantities

In order to quantify the flow stasis, the mean exposure time (MET) can be calculated. By releasing a high concentration of fluid particles at the inlets of an artery model, MET measures how long each particle reside within each element of the mesh (Gundert et al., 2011; Lonyai et al., 2010). For each element e of the computational grid, MET is defined as:

$$MET_e = \frac{1}{N_e V_e^{1/3}} \sum_{p=1}^{N_t} H_e^p(t) dt \tag{3.7}$$

where N_e is the number of times a particle passes through the element, V_e the volume of the element, N_t is the total number of particles released, and $H_e^p(t)$ is equal to 1 when a particle p is located inside the element at time t and is equal to 0 otherwise. In stented models highly anisotropic meshes with finer elements close to the struts are needed. Since MET index depends on the element size, these meshes are not suitable. Therefore, an auxiliary isotropic mesh has to be used during the post-processing step for the MET calculation.

Since the duration that a particle resides within an element is normalized by the N_e, MET is able to distinguish between recirculating particles and stagnant particles (Gundert et al., 2011). For example, a particle that passes twice through an element, each pass spanning one time unit, does not contribute as much to MET as a particle that passes once for two time units (Lonyai et al., 2010). In this particular case, the first particle is probably recirculating while the second

one is stagnant.
Other quantities have been used in the study of stented coronary artery models to analyze stagnation and recirculation regions. For example, the flow separation parameter (FSP) quantifies the fraction of time with respect to one cardiac cycle where the flow at some location on the arterial wall is separated from the mainstream flow due to stagnation or recirculation (He et al., 2005). Mathematically, FSP was calculated by He et al. (2005) as:

$$FSP = \frac{T_s}{T} \tag{3.8}$$

where T_s is the amount of time that the flow is separated from the mainstream, and T the period of the cardiac cycle. FSP only varies spatially. It is defined to occur when the wall shear has the opposite sign from the mainstream flow. A value of 0 implies no flow separation while a value of 1 constant flow separation throughout the entire flow period (recirculation or stagnation).
Equation 3.8 is valid only for a high flow condition (e.g. Reynolds number = 240, WSS = 1 $\pm$ 0.5 Pa) while, for a low flow condition (e.g. Reynolds number = 50, WSS = 0.2 $\pm$ 1 Pa), it has to be modified to account for the natural shear stress oscillation as follows (He et al., 2005):

$$FSP = \frac{T_P\left(\Phi_{pos}\right) + T_N\left(\Phi_{neg}\right)}{T} \tag{3.9}$$

where Φ_{pos} is the FSP during the time of forward mainstream flow T_P, Φ_{neg} is the FSP during the time of reverse mainstream flow T_N, and T is the period of the cardiac cycle $(T = T_P + T_N)$.
FSP is large in regions where stent strut spacing is small, as demonstrated by Berry et al. (2000) comparing *in vitro* and CFD results.

3.1.3 Bulk flow quantities

The effect of stenting procedures on the bulk flow can be evaluated through the analysis of the helicity (Chiastra et al., 2013). By definition, the helicity of a fluid flow confined to a domain D of the Euclidean space R^3 is given by the integral value of the kinetic helicity density H_k, defined as (Moffatt and Tsinober, 1992):

$$H_k = (\nabla \times \boldsymbol{v}) \cdot \boldsymbol{v} \tag{3.10}$$

where $\boldsymbol{v}$ is the velocity vector and $\nabla \times \boldsymbol{v}$ is the vorticity. To better visualize the topological features of the flow field, the kinetic helicity density can be normalized with the velocity and vorticity magnitude resulting in the local normalized helicity (LNH):

$$LNH = \frac{(\nabla \times \boldsymbol{v}) \cdot \boldsymbol{v}}{|(\nabla \times \boldsymbol{v})|\,|\boldsymbol{v}|} = \cos\theta \tag{3.11}$$

where θ is the angle between $\boldsymbol{v}$ and $\nabla \times \boldsymbol{v}$. LNH is a non-dimensional quantity that ranges between -1 and 1. Physically, this quantity describes the arrangement of fluid streams into spiral patterns as they evolve within conduits (Morbiducci et al., 2007). In fact, it is a measure of the alignment/misalignment of the local velocity and vorticity vectors and its sign is a useful indicator of the direction of rotation of helical structures: positive LNH values indicate left-handed rotating fluid structures, while negative LNH values indicate right-handed rotating structures, when viewed in the direction of the forward movement.

The helical flow is a peculiar feature of natural blood flow present in arteries (Kilner et al., 1993; Morbiducci et al., 2011) and it has been recently found to be essential in suppressing flow disturbances in healthy vessels (Gallo et al., 2012) and in stented arteries and bypass grafts (Chen et al., 2011a; Morbiducci et al., 2007; Zheng et al., 2012).

Helicity can be also evaluated calculating other descriptors. For example, in Morbiducci et al. (2007) a lagrangian-based analysis has been proposed for an aortocoronary bypass model. However, this kind of approach has not been applied to stented coronary arteries yet.

3.2 Fluid dynamic models of idealized stented geometries

In the recent years, numerous CFD studies on stented coronary arteries have been proposed in the literature. Initially, these models were characterized by two-dimensional (2D), highly simplified geometries. For example, in the study conducted by Berry et al. (2000) only a cross-section of the region very close to the arterial wall, with eight struts, was investigated. With the gradual increase of the computational resources, the analysis of 3D stented geometries became possible. Complex models, with or without bifurcations, and with the presence of multiple stents, were investigated. As proposed by Murphy and Boyle (2010b), the works on stented coronary arteries can be classified in two categories:

- *Effect-based studies*: Two or more models with a well-defined difference are compared from the fluid dynamic point view. This category includes the comparison of straight and curved coronary arteries, Newtonian versus non-Newtonian blood flow, different stent sizing, different stenting techniques.

- *Design-based studies*: The impact of the geometric configuration itself on hemodynamic quantities is investigated. This category includes the comparison between different strut designs, strut spacing or commercial stent designs.

In this section the main works on stented coronary bifurcations based on geometries that were not reconstructed through imaging techniques (idealized geometries) are presented. Indeed, the studies on idealized single-vessel geometries are discussed in details in the review by Murphy and Boyle (2010b).
Coronary bifurcations are characterized by recirculation and stagnation zones that cause low WSS, making these regions very prone to develop atherosclerosis. Many stenting techniques that involve the implantation of one or two stents, conventional or dedicated to bifurcation, exist (Section 2.3.2). Each procedure is associated with some limitations that make uncertain the choice of the best-fitting treatment.
The CFD studies presented here all belong to the effect-based category. Different stenting strategies for the treatment of bifurcation lesions are compared. The first CFD study on stented coronary bifurcations was carried out by Deplano and coworkers in 2004 (Deplano et al., 2004). These researchers studied the hemodynamic changes induced by the presence of two stents in a 90° bifurcated coronary (Fig. 3.2a). They investigated six different cases, simulating different post-implantation configurations (Fig. 3.2b). Case 1 was modeled as a healthy coronary bifurcation without any stent in order to provide a reference case; Case 2 was representative of a double implantation not followed by an enlargement of the SB cell, while Case 3 was followed by an optimum enlargement; Cases 4-6 modeled an imperfect enlargement with a partial opening of the stent struts in the MB lumen.
The Palmaz® P308 stent (Cordis Corporation, Bridgewater, NJ, USA), which belongs to an old generation of slotted tube stent, was considered in this study. A flow-rate curve recorded in a human left coronary artery (Berne and Levy, 1967) was imposed at the inlet of the models. A constant flow-rate repartition, based on the diameters of the two daughter arteries, was applied at the outlets. The no-slip condition was imposed along the walls. Blood was modeled as a Newtonian fluid characterized by a density of 1060 kg/m^3 and a dynamic viscosity of 3.6 cP. Since the Reynolds number based on the inlet diameter was $\sim$200 at peak flow rate, an order of magnitude smaller than the Reynolds num-

ber for transition to turbulence (2300) (Spurk and Aksel, 2008), the flow was assumed to be laminar. The commercial software ANSYS Fluent (ANSYS Inc.,

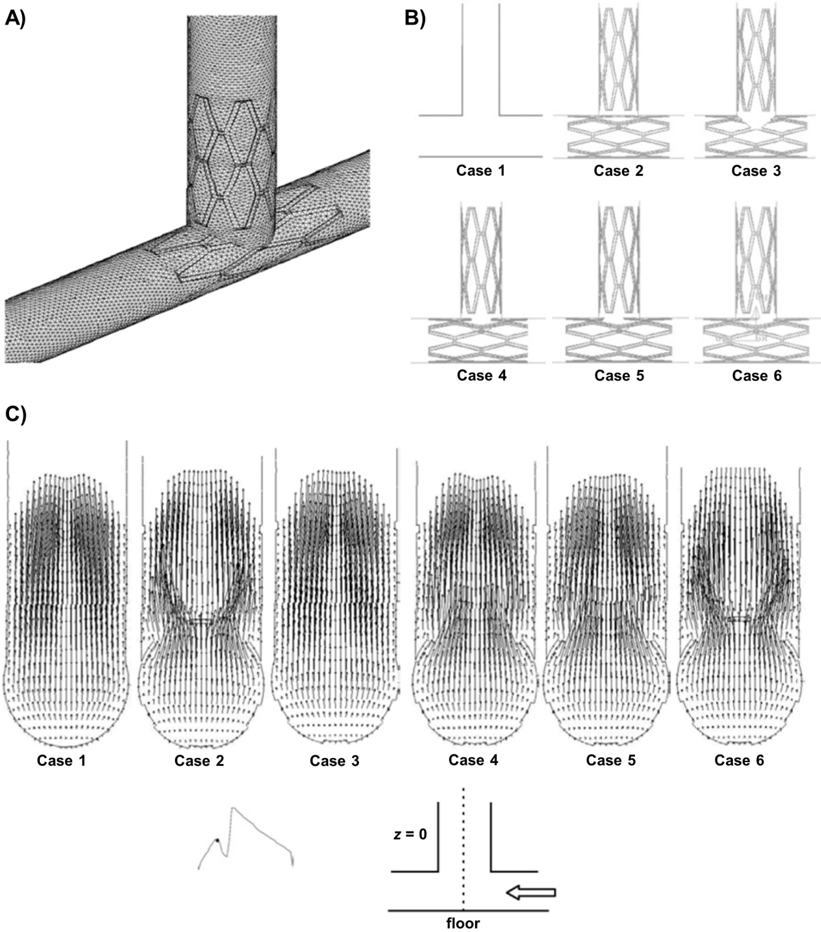

Figure 3.2: a) 90° bifurcated coronary artery model with two implanted stents used by Deplano et al. (2004). The surface mesh is shown. b) Projection views of the six investigated geometrical configurations. c) Flow evolution in the longitudinal plane (z = 0) at the first time of acceleration. *Adapted with permission from Medical and Biological Engineering and Computing 2004 Vol.42(5): 650-659. V. Deplano et al. 3D numerical simulations of physiological flows in a stented coronary bifurcation. ©(2004) Springer.*

Canonsburg, PA, USA), which is based on the finite volume method, was used to solve the Navier-Stokes equations.
Results demonstrated that, behind the protruding stent struts located near the inner and the outer walls of the SB, some flow stasis and recirculation areas develop, causing low WSS values. Figure 3.2c shows the flow characteristic in the longitudinal plane (z = 0) at the first time of acceleration. Case 1 and 3 (without stent or completely opened) are similar without stasis areas. For cases 2, 4-6 the two lateral stent struts act as a convergence pipe that orientates and accelerates the flow at the center. Moreover, for cases 2 and 6 two lateral jets are created, with stasis areas downstream from the luminal struts. The WSS at the stent wall were also investigated. High WSS values of about 20 Pa, which could stimulate platelet activation potentially leading to thrombo-embolic complications, were induced by the struts protruding into the SB. The authors concluded that, in terms of fluid dynamics, the best situation is obtained when the stent struts were ideally removed from the SB (Case 3).
Williams et al. (2010) quantified the altered hemodynamics caused by MB stenting and subsequent SB angioplasty that removed the stent struts from the ostium of a representative coronary bifurcation. Four different scenarios were compared: (1) pre-stenting, (2) post MB stenting with the best stent orientation, (3) post MB stenting with the worst stent orientation, and (4) post SB balloon angioplasty. An idealized bifurcation model was created with a typical bifurcation angle (46°) and Finet's law (Eq. 2.3) for the inlet and outlet diameter values, using a computer-aided design (CAD) software. A Boolean intersection command was implemented to subtract the geometrical model of the stent from the lumen, obtaining the fluid domain for the CFD simulation. The Taxus® Express 2™ stent (Boston Scientific, Natick, MA, USA) was considered in this work. As boundary conditions, resting and hyperemic inflow waveforms (Reynolds number ∼90 and ∼240, respectively), obtained from a canine left anterior descending coronary artery (LAD), were applied at the inlet cross-section as temporally varying Womersley velocity profiles.
In order to estimate the behavior of the downstream vasculature, a three-element Windkessel model was imposed at the outlets using a multi-domain approach (Vignon-Clementel et al., 2006). The three-element Windkessel model is defined by three parameters with physiologic meaning: R_c, C, and R_d. R_c is the characteristic impendence representing the resistance, compliance and inertance of the proximal artery of interest, C is the arterial capacitance and describes the collective compliance of all arteries beyond a model outlet, and R_d represents the total distal resistance beyond a given outlet. Blood was assumed to behave as a Newtonian fluid with a density of 1060 kg/m^3 and a dynamic viscosity

of 4cP. TAWSS and OSI were quantified. In Fig. 3.3a the contour maps of TAWSS are depicted. The non-diseased bifurcation model was not characterized by TAWSS lower than 0.4 Pa. Stenting introduced areas of low TAWSS next to the struts both under resting and hyperemic flow conditions. Moreover, eccentric regions of low TAWSS were present along the lateral wall of the MB after MB stenting. Virtual SB angioplasty resulted in a more concentric area of low TAWSS in the distal MB and along the lateral SB. Despite the regional variation in the location of low TAWSS, the luminal surface exposed to low TAWSS was similar before and after virtual SB angioplasty (rest: 43% vs. 41%; hyperemia: 18% vs. 21%). High OSI (> 0.1) were absent in the non-diseased model (Fig. 3.3b). Considering the models after MB stenting, only 4% and 8% of the luminal surface was exposed to elevated OSI during rest and hyperemia, respectively. Virtual SB angioplasty reduced the percentage area exposed to high OSI at rest (1%) but had little impact under hyperemic conditions (7%). These results demonstrated that SB angioplasty intervention could not be a real benefit from a fluid dynamic point of view.
The method for obtaining the fluid domain used in the previous works (Deplano et al., 2004; Williams et al., 2010) is exclusively based on geometrical/anatomic information that neglects both the mechanical behavior of the stent and the biological tissues, as well as their interaction during stenting procedures. To overcome this limitation, Morlacchi et al. (2011a) proposed a sequential structural and fluid dynamic approach that allowed the researchers to consider the artery deformation during stenting procedure for the creation of the fluid domain. Firstly, the PSB technique, which nowadays is the preferred coronary bifurcation stenting procedure (Behan et al., 2011), was simulated by means of structural simulations. Secondly, the final geometrical configurations obtained through structural simulations were used as fluid domains to perform transient CFD analyses. A further study based on the same sequential approach was proposed by Chiastra et al. (2012). The authors examined the different hemodynamic scenarios provoked by FKB performed with a proximal or a distal access to the SB. These last two studies (Chiastra et al., 2012; Morlacchi et al., 2011a) represent a part of this thesis and are discussed in detail in Chapter 6.
In the work by Katritsis et al. (2012) a comparison of different stenting techniques was also made from the fluid dynamic perspective. The authors investigated both single and double stenting procedures, calculating the near-wall quantities (TAWSS, OSI and RRT). In particular, they compared six cases: (1) stenting of the MB only, (2) stenting of the MB followed by balloon angioplasty of the SB, (3) balloon angioplasty of the SB followed by stenting of the MB, (4) culotte technique, (5) crush technique, (6) T-stenting. A geometrical model of

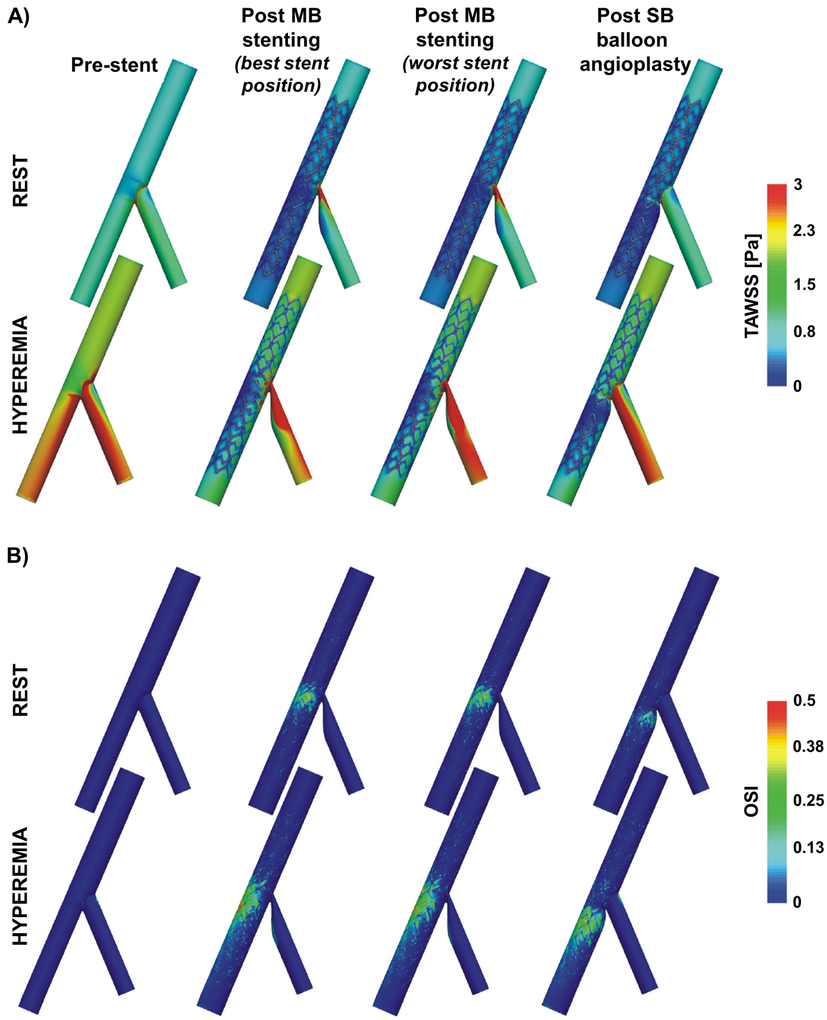

Figure 3.3: Contour maps of (a) TAWSS and (b) OSI obtained by Williams et al. (2010) for the four different scenarios: pre-stenting, post MB stenting with the best stent orientation, post MB stenting with the worst stent orientation, and post SB balloon angioplasty. Results are shown under resting and hyperemic conditions. *Adapted with permission from Medical and Journal of Applied Physiology 2010 Vol.109(2): 532-540. A.R. Williams et al. Local hemodynamic changes caused by main branch stent implantation and subsequent virtual side branch balloon angioplasty in a representative coronary bifurcation. ©(2010) The American Physiological Society.*

an idealized human LAD and its diagonal branch was considered with a bifurcation angle of 50° following the Finet's law (Eq. 2.3). A CAD software was used to draw a single stent or two stents inside the bifurcation, with a procedure similar to Williams et al. (2010), obtaining the six different investigated configurations. As stent design, the PROMUS Element™ stent (Boston Scientific) was considered. Blood was modeled as a Newtonian fluid with dynamic viscosity 3.5 cP and density 1060 kg/m^3. At the inlet a pulsatile blood flow curve was prescribed (Berne and Levy, 1967) while, at the outlet boundaries, the flow was assumed to split proportionally to the (3/2) power of the outlet diameters. CFD simulations were performed using ANSYS Fluent.
Figure 3.4 shows the contour maps of RRT for the six investigated cases. Larger areas exposed to high RRT are located in the cases with two implanted stents with respect to a single implanted stent. This result indicate that stenting of the MB with or without balloon angioplasty of the SB offers hemodynamic advantages over double stenting. This finding supported the results of large clinical trials that documented that stenting of the MB only is preferable in the majority of bifurcation lesions (Behan et al., 2011; Katritsis et al., 2009). Considering double stenting procedures, crush technique could result in better hemodynamics if compared to culotte or T-stenting.
In the end, Chen et al. (2012) investigated the role of the SB diameter, angle, and lesion on hemodynamics in case of MB stenting. 3D geometrical models of

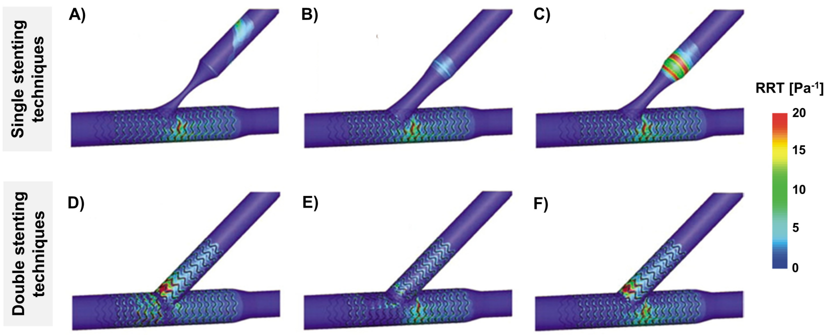

Figure 3.4: Contour maps of RRT for the six cases investigated by Katritsis et al. (2012): a) stenting of the MB only; b) stenting of the MB followed by balloon angioplasty of the SB; c) balloon angioplasty of the SB followed by stenting of the MB; d) culotte technique; e) crush technique, f) T-stenting. *Adapted with permission from Circulation: Cardiovascular Interventions 2012 Vol.5(4): 448-454. D.G. Katritsis et al. Flow patterns at stented coronary bifurcations: Computational fluid dynamics analysis. ©(2012) Wolters Kluwer Health.*

coronary bifurcation with a generic coronary stent inside were created using a CAD software. Corrected-sized as well as 5% and 10% under-sized stent models were considered. Bifurcation angles of 30° and 70° as well as bifurcations with diameter ratios of SB/MB = 1/2 and 3/4 were studied. A mild stenosis at the SB (40% in area) was also introduced in the analyses. Blood was modeled as a non-Newtonian Carreau fluid with a density of 1060 kg/m^3. At the inlet, a pulsatile velocity curve based on a human LAD was applied. At the outlets, a traction-free boundary condition was imposed. The results highlighted that the stent undersizing decreased the WSS and increased the WSSG and OSI values. Stenting of the MB in bifurcations with larger SB/MB ratios or smaller SB angle resulted in lower WSS, higher WSSG and OSI. Stenosis at the SB lowered WSS and increased WSSG and OSI. Considering these results, MB stenting could not be optimal in bifurcations with large SB diameter, small angle and SB stenosis.

3.3 Fluid dynamic models of imaged-based stented geometries

The CFD studies on stented coronary arteries mentioned in Section 3.2 are based on idealized geometries. Although in two of these works (Chiastra et al., 2012; Morlacchi et al., 2011a) a sequential structural and fluid dynamic approach was used to consider the effects of stenting procedure on the geometry of the model, realistic fluid domains obtained through imaging techniques are needed for a more reliable evaluation of stent performance and hemodynamic alterations induced by stenting, and also for a better comprehension of the ISR phenomenon.

In this section, CFD studies based on geometries reconstructed through imaging techniques are reviewed. These studies are classified in three categories according to the origin of the images used for the creation of the fluid domain: *in vitro* models (Section 3.3.1), animal models (Section 3.3.2), and patients (Section 3.3.3).

3.3.1 CFD studies from *in vitro* model images

Foin et al. (2012b) evaluated post-dilatation strategies after MB stenting. The following scenarios were compared: (1) MB stenting only, (2) stenting of the MB followed by FKB, (3) stenting of the MB concluded by 2-step sequential post-dilation. A series of DES was implanted in silicone models of coro-

nary bifurcations. Micro-computed tomography (micro-CT) scans of the stents were used to create the fluid volumes for subsequent CFD simulations (unfortunately, no detailed information were provided by the authors about this step). As boundary conditions, a flow waveform recorded in a human LAD was applied at the inlet cross-section of each model. A flow split of 70% and 30%, respectively for the MB and the SB, was imposed at the outlets. Blood was assumed to be a Newtonian fluid. The analyses were performed with the commercial software ANSYS CFX (ANSYS Inc., Canonsburg, PA, USA).
The results of the work in terms of flow patterns and shear rates are depicted in Fig. 3.5. Flow distribution toward the SB showed higher velocity near the carina and lower velocity opposite the carina. This difference was more evident in case of MB stenting because the flow directed to the SB was impaired by the stent struts covering the SB ostium. Moreover, a large area of high shear rate was located around these struts. Flow patterns in FKB and 2-step cases were more stable with a less disturbed SB flow if compared to the MB stenting only. High shear rates were situated in correspondence of the malapposed struts (i.e. the struts that are not in contact with the underlying vessel wall) near the carina.
The fluid dynamic analyses represent a part of the work of Foin et al. (2012b). The rate of strut malapposition was calculated analyzing the reconstructed geometrical models of the bifurcations. FKB and 2-step post-dilation techniques significantly reduced the rate of strut malapposition with respect to MV stenting only. However, FKB led to a higher risk of incomplete stent apposition at the proximal stent edge. Considering all the results, the authors concluded that sequential 2-step post-dilation might offer a simpler and more efficient alternative to FKB.
CFD analyses were performed also in a similar study by the same research group (Foin et al., 2012a). The crush technique followed by FKB inflation was investigated. Extensive layers of malapposed struts were observed in the lumen. The unapposed struts in the neocarina caused severe flow disturbances with high shear rate that might increase the risk of platelet adhesion and stent thrombosis.

3.3.2 CFD studies from animal models

Morlacchi et al. (2011b) investigated blood flow patterns in a realistic stented porcine coronary artery geometry using a model that combines data from *in vivo* experiments, 3D imaging techniques and CFD simulations. Twelve BiodivYsio^{TM} stents (Biocompatibles International Plc, Farnham, UK) were implanted individually into the RCA and the LAD of six healthy Yorkshire

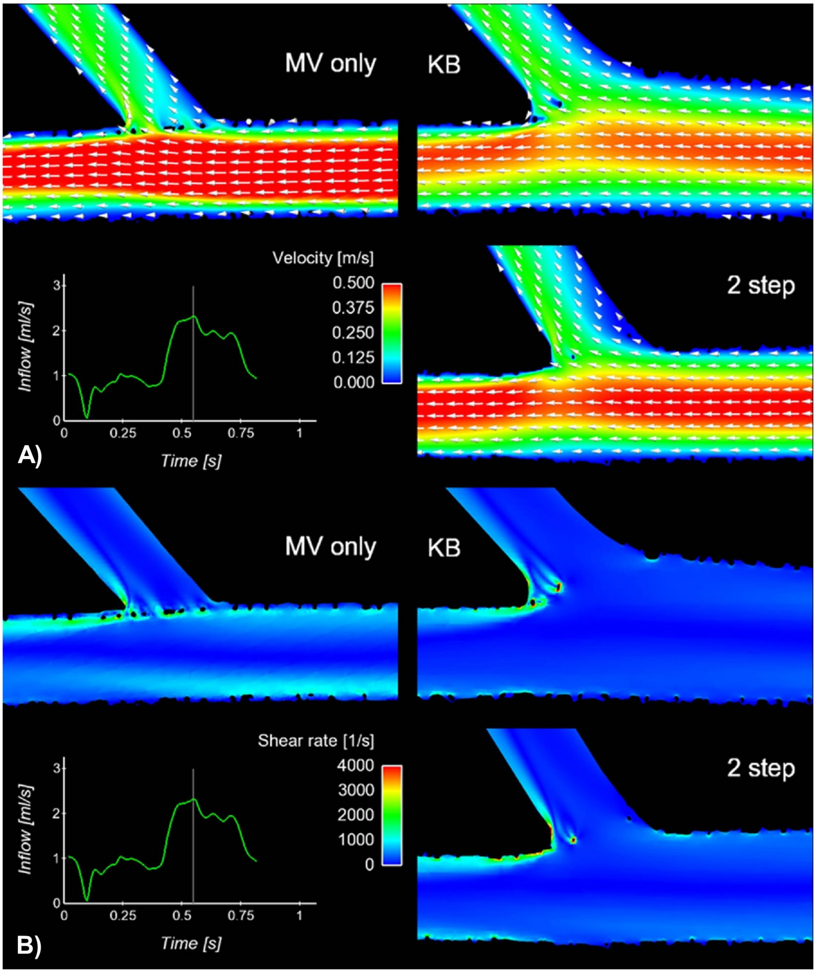

Figure 3.5: Velocity field (a) and shear rate contour maps (b) for the different stenting techniques: MB stenting only (MV only), stenting of the MB followed by FKB (KB), stenting of the MB concluded by 2-step sequential post-dilation (2 step). *Reprinted with permission from JACC: Cardiovascular Interventions 2012 Vol.5(1): 47-56. N. Foin et al. Kissing balloon or sequential dilation of the side branch and main vessel for provisional stenting of bifurcations: Lessons from micro-computed tomography and computational simulations. ©(2012) Elsevier*.

White pigs, respectively. The stents were intentionally overexpanded in order to damage the vessels and, consequently, produce a significant growth of neointimal tissue. The animals were sacrificed at different times, from 6 hours to 28 days post-implantation. The stented segments were scanned using micro-CT, and then embedded and cut with high-speed precision saw in order to obtain sections for histological analyses. One case was selected for numerical analyses (stent deployed in RCA, explanted after 14 days).
Starting from micro-CT images, the 3D geometry of the stent was reconstructed. Since the arterial wall could not be extracted from micro-CT images, a structural simulations was performed (Fig. 3.6a): the model of the artery was expanded under displacement control until its internal diameter was greater than the stent diameter; then, the artery retracted due to elastic recoil coming into contact with the undeformable structure of the stent. Fluid domain was extracted with a similar procedure used by the same research group (Morlacchi et al., 2011a). In order to reduce the high computational cost, only the first two repeating units of the proximal end of the stent were considered in the CFD analyses. As boundary conditions, at the inlet a velocity waveform of a porcine RCA taken from literature (Huo et al., 2009) was imposed with a paraboloid-shaped profile. At the outlet a relative pressure of 0 Pa was set. The artery and the stent were considered as wall boundaries. Blood was considered as a non-Newtonian Carreau fluid with a density of 1060 kg/m^3. Simulations were carried out using ANSYS Fluent. The realistic geometry obtained from micro-CT images and structural simulation was characterized by proximal overexpansion and asymmetric stent deployment leading to a non-uniform distribution of WSS values (Fig. 3.6 b,c). In particular, the regions associated to the highest risk of NH (WSS $<$ 0.5 Pa) were located at the proximal end of the stent where the abrupt enlargement of the artery was observed. A good correlation was found between the computed hemodynamic parameters and the asymmetric neointimal growth evaluated by means of histomorphometric analyses of the explanted vessels (Fig. 3.6d).
Rikhtegar et al. (2013a) studied the hemodynamics of stented coronary arteries of *ex vivo* porcine hearts. Absorbable metal stents (Biotronik AG, Blach, Switzerland) were implanted by an interventional cardiologist in the left coronary artery of *ex vivo* porcine hearts. Vascular corrosion casting was performed by injection of a radio-opaque resin into the stented coronary vascular tree under physiological pressure of 90 mmHg. Then, the stented coronary artery cast was scanned using micro-CT in order to obtain the 3D geometrical model for subsequent CFD analyses. Both steady-state and transient CFD simulations were carried out with ANSYS CFX. Blood inflow rate of 0.95 mL/s was applied at

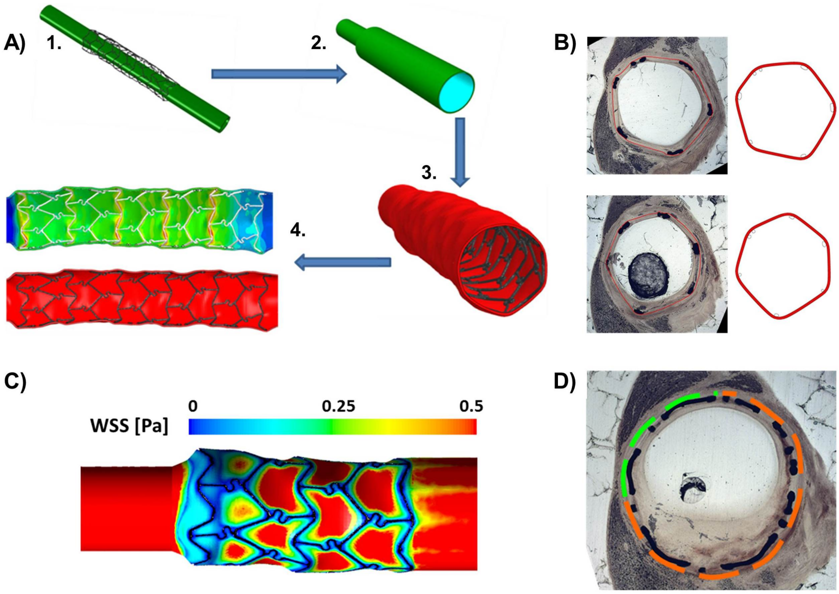

Figure 3.6: a) Structural model implemented to identify the geometrical configuration of the stented arteries of *in vivo* porcine coronary models: (1) CAD model of the undeformed artery and of the stent reconstructed from micro-CT images, (2) expansion of the artery through a cylindrical surface dilatation, (3) stent-artery coupling obtained after the recoil of the artery, and (4) longitudinal section of the final configuration. b) Comparison between two histological images (on the left) and the corresponding sections obtained with the structural simulation (on the right). c) WSS spatial distribution along the arterial wall. d) Correlation between areas characterized by low WSS (orange lines) and ISR phenomenon after 14 days in a proximal section of the stented artery. *Reprinted with permission from Annals of Biomedical Engineering 2013 Vol.41(7): 1428-1444. S. Morlacchi and F. Migliavacca. Modeling stented coronary arteries: Where we are, where to go ©(2012) Biomedical Engineering Society.*

the ostium for steady-state calculation and time-dependent flow rate replicating systolic and diastolic LCA blood flow for the transient analysis (Berne and Levy, 1967). Zero relative pressure was imposed at the outlet with the largest diameter and outflow rates were imposed at the remaining outlet according to Murray's law (Murray, 1926). No-slip condition was prescribed at the vessel wall.

Accurate local flow information were obtained thanks to the method used for the creation of the fluid domain. In fact, this method ensured anatomic fidelity, capturing arterial tissue prolapse, radial and axial arterial deformation, and stent malapposition, otherwise difficult to include in an idealized model. In Fig. 3.7a an example of malapposed struts is shown. The presence of these struts provoked tunneling of blood flow between the strut and the arterial wall, leading to perturbation of the local flow field. Low WSS were located at bifurcations and next to the struts. Low WSS were not only present close to struts arranged perpendicular to the flow direction, but also occurred in the vicinity of inter-strut connectors arranged parallel to the flow direction. The distribution of low ($<$ 0.5 Pa), intermediate (0.5 to 2.5 Pa) and high ($>$ 2.5 Pa) WSS is shown in Fig. 3.7b relative to the surface area of selected arterial segments in a vessel with two stents. In the stented sections more than 40% of the wall surface area was exposed to low WSS indicating these segments of artery as potentially athero-prone regions.

In a further study by the same research group (Rikhtegar et al., 2013b), the hemodynamics in *ex vivo* porcine left coronary arteries with overlapping stents was investigated. Six cases with partially overlapping stents were compared to five cases with two non-overlapping stents. The same methodology of their previous study (Rikhtegar et al., 2013a) was adopted. Their results showed that the area exposed to WSS lower than 0.5 Pa is higher in the overlapping stent segments than in the regions without overlap of the same samples and in the non-overlapping stents. Moreover, the configuration of the overlapping stent struts relative to each other influenced the size of the low WSS area. The positioning of the struts in the same axial location resulted in larger low WSS areas compared to alternating struts.

3.3.3 CFD studies from patient images

Gundert et al. (2011) developed a method to virtually implant a stent in patient-specific coronary artery models for CFD analyses. This method was based on the following three steps: (1) the creation of a 3D geometrical model of a human LAD starting from computed tomography (CT) scans (Fig. 3.8a), (2) the preparation of an idealized model of a thick stent matching arterial geometry (Fig. 3.8b), and (3) the production of the fluid domain by subtracting the stent volume from the coronary solid model (Fig. 3.8c). Two different stent designs were compared from the fluid dynamic perspective: an open-cell ring-and-link stent (stent A) and a closed-cell slotted tube prototype stent (stent B). As in a previous work by the same research group (Williams et al., 2010), discussed in Section 3.2, a LAD blood flow waveform at rest was applied at the inlet while a three-element Windkessel model representing the downstream vasculature was imposed at the outlets using a multi-domain approach. Blood was assumed to

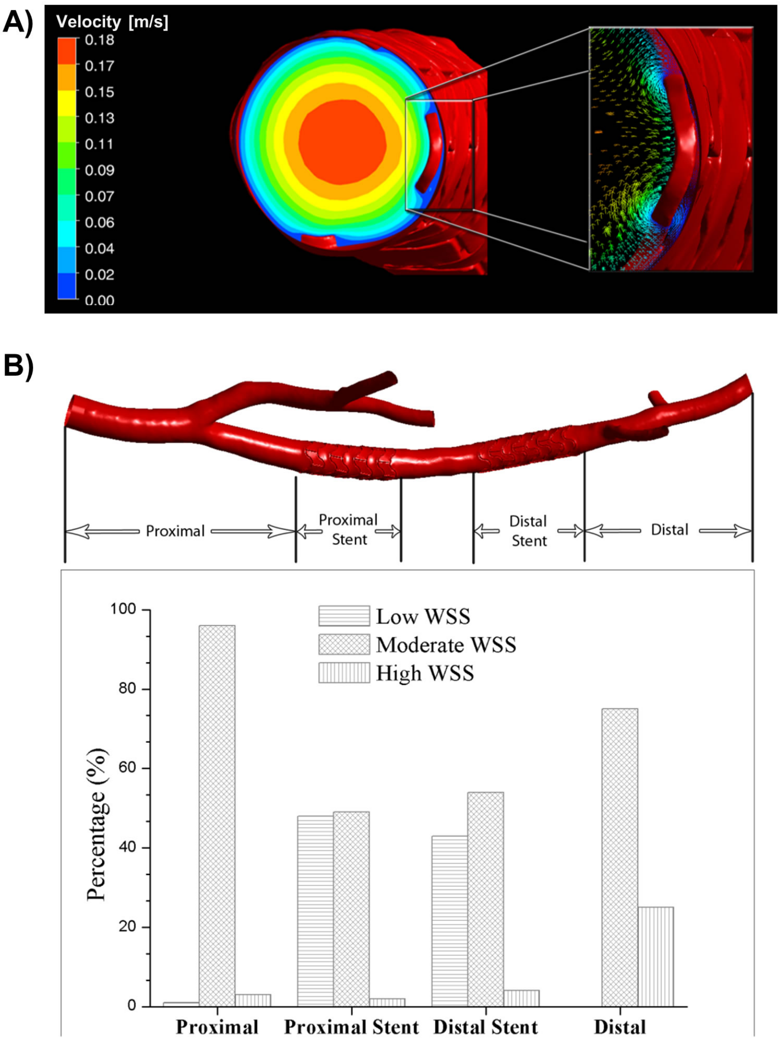

Figure 3.7: a) Contour map of velocity magnitude in an axial cross-section of the stented artery near a malapposed strut. In the magnification box, the velocity vector plot near the malapposed strut is depicted showing the presence of vortices. b) Distribution of WSS relative to the surface area of selected segments of a porcine left coronary artery model with two stents. ©*(2013) Rikhtegar et al. (2013a)*.

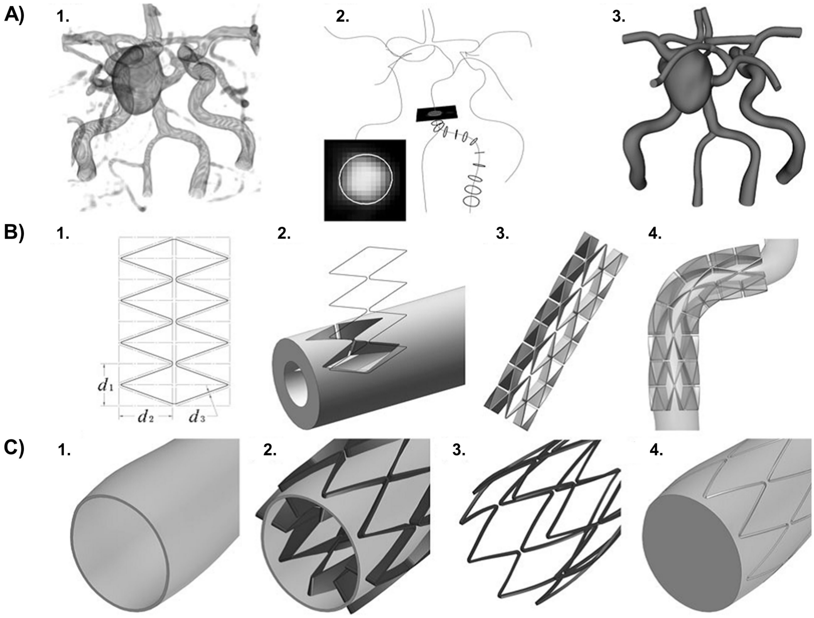

Figure 3.8: Methodology developed by Gundert et al. (2011) of patient-specific geometrical model creation for CFD analyses of stented coronary arteries: a) workflow from imaging data to 3D solid model of a patient-specific artery tree; b) preparation of an idealized model of a thick stent matching arterial geometry; c) production of the fluid domain by subtracting the stent volume from the coronary solid model. *Reprinted with permission from Annals of Biomedical Engineering 2011 Vol.39(5): 1423-1437. T.J. Gundert et al. A rapid and computationally inexpensive method to virtually implant current and next-generation stents into subject-specific computational fluid dynamics models ©(2011) Biomedical Engineering Society.*

be a Newtonian fluid with a density of 1060 kg/m^3 and a dynamic viscosity of 4 cP. CFD simulations were performed by means of the open-source software Simvascular (`https://simtk.org/`).

Regions of low TAWSS were localized close to the struts and more prevalent distal to the bifurcation in both the cases. The total intrastrut area of the lumen that was exposed to TAWSS lower than 0.4 Pa was shown to be higher for the stent A (75.6%) than for the stent B (59.3%). In Fig. 3.9 cross-sections of MET at the bifurcation are shown for the model without stent and the two stented models. The presence of the stent increased the region of high MET near the arterial wall in the MB (Fig. 3.9, bifurcation plane and cross-section A). In the SB, just distal to the stent (Fig. 3.9, cross-section B), a pronounced difference

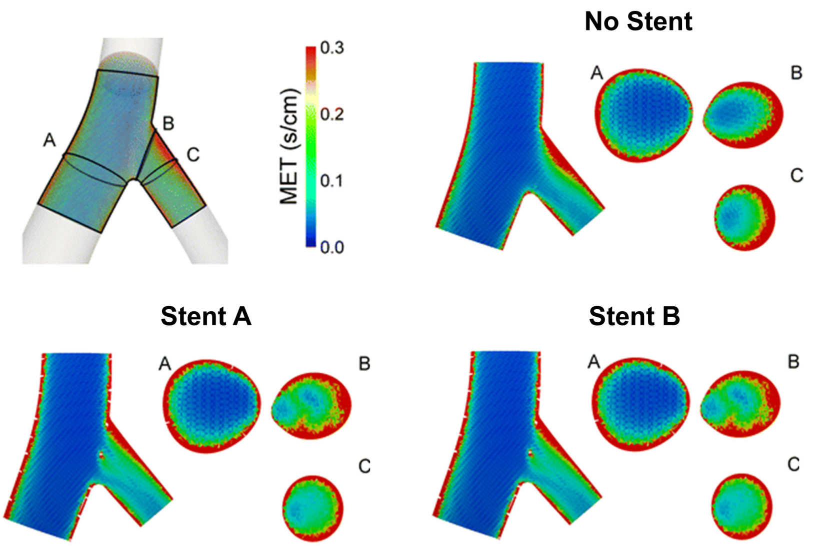

Figure 3.9: MET at the coronary bifurcation for the model without stent and the two stented models. MET is visualized in a plane parallel to the bifurcation and three planes perpendicular to the vessel. *Reprinted with permission from Annals of Biomedical Engineering 2011 Vol.39(5): 1423-1437. T.J. Gundert et al. A rapid and computationally inexpensive method to virtually implant current and next-generation stents into subject-specific computational fluid dynamics models ©(2011) Biomedical Engineering Society*.

in MET between the models can be appreciated. The stent design, placement, and number of struts in the SB influenced the exposure time of the particles. The lowest values of MET were found near the carina of the bifurcation for all the models, corresponding to an increased velocity in this zone.
In a further study by the same research group (Ellwein et al., 2011), the hemodynamics of a patient-specific stented LCX with a thrombus was investigated. The geometrical model of the vessel was reconstructed combining CT and OCT images acquired immediately post-stenting and after 6-months follow-up period. In order to obtain the fluid domains, the OCT guide-wire pathway was determined by applying a shortest path algorithm; then, segments from OCT images were registered orthogonal to the wire pathway using rotational orientation consistent with geometry estimated by CT. The stent was drawn inside the artery applying the previously developed method (Gundert et al., 2011). CFD

models were similar to those of Gundert et al. (2011). The same boundary conditions were used. Simulations were performed with the commercial flow solver LesLib (Altair Engineering Inc., Troy, MI, USA). Considering TAWSS results, the percentage area of the vessel exposed to TAWSS lower than 0.4 Pa was 11% in the post-stent model and only 3% in the follow-up model, limited to areas of localized curvature. The areas of stent-induced low WSS returned to physiological levels at follow-up and a good correlation was found with the measures of neointimal thickness in OCT images. Finally, high OSI values were present next to struts in the post-stent model and in the areas of curvature of the follow-up model.

The last study reported in this review chapter is that by Chiastra et al. (2013) who investigated the hemodynamics of two cases of pathologic LAD with their bifurcations treated with a provisional T-stenting technique. The 3D geometrical models were reconstructed starting from CTA and CCA images (Cárdenes et al., 2013). All the details about this work are presented in Chapter 7.

3.4 Limitations of the current CFD models and future remarks

The CFD studies on stented coronary arteries introduced in Sections 3.2 and 3.3 are subjected to some assumptions and limitations that need to be considered in the interpretation of the results, especially when clinical consideration is made. In this section the main limitations of the proposed models are discussed.

3.4.1 Heart motion

The motion of coronary arteries is complex because of the presence of the beating heart and can be described by overall vessel translation, stretching, bending and twisting and to a minor degree by radial expansion and axial torsion (Ramaswamy et al., 2004). In the CFD studies reviewed in this chapter the cardiac-induced motion was always neglected. However, its effects on hemodynamics are still a subject of study. Several works have been proposed in the literature with conflicting results. These studies do not analyze stented coronary arteries, but unstented vessels. In particular, Zeng et al. (2003) studied the fluid dynamics of a RCA model under physiologically realistic heart motion. The authors concluded that the motion effects were small compared to flow pulsation effects. On the contrary, Ramaswamy et al. (2004) found that heart motion substantially affects the hemodynamics in LAD. Prosi et al. (2004) considered a curved model of LAD with its first diagonal branch by attaching it to the surface of a sphere with time-varying radius based on experimental dynamic curvature data. Their results indicated that the effect of curvature dynamics on the flow field were negligible. Theodorakakos et al. (2008) studied the effect of cardiac motion on the flow field and WSS distribution of an imaged-based human LAD and its main branches in the presence of a stenosis. Their results showed that hemodynamics was considerably affected by the pulsatile nature of the flow and myocardial motion had only a minor effect on flow patterns within the arterial tree. Although the absolute values of WSS were different, the spatial distribution of WSS was very similar between the stationary and the moving coronary tree. Hasan et al. (2013) investigated the effects of cyclic motion (i.e. bending and stretching) on blood flow in a 3D model of a segment of the LAD, which was created on the basis of anatomical studies. Their results highlighted that although the motion of the coronary artery could significantly affect blood particle trajectory, it had slight effect on velocity and WSS.

3.4.2 Rigid walls

In all the studies discussed in this chapter the arterial wall and the stents are assumed to be rigid and fixed. This assumption might produce different local hemodynamic results. FSI simulations of coronary artery models were performed in a limited number of studies (Asanuma et al., 2013; Koshiba et al., 2007; Malvè et al., 2012; Torii et al., 2009; Yang et al., 2009), without considering the presence of the stents. In order to understand the effects of the wall compliance on hemodynamics quantities and to show that FSI can nowadays be carried out, we performed a FSI study on a stright coronary artery with a common open-cell stent deployed. All the details about this work are presented in Chapter 4.

3.4.3 Boundary conditions

The choice of boundary conditions in the CFD models is fundamental for obtaining reliable results. For all of the numerical models introduced in this chapter, the inlet boundary conditions used were similar and consisted of a pulsatile blood flow waveform taken from the literature applied as either a paraboloid-shaped velocity profile (e.g. Morlacchi et al. (2011a)) or a Womersley-like velocity profile (e.g. Williams et al. (2010)). For the outlet boundary conditions different choices were proposed: traction-free boundary condition (Chen et al., 2012), flow split based on empirical laws (Rikhtegar et al., 2013a), or multi-domain approach that considers a lumped-parameter model representing the downstream vasculature coupled to the 3D domain (Ellwein et al., 2011; Gundert et al., 2011; Williams et al., 2010). Since *in vivo* measurements of flow-rate and pressure in coronary arteries are highly invasive and not always required in a clinical routine exam, boundary conditions used for CFD simulations of patient-specific geometries (Section 3.3.3) were mainly based on literature data.

3.4.4 Accuracy of 3D geometrical models

The results of a fluid dynamic simulation are more accurate when the numerical analysis is performed with a geometrical model resembling the reality. Considering the CFD models of patient-specific geometries (Section 3.3.3), only the arterial vessel was obtained from imaging data while the stent was created using a CAD software. Currently, OCT is a promising imaging technique for coronary arteries, due to its high resolution (10-20 μm) and the possibility to detect both the stent and the vessel wall (Farooq et al., 2009). Thanks to these characteristics, OCT might be an useful tool to reconstruct 3D geometries of stented coronary arteries, as discussed in Chapter 8.

3.4.5 Model validation

The validation of the numerical model is an important aspect in order to guarantee the validity of the results. It is defined as the process of determining whether the CFD model is an accurate representation of the real system, for the particular objectives of each study (Law and McComas, 2001).The small dimensions of the coronary vessels (2-4 mm in diameter) and the stents (80-100 μm for the strut size) make *in vivo* local measurements of velocities and velocity gradients very difficult, resulting in the impossibility of mapping the shear stress distribution along the arterial wall. *In vitro* quantification of the local fluid dynamics of stented coronary artery models is also very complex to realize mainly because of the small dimensions.

In the works introduced in Sections 3.2 and 3.3 validation was not directly done. However, in an older study (Berry et al., 2000) both CFD simulations and *in vitro* experiments were performed. The hemodynamic effects of two different stent geometries were investigated using CFD and dye injection flow visualization. A simplified 2D CFD model of the region very close to the arterial wall was considered. Numerical results were qualitative in agreement with the experiments. Morlacchi (2013) compared particle image velocimetry (PIV) flow

measurements in *in vitro* stented and non-stented coronary bifurcation models with the fluid dynamic results of the corresponding numerical replica of the experimental cases. Despite the intrinsic differences and modeling assumptions of the two approaches, the results were qualitatively in agreement. Both PIV and CFD analyses were able to capture the main features of the fluid flows, highlighting the influence of different bifurcation angles and stenting procedures.
Validation remains a key aspect of 3D numerical models of stented coronary arteries. In the future, the improvement of experimental techniques for fluid dynamic measurements such as PIV (Charonko et al., 2009) or 3D particle tracking velocimetry (Gülan et al., 2012) will allow a quantitative comparison between CFD and *in vitro* models of stented coronary arteries.

Chapter 4

On the necessity of modeling FSI for stented coronary arteries

Fluid dynamic studies of stented coronary arteries generally assume the arterial wall and the stents as rigid and fixed bodies. This assumption might produce different local hemodynamic results if compared to a compliant vessel. In this chapter FSI analyses of a stented coronary artery are presented with the aim of understanding the effects of the wall compliance on the hemodynamic quantities. Two different materials are considered for the stents: CoCr and PLLA. The results of the FSI and the corresponding rigid-wall models are compared.
Results showed similar trends in terms of WSS and TAWSS between compliant and rigid-wall cases. In particular, the difference of percentage area exposed to TAWSS lower than 0.4 Pa between the CoCr FSI and the rigid-wall cases was $\sim$ 1.5 % while between the PLLA cases $\sim$ 1.0 %. Results indicate that, for idealized models of a stented coronary artery, the rigid-wall assumption appears adequate when the aim of the study is the analysis of near-wall quantities.

The contents within this chapter can be found in:
Chiastra, C., Migliavacca, F., Martínez, M.A., and Malvè, M. (2014). On the necessity of modelling fluid-structure interaction for stented coronary arteries. *Journal of the Mechanical Behavior of Biomedical Materials* (accepted for publication).

4.1 Introduction

NUMEROUS CFD studies have been proposed in the literature, considering idealized (Gundert et al., 2013, 2012; Murphy and Boyle, 2010b; Pant et al., 2010) or more complex image-based stented coronary models (Chiastra et al., 2013; Ellwein et al., 2011; Gundert et al., 2011), as previously exposed in Chapter 3. Despite providing a great deal of information, in these fluid dynamic models the arterial wall and the stent are assumed to be rigid and fixed, an assumption that may influence the WSS and flow pattern results.

In the recent past the FSI approach has been applied to a wide range of arterial problems including the aorta (Figueroa et al., 2006), abdominal aortic aneurysms (Leung et al., 2006; Scotti and Finol, 2007; Scotti et al., 2008; Tezduyar et al., 2007; Wolters et al., 2005), cerebral aneurysms (Gerbeau et al., 2005; Takizawa et al., 2012, 2011; Tezduyar et al., 2007), carotid artery bifurcations (Filipovic et al., 2013; Gao et al., 2009; Gerbeau et al., 2005; Lee et al., 2012; Perktold and Rappitsch, 1995; Tezduyar et al., 2007), and anastomoses of bypass grafts (Hofer et al., 1996; Leuprecht et al., 2002). The extensive study of Tang and coworkers on human carotid atherosclerotic plaque (Tang et al., 2001, 2004, 1999, 2008; Teng et al., 2010; Yang et al., 2010, 2011) deserves special mentioning. Indeed, they provided structural and hemodynamics markers for the initiation and development of atherosclerosis in carotid arteries using the FSI approach. In a further study, Belzacq et al. (2012) investigated the effect of the length, the stiffness, and the severity of an asymmetric carotid atherosclerotic plaque on the mechanical action of the blood flow by developing a parametric FSI model.

FSI simulations of coronary artery models have been performed only in a limited number of studies, without considering the presence of stents. Koshiba et al. (2007) simulated blood flow, arterial wall deformation and filtration flow in the wall of a coronary artery with multiple bends. The results of the FSI simulation were used to analyze the LDL transport in the arterial lumen and wall by solving the advection-diffusion-reaction equation. Yang et al. (2009) developed a FSI model of the middle segment of the human RCA with atherosclerotic plaques, based on IVUS images, in order to quantify the effects of anisotropic vessel properties and cyclic bending of the coronary plaque on flow and plaque stress/strain conditions. A similar study was recently conducted by Asanuma et al. (2013) who investigated the distributions of shear stress and tissue stresses in the proximal segment of a stenotic human LCA. Torii et al. (2009) performed a FSI analysis of a human stenotic RCA using physiological velocity and pres-

sure waveforms to investigate the effects of wall compliance on hemodynamics. A comparison between a FSI and a rigid-wall model was carried out showing noticeable differences in instantaneous WSS profiles. Finally, Malvè et al. (2012) made a comparison between the WSS distribution of a compliant and a rigid-wall model of a human LMCA with its main branches. WSS distributions were substantially affected by the arterial wall compliance, in particular considering the minimum and maximum values of WSS.
The aim of the present work is to perform FSI analyses of a stented coronary artery in order to understand the effects of the wall compliance and the blood pressure on hemodynamic quantities. Both a bare-metal (CoCr) and a polymeric (PLLA) stent are considered. The choice of the polymeric stent, with the same design of the metallic one, is done because of the different stiffness of the device which could produce bigger deformations with a great influence on the fluid dynamics. The results of the FSI and the corresponding rigid-wall models are then compared, focusing in particular on the analysis of the WSS distribution.

4.2 Materials and methods

4.2.1 Geometry

A geometrical model of a straight coronary artery and a typical open-cell stent were created using the CAD software Rhinoceros v.4.0 (McNeel & Associates, Indianapolis, IN, USA). The geometry of the artery was created with a length of 20 mm, an internal diameter of 2.7 mm and an arterial wall thickness of 0.9 mm. The stent model is characterized by eight rings with a total length of 8.5 mm, an external diameter of 1.55 mm (uncrimped configuration) and strut thickness of 90 μm.
In order to obtain the geometrical model of a stented artery which is not based only on geometrical assumptions but also takes into account the deformation of the vessel caused by the stent deployment, the device was expanded inside the vessel through a structural analysis reaching the final diameter of 3 mm. The simulation was carried out by means of ABAQUS/Explicit (Dassault Systemes, Simulia Corp., RI, USA) following the method proposed in Gastaldi et al. (2010).
The final geometrical configuration, after the elastic recoil, was exported as a triangulated surface and used to create the fluid and solid domains for the subsequent FSI and CFD analyses (Morlacchi et al., 2011a). An extension with a length of four diameters (10.8 mm) was added at both extremities of the arte-

rial model (Fig. 4.1a) in order to obtain a developed flow near the region of the stent and avoid border effects due to the constrains in the inlet and outlet cross-sections, thus reducing their influence on the results.

4.2.2 Numerical grids

The geometry of the artery is complex in the vicinity of the stent struts making the compatibility between the fluid and solid domains critical during a FSI simulation. To minimize this problem, the two domains were discretized simultaneously obtaining coincident nodes at the fluid-structure interface.
The meshing software ANSYS ICEM CFD v.14.0 (ANSYS Inc., Canonsburg, PA, USA) was used. An unstructured tetrahedral mesh was generated in the fluid domain using smaller elements close to the struts (Fig. 4.1c), as done in Chiastra et al. (2012). The fluid grid, which was chosen after an appropriate mesh independence study, had 1,121,130 elements (222,476 nodes).
In the solid domain an unstructured hybrid tetrahedral and prismatic grid was created (Fig. 4.1d). In particular, the stent and the inner part of the arterial wall were meshed with tetrahedral elements because of the complexity of the geometry and the necessity of obtaining coincident nodes between the fluid and solid domains. The external part of the arterial wall was meshed with a layer of prismatic elements. This choice allowed us to create elements oriented in the radial direction of the vessel, with an optimal quality (determinant criterion close to 1). The total number of elements was also reduced with respect to a pure tetrahedral grid. In particular, the mesh contained 899,710 elements (189,521 nodes). The final solid mesh is finer than that obtained after an independence study performed on the artery without stent. In fact, the device adds complexity to the geometry and needs to be correctly refined.
The Octree method was chosen for the creation of the tetrahedral meshes for both the domains. This method ensures refinement of the mesh where necessary, but maintains larger elements where possible. For the solid domain a full tetrahedral mesh was initially created, prisms were then created by extrusion of the surface mesh, and the resulting prisms were made conformal with the existing tetrahedral volume mesh.

4.2.3 Material properties

The arterial wall was modeled as a hyperelastic incompressible isotropic and homogeneous material. The following strain energy function was considered:

$$W = A\left[exp\left(B\left(\overline{I}_1 - 3\right)\right) - 1\right] \tag{4.1}$$

where $\overline{I}_1$ is the first invariant of the deviatoric right Cauchy-Green tensor $\overline{\boldsymbol{C}} = J^{-2/3}\mathbf{F}^T\mathbf{F}$, $J = det\,(\mathbf{F})$ is the Jacobian, $\mathbf{F}$ is the standard deformation gradient, and A, B are the material constants, which were set to 3.71 Pa and 140.2, respectively. This strain energy density function was first proposed by Demiray (1972), and later used by Delfino et al. (1997) for a carotid artery bifurcation model and Rodríguez et al. (2008) for an abdominal aortic aneurysm model. The function parameters were fitted using the experimental tests of human coronary arteries obtained by Carmines et al. (1991). This material modeling was successfully applied to a coronary artery in a previous study (Malvè et al., 2012). This model takes into account the effect of the axial pre-stretch since the used experimental data also included it. The viscoelasticity, the active behavior of muscle fibers of the artery, and the intrinsic anisotropy, due to the preferential directions of collagen and muscle fibers, were neglected. This assumption might alter the results obtained for the structural part in terms of stresses and strains, but does not alter the overall compliance of the artery in presence of the stent due to the fact that the material model used for the artery fitted experimental data. Since the aim of the work is the analysis of the compliant artery and not the evaluation of the stresses inside it, in first approximation the results have to be considered acceptable.

The stent material was considered linear elastic, isotropic and homogeneous. Two different cases were analyzed maintaining the same geometry: CoCr (Young's modulus = 233 GPa and Poisson's ratio = 0.35) and PLLA stent (Young's modulus = 900 MPa and Poisson's ratio = 0.30).

Relative displacements were not allowed between the stent and the arterial wall. In fact, the volume was meshed with coincident nodes at the interface between the stent and the arterial wall. Although non-physiological, this condition allowed a significant reduction in the complexity of the model.

The blood was modeled as an incompressible Newtonian fluid, with a density of 1060 kg/m^3 and a dynamic viscosity of 0.0035 Pa s (Rikhtegar et al., 2013a). Since the Reynolds number based on the inlet diameter was 210 at peak flow rate, an order of magnitude smaller than the Reynolds number for transition to turbulence (2300) (Spurk and Aksel, 2008), the flow was assumed to be laminar under unsteady conditions. The Womersley number was 1.95.

4.2.4 Boundary and flow conditions

The extremities of the extensions of the solid model were constrained by preventing rigid-body axial and transaxial motion. The constrains were applied far from the stented region, at a distance longer than four diameters (Fig. 4.1a).

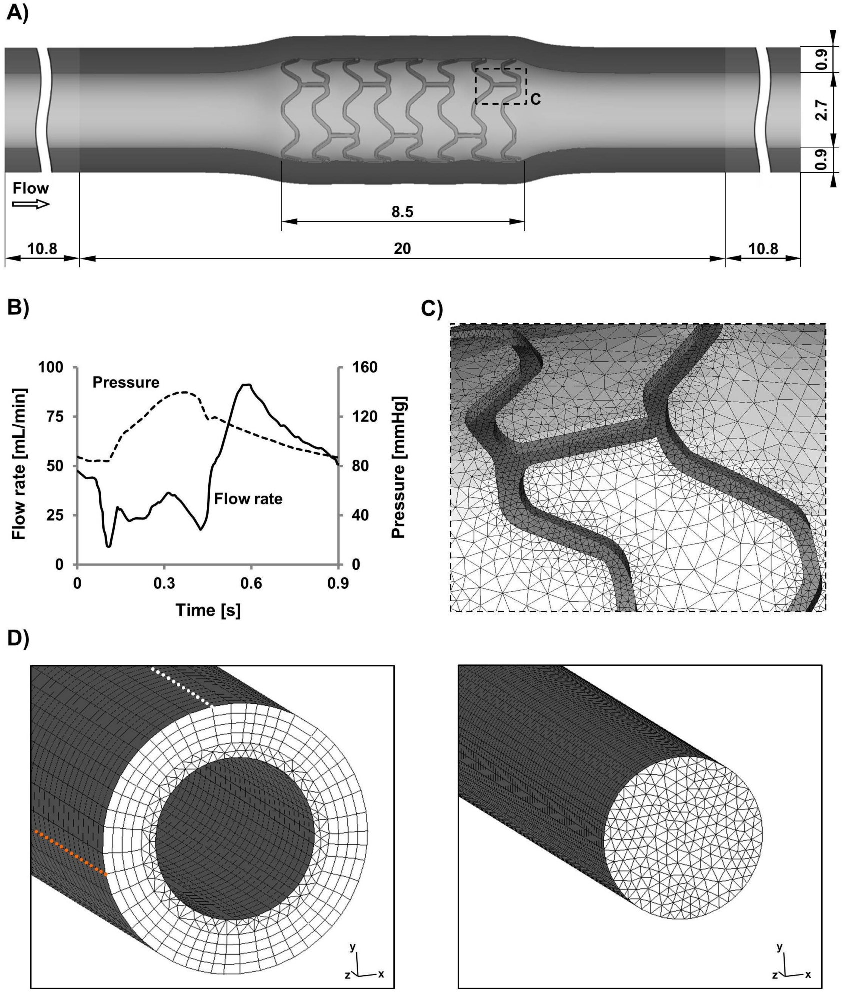

Figure 4.1: a) Geometrical model of the straight coronary artery with a typical deployed open-cell stent. The fluid domain is displayed in light gray while the solid domain in dark gray. Extensions with a length of four diameters were added at the extremities of the model. Dimensions are in millimeters. b) Flow rate and pressure waveforms of a human LAD (Davies et al., 2006) applied at the inlet and at the outlet cross-section, respectively. c) Detail of the tetrahedral grid obtained at the fluid-structure interface in the vicinity of the stent struts. The mesh has smaller elements close to the struts. d) Particular of the mesh of the solid (left) and the fluid (right) domain at the inlet cross-section. The solid domain is discretized by prismatic elements with triangular base in the inner part and by a layer of prismatic elements with rectangular base in the external part. The dots aligned with z-axis indicate the constrains which were added in the extended regions to avoid the motion of the vessel outside its axis during the cardiac cycle. For the set of nodes in x direction (orange dots), movement in y direction was not allowed while for the set of nodes in y direction (white dots), movement in x direction was not allowed.

Therefore, the influence of these conditions on the stented region is very limited. In order to avoid the motion of the vessel outside of its axis (z-axis) during the cardiac cycle, constrains were added in x and y direction to sets of nodes along the length of the extensions (Fig. 4.1d). In particular, along the extensions, starting from the top and bottom surfaces, for the nodes set in x direction (Fig. 4.1d - orange dots), the movement in y direction was not allowed while, for the nodes set in y direction (Fig. 4.1d - white dots), the movement in x direction was not allowed. These conditions, although non-physiological, are often used for biomechanical studies of coronary arteries (Malvè et al., 2012; Torii et al., 2009), abdominal aneurisms (Scotti et al., 2008; Takizawa et al., 2011; Torii et al., 2006, 2010) and carotid arteries (Malvè et al., 2013).
The artery was initially pressurized by applying at the inlet cross-section a ramp of velocity from 0 m/s to 0.138 m/s and, at the outlet, a ramp of pressure from 0 mmHg to 80 mmHg. Then, the velocity and pressure waveforms measured by Davies et al. (2006) in a human LAD (Fig. 4.1b) were imposed at the inlet and the outlet, respectively. A flat velocity profile was adopted at the inlet cross-section. The average flow rate was 45 mL/min and the duration of the cardiac cycle was 0.9 s. The no-slip boundary condition was applied to the fluid-structure interface (surface representing the endothelial wall and the stent struts).

4.2.5 Numerical simulations

The following four analyses were performed: FSI and rigid-wall simulation of the arterial model with the CoCr stent, and FSI and rigid-wall simulation of the model with the PLLA stent. All the simulations were carried out using the commercial finite element package ADINA v.8.7.3 (ADINA R&D, Inc., Watertown, MA, USA).

FSI simulations

Fully coupled FSI simulations were performed. The numerical approach uses the arbitrary Lagrangian-Eulerian (ALE) formulation (Bathe and Zhang, 2004; Bathe et al., 1999) for the fluid domain and a typical Lagrangian formulation of the solid domain (Bathe and Zhang, 2004; Donea et al., 1982).
Considering the moving reference velocity, the Navier-Stokes equation can be written as:

$$\rho_F \frac{\partial \mathbf{v_F}}{\partial t} + \rho_F \left(\left(\mathbf{v_F} - \mathbf{w} \right) \cdot \nabla \right) \mathbf{v_F} = -\nabla p + \mu \nabla^2 \mathbf{v_F} + \mathbf{f_F^B} \tag{4.2}$$

where the term $\mathbf{w}$ is the moving mesh velocity vector, $\mathbf{v_F}$ is the velocity vector, p is the pressure, $\mathbf{f_F^B}$ is the body force per unit volume, ρ_F is the fluid density, and μ is the dynamic viscosity. In the ALE formulation, $(\mathbf{v_F} - \mathbf{w})$ is the relative velocity of the fluid with respect to the moving coordinate velocity.
The governing equation of the solid domain is the following momentum conservation equation:

$$\nabla \cdot \boldsymbol{\sigma_s} + \mathbf{f_F^B} = \rho_s \ddot{\mathbf{u}}_\mathbf{s} \tag{4.3}$$

where ρ_s is the solid density, $\boldsymbol{\sigma_s}$ is the solid stress tensor, $\mathbf{f_F^B}$ is the body force per unit volume and $\ddot{\mathbf{u}}_\mathbf{s}$ is the local acceleration of the solid. The domains described by Eqs. 4.2 and 4.3 are then coupled through displacement compatibility and traction equilibrium (Bathe and Zhang, 2004) with the following equations:

$$\mathbf{u_S} = \mathbf{u_F} \qquad (x, y, z) \in \Gamma^F_{wall} \cap \Gamma^S_{wall} \tag{4.4}$$

$$\boldsymbol{\sigma_S} \cdot \mathbf{n_S} + \boldsymbol{\sigma_F} \cdot \mathbf{n_F} \qquad (x, y, z) \in \Gamma^F_{wall} \cap \Gamma^S_{wall} \tag{4.5}$$

where Γ^F_{wall} and Γ^S_{wall} are the boundaries of the fluid and solid domains, respectively. Equation 4.5 is an equilibrium condition between the stresses acting in normal direction on both domain boundaries Γ^F_{wall} and Γ^S_{wall}.
The governing equations were solved with the finite element method, which discretizes the computational domain into finite elements that are interconnected by element nodal points.
For the structural model, a sparse matrix solver was used to solve the system. The full Newton-Raphson method (Bathe, 2006a) with a maximum of 500 iterations in each time step was chosen as iteration scheme.
The fluid domain employs special flow-condition-based-interpolation (FCBI-C) tetrahedral elements (Bathe, 2006b). All solution variables are defined in the center of the element and the coupling between the velocity and the pressure is handled iteratively. FCBI-C elements require the segregated method to solve the nonlinear equations. The sparse linear equation solver based on Gaussian elimination was used.
To solve the coupling between the fluid and the structural models, the iterative method was chosen (Bathe, 2006b). In this computing method, the fluid and solid solution variables are fully coupled. The fluid equations and the solid equations are solved individually in succession, always using the latest information provided from another part of the coupled system. This iteration is continued until convergence in the solution of the coupled equations is reached. The maximum number of fluid-structure iterations for each time step was set to

1000. The time step size was set to 0.001 s (900 time steps were necessary for one cardiac cycle).
Simulations were performed in parallel on one node of a cluster with an Intel processor, 8 CPUs, with a CPU speed of 2268MHz and a total memory of 24 Gb. One cardiac cycle was modeled. In order to verify that one cardiac cycle was enough to guarantee correct results, the CoCr FSI model and the corresponding rigid-wall model were investigated by simulating three cardiac cycles. No significant differences were found in the WSS results between the first and the third cardiac cycle. The calculation time of the FSI simulation was around 500 hours for one cardiac cycle.

Rigid-wall simulations

The same settings chosen for the fluid domain of the FSI models were used. In order to obtain a more realistic comparison between FSI and rigid-wall simulations, the geometries of the CoCr and PLLA cases, pressurized at 80 mmHg, were considered.
More in detail, the structural model of the stented artery, for both cases, PLLA and CoCr, is initially not pressurized. For this reason, before a cardiac cycle can be applied, the diastolic pressure has to be reached. In order to start the heart cycle with identical geometrical configurations and properly perform a comparison of hemodynamics variables between rigid-wall and FSI simulations, the reference diastolic configuration of the artery was considered for the rigid-wall analyses. By means of the commercial software MATLAB (MathWorks Inc. - Natick, MA, USA), the deformed mesh obtained from the FSI simulation at the beginning of the cardiac cycle was used to generate an input grid for the CFD computations. This mesh allows that the performed simulations, rigid-wall and FSI analyses, could be compared taking into account only the compliance of the arterial wall due to the cardiac cycle.
In Fig. 4.2 the comparison between the initial undeformed configuration and the diastolic configuration of the CoCr and PLLA models is presented.

4.2.6 Results quantification

For the FSI cases, the displacements of the fluid-structure interface during the cardiac cycle were analyzed. Moreover, four different cross-sections (S_1, S_2, S_3, S_4) were chosen to evaluate the variation of area and the corresponding diameter (Fig. 4.3). The area variation ($A_{pp} - A_{lp}$) expressed in percentage was calculated as:

$$\textit{Area variation [\%]} = \frac{A_{pp} - A_{lp}}{A_{lp}} 100 \tag{4.6}$$

where A_{pp} is the area of the cross-section at peak pressure and A_{lp} is the area of the cross-section at the minimum pressure during the cardiac cycle.
The diameter variation ($d_{pp} - d_{lp}$) expressed in percentage was calculated as:

$$\textit{Diameter variation [\%]} = \frac{d_{pp} - d_{lp}}{d_{lp}} 100 \tag{4.7}$$

where d_{pp} is the diameter of the cross-section at peak pressure and d_{lp} is the

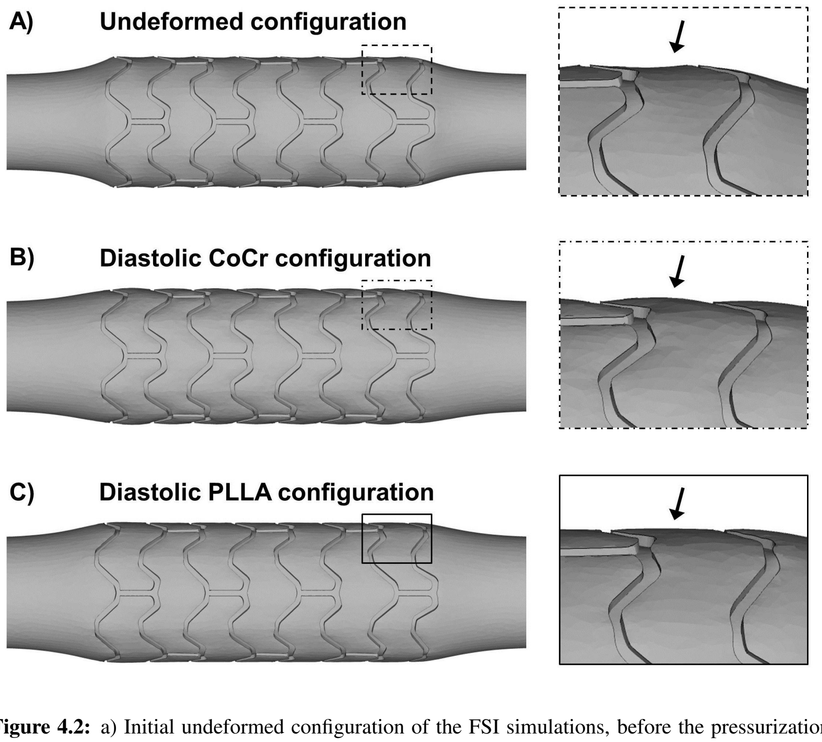

Figure 4.2: a) Initial undeformed configuration of the FSI simulations, before the pressurization step. This configuration is identical for both CoCr and PLLA FSI cases. b) Diastolic CoCr configuration. c) Diastolic PLLA configuration. In the magnification boxes on the right, the tissue between two rings of the stent is shown. As indicated by the black arrows, in the undeformed configuration the tissue is prolapsed between the struts toward the interior of the vessel while in the diastolic configurations it is prolapsed toward the exterior for the effect of the blood pressure.

diameter of the cross-section at the minimum pressure during the cardiac cycle. Since cross-sections S_1 and S_2 are not circular (Fig. 4.3) because of the presence of the stent struts, the hydraulic diameter was calculated for these locations as:

$$d_h = \frac{4A}{p} \tag{4.8}$$

where A is the area of the cross-section and p its wetted perimeter.
To compare the FSI and rigid-wall models, WSS and TAWSS were considered. These quantities were analyzed in the region of the fluid-structure interface that contains the stent (in the following, we refer to it as the 'region of interest' (ROI); Fig. 4.3). In particular, the percentage area exposed to low WSS was calculated in the ROI as the ratio between the area exposed to WSS lower than 0.4 Pa and the total area of the ROI. The area distribution of WSS was also visualized using histograms by displaying the amount of area of the ROI contained between specific intervals of the variable value (Murphy and Boyle, 2010a).

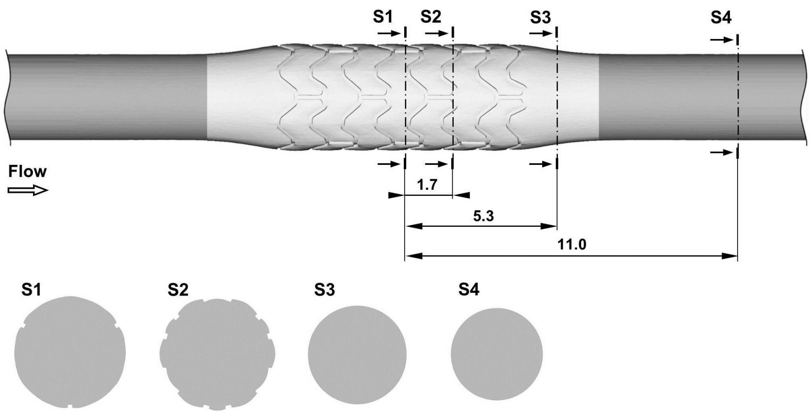

Figure 4.3: Location of the four cross-sections that were chosen to evaluate the variation of area and the corresponding diameter during the cardiac cycle. The ROI for the analysis of the WSS (region of the fluid-structure interface that contains the stent) is representated in light gray. Dimensions are in millimeters

4.3 Results and discussion

The displacements of the fluid-structure interface that occur during the cardiac cycle for the two FSI models were first analyzed. The maximum displacements take place at peak pressure (t = 0.37 s, p = 139.6 mmHg); they are localized in the arterial wall portions immediately before and after the stent (Fig. 4.4a) and they are equal to 0.215 mm and 0.240 mm, respectively for case FSI CoCr and FSI PLLA. A qualitative comparison of the contour maps of displacement magnitude shown in Fig. 4.4a highlights the different influence of the CoCr and PLLA stents on the arterial wall deformation: CoCr struts do not move as a consequence of the blood pressure variation; only the arterial wall portions within the stent cell dilate. On the contrary, PLLA struts, with a Young's modulus of two orders of magnitude lower than the CoCr, significantly move; the displacement value is between 0.09 mm and 0.15 mm in all the stented region. The same behavior is evident looking at the displacements on a line in the axial direction of the vessel for the two FSI cases (Fig. 4.4b).
The variation of area and the corresponding diameter of the four cross-sections chosen for the FSI models are reported in Table 4.1. These data confirms the rigid behavior of the CoCr stent. The cross-sections characterized by the presence of the stent struts (S_1 and S_2) show lower area and diameter variations if compared to the cross-sections outside the stented region (S_3 and S_4). In particular, S_2, which is characterized by the higher amount of struts, has the lowest area and diameter variation, 0.47$\%$ and 0.11$\%$, respectively. Cross-sections S_3 and S_4 have values of area and diameter variations comparable to the FSI PLLA model, about 4.3$\%$ and 2.1$\%$, respectively. The FSI PLLA case shows a more uniform behavior than the FSI CoCr case, with similar values of area and diameter variations for all the analyzed cross-sections.
The values of diameter variation outside the stented region (S_3 and S_4) can be

Table 4.1: Variations of area and diameter of the four analyzed locations of FSI CoCr and FSI PLLA models.

Location	Area variation [mm^2]		Area variation [$\%$]		Diameter variation [mm]		Diameter variation [$\%$]	
	FSI CoCr	FSI PLLA	FSI CoCr	FSI PLLA	FSI CoCr	FSI PLLA	FSI CoCr	FSI PLLA
S1	0.802	3.948	0.86	4.07	0.013	0.071	0.41	2.12
S2	0.418	3.975	0.47	4.23	0.003	0.071	0.11	2.32
S3	3.051	3.370	4.32	4.42	0.064	0.068	2.14	2.19
S4	2.653	2.587	4.31	4.20	0.060	0.058	2.13	2.08

compared to literature data. The values are similar to those found by Malvè et al. (2012) and Torii et al. (2009) with their FSI models of coronary arteries. Moreover, the FSI simulations of the present study show comparable values of

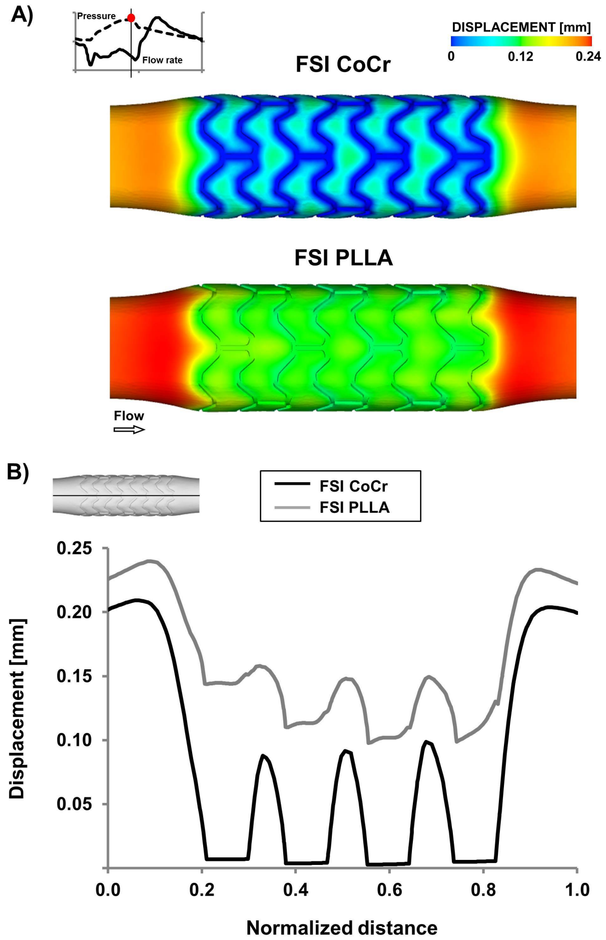

Figure 4.4: a) Contour maps of displacement magnitude along the fluid-structure interface of case FSI CoCr (top) and FSI PLLA (bottom) at peak pressure (t = 0.37 s, p = 139.6 mmHg), in the ROI. b) Displacements on a line in the axial direction of the vessel for the cases FSI CoCr and PLLA at peak pressure. The distance is normalized in the ROI. The reference line is shown on the top left image of the vessel model.

diameter variation to the experimental findings by Schaar et al. (2005) based on IVUS palpography measurements. The values of area variation outside the stented region are in accordance with those reported for patients with coronary artery disease by Kelle et al. (2011) (mean area change equal to 2.9 %, calculated using angiography, and to 5.3 %, using magnetic resonance imaging) and by Peters et al. (1996) and Weissman et al. (1995) (range from 2.0 % to 5.9 %, calculated using IVUS).
As previously shown by experimental and computational studies (Haluska et al., 2007; Tada and Tarbell, 2005), the temporal variation of vessel diameters is in phase with the pressure.
In order to study the effects of the wall compliance on the hemodynamics of a coronary stented artery model, the WSS patterns were analyzed. In Fig. 4.5a the contour maps of TAWSS along the fluid-structure interface for the FSI and rigid-wall cases are depicted. Low TAWSS are located next to the stent struts. For each repeating stent cell, the values of TAWSS increase from the zones near the struts towards the center of each cell. These findings are in agreement with several previous computational studies (Balossino et al., 2008; Duraiswamy et al., 2008; Gundert et al., 2013). A qualitative comparison of the contour maps of both the CoCr and PLLA cases does not point out any significant difference between the FSI and rigid-wall models. In Fig. 4.6 the TAWSS on a line in the axial direction of the vessel is displayed for the CoCr and PLLA cases. The values of TAWSS are slightly higher in the FSI model in the portions of the fluid-structure interface outside the stent, while they are similar in the vicinity of the struts. This means that the stent makes the vessel wall stiffer, thus reducing the WSS differences.
The percentage area exposed to TAWSS lower than 0.4 Pa in the ROI (Table 4.2) is similar between the FSI and rigid-wall cases. In particular, the percentage difference between the CoCr FSI and rigid-wall cases is equal to 1.57% while between the PLLA cases is 1.05%.
In Fig. 4.7 the area distribution of TAWSS in the ROI are presented for the four analyzed cases. To better visualize the differences between the histograms, the bars with an absolute difference greater than 0.005 between the FSI and rigid-wall models are indicated by symbols. Differences between the bars are small: the maximum absolute difference for the CoCr cases is 0.022 (interval 1.4-1.5 Pa) while for the PLLA cases is 0.008 (interval 1.4-1.5 Pa).
In addition to the TAWSS, which is an average quantity, the instantaneous WSS were studied. The time instants corresponding to peak pressure and peak flow rate (t = 0.59 s, Q = 91.1 mL/min) were chosen. In Figs. 4.8 and 4.9 the distributions of WSS in the ROI are presented, respectively at peak pressure and

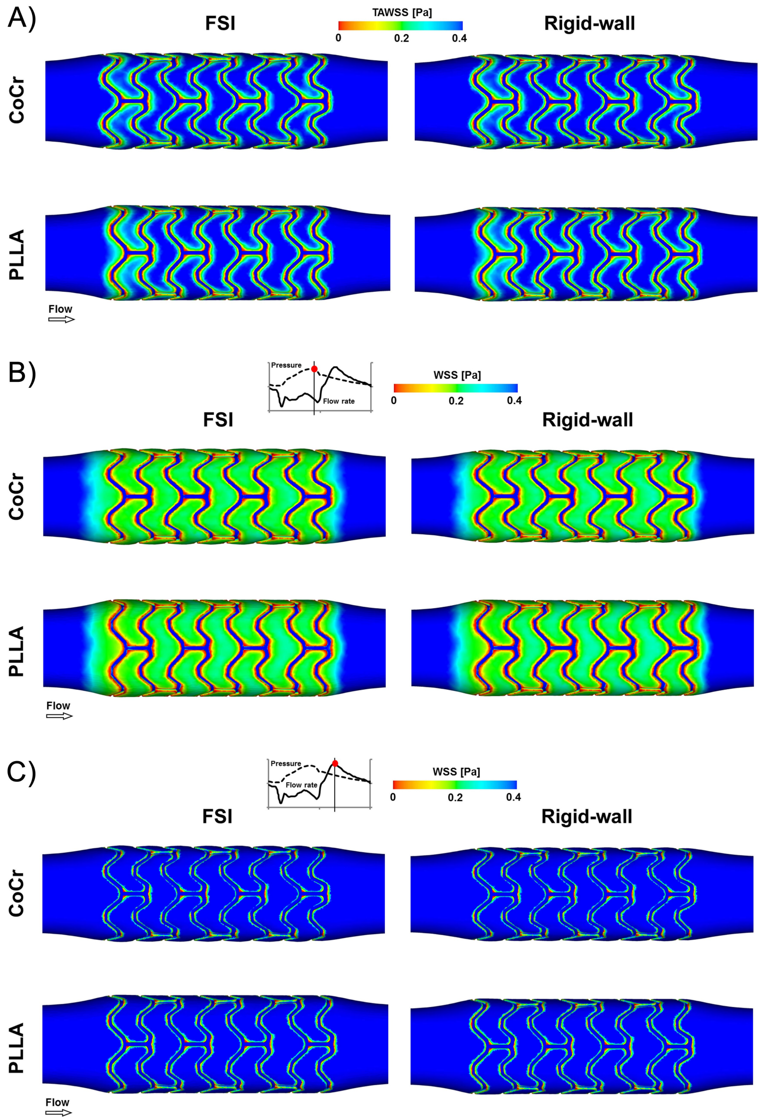

Figure 4.5: Contour maps of (a) TAWSS, (b) WSS at peak pressure (t = 0.37 s, p = 139.6 mmHg), (c) WSS at peak flow rate (t = 0.59 s, Q = 91.1 mL/min) along the fluid-structure interface: left) CoCr and PLLA FSI models; right) CoCr and PLLA rigid-wall models. Low values of WSS are indicated in red.

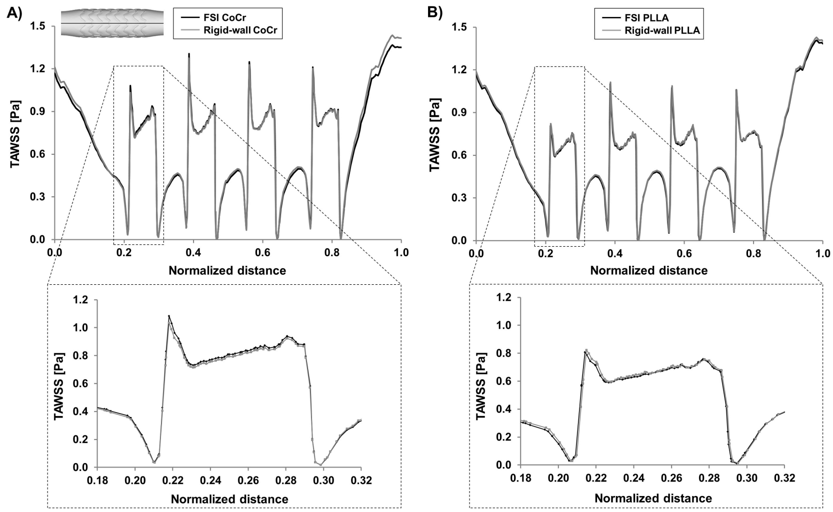

Figure 4.6: TAWSS on a line in the axial direction of the vessel: a) FSI and rigid-wall CoCr models; b) FSI and rigid-wall PLLA models. The distance is normalized in the ROI. The reference line is shown on the top left image. In the magnification area, an exemple of WSS peaks due to the presence of stent struts is displayed

flow rate (the corresponding contour maps of WSS are depicted in Fig. 4.5 b,c). No significant differences between FSI and rigid-wall models can be detected, also considering the instantaneous quantities.

4.4 Limitations

Although this study proposes a novel aspect of the comparison between a stented artery analyzed under FSI and rigid-wall approach, some necessary assumptions were adopted.

The velocity and pressure waveforms imposed as boundary conditions of the models were taken from *in vivo* data (Davies et al., 2006). Therefore, flow conditions are quite reliable. However, the heart motion, typical of the diastolic coronary flow, was neglected in this work, isolating the effects of the pure coronary artery intravascular flow on the wall compliance. In the literature, several works about the effects of cardiac-motion on hemodynamics have been proposed with conflicting results. According to these numerical studies (Hasan et al., 2013; Prosi et al., 2004; Theodorakakos et al., 2008; Zeng et al., 2003)

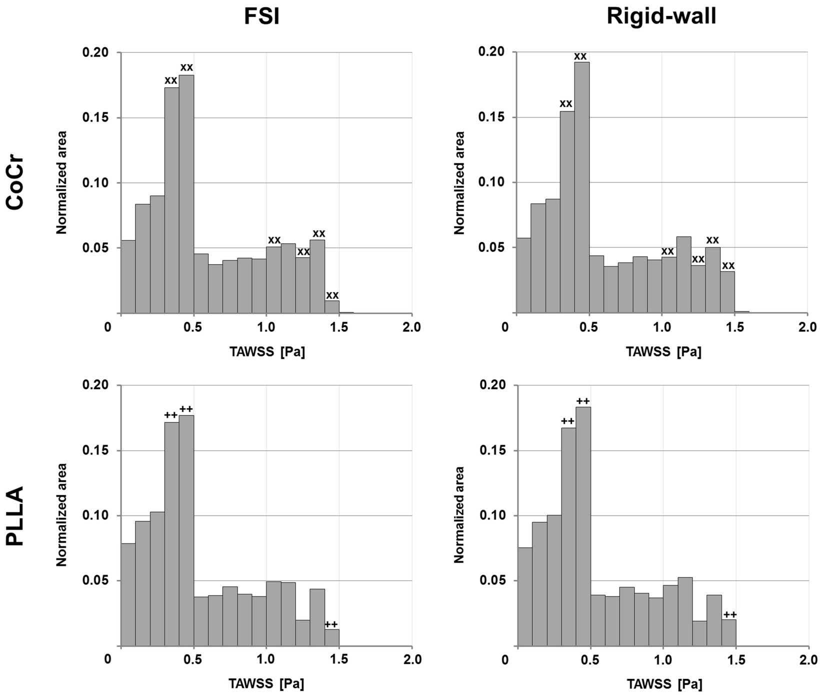

Figure 4.7: TAWSS distributions: left) CoCr and PLLA FSI models; right) CoCr and PLLA rigid-wall models. Each bar of the histograms represents the amount of normalized area with a defined range of TAWSS. Bar widths are 0.1 Pa. The bars with an absolute difference greater than 0.005 between the FSI and rigid-wall models are indicated by the symbols ”xx” and ”++”, respectively for the CoCr and PLLA cases.

Table 4.2: Percentage of area exposed to WSS lower than 0.4 Pa in the ROI.

	Percentage area with WSS $<$ 0.4 Pa [%]			
	Cocr		PLLA	
Time instant	FSI	Rigid-wall	FSI	Rigid-wall
t = 0.37 s	67.68	66.41	70.96	69.85
t = 0.59 s	12.58	12.79	16.10	15.68
Time averaged	40.22	38.65	44.91	43.86

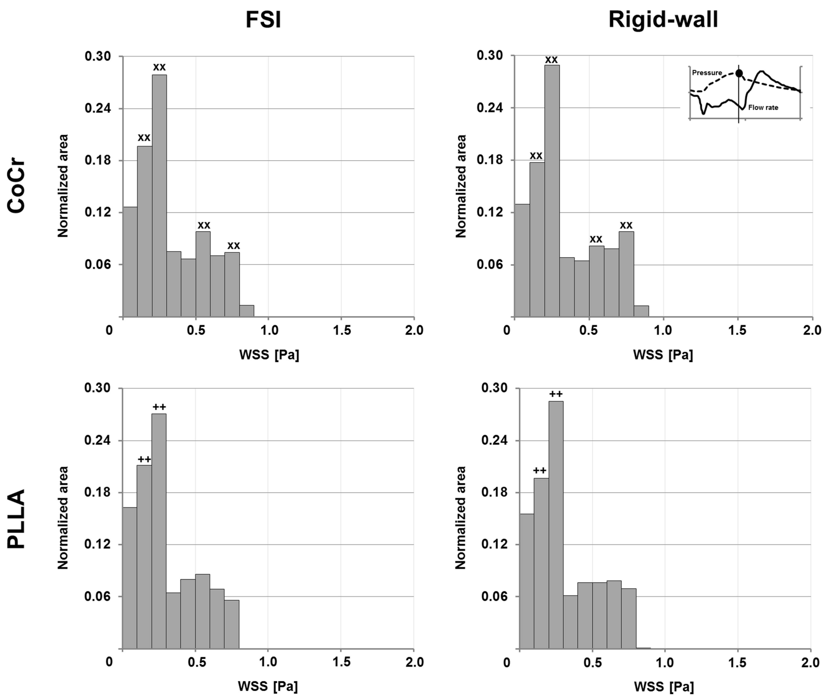

Figure 4.8: WSS distributions at peak pressure (t = 0.37 s, p = 139.6 mmHg): left) CoCr and PLLA FSI models; right) CoCr and PLLA rigid-wall models. Each bar of the histograms represents the amount of normalized area with a defined range of TAWSS. Bar widths are 0.1 Pa. The bars with an absolute difference greater than 0.01 between the FSI and rigid-wall models are indicated by the symbols "xx" and "++", respectively for the CoCr and PLLA cases.

cardiac-motion does not significantly affect the hemodynamics of coronary tree. In Section 3.4.1 more details about this topic are given.

The second assumption of this work is related to the modeling of the arterial wall, which was considered as a hyperelastic incompressible isotropic and homogeneous material using the strain energy function originally proposed by Demiray (1972). A more realistic model for the material might be implemented taking into account the anisotropy related to collagen fiber dispersion in the tissue (Gasser et al., 2006) and the three-layered characterization of the arterial wall (Holzapfel et al., 2005). Moreover, the initial stresses due to the stent deployment were neglected in this preliminary study. This aspect may over-

estimate the computation of the displacements in the arterial wall.
Lastly, the initial structural simulation of stent deployment was used exclusively to obtain the geometry for the subsequent FSI and rigid-wall fluid dynamic simulations. The stress state of the artery and the stent due to the expansion of the device were not considered in the FSI analyses. Therefore, the stress in the artery and in the stent calculated in these analyses might be underestimated. Even though this approximation may strongly affect the wall stresses and strains computation, the compliance, which was evaluated in this study, is relatively unaffected, depending basically only on the pressure field.

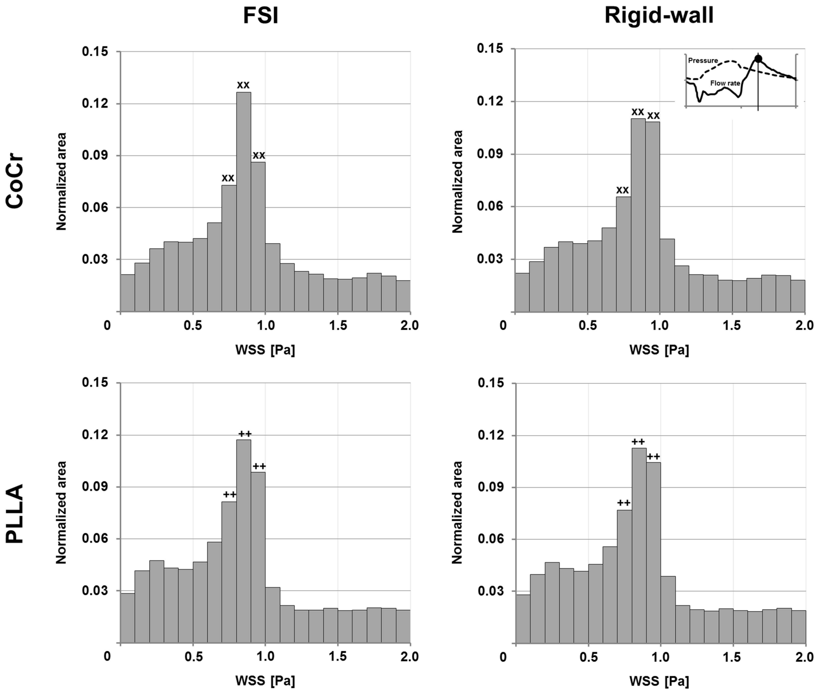

Figure 4.9: WSS distributions at peak flow rate (t = 0.59 s, Q = 91.1 mL/min): left) CoCr and PLLA FSI models; right) CoCr and PLLA rigid-wall models. Each bar of the histograms represents the amount of normalized area with a defined range of TAWSS. Bar widths are 0.1 Pa. The bars with an absolute difference greater than 0.01 between the FSI and rigid-wall models are indicated by the symbols ”xx” and ”++”, respectively for the CoCr and PLLA cases.

4.5 Conclusions

A FSI model of an idealized straight stented coronary artery was created and compared to the corresponding rigid-wall model in order to understand the effects of the wall compliance on the hemodynamics. The effect of two different stent materials, CoCr and PLLA, on the results was evaluated.
Similar results were found in terms of TAWSS and instantaneous WSS between compliant and rigid-wall cases: the contour maps of WSS and also the WSS profiles are qualitatively similar; the difference of percentage area exposed to TAWSS lower than 0.4 Pa in the stented region between the FSI and the rigid-wall cases is low (about 1.5 % and 1.0 %, respectively for the CoCr and PLLA cases).
The comparison between compliant and rigid-wall cases showed similar results in terms of WSS although CoCr and PLLA FSI models deform differently during the cardiac cycle, with higher values of displacement in the stented region for the PLLA FSI case.
The results of the present work indicate that, for idealized models of a stented coronary artery, the rigid-wall assumption for fluid dynamic simulations appears adequate when the aim of the study is the analysis of near-wall quantities like WSS.

Chapter 5

Hybrid meshing method for stented coronary artery CFD models

CFD analyses have been frequently conducted to study the influence of stent implantation on blood flow. However, due to the complexity of the geometry of stented arteries, the high computational cost required for this kind of simulations has strongly limited their use both in the clinical and industrial field. Hence, the present study focuses on the development of an efficient volume meshing method, which allowed us to obtain accurate results on 3D complex geometries in a short time compatible with the available computational resources. A hybrid meshing strategy was chosen, using both tetrahedral and hexahedral elements. The efficacy of this new meshing strategy was evaluated by comparing the hybrid mesh with a standard fully tetrahedral mesh. The hybrid mesh allowed to halve the computational time required for a steady-state simulation, obtaining at the same time similar results in terms of WSS and velocity field.

The contents within this chapter have been published in:
Chiastra, C., Morlacchi, S., Pereira, S., Dubini, G., and Migliavacca, F. (2012). Computational fluid dynamics of stented coronary bifurcations studied with a hybrid discretization method. *European Journal of Mechanics B/Fluids*, 35: 76-84.

5.1 Introduction

RECENTLY, fluid dynamic numerical models have been recognized as a very useful tool for studying macro and micro aspects of blood flow through stented vessels (Chapter 3). However, the complexity of the fluid domain characterized by the presence of stent struts in contact with the arterial wall together with the need of a fine and highly regular discretization concurs in greatly increasing the degrees of freedom of the CFD problems. As a consequence, the high computational resources needed to solve these models are a great limitation to further improve and routinely apply these models in industry and in the clinical field. Thus, the present study focuses on the development of an efficient volume meshing method, which allowed us to obtain accurate results on 3D complex geometries in a short time compatible with the available computational resources.

A hybrid meshing strategy was chosen, combining tetrahedral elements, which are able to describe the complex surface geometry of a stented artery, and hexahedral elements for the internal core of the domain, to reduce the number of degrees of freedom of the model and consequently its computational cost. The efficacy of this new meshing strategy was evaluated by comparing the computational time and the fluid dynamic results (WSS and velocity field) that were obtained using the hybrid mesh with the ones obtained with a standard fully tetrahedral mesh.

A straight artery with one stent repeating unit was considered in the study. The fluid domain was reconstructed from the final geometrical configuration obtained in a structural finite element simulation similar to those described in Gastaldi et al. (2010). In this way, the fluid volume of the CFD simulation is not only based on geometrical assumptions but takes into account the different mechanical behaviour of the artery and the stent and the interactions of the different parts during the stenting procedure (Morlacchi et al., 2011a).

5.2 Materials and methods

Three steps are involved in the implementation of the new meshing method: (1) the creation of the fluid domain; (2) the construction of an accurate fully-tetrahedral mesh; (3) the creation of a hybrid mesh that was finally compared to the fully-tetrahedral mesh.

5.2.1 Geometry

The geometry of a straight coronary artery was created using Rhinoceros v.4.0 CAD software (McNeel & Associates, Indianapolis, IN, USA) (Fig. 5.1). The length of the vessel is 20 mm while the inlet and outlet diameters are 2.70 mm. One repeating unit of a typical open-cell coronary stent was expanded inside the vessel through a structural simulation performed in ABAQUS/Explicit (Dassault Systemes, Simulia Corp., RI, USA) reaching a final diameter of 3.00 mm. All the details about a similar stent expansion are reported in Gastaldi et al. (2010). The stent model is characterized by a thickness of 150 μm and an external diameter in the non-crimped configuration of 1.55 mm. The final geometrical configurations after the elastic recoil were exported as triangulated surfaces in the meshing software.

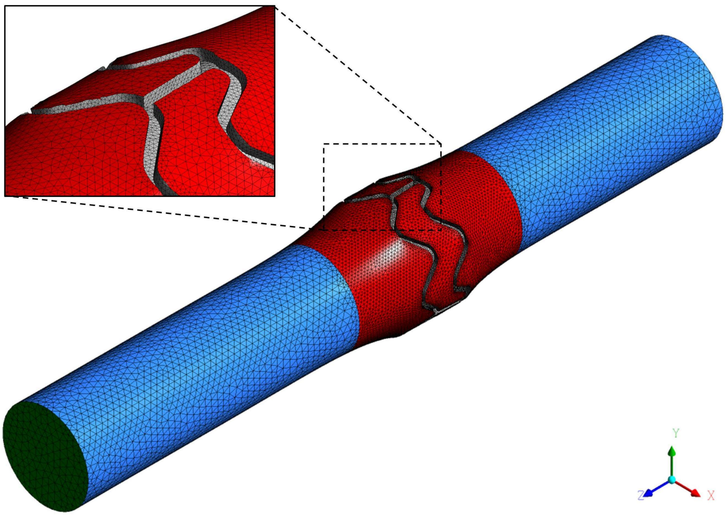

Figure 5.1: Straight real-dimensioned coronary artery with one deployed stent repeating unit. The different parts in which the 3D model was subdivided are differently colored. In the stented region (red part) a finer tetrahedral mesh was created in order to obtain more accurate fluid dynamic results. *Reprinted with permission from European Journal of Mechanics B/Fluids Vol.35, 76-84. C. Chiastra et al. Computational fluid dynamics of stented coronary bifurcations studied with a hybrid discretization method.* ©*(2012) Elsevier Masson SAS.*

5.2.2 Fully tetrahedral discretization method

The reduced model was initially meshed with only tetrahedral elements by the use of the Octree algorithm available in ANSYS ICEM CFD v.13.0 (Ansys Inc. - Canonsburg, PA, USA). It is a ”top down” method that has been found to be particularly robust and easy to setup for biomedical applications. The inputs include the geometry, a max size and a ”material point” location. The method is automated and has several main phases, including ”refinement”, ”cutting”, ”flood fill” and ”smoothing”.

The refinement algorithm works by first creating a region that is equivalent to a far field bounding box, scaled up to be divisible by the specified max size. This region is then subdivided down to the max cell size without regard for the geometry. For each iteration, each cell is checked to look for any entities with a lower max size than the cell. If the response is true, the cell is subdivided in the three Cartesian directions. One 3D hexahedral element is broken into 8 smaller elements, hence the name ”Octree”. After refinement is complete, the mesh is converted into tetrahedral elements using a 1 hexahedron to 12 tetrahedron pattern that provides higher element quality than similar alternatives. At the end of the refinement portion, mesh is generated both inside and outside of the geometry, but without any respect to its boundaries.

The cutter phase of the Octree process compares a tessellated version of the model (controlled by triangulation tolerance) with the octree volume mesh and subdivides and adjusts elements to fit the geometry. Shell elements are created between these surface projected nodes.

The third stage of the process is commonly referred to as the flood fill. Here, the material point location is used to identify an element that the user wants to keep. Iteratively, adjacent elements are added to the volume part in all directions. The flood fill is limited by the surface projected shell elements and will stop when the volume region is surrounded on all faces by shells.

The final stage of the Octree process is smoothing. The smoother adjusts node locations to improve individual element quality, but the flexibility of each node is constrained by the underlying geometry entities. The final result is a rather ordered isotropic tetrahedral mesh.

In order to assure accurate results in the region of interest of the reduced stented artery model, an appropriate grid independence analysis was performed. Different element sizes were associated to the different parts of the model. In particular, a more refined mesh was created in the stented region, i.e. the portion of the artery close to the stent (Fig. 5.1). Four different fully tetrahedral meshes were created (Fig. 5.2) varying the following parameters: the global model element size, the element size of the stented region of the artery and the stent element size. Table 5.1 summarizes the main features of the four meshes.

Table 5.1: Meshes used for grid independence study.

Mesh	Global element size	Stented region element size	Stent element size	Number of elements	Number of nodes
A	0.40	0.40	0.20	192,000	34,179
B	0.20	0.20	0.10	367,000	64,090
C	0.20	0.10	0.05	433,000	76,016
D	0.20	0.05	0.05	778,000	138,247

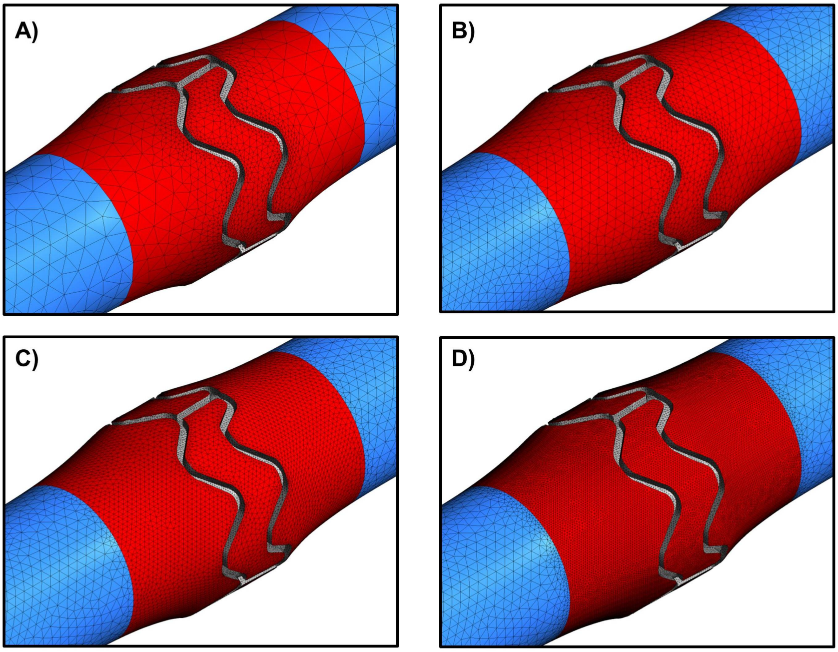

Figure 5.2: Four different meshes used for the mesh independence study: a) Tetra 0.40 0.40 0.20; b) Tetra 0.20 0.20 0.10; c) Tetra 0.20 0.10 0.05; d) Tetra 0.20 0.05 0.05. Mesh C parameters were chosen for creating the hybrid mesh. *Reprinted with permission from European Journal of Mechanics B/Fluids Vol.35, 76-84. C. Chiastra et al. Computational fluid dynamics of stented coronary bifurcations studied with a hybrid discretization method.* ©*(2012) Elsevier Masson SAS.*

Then, steady-state fluid dynamic simulations were performed using these meshes. The commercial finite-volume software ANSYS Fluent v.13.0 (ANSYS Inc., Canonsburg, PA, USA) was used to solve the following continuity and Navier-Stokes equations for steady-state incompressible flow:

$$\nabla \cdot \mathbf{v} = 0 \tag{5.1}$$

$$\rho\left(\mathbf{v} \cdot \nabla \mathbf{v}\right) = -\nabla p + \mu \nabla^2 \mathbf{v} \tag{5.2}$$

where $\mathbf{v}$ is the velocity vector, p is the pressure, ρ is the fluid density and μ is its dynamic viscosity.
At the inlet cross-section a constant paraboloid-shaped velocity profile (mean velocity = 0.3 m/s) was imposed, while at the outlet cross-section a reference zero pressure was chosen. This assumption is justified by the fact that the vessel and stent struts were assumed to be rigid. Thus, the velocity field is not influenced by the absolute values of pressure. A no-slip condition was imposed at the arterial wall. Blood was defined as an incompressible non-Newtonian fluid with a density of 1,060 kg/m^3. Its viscosity was described using the Carreau model:

$$\mu = \mu_\infty + (\mu_0 - \mu_\infty) \cdot \left[1 + \left(\lambda \cdot \dot{S}\right)^2\right]^{(n-1)/2} \tag{5.3}$$

where μ is the dynamic viscosity, $\dot{S}$ is the shear rate, μ_0 and μ_∞ are the viscosity values at $\dot{S}$ equal to zero and infinite, which respectively are equal to 0.25 Pa·s and 0.0035 Pa·s, λ is the time constant equal to 25 s and n is the Power-Law index equal to 0.25 (Seo et al., 2005).
The ANSYS Fluent pressure-based coupled algorithm which solves simultaneously continuity and momentum equations was used to calculate the solution. A second-order upwind scheme for the momentum spatial discretization was chosen. Under-relaxation factors were set equal to 0.75 for the pressure and the momentum and equal to 1 for density. The Courant number was set to 200. Convergence criterion for continuity and velocity residuals was set to 10^{-7}. Simulations were performed in parallel on 2 cores of a desktop computer equipped with one Intel i7-870 (2.93 GHz) quad-core processor and 16 GB RAM.
The mesh independence study was done comparing the following quantities:

- *area-weighted average wall shear stress (awa-WSS) in the stented region:*

$$awa - WSS = \frac{1}{A} \int WSS \, da = \frac{1}{A} \sum_{i=1}^{n} WSS \, |A_i| \tag{5.4}$$

where A is the total area of the region of interest, A_i is the area of the single face i and n is the number of faces of the region of interest. The different meshes were compared by calculating the percentage difference of awa-WSS of each mesh with respect to the finest one.

- *WSS on a line in the axial direction of the vessel;*
- *total CPU time*, which is the sum of the time used by each computing core during the numerical simulation, without including time for load imbalances or for communications;
- *computational wall-clock time*, which is defined as the time that elapses from the start to the end of the simulation, including the CPU time, the input/output time and potential channel delays.

5.2.3 Hybrid discretization method

Results obtained with the fully tetrahedral mesh were successively compared to those obtained with the new hybrid meshing method that comprises both tetrahedral and hexahedral elements. Hexahedral elements should be preferred because of their higher accuracy and reduced number of elements necessary to discretize a certain volume resulting in better performances in terms of computational speed. On the other hand, producing fully hexahedral elements for highly complex geometrical structures, i.e. intersection zones between the stent struts and the arterial wall, is not practical. A hybrid solution that uses hexahedral elements in the simple regions and tetrahedral elements in the stent-near-wall region was chosen as a good compromise.
The first steps of this meshing method were the creation of an internal cylinder along the whole vessel length (Fig. 5.3a-2) and the corresponding hexahedral mesh (Fig. 5.3a-3). Then, in the region between the internal cylinder and the arterial wall a tetrahedral mesh was generated. In the end, the two meshes were merged together (Fig. 5.3a-4). The final hybrid mesh obtained with this procedure is shown in Fig. 5.3b for one cross-section of the model.
The choice of the cylinder diameter is a trade-off between the opportunity of creating a wide hexahedral internal region to decrease the computational cost and the necessity of an adequate spacing from the arterial wall to allow a smooth transition between the hexahedrons and fine tetrahedral surface elements.
Tetrahedral mesh parameters were chosen in accordance with the previous grid independence analysis (Section 5.2.2). Accordingly, the hexahedral mesh density was decided so that velocity fields and bulk flow quantities were not dependent on grid dimension. The ANSYS ICEM CFD mesh merging algorithm

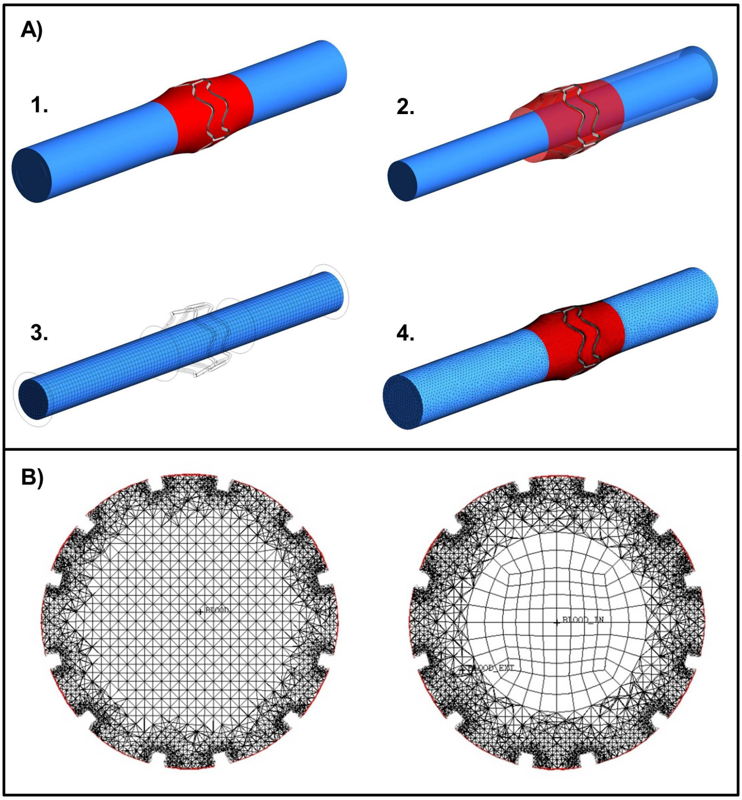

Figure 5.3: a) Steps for the creation of the hybrid mesh: (1) 3D geometry obtained through a previous structural simulation of the stent expansion; (2) creation of the internal cylinder; (3) hexahedral meshing of the internal cylinder; (4) tetrahedral meshing and merging of the two meshes. b) Fully tetrahedral mesh (left) and hybrid mesh (right) of the same cross-section. *Reprinted with permission from European Journal of Mechanics B/Fluids Vol.35, 76-84. C. Chiastra et al. Computational fluid dynamics of stented coronary bifurcations studied with a hybrid discretization method. ©(2012) Elsevier Masson SAS.*

can merge hexahedral or hybrid meshes with a tetrahedral mesh region. The method makes all the adjustments on the tetrahedral side of the merge, while the other side remains frozen. The algorithm starts by aligning the boundary perimeter between the regions. Nodes within a specified tolerance are moved to alignment and merged. Nodes that cannot be aligned within a tolerance result in a split of the perimeter edges so that there is a node to merge with in the following iteration. After the perimeter is aligned, internal nodes are adjusted in a similar way marching inward from the perimeter. Hexahedral elements are capped with pyramids as transition elements. Tetrahedral elements are split or merged as necessary to provide a conformal mesh merge.

5.3 Results and discussion

In order to obtain reliable results in compatible times with the available computational resources, a new hybrid meshing method was developed. At the beginning, a grid independence analysis was performed to obtain an accurate tetrahedral discretization of the stented artery model. In Table 5.2, the main quantitative results of this grid independence study are reported. awa-WSS values in the stented region are similar for all the considered meshes. Starting from the coarsest mesh to the finer ones, the percentage difference of awa-WSS with respect to the finest mesh (Mesh D) is lower than 1.5 %. It is also possible to notice that the computational time (total CPU time and wall-clock time) increases linearly with the increase of the mesh element number. Figure 5.4 shows WSS on a line in the axial direction of the vessel for the four compared meshes. A qualitative comparison of the four curves shows a similar pattern and no significant differences can be found.
As the percentage difference of awa-WSS between mesh C and D is lower than 0.25 % and the computational time of mesh C is significantly lower than mesh D (about 30 %), grid parameters of mesh C were chosen for creating the hybrid mesh.
The effect of the presence of a boundary layer in the mesh was also investigated and no significant differences were present.
In Table 5.3, Fig. 5.5 and Fig. 5.6, the comparison between tetrahedral and hybrid mesh is reported to validate the new meshing method in terms of near-wall variables (awa-WSS), bulk-flow quantities (velocity magnitude), and computational time requests. The use of the hybrid mesh allows to halve the wall-clock

Table 5.2: Results of grid independence study.

	Mesh A	Mesh B	Mesh C	Mesh D
awa-WSS [Pa] *percentage diff.*	0.941 *1.40 %*	0.925 *0.32 %*	0.930 *0.22 %*	0.928
Total CPU time [s]	104.9	228.2	351.2	494.4
Wall-clock time [s]	52.8	115.0	177.6	250.7

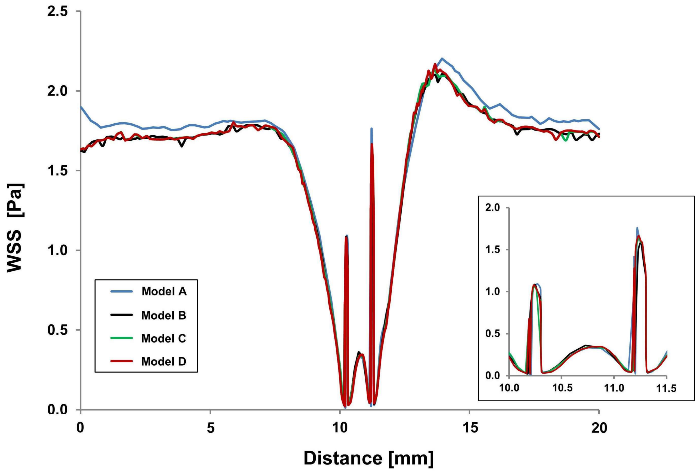

Figure 5.4: WSS on a line in the axial direction of the vessel for the four different meshes considered. In the magnification area, WSS peaks corresponding to the influence of stent struts are shown. *Reprinted with permission from European Journal of Mechanics B/Fluids Vol.35, 76-84. C. Chiastra et al. Computational fluid dynamics of stented coronary bifurcations studied with a hybrid discretization method. ©(2012) Elsevier Masson SAS.*

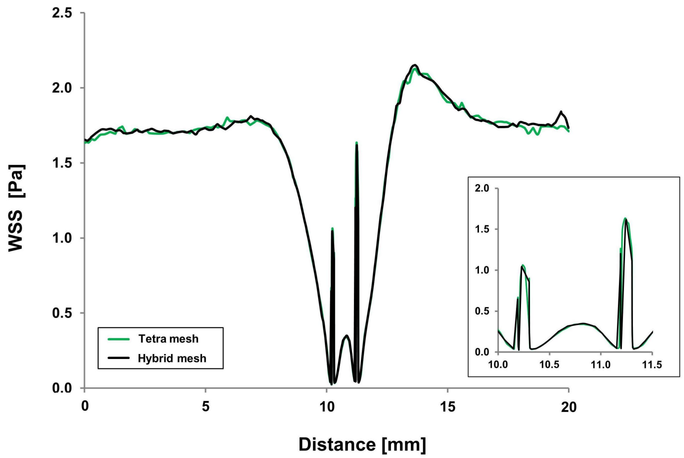

Figure 5.5: WSS on a line in the axial direction of the vessel for the tetrahedral and hybrid meshes. In the magnification area, WSS peaks corresponding to the influence of stent struts are shown. *Reprinted with permission from European Journal of Mechanics B/Fluids Vol.35, 76-84. C. Chiastra et al. Computational fluid dynamics of stented coronary bifurcations studied with a hybrid discretization method. ©(2012) Elsevier Masson SAS.*

time, obtaining at the same time similar results (Table 5.3). In fact, the awa-WSS percentage difference between the two models is 0.15 %. Looking at Fig. 5.5, which shows the comparison between tetrahedral and hybrid meshes through WSS on a line in the axial direction of the vessel, no significant differences are present, too. Moreover, in Fig. 5.6 the comparisons between velocity profiles computed in three different locations with the hybrid (dotted line) and fully tetrahedral (solid line) meshes are proposed. Results highlight that hexahedral mesh density allows to correctly replicate velocity field in the core of the coronary artery. Acceptable differences were found in the transition between hexahedral and tetrahedral regions. Thus, the hybrid mesh appears to be a powerful tool to obtain correct fluid dynamic results in complex geometries like stented coronary arteries with a relatively low computational cost. In case of curved and asymmetric image-based models, the implementation of the hybrid mesh could be more complicated, still maintaining its computational advantages.

5.4 Conclusions

3D geometries of stented artery models are very complex, resulting in high computational requests for CFD simulations. The hybrid meshing method proposed in the present study aims to obtain accurate CFD results in a short time compatible with the available computational resources. This objective could be considered as a first step to obtain useful results for clinicians in a short time with the future perspective to run CFD simulations during the surgical planning phase.

The new meshing strategy was successfully developed on a straight real-dimensioned coronary artery. The computational time resulted to be halved using a hybrid mesh instead of a traditional tetrahedral grid, obtaining at the same time similar results.

In the end, the hybrid meshing method appears to be a powerful tool to ob-

Table 5.3: Comparison between the hybrid mesh and the standard tetrahedral mesh.

	Hybrid mesh	Tetrahedral mesh (Mesh C)
awa-WSS [Pa]	0.928	0.930
percentage diff.	*0.22 %*	
Total CPU time [s]	162.6	351.2
Wall-clock time [s]	82.2	177.6

tain correct fluid dynamic results in complex geometries like stented coronary arteries with a relatively low computational cost.

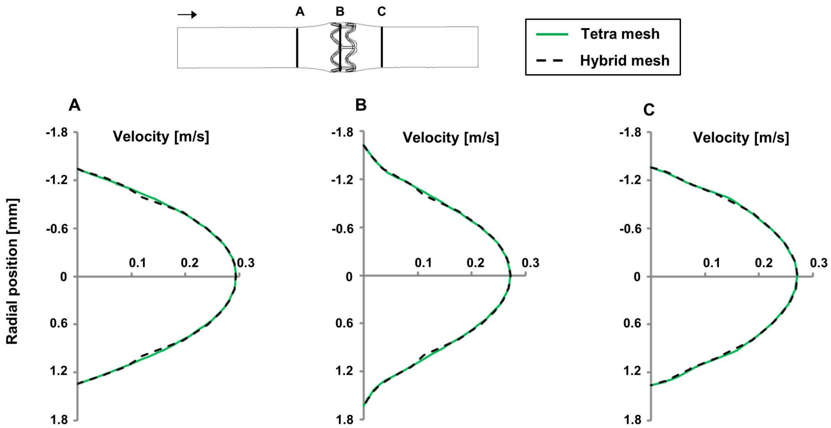

Figure 5.6: Comparisons between velocity profiles computed in three different locations of the vessel with the hybrid and fully tetrahedral meshes. *Reprinted with permission from European Journal of Mechanics B/Fluids Vol.35, 76-84. C. Chiastra et al. Computational fluid dynamics of stented coronary bifurcations studied with a hybrid discretization method. ©(2012) Elsevier Masson SAS.*

Chapter 6

Hemodynamic assessment of stenting procedures for coronary bifurcations

Stent implantation in coronary bifurcations is still a challenging area in interventional cardiology. A great number of stenting procedures has been proposed. However, each technique is associated with some limitations that make uncertain the choice of the treatment. CFD analyses on idealized stented coronary bifurcation models were performed in order to study the hemodynamic influence of different stenting techniques. Firstly, FKB inflation within PSB stenting approach, which is the current preferred strategy for the treatment of coronary bifurcations, is investigated. Secondly, the different hemodynamic scenarios provoked by FKB performed with a proximal or a distal access to the SB are compared. Lastly, the double stenting culotte technique is studied, comparing the behavior of a dedicated stent with a conventional one.

The contents within this chapter have been published in:

Morlacchi, S., Chiastra, C., Gastaldi, D., Pennati, G., Dubini, G., and Migliavacca, F. (2011). Sequential structural and fluid dynamic numerical simulations of a stented bifurcated coronary artery. *Journal of Biomechanical Engineering*, 133, art.no. 121010.

Chiastra, C., Morlacchi, S., Pereira, S., Dubini, G., and Migliavacca, F. (2012). Computational fluid dynamics of stented coronary bifurcations studied with a hybrid discretization method. *European Journal of Mechanics B/Fluids*, 35: 76-84.

6.1 PSB approach: kissing balloon inflation

6.1.1 Introduction

NOWADAYS PSB stenting approach is the preferred strategy employed by interventional cardiologists for the treatment of coronary bifurcation lesions because of its simplicity, flexibility for different sorts of lesions and bifurcated geometries, and good clinical outcomes (Lefèvre et al., 2010b; Mylotte et al., 2013). It implies the stenting of the MB followed by the optional treatment of the SB if the clinical conditions of the patient are considered sub-optimal after the first stent implantation. In this way, the highly non-physiological biomechanical influence induced by the simultaneous presence of two devices in the bifurcation is only limited to those cases that truly require it. This approach differs from the routine double stenting approach where the choice of implanting two stents is taken at the beginning of the treatment.
Frequently, the PSB approach is concluded with the final kissing balloon (FKB) procedure, which consists in the simultaneous expansion of two angioplasty balloons in both branches of the bifurcation. FKB procedure aims to free the access to the SB from the stent struts protruding into the lumen, allowing the optional implantation of a stent in the SB; furthermore, it improves the fluid dynamics downstream from the bifurcation.
Various clinical studies (Chen et al., 2008) have proven the idea that the FKB procedure causes an improvement in the clinical results in complex double stenting procedures like crush or culotte techniques. However, major uncertainty still remains on the application of the FKB procedure within one stent techniques as performed in the PSB stenting approach (Ormiston et al., 1999). For this reason, a better investigation of the PSB stenting biomechanical influences is still needed. Fluid dynamic simulations were performed in order to examine hemodynamic forces on the intimal layer of the vessel before and after the FKB procedure, enlightening both its benefits and drawbacks. Furthermore, a new tapered balloon dedicated to bifurcations was proposed to limit the structural damage induced to the arterial wall and to enhance WSS pattern at the intimal layer of the bifurcation.

6.1.2 Materials and methods

Creation and discretization of the fluid domain

A CAD model representative of the bifurcation of LAD with its first diagonal branch was created using Rhinoceros v.4.0 CAD program (McNeel & Asso-

ciates, Indianapolis, IN, USA). The model has a bifurcation angle of 45° (Pfled-erer et al., 2006) and includes the presence of two asymmetric atherosclerotic plaques corresponding, for the most critical section, to a 30.2% of area stenosis and a 2.06 mm hydraulic diameter (Fig. 6.1a). The internal diameters of the MB and the SB are respectively 2.78 and 2.44 mm (Lefèvre et al., 2000) while the thickness of the arterial wall (0.9 mm) was considered constant along the whole artery. The arterial wall was divided into three layers with different thicknesses corresponding to the intima (0.24 mm), the media (0.32 mm) and the adventitia (0.34 mm) in accordance to the work of Holzapfel et al. (2005).
The plaques were placed in correspondence of the external sides of the bifurcation as these zones are characterized by low and oscillating WSS and are a very athero-prone environment (Nakazawa et al., 2010).
The model of the stent (Fig. 6.1b) resembles the geometry of the CoCr Multi-Link Vision® coronary system (Abbott Laboratories, Abbott Park, Illinois, U.S.A). This stent is characterized by a total length of 15.5 mm, a thickness of 0.09 mm and an external diameter in the non-crimped configuration of 1.76 mm.
Structural simulations of stent deployment were performed by means of ABAQUS/Explicit (Dassault Systemes Simulia Corp., RI, USA) simulating the PSB stenting approach. Both standard cylindrical polymeric balloons and a novel tapered balloon dedicated to FKB inflation were used. The tapered balloon is characterized by a proximal conical part, a zone of transition and a distal cylindrical part as depicted in Fig. 6.1c. In Fig. 6.2 the steps of the PSB technique are schematized. All the details about these structural simulations can be found in Morlacchi et al. (2011a). At each significant procedural stage, the surfaces of the stent and the biological tissues defining the blood volume were exported from ABAQUS in terms of triangulated surfaces (Fig. 6.3). Afterwards, these surfaces were imported into the meshing software ANSYS ICEM CFD (Ansys Inc., Canonsburg, PA, USA). In order to reduce the number of elements and to increase the computational speed, the hybrid discretization method proposed in Chapter 5 was applied (Chiastra et al., 2012).
Hybrid meshes of three different cases were implemented: (1) bifurcation after stenting of the MB (model MBst); (2) bifurcation after 'standard FKB' (model FKBstd); (3) bifurcation after 'modified FKB' (model FKBmod). Mesh parameters (in particular, maximum element size) were chosen after an appropriate mesh independence study on WSS in the region close to the stent, resulting in the number of elements summarized in Table 6.1 and ensuring that results were independent from the number of mesh elements.

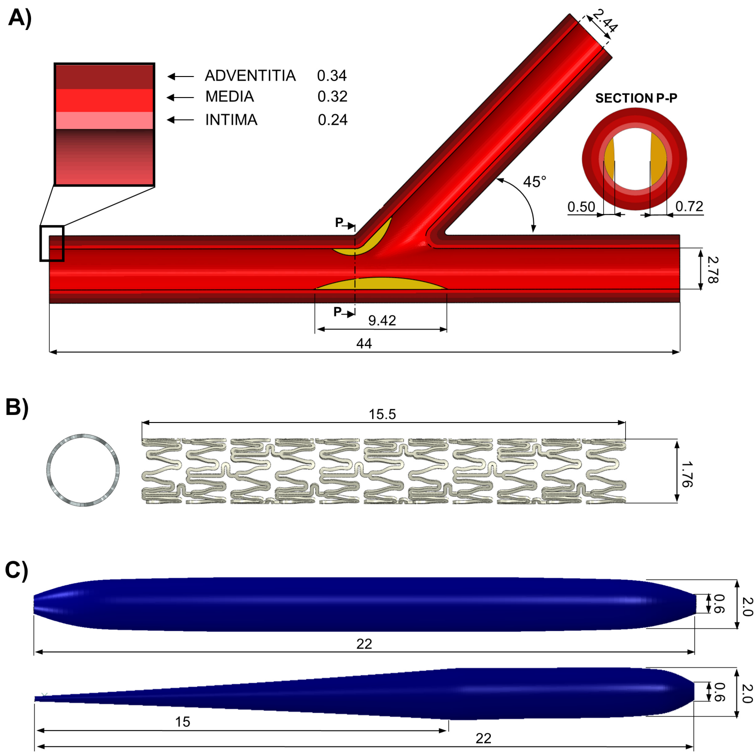

Figure 6.1: a) Geometric model of the atherosclerotic coronary bifurcation. In the magnification area on the left, the stratification of arterial wall in the three layers (intima, media and adventitia) is depicted; on the right, the illustration of the section corresponding to the maximal stenosis (30.2 % of stenosis area) provoked by the presence of the two atherosclerotic plaques. b) CAD model of the Multi-Link Vision® stent (Abbott Laboratories, Abbott Park, Illinois, U.S.A). c) Example of the two different models of polymeric balloons: a standard cylindrical balloon (top) and a tapered balloon characterized by a conical proximal part and a cylindrical distal part (bottom). Dimensions are in millimeters. *Adapted with permission from Journal of Biomechanical Engineering 2011 Vol.133(12): 121010. S. Morlacchi et al. Sequential structural and fluid dynamic numerical simulations of a stented bifurcated coronary artery. ©(2011) ASME.*

Simulations settings

The following continuity and Navier-Stokes equations for transient incompressible flow were solved using the commercial software ANSYS Fluent v.12.1 (Ansys Inc., Canonsburg, PA, USA):

$$\nabla \cdot \mathbf{v} = 0 \tag{6.1}$$

$$\rho \frac{\partial \mathbf{v}}{\partial t} + \rho \left(\mathbf{v} \cdot \nabla \mathbf{v} \right) = -\nabla p + \mu \nabla^2 \mathbf{v} \tag{6.2}$$

where $\mathbf{v}$ is the velocity vector, t is the time, p is the pressure, ρ is the fluid density and μ is its dynamic viscosity. A coupled solver was chosen with a second-order upwind scheme for the momentum spatial discretization and a first-order time implicit scheme to discretize the governing equations. A time step size of 10^{-4} s was considered. Under-relaxation factors of 0.4 for pressure and momentum and 1 for density were used. Convergence criterion for continuity and velocity residuals was set to 10^{-6}. Blood was assumed as an incompressible, non-Newtonian fluid with the density equal to 1,060 kg/m^3. The viscosity was described using the Carreau model (Eq. 5.3) with the parameter values proposed by Seo et al. (2005).

Definition of the boundary and flow conditions

Artery and stent struts were assumed to be rigid and defined with a no-slip condition. A pulsatile blood flow tracing was applied at the inlet as a paraboloid-shaped velocity profile with an average flow rate of 80.7 mL/min according to Charonko et al. (2009) (Fig. 6.4a). The definition of the boundary conditions at the outlets of the bifurcation was achieved by combining in a multi-domain approach the 3D CFD model of the bifurcation with a lumped parameter model applied at the outlets (Quarteroni and Veneziani, 2003) (Fig. 6.4b). In this work, preliminary simulations were carried out for a non-stented model of bifurcation without and with plaques, considering a part of the lumped parameter scheme proposed by Pietrabissa et al. (1996). The value of each element used in the lumped parameter scheme is reported in Table 6.2. Four cardiac cycles were simulated in order to guarantee convergence of the multi-domain approach

Table 6.1: Mesh element number of the three investigated models: bifurcation after stenting of the MB (MBst), bifurcation after 'standard FKB' (FKBstd) and bifurcation after 'modified FKB' (FKBmod).

	Number of elements	Number of nodes
MBst	2,639,271	496,924
FKBstd	2,665,097	508,822
FKBmod	2,576,539	495,845

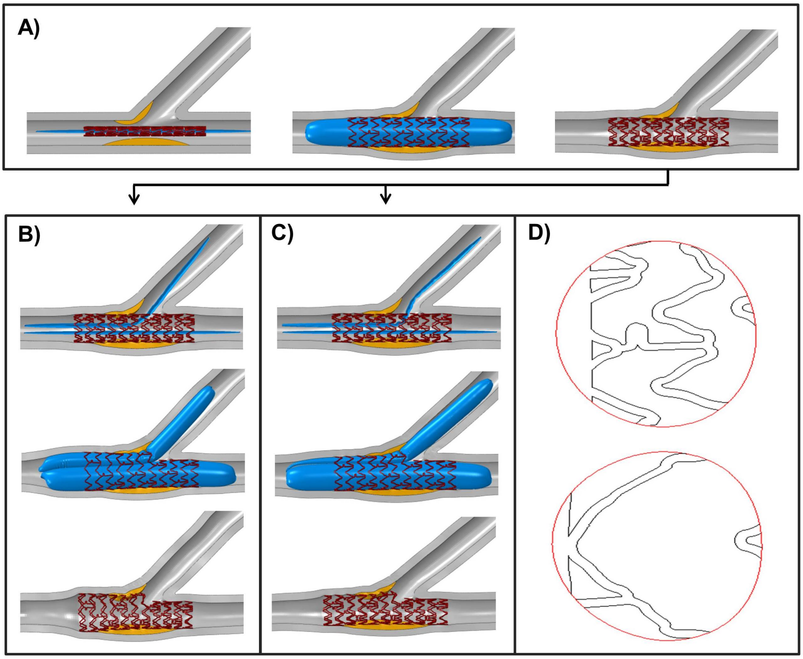

Figure 6.2: PSB technique steps: a) positioning of the crimped stent in the bifurcation, implantation in the MB, elastic recoil; b) final step called "standard FKB" inflation, performed with two cylindrical balloons in both branches; c) "modified FKB" carried out by deploying a cylindrical balloon in the MB and a tapered one in the SB. d) Deformed configurations of the stent struts in proximity of the bifurcation before (top) and after (bottom) the standard FKB (view from the access to the SB). *Reprinted with permission from Journal of Biomechanical Engineering 2011 Vol.133(12): 121010. S. Morlacchi et al. Sequential structural and fluid dynamic numerical simulations of a stented bifurcated coronary artery. ©(2011) ASME.*

used. Results in terms of flow rates at the outlets were virtually identical for both the two limit cases. This occurrence showed that downstream districts play a dominant role in establishing the blood flow distribution to downstream tissues. In other words, the flow resistance created by the stent struts in the SB area is not influencing the flow distribution between the distal MB and the SB. This assumption is in accordance with the results obtained by Balossino et al. (2009) for a carotid artery bifurcation where only a 90% stenosis affected the flow split between the branches of the carotid bifurcation. As a consequence, flow tracings at boundaries (Fig. 6.4a) were maintained constant in the investigated cases, which were solved as stand-alone models. In particular, at the MB outlet section, the flow resulting from the lumped parameter model of the coronary tree was applied as an outflow boundary condition while a reference pressure was imposed at the SB outlet cross-section. By neglecting the lumped parameter model at the outlet cross-sections we had the opportunity of obtaining correct results with a greater time step size (10^{-2} s versus 10^{-4} s, respectively for the stand-alone and the multi-domain model) and without simulating more consecutive cardiac cycles. This choice was done after a temporal sensitivity analysis and reduced the computational time to almost 40 hours for each transient simulation using a desktop computer equipped with a Intel i7-860 (2.93 GHz) quad core processor with 8Gb RAM.

Analysis of the results

The results of the CFD simulations were analyzed considering the following hemodynamic quantities: TAWSS and OSI, in order to investigate the forces acting on the arterial wall, and velocity magnitude and helicity in the transversal plane, to examine the influences of the stent struts on the local blood flow. These quantities are defined in Section 3.1. The percentage of area exposed to low TAWSS was calculated in the portion of the arterial wall which contains the stent (in the following we refer to it as the 'stented region') as the ratio between the area exposed to WSS < 0.5 Pa and the total area of the stented region.

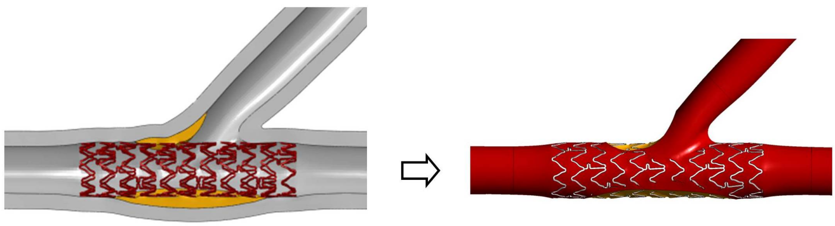

Figure 6.3: Creation of the fluid domain (right) from the final geometrical configuration obtained through structural simulations (left). *Adapted with permission from Journal of Biomechanical Engineering 2011 Vol.133(12): 121010. S. Morlacchi et al. Sequential structural and fluid dynamic numerical simulations of a stented bifurcated coronary artery. ©(2011) ASME.*

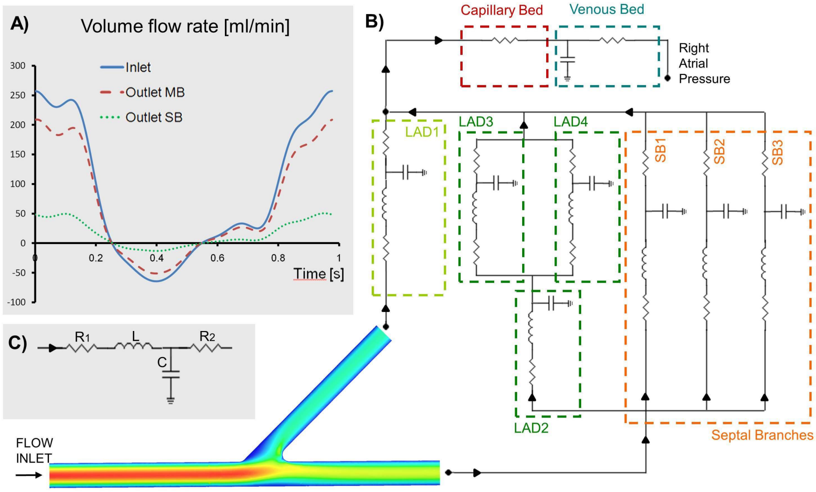

Figure 6.4: Multi-domain model of LAD with its diagonal branch. a) Flow tracing used as inlet condition (solid line) proposed in Charonko et al. (2009) and the flow tracings obtained at the MB (line-dotted model) and at the SB (dotted line). b) 3D model of the coronary bifurcation with the lumped parameter model of part of the coronary tree connected to the outlets. c) Example of the lumped parameter scheme used to model a segment of a coronary vessel characterized by two resistances, a capacitance and an inductance. *Reprinted with permission from Journal of Biomechanical Engineering 2011 Vol.133(12): 121010. S. Morlacchi et al. Sequential structural and fluid dynamic numerical simulations of a stented bifurcated coronary artery. ©(2011) ASME.*

Table 6.2: Values of the lumped parameter model of left coronary tree by Pietrabissa et al. (1996).

Branch	Resistance R_1 $[mmHg \cdot s/mL]$	Inductance L $[mmHg \cdot s^2/mL]$	Capacitance C $[mL/mmHg]$	Afterload R_2 $[mmHg \cdot s/mL]$
LAD1	3.1	0.10	$1.3 \cdot 10^{-3}$	115.6
LAD2	0.9	0.04	$1.2 \cdot 10^{-3}$	-
LAD3	6.7	0.10	$2.8 \cdot 10^{-4}$	425.0
LAD4	4.7	0.16	$1.9 \cdot 10^{-3}$	55.2
SB1	3.1	0.10	$1.3 \cdot 10^{-3}$	115.6
SB2	6.7	0.10	$2.8 \cdot 10^{-4}$	327.5
SB3	18.3	0.14	$9.8 \cdot 10^{-5}$	327.0
Capillaries	10.6	-	-	-
Venous bed	3.0	-	$6.0 \cdot 10^{-2}$	-

6.1.3 Results

The hemodynamic forces acting on the internal layer of the artery were analyzed in terms of TAWSS magnitude and OSI (Fig. 6.5). The percentage of area exposed to TAWSS lower than 0.5 Pa is 62.3% for MBst, 79.0% for FKBstd, and 71.3% for FKBmod. FKBstd creates a wider region with low WSS in the proximal part of the MB, in particular at the entrance of the stent, than MBst (Figs. 6.5a and 6.5b). The situation is partially improved by the introduction of the modified balloon (Fig. 6.5c), resulting in a smaller area exposed to low TAWSS (71.3%). Figure 6.5 illustrates the contours of the OSI, as well.
Figure 6.6 shows the stent strut influence on the local blood flow pattern in terms of velocity magnitude field and helicity before and after inflation of the modified FKB (Figs. 6.6a and 6.6b, respectively). Contours are plotted on the plane transversal to the bifurcation. A qualitative analysis of the results shows the positive influence of the FKB that removes the stent struts from the blood flow, freeing the access to the SB and lowering the hemodynamic disturbances downstream from the bifurcation.

6.1.4 Discussion

The fluid dynamic influence of FKB within PSB stenting approach was investigated. Three different cases were considered (MBst, FKBstd, FKBmod), corresponding to different steps of stenting procedure or balloon shapes. As expected, the three structural simulations generated very different deformed configurations for the artery and the stent, enhancing the importance of a structural simulation to obtain reasonable geometries for CFD simulation after stenting. These geometries could not have been deduced *a priori*.
The decision on whether performing or not the FKB after a single stenting techniques like PSB is still an open question (Lefèvre et al., 2010b). In agreement with this debate, numerical simulations carried out in the present work highlight both advantages and limits of performing the FKB procedure. For instance, our results highlight that stenting of the MB permits total recovery of the vessel lumen, but reduces access to the SB by interposing metallic struts in the midst of the blood flow. Figure 6.6a clearly shows the fluid dynamic alterations caused by the presence of the hanging struts. Execution of the FKB allows the displacement of these struts and frees the access to the SB, while maintaining at the same time a straight configuration of the device (Fig. 6.2). These results point to improvements in the local blood flow pattern in terms of a more regular flow downstream of the bifurcation and a decrease of the helicity magnitude field (Fig. 6.6b). On the other hand, FKB creates a non-physiological overex-

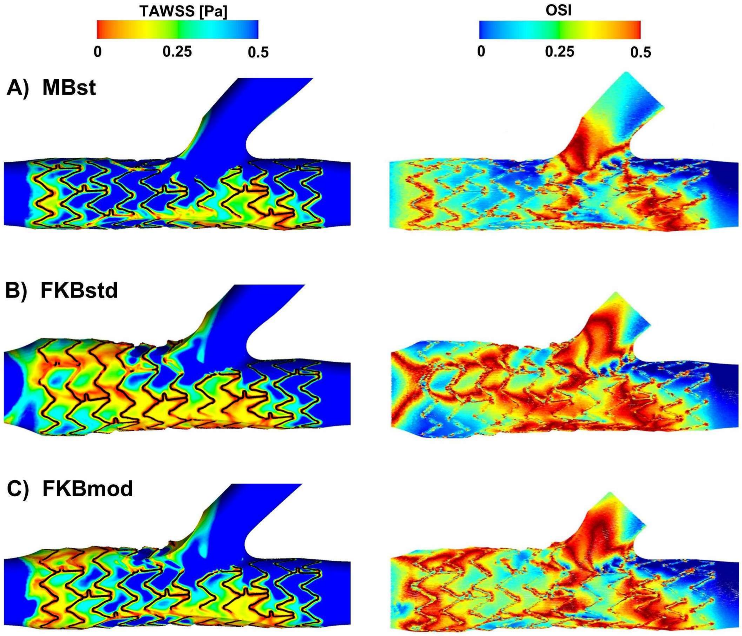

Figure 6.5: Hemodynamic forces acting on the endothelial layer. Contours of TAWSS (left) and OSI (right) for the analysed cases: a) stenting of the MB, b) standard FKB inflation performed with two cylindrical balloons (3.00 mm in the MB and 2.00 mm in the SB), c) modified FKB inflation performed with a cylindrical 3.00 mm balloon in the MB and a dedicated conical balloon in the SB. *Reprinted with permission from Journal of Biomechanical Engineering 2011 Vol.133(12): 121010. S. Morlacchi et al. Sequential structural and fluid dynamic numerical simulations of a stented bifurcated coronary artery.* ©*(2011) ASME.*

pansion in the proximal part of the MB due to the simultaneous presence of two balloons. The hemodynamic forces acting on the endothelial cells are altered: after the FKB (Fig. 6.5b) the area characterized by TAWSS lower than 0.5 Pa is wider than in the case of MB stenting only (Fig. 6.5a), rising from 62% to 79%. This phenomenon is more evident in the proximal part of the MB and, particularly, at the entrance of the stented area. This region is particularly critical also because of the high OSI values calculated.
The last considerations proposed in this work are related to the use of a different balloon specifically designed to overcome the major limitation provoked by a standard FKB inflation: the overexpansion in the proximal part of the MB. This balloon is characterized by three different regions: a tapered proximal part, a

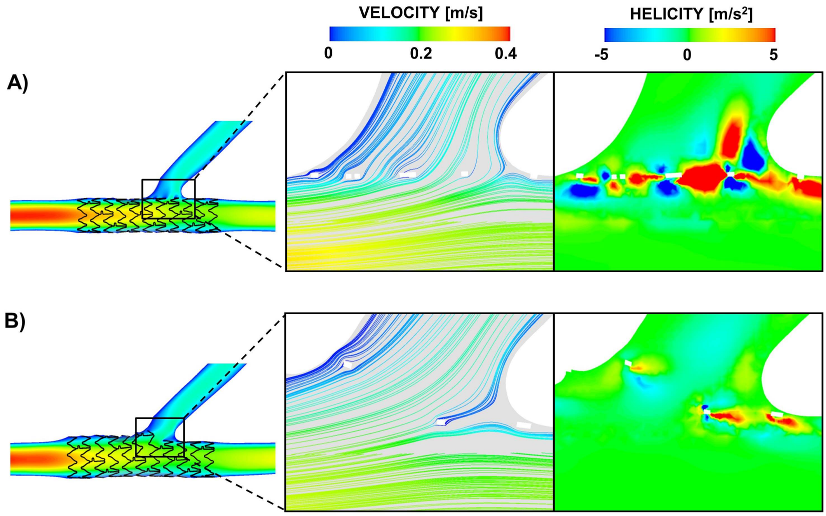

Figure 6.6: Velocity magnitude, streamlines, and helicity at the average flow rate in the transversal plane after the MB stenting (a) and the modified FKB (b), respectively. *Reprinted with permission from Journal of Biomechanical Engineering 2011 Vol.133(12): 121010. S. Morlacchi et al. Sequential structural and fluid dynamic numerical simulations of a stented bifurcated coronary artery. ©(2011) ASME.*

transition zone and a distal standard cylindrical part (Fig. 6.1c). By performing a modified FKB with the tapered balloon, the overexpansion of the MB decreases while maintaining, at the same time, the positive effects of this procedure from the hemodynamic point of view. Simulations showed that the use of a tapered balloon improves the hemodynamic influence of the FKB by decreasing the zone characterized by low and oscillating WSS (Fig. 6.5c) if compared to the standard FKB procedure (Fig. 6.5b).

6.1.5 Conclusions

The hemodynamic influence of the FKB during the PSB approach, which nowadays is the preferred bifurcation stenting strategy, was investigated.
Results of fluid dynamic simulations highlighted the advantages of FKB inflation in terms of better flow pattern and access to the SB, but also its drawbacks in terms of overexpansion of proximal part of the MB. In particular, FKB provokes a wider region characterized by low and oscillating WSS, which is asso-

ciated to the risk of ISR. In the end, this work shows that the use of a tapered balloon deployed in the SB during FKB might reduce the main drawbacks of this procedure.

6.2 PSB approach: proximal or distal access to side branch?

6.2.1 Introduction

As previously exposed in Section 6.1.1, PSB approach is usually concluded by FKB procedure which consists in the simultaneous expansion of two balloons in both the coronary bifurcation branches. Several kinds of accesses to the SB can be used to perform FKB resulting in different final geometrical configuration of both artery and implanted stent and, consequently, altered hemodynamic scenarios. Clinical experience showed that opening the stent struts through the most distal strut available (Fig. 6.7c) improves the structural support to the SB, the apposition of stent struts to the arterial wall favouring a correct drug elution and the blood flow pattern across the bifurcation. On the other hand, performing FKB with a proximal access to the SB (Fig. 6.7b) might result in the protrusion of some stent struts in the MB leading to strut malappositions and major disturbances to the blood flow. However, the current preference for the distal access is purely based on clinical experience and no quantitative data on the actual modifications of the blood flow have been presented in scientific literature, yet. Hence, the aim of this work is the implementation of a CFD model to quantitatively investigate the different hemodynamic scenarios provoked by a PSB procedure performed with a proximal or a distal access to the SB.

6.2.2 Materials and methods

An idealized coronary bifurcation (Pflederer et al., 2006) representative of the junction between the LAD and its first diagonal branch was built in the CAD software Rhinoceros v.4.0. The bifurcation angle is 45° and the diameters of the MB and the SB of 2.78 mm and 2.44 mm, respectively.
The geometry of the stent model resembles the commercial Multi-link Vision® (Abbott Laboratories). The geometrical configuration of the stented artery was calculated by means of a structural simulation carried out using the ABAQUS/Explicit commercial code (Gastaldi et al., 2010). In the simulation, the stent was positioned across the bifurcation and expanded by the inflation of a 3.00 mm polymeric balloon (Fig. 6.7a) to mimic the stenting of the MB.

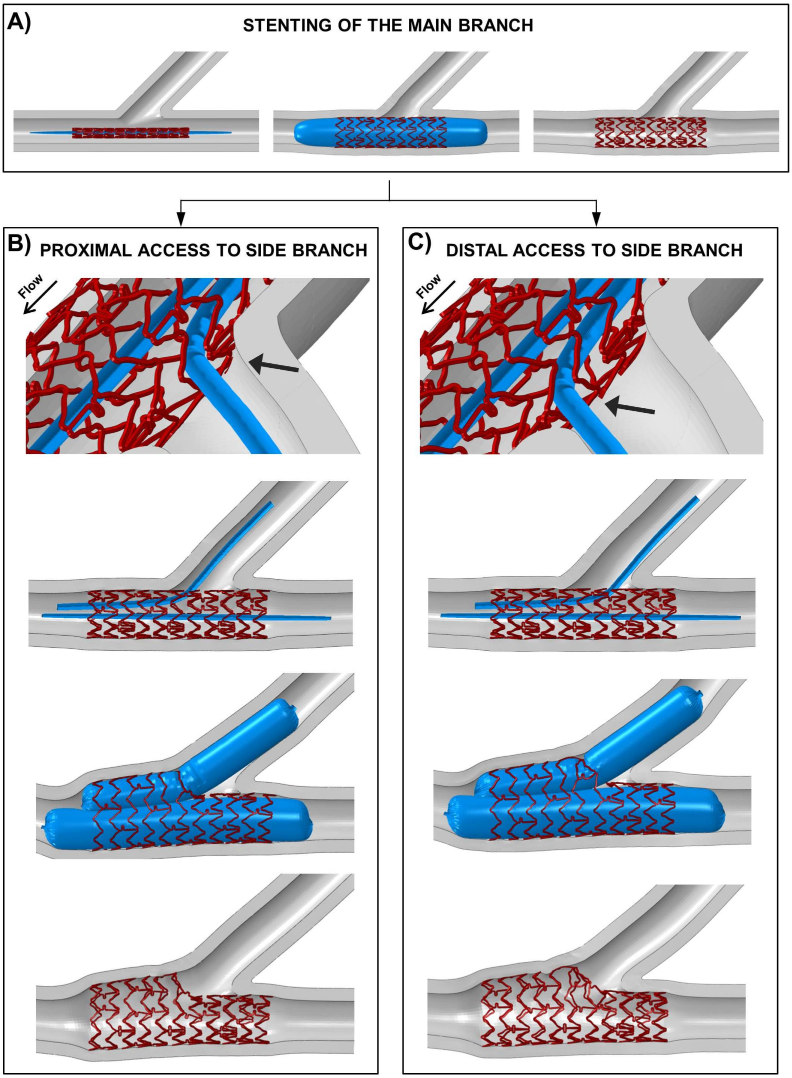

Figure 6.7: PSB approach: a) stenting of MB. b) FKB inflation performed with a proximal access to the SB. c) FKB performed with a distal access to the SB. Dark grey arrows indicate the access to the SB used during the FKB procedure. *Adapted with permission from European Journal of Mechanics B/Fluids 2012 Vol.35: 76-84. C. Chiastra et al. Computational fluid dynamics of stented coronary bifurcations studied with a hybrid discretization method. ©(2012) Elsevier Masson SAS.*

Then, while simulating the FKB inflation with a 3.00 mm balloon in the MB and a 2.5 mm balloon in the SB, two different options were investigated: in Fig. 6.7b, the MB stent is crossed through the most proximal strut available at the bifurcation while Fig. 6.7c shows an example of a distal SB access.
The two final geometrical configurations were used to perform transient fluid dynamic simulations. The fluid volumes were discretized using the hybrid mesh method described in Chapter 5 with about 2,500,000 elements (2,440,000 tetrahedrons and 60,000 hexahedrons).
Transient fluid dynamic simulations were performed using ANSYS Fluent v.13.0. A pulsatile blood flow tracing (Fig. 6.8) was applied at the inlet as a paraboloid-shaped velocity profile according to Davies et al. (2006). The average flow rate value is 60 mL/min (mean velocity = 0.13 m/s) and the duration of the cardiac cycle is 0.903 s. The adopted profile is representative of a typical flow tracing of a human LAD. At the outlet cross-sections, a flow split of 70 % in the MB and 30 % in the SB was imposed according to the study of Perktold et al. (1998). The no-slip condition was imposed along the walls. Blood parameters were set as reported in Section 5.2.2.
A coupled solver was used with a second-order upwind scheme for the momentum spatial discretization. Under-relaxation factors of 0.3 for pressure and momentum and 1 for density were used. Convergence criterion for continuity and velocity residuals was set to 10^{-6}. Time step size was set to 0.01806 s, after

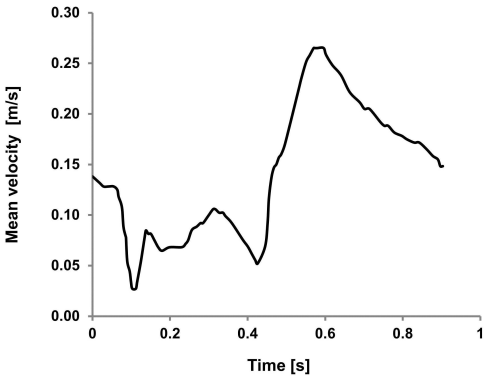

Figure 6.8: Pulsatile velocity tracing applied at the inlet cross-section of the models. *Reprinted with permission from European Journal of Mechanics B/Fluids 2012 Vol.35: 76-84. C. Chiastra et al. Computational fluid dynamics of stented coronary bifurcations studied with a hybrid discretization method. ©(2012) Elsevier Masson SAS.*

an appropriate temporal sensitivity analysis. Simulations were performed on a desktop computer equipped with a Intel i7-870 (2,93 GHz) quad-core processor with 16 GB RAM using four processors in parallel. An analysis of the results similar to the one presented in Section 6.1.2 was conducted.

6.2.3 Results and discussion

In Fig. 6.9a, TAWSS contour maps are shown. A qualitative comparison between the distal and proximal access contour maps shows that distal access leads to a lower area characterized by TAWSS < 0.5 Pa, especially in the proximal part of the stent and in the bifurcation region. In particular, the area exposed to low TAWSS in the case of the distal access is 84.7 $\%$ while in the proximal access it increases until 88.0 $\%$. Figure 6.10 reports the bar graph of TAWSS in the stented region proving the previously mentioned result.
Although most researches on atherosclerosis focuses primarily on WSS as indicator of disturbed flow, flow-driven mechanisms associated with vascular physiopathology also deal with four-dimensional phenomena such as species transport. Quantities like velocity, helicity and vorticity are primarily responsible for particle transport and mixing of low diffusivity species in fluids (including blood) (Morbiducci et al., 2010). Thus, WSS-based analyses might be incomplete and they should be complemented by a description of the bulk flow (Morbiducci et al., 2010; Stonebridge et al., 1996). Looking at the velocity contour map and at the velocity streamlines in the case of the proximal access (Fig. 6.9b) low velocity zones can be observed in the flow divider region due to the presence of the stent struts inside the vessel. These struts disturb the access to the SB, modifying the flow patterns. A lower distortion of the flow can be detected in the distal access case where the opened struts are moved towards the external side of the SB wall. This evidence supports the clinical experience which shows that opening the stent struts through the most distal strut available improves the blood flow distribution across the coronary bifurcation. A qualitative evaluation of the flow disturbance can be also observed in Fig. 6.9c, which shows the helicity field on the middle plane of the models, giving a description of the bulk flow behaviour. The helicity is higher in the case of proximal access than in the distal one, resulting in a more disturbed flow condition.
In conclusion, the fluid dynamic results of the present work give a quantitative support to the clinical experience that suggests to perform the distal access instead of the proximal one when the PSB stenting strategy is chosen.

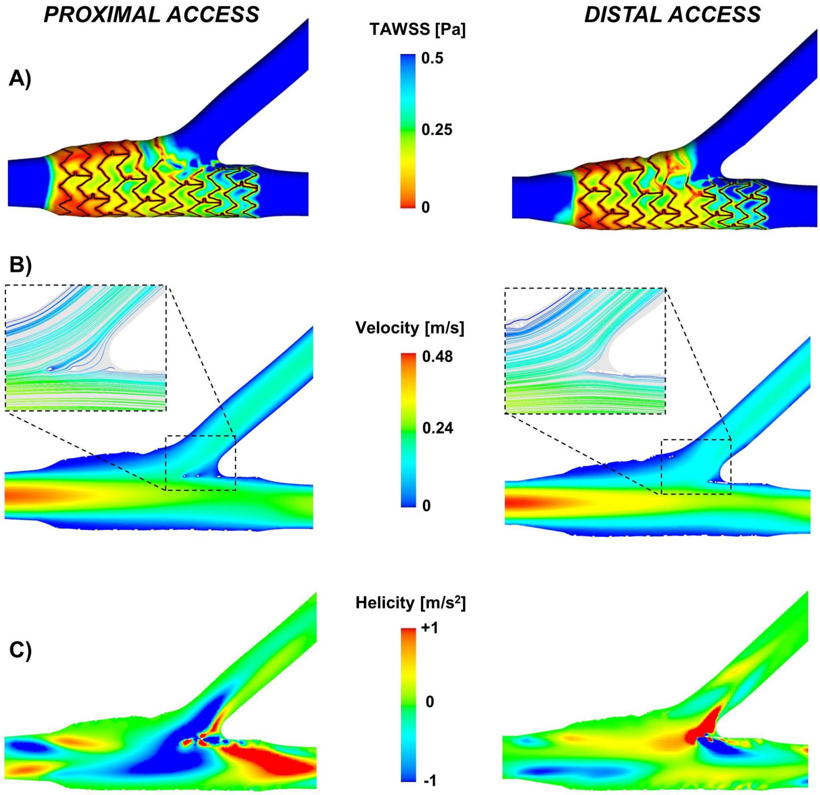

Figure 6.9: Comparison of proximal (on the left) and distal (on the right) access within the PSB approach: a) TAWSS contours; b) velocity contours in the middle plane and velocity streamlines (in the boxes); c) helicity field in the middle plane. *Reprinted with permission from European Journal of Mechanics B/Fluids 2012 Vol.35: 76-84. C. Chiastra et al. Computational fluid dynamics of stented coronary bifurcations studied with a hybrid discretization method. ©(2012) Elsevier Masson SAS.*

6.2.4 Conclusions

Pulsatile CFD simulations were performed in order to investigate and to compare the proximal and distal access to the SB within the PSB approach. In particular, by looking at WSS distribution along the arterial wall, the velocity and the helicity field, the distal access resulted to be better than the proximal one.

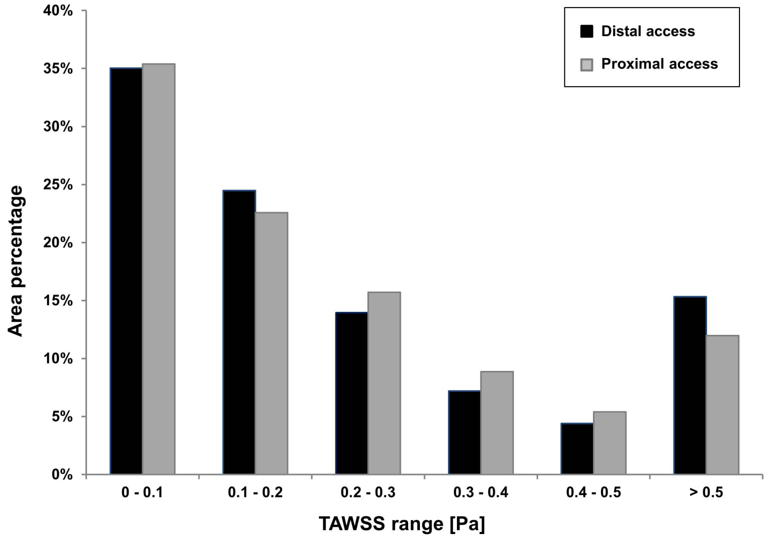

Figure 6.10: Bar graph of TAWSS in the stented region of the two investigated models. Black bars are associated to the distal access case while grey bars refer to the proximal access. *Reprinted with permission from European Journal of Mechanics B/Fluids 2012 Vol.35: 76-84. C. Chiastra et al. Computational fluid dynamics of stented coronary bifurcations studied with a hybrid discretization method. ©(2012) Elsevier Masson SAS.*

Fluid dynamic simulations provided a valid tool to quantitatively support the clinical experience that suggests to perform the distal access instead the proximal one in the case of the PSB approach.

6.3 Culotte technique: conventional or dedicated stents?

6.3.1 Introduction

The asymmetrical shape and great anatomic variability present in coronary bifurcations can make current PCI techniques with conventional stents laborious and limited by the degree of anatomic/morphologic complexity encounter (Latib and Colombo, 2008). Common complex techniques with double stenting are associated with stent underexpansion or gap at the SB ostium, excessive metal density at the carina, malapposition, and stent distortion or disruption. To

overcome some of the limitations associated with conventional stenting in bifurcations, dedicated bifurcation devices were developed and introduced (Collet et al., 2011) (Section 2.3.2).
In this work, the dedicated bare-metal stent Tryton™ (Tryton medical, Newton, MA, USA) is considered (Fig. 2.11b). It has been proposed on the market to overcome the drawbacks of the culotte technique, which is one of the most commonly applied double stenting procedures (Latib and Colombo, 2008). This technique consists in the implantation of a device in the SB of the bifurcation, the re-wiring, the treatment of MB through the struts of the previously implanted stent and, finally, the FKB inflation. Main advantages of the culotte technique are the good coverage of the whole bifurcation and the suitability for all the bifurcation angles. However, this procedure provokes a high concentration of metal in the proximal part of the MB due to the overlap of the devices that could lead to ISR and thrombosis. The particular design of Tryton™ stent, characterized by few struts in its proximal part, should allow a decrease of the overlap region and also an easy access to the implantation site for the second device.
The aim of this work is the analysis of the fluid dynamics induced by culotte procedure, in order to compare the behavior of the Tryton™ stent with respect to a conventional one.

6.3.2 Materials and methods

An ideal coronary bifurcation model was created with a bifurcation angle of 45° using Rhinoceros v.4.0 CAD program. The internal diameters of the bifurcation respected the ratios proposed by the Murray's law (Eq. 2.1) (Murray, 1926) and were 3.28 mm, 2.78 mm and 2.44 mm for the proximal part of the MB, the distal part of the MB and the SB, respectively.
Stent geometries (Fig. 6.11) were obtained using the previously mentioned CAD software and resembled the Tryton™ and the Multi-Link Vision® stents. Numerical simulations of stents deployment were performed using ABAQUS/Explicit commercial code, following the procedure defined in Gastaldi et al. (2010) and Morlacchi et al. (2011a). Two different simulations of the culotte technique were carried out:

- *Tryton-based culotte (TRY-CUL)*: the Tryton™ stent was expanded as a SB device with a Multi-Link Vision® stent implanted in the MB as a workhorse stent;
- *conventional culotte (CUL)*: the bifurcation was treated with two standard Multi-Link Vision® devices in either the SB and the MB.

The whole culotte technique can be summarized through the following steps (Fig. 6.12): (1) stenting of the SB with a 2.5 mm balloon; (2) opening of the MB access by deploying a 3 mm balloon through the struts of the first device; (3) expansion of the second device across ostium of the SB; (4) FKB procedure by simultaneously expanding a 3 mm balloon in the MB and a 2.5 mm balloon in the SB.
The fluid domains were created starting from the final geometrical configurations of the structural simulations (Morlacchi et al., 2011a). The hybrid mesh method proposed in Chapter 5 was applied (Chiastra et al., 2012).
Transient fluid dynamic simulations were carried out using ANSYS Fluent v.13.0. The artery and the stent struts were assumed to be rigid and defined with a no-slip condition. As previously done in the work reported in Section 6.2.2, a pulsatile blood flow tracing was applied at the inlet as a paraboloid-shaped velocity profile according to the study by Davies et al. (2006). The average flow rate value was 60 mL/min (mean velocity = 0.13 m/s) and the duration of the cardiac cycle was 0.903 s. At the outlet cross-sections, a flow split of 70 % in the MB and 30 % in the SB was imposed. Blood flow was modeled as a non-Newtonian fluid with a density of 1,060 kg/m^3. Its viscosity was described through the Carreau model (Eq. 5.3), using the parameter values proposed by Seo et al. (2005).
A coupled solver was used with a second-order upwind scheme for the momentum spatial discretization and a second-order time implicit scheme to discretize the governing equations. Under-relaxation factors of 0.3 for pressure and mo-

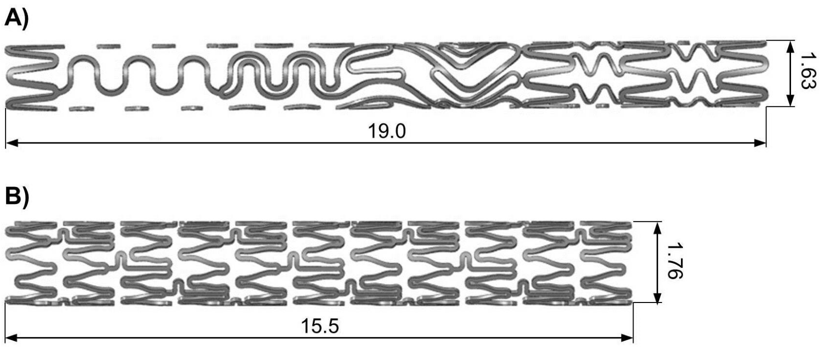

Figure 6.11: CAD model of the two investigated stents: a) dedicated stent Tryton^{TM} (Tryton medical, Newton, MA, USA); b) conventional stent Multi-Link Vision® (Abbott Laboratories, Abbott Park, Illinois, U.S.A). All measures are in millimeters.

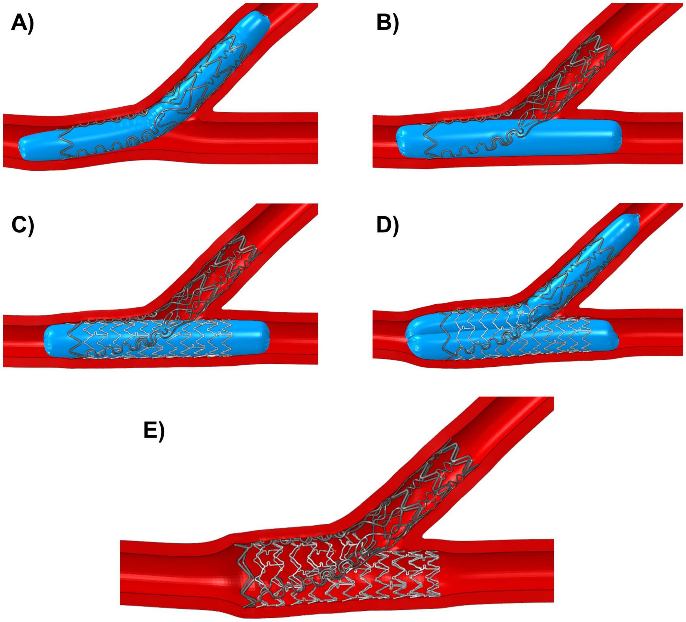

Figure 6.12: Main steps of the culotte technique: a) positioning of the SB stent by inflating a 2.5 mm cylindrical balloon; b) opening of the MB access by crossing and deploying a 3 mm cylindrical balloon through the struts of the SB device; c) positioning and deployment of the second device in the MB across the bifurcation; d) FKB procedure with a 3 mm balloon and a 2.5 mm balloon in the MB and the SB respectively and e) final configuration achieved. All the balloons are inflated at 15 atm. In this figure the implantation of the dedicated stent is shown.

mentum and 1 for density were used. Convergence criterion for continuity and velocity residuals were set to 10^{-6}. Simulations were performed on a desktop computer equipped with a Intel i7-870 (2,93 GHz) quad-core processor with 16 GB RAM using four processors in parallel.

Fluid dynamic results were evaluated in terms of near-wall quantities. In particular, TAWSS, OSI and RRT were calculated. The percentage of area exposed to low TAWSS was calculated in a ROI as the ratio between the area exposed to WSS < *threshold* and the total area of the region of interest. Two ROI were considered: the 'stented region', i.e. the portion of the arterial wall which contains the stent, and the proximal part of the MB. Different thresholds (0.5 Pa, 0.25 Pa) were evaluated in order to highlight the differences between the two investigated cases. The percentage area in the stented region and in the proximal region of the MB exposed to high OSI (> 0.1) and high RRT (> 20) was also calculated.

6.3.3 Results and discussion

A critical point of double stenting procedures, particularly evident in the culotte technique, is the occurrence of double or even triple metallic layers in the proximal part of the MB due to the overlap of the stents (Latib and Colombo, 2008). This issue results in a non-physiological biomechanical condition which could lead to ISR or sub-acute thrombosis. Figure 6.13 illustrates the amount of struts in contact with the arterial wall in the proximal part of the MB where the two devices overlap. The use of Tryton^{TM} stent, thanks to the fewer struts in its proximal design, reduces the metal-to-artery ratio (ratio between the total area of the external surfaces of the stents and the area) from 27.4 % to 20.6 %. The presence of a double-metallic layer has a negative influence on the hemodynamic field as well. Stent struts provoke a decrease of the WSS acting on the arterial wall (Fig. 6.14a); this is particularly evident in the proximal MB where the two stents overlap. However, significant differences between the two investigated models are disclosed at the level of this region. Table 6.3 reports the results of near-wall quantities in terms of percentage areas in the proximal part of MB for the two investigated cases. The particular design of the dedicated device, characterized by fewer struts in its proximal part, markedly decreases the areas characterized by low TAWSS (73.5 % versus 90.9 %, respectively for TRY-CUL and CUL), which are considered as risk factors of ISR. High OSI are present in correspondence of the regions of the artery characterized by low TAWSS for both investigated models (Fig. 6.14b). The implantation of

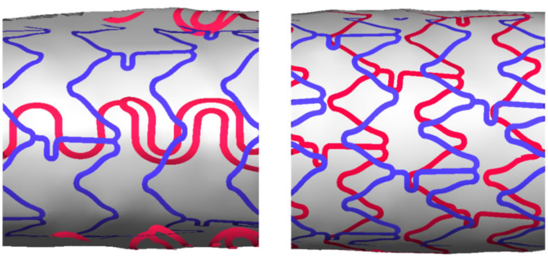

Figure 6.13: Metal-to-artery ratios for the two investigated cases: a) Tryton-based culotte (TRY-CUL); b) conventional culotte (CUL). The measured ratios in the same region of the proximal MB are 20 % and 27.4 %, respectively for TRY-CUL and CUL.

Table 6.3: Results of near-wall quantities in terms of percentage areas in the proximal part of the MB for the two investigated cases.

	TRY-CUL	CUL
Percentage area TAWSS < 0.25 Pa	73.5 %	90.9 %
Percentage area OSI > 0.1	33.9 %	29.7 %
Percentage area RRT $>$ Pa^{-1}	26.8 %	35.3 %

Table 6.4: Results of near-wall quantities in terms of percentage areas in the stented region for the two investigated cases.

	TRY-CUL	CUL
Percentage area TAWSS < 0.25 Pa	74.2 %	79.7 %
Percentage area OSI > 0.1	17.6 %	14.5 %
Percentage area RRT > 20 Pa^{-1}	15.5 %	17.8 %

Tryton™ stent instead of a standard one within culotte technique could not produce better OSI results. In fact, TRY-CUL shows a percentage area with high OSI in the proximal MB region higher than CUL model. The use of the dedicated stent shows better outcomes than the standard stents in terms of RRT (Fig. 6.14c), with a lower percentage area characterized by high RRT (26.8 % versus 35.3 %, respectively for TRY-CUL and CUL). This quantity is a combination of TAWSS and OSI but it has a more tangible connection to the biological mechanisms underlying atherosclerosis (Himburg et al., 2004).
Considering the whole stented region, similar results can be found, although the differences between the two investigated models are smaller (Table 6.4). TRY-CUL shows better outcomes, with a smaller area characterized by low TAWSS and high RRT in comparison to CUL model.
The analysis of near-wall quantities highlight that the use of the dedicated device within the culotte technique can potentially improve the hemodynamic conditions by decreasing the percentage of areas with low TAWSS and high RRT.

6.3.4 Conclusions

CFD simulations were performed in order to study the culotte technique, a commonly applied double stenting procedure, comparing the behavior of a stent dedicated to coronary bifurcations (Tryton™ stent) with a conventional one (Multi-Link Vision® stent).

One of the critical aspects of the culotte technique is the presence of double metallic layers in the proximal part of the MB. The use of the Tryton^{TM} stent, which is characterized by few struts in its proximal part, allows to reduce the amount of these layers, resulting in a lower metal-to-artery ratio with respect to the Multi-Link Vision®. Furthermore, the design of the dedicated stent markedly reduced the areas with low TAWSS and high RRT, especially in the proximal MB. These results indicate that the use of the dedicated stent within culotte technique might improve the hemodynamics, thus reducing the regions associated to the risk of ISR.

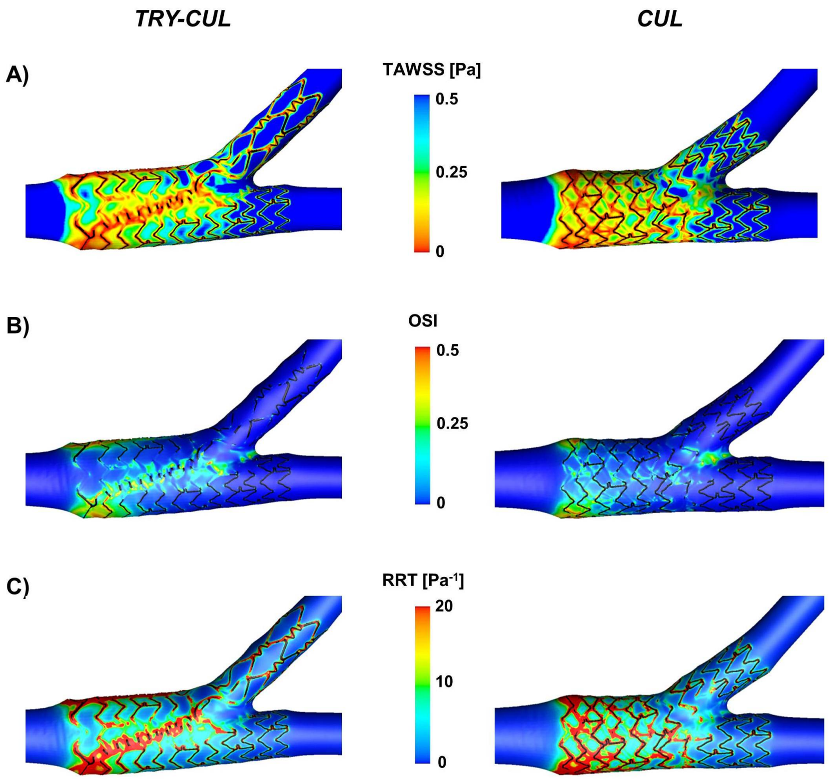

Figure 6.14: Contour maps of (a) TAWSS, (b) OSI, and (c) RRT for the two investigated cases: Tryton-based culotte (TRY-CUL) (left); conventional culotte (CUL) (right).

6.4 Limitations

Any clinical consideration derived from these three studies should be interpreted with caution bearing in mind that some limitations are introduced in these models.

The geometries of the coronary bifurcation were drawn through a CAD software, representing idealized models, and they were not reconstructed from patient-specific images. Reasonable values were adopted to describe the main features of the bifurcation of the LAD with its first diagonal branch (Perktold et al., 1998; Pflederer et al., 2006). However, diameter ratios defined by Murray's law (Murray, 1926) were considered only in the bifurcation model of the third study (Section 6.3). Atherosclerotic plaques were not included in the second (Section 6.2) and third (Section 6.3) work.

One hemodynamic state was investigated in each study. In the first work (Section 6.1) the flow-rate waveform was taken from an *in vitro* investigation (Charonko et al., 2009) and it is not representative of the basal coronary pulse although its tracing has a pattern similar to that observed in *in vivo* measurements for LAD (De Bruyne et al., 1996; Sakuma et al., 1999). Average flow rate (80.7 mL/min) is significantly high corresponding to the upper values of the range (53.4 ± 32.8 mL/min) proposed by Kessler et al. (1998) who quantified coronary flow in humans using phase difference magnetic resonance imaging. Even if this kind of measurements for obtaining coronary flow rate have significant inaccuracies because of the inherent arterial movement and invasive measurements using Doppler guidewire provide more accurate flow data, the flow curve used is in our opinion still valid for this comparative study. In this light, the results based on the used waveform need to be carefully interpreted and not taken as absolute results for coronary arteries.

Additionally, fluid dynamic models did not consider the vessel movements during the cardiac cycle. This assumption could result in a different WSS distribution and flow disturbances as previously discussed in Section 3.4.1.

In conclusion, the numerical models proposed in the present chapter could not provide patient-specific indications but only general guidelines that must be carefully interpreted and adapted to every specific clinical case.

Chapter 7

CFD analyses of image-based stented coronary bifurcation models

In this chapter the study of the hemodynamics of image-based stented coronary artery models which replicate the complete clinical procedure of stenting implantation is presented. Two cases of LAD with their bifurcations are reconstructed from CTA and CCA images.
Results of WSS and RRT show that the wall regions more prone to the risk of restenosis are located next to stent struts, to the bifurcations and to the stent overlapping zone for both investigated cases. Considering a bulk flow analysis, helical flow structures are generated by the curvature of the zone upstream from the stent and by the bifurcation regions. Helical recirculating microstructures are also visible downstream from the stent struts.
This study demonstrates the feasibility to virtually investigate the hemodynamics of image-based coronary bifurcation geometries.

The contents within this chapter have been published in:
Chiastra, C., Morlacchi, S., Gallo, D., Morbiducci, U., Cárdenes, R., Larrabide, I., and Migliavacca, F. (2013). Computational fluid dynamic simulations of image-based stented coronary bifurcation models. *Journal of the Royal Society of Interface*, 10(84), art.no. 20130193.

7.1 Introduction

THE increasing impact of CFD in studying the hemodynamics in stented arteries with great resolution does find reason in the widely accepted evidence that the biological processes leading to stent failure (e.g., ISR) have been found to be partially flow dependent (Murphy and Boyle, 2012). For this reason, in recent years sophisticated numerical models have been proposed in the literature, considering coronary bifurcations and introducing increasingly refined hemodynamic indicators for the risk of restenosis. However, as previously exposed in Chapter 3, the majority of these works consider idealized geometries limiting the discussion to a comparison between different stenting techniques. Only in two recent works fluid domains are reconstructed from patient-specific data (Section 3.3.3). Briefly, Gundert et al. (2011) developed a method to virtually draw a stent in a LAD model created from CT scans. Two different stent designs (an open-cell ring-and-link design and a close-cell slotted tube prototype design) were compared from the fluid dynamic point of view. In a further study by the same research group (Ellwein et al., 2011), the fluid dynamics of a stented LCX with a thrombus was investigated. The geometry of the vessel was reconstructed combining OCT and CT images while the stent was drawn inside the artery applying their previously developed method (Gundert et al., 2011). Those two works are affected by the same limitation: the deformation provoked by stent implantation is not considered, probably leading to an altered quantification of the local hemodynamics.

In this context, the aim of the work presented in this chapter is to study the fluid dynamics in image-based stented coronary artery models which replicate the complete clinical procedure of stenting implantation, with particular emphasis on how local hemodynamic structures might influence flow-related processes leading to restenosis. In particular, two cases of pathologic LAD with their bifurcations treated at University Hospital Doctor Peset (Valencia, Spain) are studied. The vessels are reconstructed using the pre-operative CTA and CCA images (Cárdenes et al., 2013). Then, the fluid domains are obtained from the structural simulations which replicate the stenting procedures followed by the clinicians who performed the interventions (Morlacchi et al., 2013). Both near-wall and bulk flow quantities are investigated, thus providing a complete study of the hemodynamics of the two analyzed cases.

7.2 Material and methods

7.2.1 Fluid dynamic models

The hemodynamics of two clinical cases of adult females treated with a provisional T-stenting technique without FKB inflation was studied. Case A involves the proximal section of the LAD while case B both the proximal and mid-part of the LAD. Two different CoCr DES were used in the interventions. In case A, the Xience Prime™ (Abbott Laboratories, Abbott Park, IL, USA) was implanted. This device is characterized by an external diameter of 1.76 mm (uncrimped configuration), a length of 28 mm, and a strut thickness of 81 μm. In case B, two Endeavor® Resolute (Medtronic, Minneapolis, MN, USA) were deployed. These devices have an external diameter of 1.6 mm (uncrimped configuration), a length of 15 mm, and strut thickness of 91 μm.

Pre-treatment CTA and CCA were used to create the internal surfaces of the pre-stenting geometries following the methodology proposed by Cárdenes et al. (2011). The combination of these two imaging modalities provides a more realistic reconstruction than just using one of them alone. CTA gives the 3D trajectories followed by the arteries while CCA gives an accurate lumen radius estimations. The internal surfaces were used to construct 3D solid models of the two investigated coronary bifurcations (Fig.7.1a) (Morlacchi et al., 2013). The external wall surfaces were created by smoothly connecting circumferential cross-sections perpendicular to the centerlines of the models using the CAD software Rhinoceros v.4.0 (McNeel & Associates, Indianapolis, IN, USA) (Morlacchi et al., 2013). The diameters of the external walls were chosen in order to comply with the internal diameter and wall thickness of arterial branches investigated in a physiological healthy state (Gradus-Pizlo et al., 2003).

Subsequently, structural simulations which replicate all the stenting implantation steps performed by the clinicians were carried out by means of the finite element commercial software ABAQUS (Dassault Systemes Simulia Corp., RI, USA) (Fig.7.1b) (Gastaldi et al., 2010; Morlacchi et al., 2011a, 2013). Two CAD models were created resembling the stents implanted during the interventions and including the real cross-section geometry, namely squared for Xience Prime™ and circular for the Endeavour® Resolute. The atherosclerotic plaques were considered and they were defined with an identification process based on the calculation of the distance between each structural mesh node and the centerline of the external wall. A comprehensive description of these patient-specific structural models can be found in Morlacchi et al. (2013).

Lastly, the final geometrical configurations obtained through the structural simulations were used as fluid domain to perform the fluid dynamic analyses

(Fig.7.1c) (Morlacchi et al., 2011a). The fluid domains are characterized by the following dimensions: regarding case A, the inlet diameter is 3.36 mm while the diameter of the outlet of MB is 2.33 mm and of SB is 1.52 mm; for case B, the inlet diameter is 3.45 mm, the diameter of the outlet of the MB is 1.97 mm and the diameters of the SB are 2.13 mm and 0.90 mm, respectively for the first bifurcation and the second bifurcation.
The hybrid discretization method proposed in Chapter 5 was applied (Fig. 7.2). The final meshes used in the work have 8,869,716 and 7,527,350 elements (1,633,883 and 1,387,985 nodes), respectively for case A and B. The squared stent struts of case A are discretized by 5 to 8 elements on each side of the strut while the circular struts of case B by about 25 elements, radially.

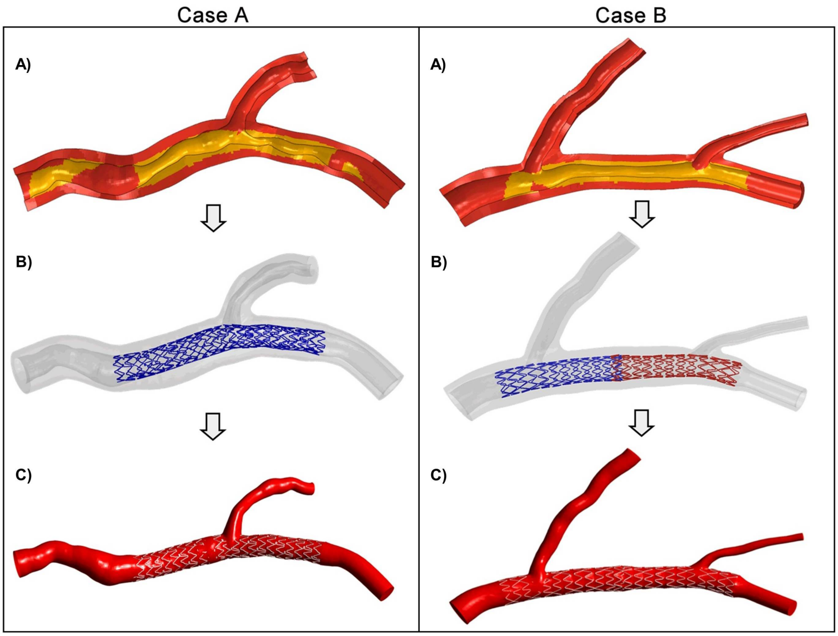

Figure 7.1: a) Sectional view of the 3D solid models of case A (left panel) and case B (right panel). The arterial wall is colored in red while the plaques in yellow. b) Final geometrical configurations obtained through structural simulations which replicate all the stenting implantation steps performed by the clinicians. c) Fluid domains extracted from structural simulations. *Reprinted with permission from Journal of the Royal Society of Interface 2013 Vol.10(84), art.no. 20130193. C. Chiastra et al. Computational fluid dynamic simulations of image-based stented coronary bifurcation models. ©(2013) Royal Society.*

Transient fluid dynamic simulations were carried out by means of ANSYS Fluent v.14.0 (ANSYS Inc., Canonsburg, PA, USA). At the inlet cross-section a pulsatile flow tracing which is representative of a human LAD (Fig. 3) (Davies et al., 2006) was applied as a paraboloid-shaped velocity profile. The flow curve amplitude was tuned on the inlet diameters of the two analyzed cases in order to obtain the average flow rate calculated through the equation proposed by van der Giessen et al. (2011):

$$q = 1.43 \cdot d^{2.55} \tag{7.1}$$

where q is the flow and d is the diameter of the coronary artery. The coefficients of this equation were obtained by van der Giessen and colleagues fitting the data of blood flow of 18 human coronary bifurcations (Doriot et al., 2000) by means of a non-linear regression analysis. In particular, the blood flow velocity was measured by intracoronary Doppler ultrasound while the cross-sectional areas

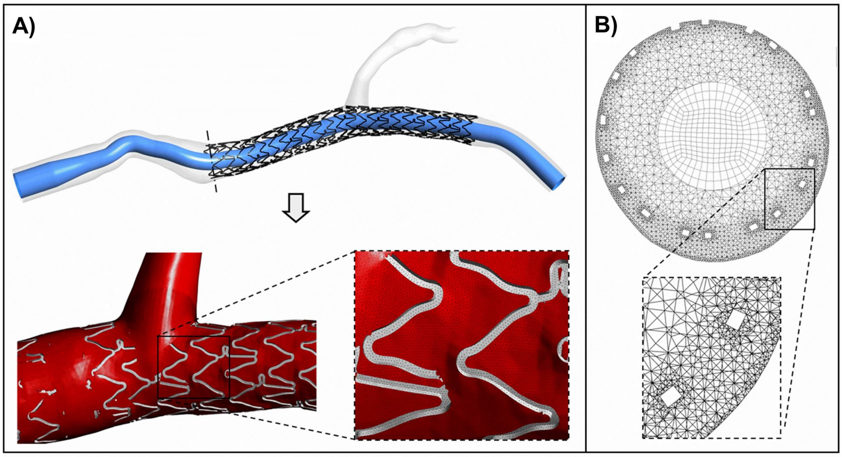

Figure 7.2: a) Generation process of the hybrid mesh: first, an internal cylinder is created inside the geometrical model and discretized using hexahedral elements (top); second, the region between the cylinder and the arterial wall is meshed with tetrahedral mesh obtaining the final grid (bottom). b) Example of a cross-section of the proximal region of case A characterized by the hybrid mesh. Hexahedral elements are clearly visible in the core region of the section. Tetrahedral elements are present in the external regions and they are smaller near the wall and the stent struts. It is possible to notice that the top stent struts are in contact with the arterial wall while the bottom struts are malapposed. A magnification of the tetrahedral mesh around two malapposed struts is shown in the box. *Reprinted with permission from Journal of the Royal Society of Interface 2013 Vol.10(84), art.no. 20130193. C. Chiastra et al. Computational fluid dynamic simulations of image-based stented coronary bifurcation models. ©(2013) Royal Society.*

were determined by 3D analysis of biplane angiography. From these data the blood flow and the diameter for each coronary branch were calculated assuming a parabolic flow profile and circular vessel area (van der Giessen et al., 2011). Applying equation 7.1, an average flow rate of 42.2 mL/min was calculated for case A and 45.1 mL/min for case B.
The same measurements (Doriot et al., 2000) were used by van der Giessen et al. (2011) to derive the relation between the diameter ratio of two daughter branches and the flow ratio through the branches:

$$\frac{q_{D2}}{q_{D1}} = \left(\frac{d_{D2}}{d_{D1}}\right)^{2.27} \tag{7.2}$$

where q_{D1} and q_{D2} are respectively the flow through the daughter branches D_1 and D_2. Starting from this equation, the following flow splits were imposed to the models: case A, 72.8% for the MB and 27.2% for the SB; case B, 57.6% for the MB, 32.9% for the proximal SB and 9.5% for the distal SB.
The no-slip boundary condition was applied to all the surfaces representing the arterial wall and the stent struts. The arterial wall and the stents were assumed to be rigid. The blood density was considered constant with a value of 1060 kg/m^3. The non-Newtonian nature of the flow was taken into account using the Carreau model (Eq. 5.3) with the parameter values proposed by Seo et al. (2005). The flow was assumed to be laminar since the maximum Reynolds number was 195 for case A and 260 case B at peak flow rate (79.1 mL/min and 84.7 mL/min, respectively). These values are an order of magnitude smaller than the Reynolds number for transition to turbulence (2300) (Spurk and Aksel, 2008) and hence justify consideration of flow to be laminar. The Womersley number was approximately 1.9 for case A and 1.4 for case B.
A coupled solver was used with a second-order upwind scheme for the momentum spatial discretization and second-order implicit scheme for the time. The flow Courant number was set to 50. The under-relaxation factors were set to 0.15 for the pressure and the momentum and to 1 for density. Convergence criterion was set to 10^{-5} for continuity and 10^{-6} for velocity residuals. A time step of 0.009 s was chosen for running the simulations (100 time steps were necessary for one cardiac cycle). This time step is sufficient to ensure temporal convergence (Chiastra et al., 2012). One cardiac cycle was simulated. As verified in previous studies (Chiastra et al., 2012; Morlacchi et al., 2011a), standalone fluid dynamic analyses without coupling with lumped parameter models that represent the downstream districts do not require multiple cardiac cycles to guarantee correct results. Computations were performed in parallel on one node of a cluster (2 quad-core Intel Xeon CPU E5620 @ 2.40GHz, 24 GB RAM for

each node, InfiniBand Mellanox for the main cluster interconnections).
In order to ascertain from simulation results what effects on hemodynamics are due to the stent presence per se and what effects are attributable to the complex vascular geometry, two additional transient simulations in the same geometries of case A and B with the stents removed were also performed. All the simulation settings were kept equal to those applied to case A and B.
As for the quality of the simulated flow fields, a sensitivity analysis was performed on case B in order to ensure the independence of the results on the mesh size. The same procedure as in Chiastra et al. (2012) was followed. Briefly, three meshes were considered, from a coarser to a finer one: 4034069, 7527350 and 11375228 elements. Steady state simulations were performed applying the average flow rate (45.1 mL/min) at the inflow section. All the other simulation settings were kept equal to those previously described. The different meshes were compared considering the area-weighted average WSS (awa-WSS) in the stented region. As the maximum difference between the intermediate and the finest mesh was lower than 0.5$\%$ for the awa-WSS the intermediate mesh (7,527,350 elements) was considered sufficiently accurate for the transient simulation. The same meshing strategy was applied to case A.

7.2.2 Analysis of the results

TAWSS and RRT were evaluated. The definition of these quantities can be found in Section 3.1.1. TAWSS was investigated not only by means of a contour map but also in quantitative way. In particular, the percentage of area exposed to low TAWSS was calculated in the arterial wall which contains the stent (in the following we refer to it as the 'stented region') as the ratio between the area exposed to WSS lower than 0.4 Pa and the total area of the stented region. Moreover, the area distribution of TAWSS was visualized using histograms by displaying the amount of area of the stented region contained between specific intervals of the variable value (Murphy and Boyle, 2010a). The area-averaged mean, skewness and kurtosis of the distributions were calculated.
The area-averaged mean of TAWSS is defined as:

$$\mu = \frac{\sum_{j=1}^{N}\left(A_j \cdot TAWSS_j\right)}{\sum_{j=1}^{N} A_j} \tag{7.3}$$

where $TAWSS_j$ is the face-averaged TAWSS value at the face j, A_j is the surface area of the face j and the summation is over N faces.
The area-averaged skewness of the TAWSS distributions is calculated as:

$$S = \frac{\sum_{j=1}^{N}\left[(A_j)\cdot(TAWSS_j-\mu)^3\right]}{\sum_{j=1}^{N}(A_j\cdot\sigma^3)} \tag{7.4}$$

where σ is area-averaged standard deviation calculated as:

$$\sigma = \sqrt{\frac{\sum_{j=1}^{N}\left[(A_j)\cdot(TAWSS_j-\mu)^2\right]}{\sum_{j=1}^{N}A_j}} \tag{7.5}$$

The skewness is a measure of the lack of symmetry of a distribution. The skewness for a normal distribution is zero, and any symmetric data have a skewness near zero. Negative values for the skewness indicate data that are skewed left and positive values for the skewness indicate data that are skewed right.
The area-averaged kurtosis is defined as:

$$K = \frac{\sum_{j=1}^{N}\left[(A_j)\cdot(TAWSS_j-\mu)^4\right]}{\sum_{j=1}^{N}(A_j\cdot\sigma^4)} \tag{7.6}$$

where the terms are as above. Kurtosis characterizes the relative peakedness or flatness of a distribution compared with the normal distribution. Positive kurtosis indicates a relatively peaked distribution. Negative kurtosis indicates a relatively flat distribution.
The impact of coronary stenting on local hemodynamics was also contextualized with respect to the helicity, a quantity successfully applied to quantify the interplay between rotational and translational blood motion in stenosed (Massai et al., 2012) and healthy arteries (Gallo et al., 2012; Morbiducci et al., 2011). The LNH quantity, defined in Section 3.1.3, was calculated.

7.3 Results

Figure 7.3 shows the streamlines of the two computational models at peak flow rate, colored by velocity magnitude. The proximal part of case A, immediately before the device, is characterized by a jet with the highest velocity directed towards the stent and an evident recirculation and stagnation zone near the external side (Fig. 7.3a). This flow pattern is caused by the particular tortuosity of the vessel. It is also possible to notice that the first stent struts are not well apposed to the wall. This aspect is captured by the fluid dynamic model because the streamlines pass throughout these malapposed struts. Lastly, the flow

patterns in the bifurcation regions of the two cases are highlighted. The flow division is clearly visible at the bifurcations; it is possible to observe that the direction of the fluid elements inside these regions is locally modified by the presence of the stent. The stent struts behave as an obstacle to the blood flow inducing a ripple effect on the streamlines (especially in case A).
Figure 7.4 shows the contour maps of TAWSS along arterial wall for case A and B, with and without stent. Considering the stented cases (Fig. 7.4 top), low WSS (red colored) are located next to all the struts in both the models. Moreover, larger areas of low WSS are present near the bifurcations and, for the case B, in the overlapping zone between the two stents. The regions outside the stents have WSS higher than 0.4 Pa except the proximal part of case A. In this region the stagnation zone which results in low WSS is clearly visible. The percentage of area exposed to low TAWSS in the stented region is 35.0% and 38.4%, respectively for case A and B. Considering the cases without stent (Fig. 7.4 bottom), low WSS are only located in the regions near the branches and, for case A, in the proximal part of the model. The low WSS spots that appear in the stented region of case B are probably provoked by the surface of the arterial wall which remained lightly pleated after the removing of the stents. The percentage of area exposed to low TAWSS in the stented region is 2.6% and 3.5%, respectively for case A and B without stent.
The distribution of TAWSS is presented in Fig. 7.5 where dark grey bars refer to the stented region while the light grey bars to the remaining part of the arterial wall ('non-stented region'). The mean TAWSS value, the skewness and the kurtosis of the distributions are reported in Table 7.1.
In Fig. 7.6 the contour maps of RRT lower than 5 Pa^{-1} are presented. High

Table 7.1: Statistical quantities associated to the TAWSS distribution of case A and B, with and without stent: mean, skewness and kurtosis.

		Mean [Pa]	Skewness	Kurtosis
Case A (with stent)	stented region	0.599	2.086	13.338
	whole model	1.046	2.010	12.679
(without stent)	stented region	1.020	1.628	10.882
	whole model	1.207	2.205	14.273
Case B (wit stent)	stented region	0.633	2.901	21.802
	whole model	1.189	1.770	9.732
(without stent)	stented region	0.976	3.834	33.288
	whole model	1.298	2.267	12.548

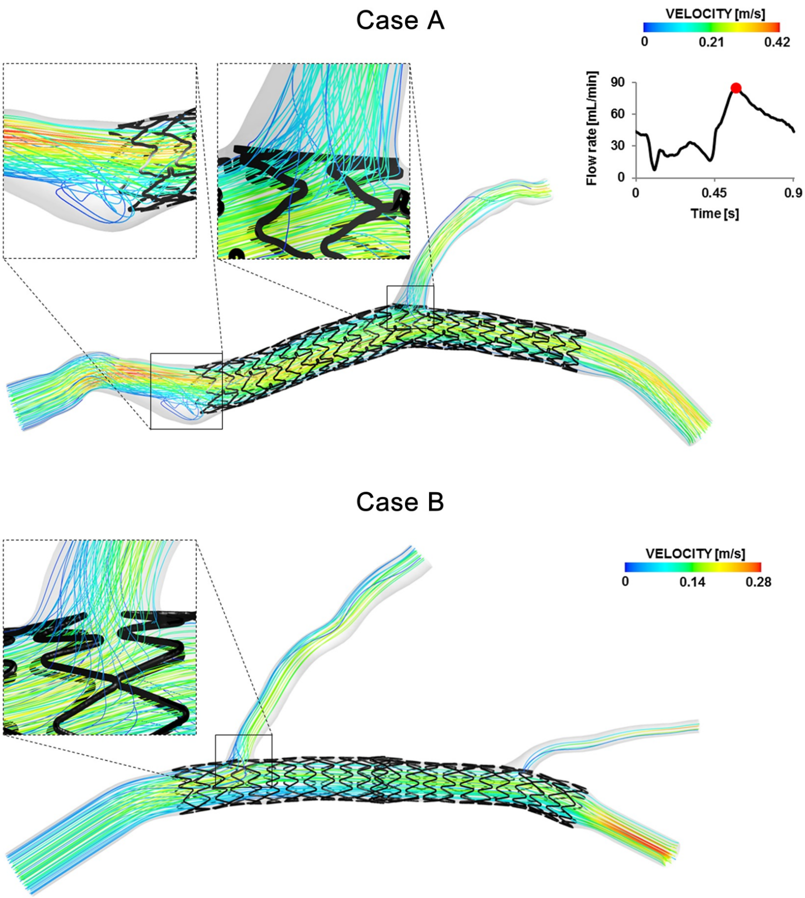

Figure 7.3: Velocity streamlines for case A (top) and B (bottom) at peak flow rate. In the magnification boxes of case A an evident recirculation and stagnation zone near the external side (left) and the disturbed flow through the stent struts near the bifurcation region (right) are clearly detectable. In the magnification box of case B the flow passing through the struts of the first bifurcation is evident. On the top right the shape of the flow waveform which was applied at the inlet section of the models is shown. The flow curve amplitude was scaled on inlet diameters of each case to obtain the average flow rate calculated through the relations by van der Giessen et al. (2011). *Reprinted with permission from Journal of the Royal Society of Interface 2013 Vol.10(84), art.no. 20130193. C. Chiastra et al. Computational fluid dynamic simulations of image-based stented coronary bifurcation models. ©(2013) Royal Society.*

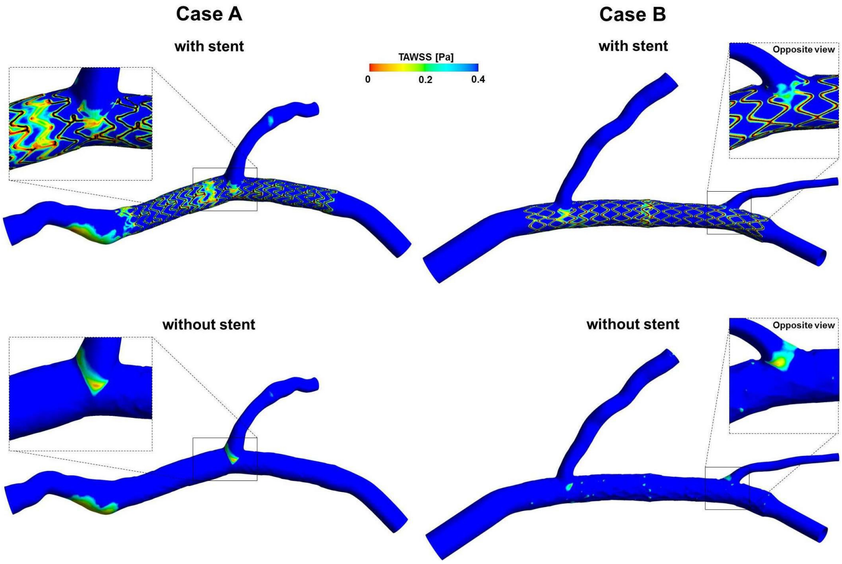

Figure 7.4: Contour maps of TAWSS along arterial wall for case A (left) and case B (right), with and without the presence of the stents. Low WSS regions are indicated in red. Regions where the stent struts are in contact with the arterial wall are colored in black. *Reprinted with permission from Journal of the Royal Society of Interface 2013 Vol.10(84), art.no. 20130193. C. Chiastra et al. Computational fluid dynamic simulations of image-based stented coronary bifurcation models. ©(2013) Royal Society.*

values of RRT (red colored) are located next to all the stent struts, to the bifurcations and to the stent overlapping zone. Also the stagnation zone of the proximal part of case A is characterized by high RRT.

To visualize peculiar topological features in the bulk flow, the mutual orientation of velocity and vorticity vectors, given by LNH, is used. Adopting a threshold value of LNH ($\pm$ 0.4) for the visualization of fluid structures, different topological blood flow features can be observed in Figs. 7.7 and 7.8. As a general observation, in both the two investigated cases helical flow structures originate in the region of the vessel upstream from the stent, with a helicity-generation process which appears to be mainly driven by the curvature, tortuosity and torsion of the non-stented segment upstream from the stented one. This statement is enforced by the observation that: (1) for case A, large LNH isosurface regions appear immediately upstream from the stent, where the flow arrangement consists in counter-rotating helical structures that persist trough-

out the cardiac cycle due to the tortuous path of the blood flow (Fig 7.7, left panel: left-handed, negative LNH values; right-handed, positive LNH values). Notably, LNH isosurfaces emphasize the flow separation region that has been pointed out previously in Fig. 7.3; (2) for case B, the arrangment of the streaming blood in helical patterns is less marked, most likely because the upstream region in case B is less tortuos than case A (Fig 7.7, right panel).
From Fig. 7.7 it emerges also that the straightening of the vessel as induced by the stent implantation determines the gradual disappearance of large helical fluid structures and that the presence of branching vessels is involved in the generation of helical fluid structures, their strenght being related to organ perfusion from branch vessels (due to the centripetal spin, i.e., imparted tangential velocities, induced in blood), as previously observed by Frazin et al. (1996).
Using LNH for the visualization of the topological features of the flow field, it is possible to observe the impact that the presence of stent struts has on near-wall flow patterns. Fig. 7.8 (top) shows that helical fluid structures at different lengthscale are present close to the wall, going from the order of magnitude of strut dimensions to larger structures. These larger helical structures are also present in the corresponding cases without stent (Fig. 7.8 bottom) while the small structures are absent.

7.4 Discussion

The mechanisms and the causes of ISR in coronary arteries are not fully understood. One of the most relevant phenomena which seems to be associated to the formation of NH is an altered hemodynamics in the stented wall region which leads to persistent low WSS (Wentzel et al., 2008). Local measurements of the velocities and velocity gradients in human coronary arteries *in vivo* are very difficult and can therefore not be applied to map the shear stress distribution at the wall (Wentzel et al., 2008). Alternatively, virtual models of patient-specific coronary arteries allow studying local fluid dynamics, calculating the WSS and other quantities which can be related to the risk of restenosis. As a consequence, these models also permit to give some indications to the clinicians. In the present work, a comprehensive study of the fluid dynamics of two image-based stented coronary models was carried out.
Looking at the near-wall quantities, both the stented cases are characterized by low WSS next to the struts (Fig. 7.4), in agreement with the findings by Gundert et al. (2011) and Ellwein et al. (2011). In particular, for each repeating stent cell, the values of TAWSS increase from the zones near the stent struts towards the center of each cell, as previously found in other studies (Balossino et al.,

2008; Gundert et al., 2013).
A wider area with low TAWSS is present in the region close to the branches. This is due to the vessel geometry and not to the presence of stents. In fact the wider area with low TAWSS is evident both in the cases with stent and in the corresponding cases without stent (Fig. 7.4). As experimentally observed in left and right human coronary arteries by Asakura and Karino (1990), the flow in the proximity of the outer wall of the branches is slow with the formation of

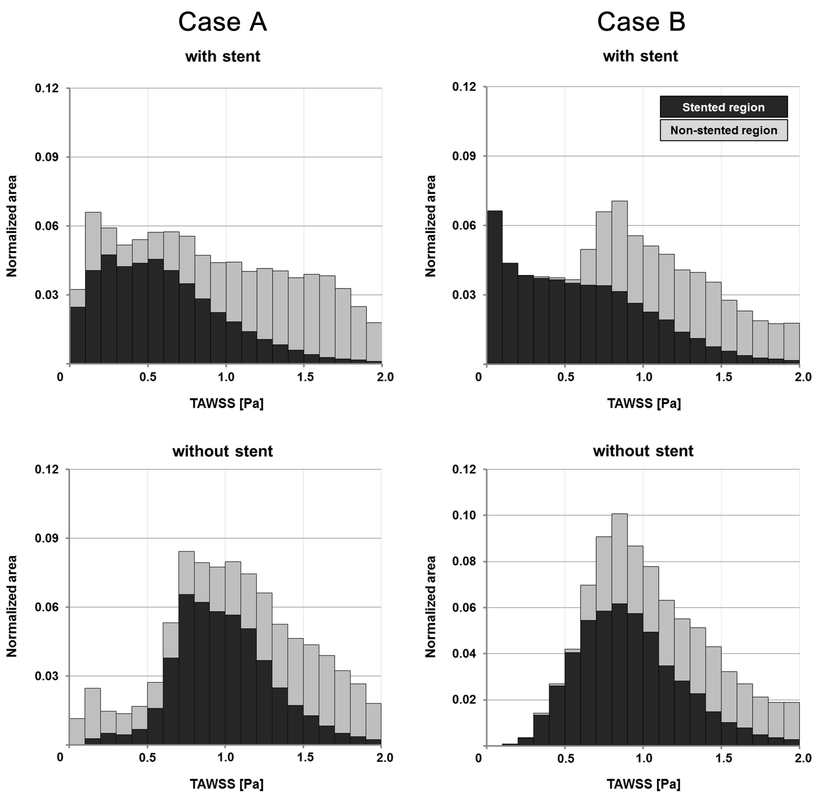

Figure 7.5: TAWSS distribution in case A (left) and case B (right), with and without the presence of the stents. Each bar of the histograms represents the amount of normalized area with a defined range of TAWSS. Dark grey bars refer to the stented region while the light grey bars to the remaining part of the arterial wall. Bar widths are 0.1 Pa. *Reprinted with permission from Journal of the Royal Society of Interface 2013 Vol.10(84), art.no. 20130193. C. Chiastra et al. Computational fluid dynamic simulations of image-based stented coronary bifurcation models. ©(2013) Royal Society.*

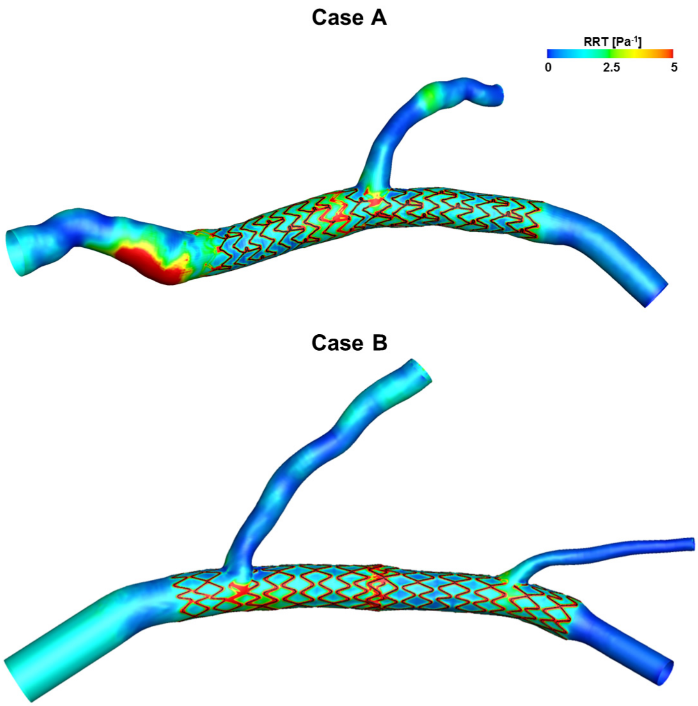

Figure 7.6: Contour maps of RRT for case A (top) and case B (bottom). *Reprinted with permission from Journal of the Royal Society of Interface 2013 Vol.10(84), art.no. 20130193. C. Chiastra et al. Computational fluid dynamic simulations of image-based stented coronary bifurcation models. ©(2013) Royal Society.*

slow recirculation and secondary flows which lead to low WSS in those zones. A wider area characterized by low TAWSS is also visible in the stent overlapping zone of case B. In this zone stent struts protrude inside the lumen in a more marked way compared to the other stented regions. The protrusion locally generates a more disturbed flow, with the consequence that a wider area is subjected to low TAWSS. Considering the stented region, the percentage area exposed to values of TAWSS lower than 0.4 Pa, which are strongly correlated with endothelial permeability and can promote NH (Ku, 2007; Malek et al., 1999), is significant: 35.0% for case A and 38.4% for case B. This result is also evident in the TAWSS distributions (Fig. 7.5 top, dark grey bars). As reported

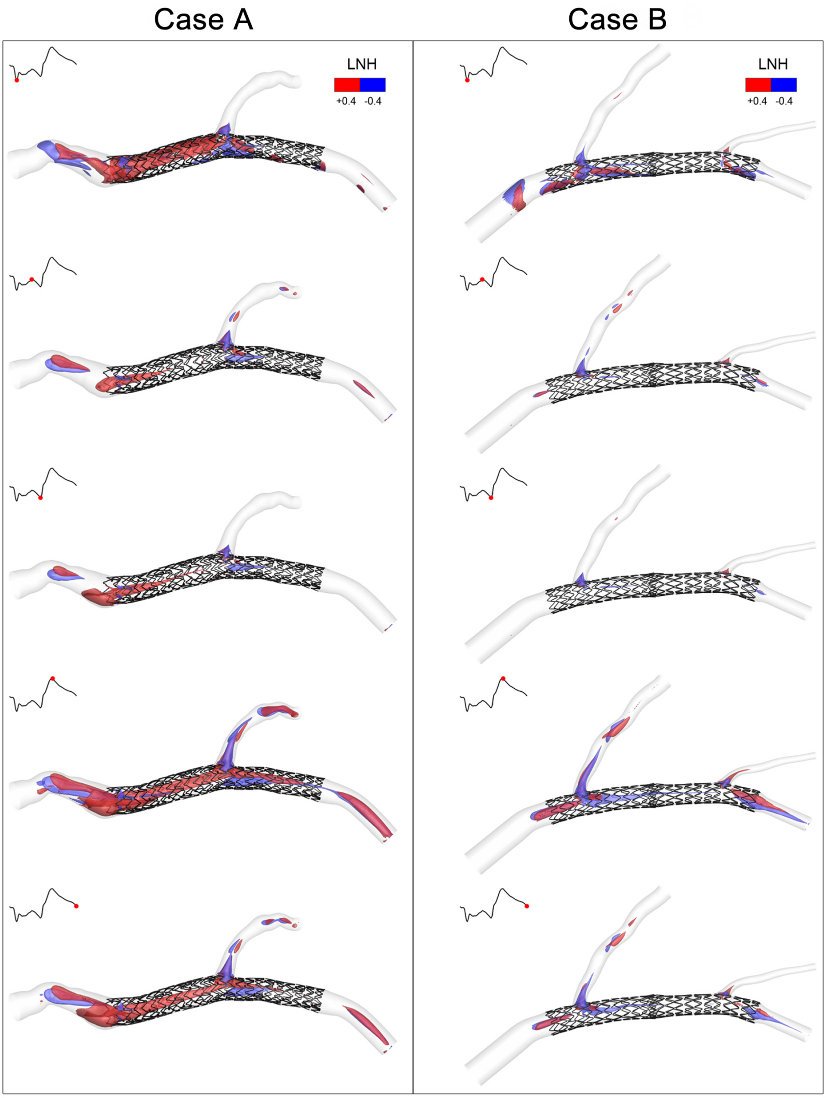

Figure 7.7: Isosurfaces of LNH at five different phases of the cardiac cycle for case A (left panel) and B (right panel). Threshold values of LNH ($\pm$ 0.4) are used for the visualization of the mutual alignment of velocity and vorticity vector fields (i.e., the necessary condition revealing the presence of helical flow structures). Positive and negative LNH values indicate counter-rotating flow structures. *Reprinted with permission from Journal of the Royal Society of Interface 2013 Vol.10(84), art.no. 20130193. C. Chiastra et al. Computational fluid dynamic simulations of image-based stented coronary bifurcation models. ©(2013) Royal Society.*

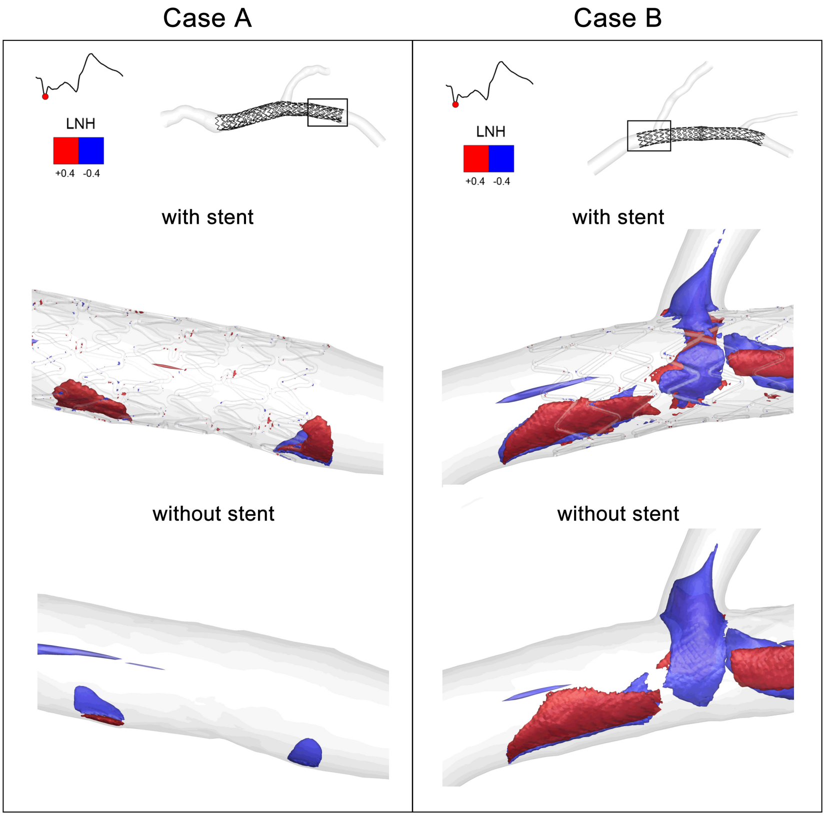

Figure 7.8: Example of LNH isosurfaces visualization (LNH=0.4) used to highlight the presence of helical structures at different length scales close to the wall. LNH isosurfaces are relative to the systolic phase. Left panel: case A, with and without stent; right panel: case B, with and without stents. *Reprinted with permission from Journal of the Royal Society of Interface 2013 Vol.10(84), art.no. 20130193. C. Chiastra et al. Computational fluid dynamic simulations of image-based stented coronary bifurcation models. ©(2013) Royal Society.*

in Table 7.1, these distributions are characterized by a similar value of area-averaged mean TAWSS (about 0.6 Pa) but the distribution of case B is more peaked (higher kurtosis value) and more skewed to the right (higher skewness value). This means that the entire stented wall region of case B is characterized by a larger area with low WSS and, from a merely fluid dynamic point of view, might be more prone to the risk of restenosis.

In case A, the region immediately before the stent shows values of TAWSS lower than 0.4 Pa. This is due to the marked tortuosity of the vessel which causes the formation of an evident recirculation and stagnation zone (Fig. 7.3 a). The contribution of this region to low TAWSS distribution can be appreciated looking at the light grey bars in Fig. 7.5 (top). This contribution is lower if compared to the one caused by the stent presence. In case B, the contribution of the non-stented vessel segments to TAWSS lower than 0.4 Pa is almost zero. These results confirm that the regions of the arterial wall with low TAWSS are mainly induced by the presence of the stents. Comparing the TAWSS distributions of cases with and without the stent presence, it can be appreciated that the stent induces lower TAWSS values at the arterial wall of the stented regions. More in detail: (1) TAWSS distributions of models without stent are more shifted to the right than the cases with stents; (2) in the stented region (Fig. 7.5, dark gray bars) the percentage of area exposed to TAWSS lower than 0.4 Pa is significantly higher for the cases with stent.
The RRT contour maps (Fig. 7.6) confirm the results obtained on the two computational models for TAWSS: high values of RRT are located next to the stent struts, to the bifurcations and to the stent overlapping zone. RRT is a more complete quantity than TAWSS because it considers not only the magnitude of WSS but also the oscillatory WSS. High values of RRT also indicate that the residence time of the particles near the wall is prolonged (Himburg et al., 2004) with the possibility of inducing the ISR phenomenon.
As natural blood flow in arteries has been found to be helical (Gallo et al., 2012; Kilner et al., 1993; Morbiducci et al., 2011), in this work an helicity-based description was used to characterize the bulk flow structures in stented coronary arteries. More in depth, the analysis was focused on the helical flow because it has been demonstrated that it is the consequence of the natural optimization of fluid transport processes in the cardiovascular system (Kilner et al., 1993; Morbiducci et al., 2011), that it is strictly related to transport phenomena of oxygen and lipoproteins (Lantz and Karlsson, 2012; Liu et al., 2010) and that it is instrumental in suppressing flow disturbances (Gallo et al., 2012; Morbiducci et al., 2007). By visualization of LNH isosurfaces as an indicator of the alignment/misalignment of velocity and vorticity vectors, it was observed that: (1) large helical structures differently characterize the bulk flow in the stented regions, in the two investigated cases (Fig. 7.7); (2) small helical structures are generated as a consequence of the presence of the stent struts protruding into the lumen of the vessel (Fig.7.8); in fact these small structures can be only observed in the stented vessels and not in the same geometries, where the stent is removed.

While it is still not fully clarified which role (i.e., beneficial or detrimental) the small scale helical flow structures play in the ISR, here the arrangement of fluid structures in large helical patterns seems to be mainly driven by the shape of the vessel upstream from the stented segment of the vessel and partially by the presence of branched vessels. On the contrary, the straightening induced by the device implantation promotes large helical fluid structures mitigation along the stented segment. Interestingly, it was also found that, at the same time, the percentage area of the stented region exposed to low WSS is mildly lower for case A than for case B and it is accompanied by the presence of a more marked arrangement of the flow field in helical structures for case A (Fig. 7.7). These findings, even if preliminary, confirm previous observations in healthy vascular districts (Gallo et al., 2012), in surgical connections (Morbiducci et al., 2007) and in stented vessels (Chen et al., 2011b; Sun et al., 2012), that there is a link between the surface area exposed to disturbed shear and helical fluid structures in the bulk flow.

The regions of the coronary arteries where the risk of ISR is higher from the fluid dynamic point view have been identified for the two analyzed cases. However, other aspects should be contemporarily studied to make the virtual model more predictive. In particular, the study of the drug release from the stents would be extremely important. A virtual model that takes into account the hemodynamics and the drug release would be useful in order to better predict ISR regions. In the literature, some works on the study of the fluid dynamics coupled with the drug transport have been already proposed but they consider simplified vessel geometries (Kolachalama et al., 2009) or they approximate the stent as a line and not as a complex 3D structure (Cutrì et al., 2013; D'Angelo et al., 2011). Clinical follow-ups of the studied cases will help in a better understanding of the link between hemodynamics and ISR.

7.5 Limitations

The fluid dynamic solution relies on the initial stented geometry which is supplied by a preliminary finite-element structural analysis. This preliminary structural simulation predicts the final geometrical configuration of the stented artery from the pre-operative geometry. As a consequence, the reconstruction of the pre-operative geometry and the subsequent structural simulation have to be reliable. In this study the reconstruction of the vessel models was made under the assumption of circular cross-section of the vessel, which is true in 70 to 80% of the cases (Arbab-Zadeh et al., 2010), but not necessarily in the presence of stenosis. This could result in a sub-optimal representation of the stent and

wall interaction during stent expansion. Looking at the results of the structural analyses (Morlacchi et al., 2013), in case A a good matching between the stent implanted in the patient and the simulation was found while in case B the distal side of the stent implanted distally was slightly dislocated with respect to the real one. This mismatch was limited to the final portion of the stent showing a good resemblance in the remaining locations.
The movements and the vessel deformations caused by the presence of a beating heart were not taken into account. As discussed in Section 3.4.1, the effects of cardiac-motion on hemodynamics are still a subject of study. According to some numerical studies (Prosi et al., 2004; Theodorakakos et al., 2008; Zeng et al., 2003) cardiac-motion does not significantly affect the hemodynamics of coronary tree.
Concerning the choice of the boundary conditions, it was not possible to perform the recording of blood flow velocity nor velocity profiles on the patients and locations selected for the present study. As a consequence, an assumption was made imposing a flow waveform of a human LAD taken from the literature (Davies et al., 2006) and using the relations by van der Giessen et al. (2011) to calculate the mean flow rate and the flow splits. An additional assumption was needed for the shape of the velocity profile at the inlet section (as requested by the imposition of a Dirichlet condition as inflow boundary), because of the lack of any information about the velocity profile entering the LAD models. The choice of imposing a paraboloid-shaped velocity profile at the inlet section, which is a reasonable assumption that has been previously used by other authors for fluid dynamics studies in coronary arteries (Sun et al., 2012; van der Giessen et al., 2011), was made.

7.6 Conclusions

A comprehensive study of the fluid dynamics of two realistic stented coronary bifurcation models which replicate the complete clinical procedure of stenting implantation was proposed. The attention was focused on how local hemodynamic structures might influence flow-related processes leading to ISR. Thus, both near-wall quantities and the bulk flow were investigated.
Results of WSS and RRT showed that the regions more prone to the risk of restenosis are located next to stent struts, to the bifurcations and to the stent overlapping zone. Looking at the bulk flow, helical flow structures were generated by the shape of the vessel upstream from the stented segment and by the bifurcation regions. Helical recirculating microstructures were also visible downstream of the stent struts.

The present work proves how a realistic virtual model can be useful to better understand the effect on the local hemodynamics of stent implantation in coronary bifurcations, identifying, from a merely fluid dynamic point of view, the regions that are more prone to the risk of restenosis.

Chapter 8

From OCT to CFD simulations: a preliminary study

OCT seems to be a useful tool to reconstruct 3D geometries of stented coronary arteries due to its higher resolution compared to the other imaging techniques that are used for the diagnosis of coronary artery disease and to the possibility to detect both the vessel lumen and the stent. In this chapter reconstruction methods of stented coronary artery models for CFD simulations based on OCT images are presented. In particular, a reconstruction method was initially developed for an in vitro model of a stented coronary bifurcation and the obtained geometry was used to perform CFD simulations. Subsequently, the reconstruction method was adapted for an in vivo case.
Although these methods are preliminary, they represent a first step towards the semi-automatic creation of stented coronary artery models for CFD simulations that are purely based on clinical patient-specific images.

This work was carried out in collaboration with Dr. Francesco Burzotta (Department of Cardiovascular Medicine, Università Cattolica del Sacro Cuore, Rome, Italy), Prof. Luca Mainardi and Eros Montin (Department of Electronics, Information, and Bioengineering, Politecnico di Milano, Milan, Italy).

8.1 Introduction

THE results of a CFD simulation are more accurate when the numerical analysis is performed with a geometrical model reproducing the reality. In few studies (Chiastra et al., 2013; Ellwein et al., 2011; Gundert et al., 2011) image-based geometrical models of patient-specific coronary arteries were reconstructed for performing CFD simulations (Section 3.3.3). However, in these studies only the vessel lumen was obtained from imaging data. The stents were virtually drawn inside the artery using CAD operations (Ellwein et al., 2011; Gundert et al., 2011) or deployed through structural simulations that replicate the complete stenting procedure followed by the clinicians during the intervention (Chiastra et al., 2013).

Currently, optical coherence tomography (OCT) is a promising imaging technique for coronary arteries. OCT is a catheter-based imaging modality that performs optical cross-sectional images of internal structure in biological systems and materials (Fujimoto, 2001). It was first introduced by Huang et al. (1991) and it was initially applied for imaging of the eye (Fercher et al., 1993; Swanson et al., 1993), becoming the clinical standard for the assessment of ocular structure (Gabriele et al., 2010). OCT was first used for intravascular imaging of coronary arteries by Jang et al. (2002).

Compared to the other imaging techniques for the diagnosis of coronary artery disease, i.e. CCA, CT, magnetic resonance imaging (MRI) and IVUS, OCT is characterized by higher spatial resolution and the possibility to detect both the stent and the vessel lumen (Table 8.1) (Farooq et al., 2009; Ferrante et al., 2013). These advantages allow the OCT to be successfully applied in the assessment of atherosclerotic plaque, stent apposition, and tissue coverage (Regar et al., 2011). Moreover, thanks to these two characteristics, OCT seems to be a useful tool to reconstruct 3D geometries of stented coronary arteries. Therefore, the aim of this work is to develop reconstruction methods of stented coronary artery models starting from OCT images. The geometries obtained through these methods should be suitable for performing CFD simulations in order to quantify near-wall quantities that are related to the ISR process.

A reconstruction method was initially developed for an *in vitro* model of a stented coronary bifurcation and the obtained geometry was used to perform feasibility CFD simulations. Subsequently, the reconstruction method was adapted for an *in vivo* case.

The works presented in this chapter are preliminary. However, they represent a first step towards the semi-automatic creation of image-based stented coronary artery models for fluid dynamic simulations. In particular, the stent is

Table 8.1: Characteristics and main pros and cons of the imaging techniques that are performed in clinical practice for detection of coronary artery disease: conventional coronary angiography (CCA), computed tomography (CT), magnetic resonance imaging (MRI), intravascular ultrasound (IVUS) and optical coherence tomography (OCT) (Schmitt et al., 2005; Zimmerman and Vacek, 2011).

Imaging technique	Invasiveness	Energy source	Radiocontrast agent	Resolution	Plaque characterization
CCA	+	X-ray	yes	100-200 μm	no
CT	+	X-ray	yes	350-700 μm	no
MRI	+	radio wave	yes/no	$\sim$1 mm	no
IVUS	+++	ultrasound	no	100-200 μm	yes
OCT	+++	near-infrared	yes/no	10-20 μm	yes

Key: + least, ++ moderate, +++ most.

reconstructed directly from patient-specific images, without performing a virtual implantation as done, for example, in the work reported in Chapter 7.
The present chapter is organized in the following sections: in Section 8.2 an introduction to OCT (working principle, applications related to coronary artery disease, image processing) is given; in Section 8.3 the reconstruction method developed for the *in vitro* case and the subsequent CFD simulations are presented; in Section 8.4 the reconstruction method for the *in vivo* case is explained; in Section 8.5 the main limitation of the works and the future perspectives are discussed.

8.2 Optical coherence tomography

8.2.1 Working principle

OCT is an optical technique that generates cross-sectional images by measuring the echo time delay and intensity of light that is reflected or backscattered from internal structures of a tissue (Huang et al., 1991). In Fig. 8.1 a schematic diagram of OCT is shown. This imaging technique is based on low-coherence interferometry (Brezinski et al., 1996; Farooq et al., 2009). A near-infrared light (wave-length $\sim$ 1300 nm), which is generated by a laser source, is delivered to the site of interest using a single optical fiber. The light is split equally into a reflected and transmitted beam (sample and reference arms, respectively) by means of a fiber-optic beam splitter. The sample arm is then reflected from the tissue and consists of multiple echoes giving information about the distance and the thickness of different structures of the tissue. The reference arm is reflected

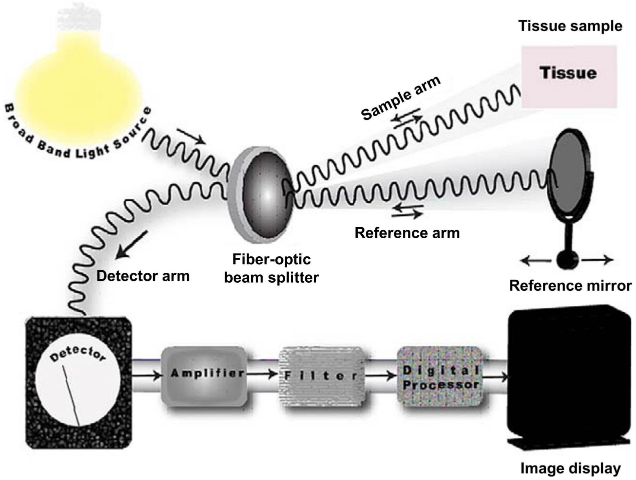

Figure 8.1: Schematic diagram of the OCT. A near-infrared light is split equally into the sample and reference arm by a fiber-optic beam splitter. The sample arm is reflected from the tissue while the reference arm is reflected from a reference mirror and travels back to the splitter where it interferes with the reflected sample arm. The resulting interference signal is measured by a photodetector, and then amplified, digitalized, and processed by a computer for OCT image reconstruction. *Adapted with permission from Vascular Medicine Vol.14: 63-71. M.U. Farooq et al. The role of optical coherence tomography in vascular medicine. ©(2009) SAGE Publications.*

from a reference mirror, whose spatial position is known, and travels back to the splitter where it interferes with the reflected sample arm. The resulting interference signal is measured by a photodetector, obtaining the reflectively profile along the beam axis, which is called A-scan (Fig. 8.2a). A series of A-scans is captured by scanning the beam across the sample in order to produce a 2D cross-sectional image (i.e. B-scan). Current OCT systems are able to generate hundreds of B-scans per second (Prati et al., 2011).
In intravascular applications, OCT imaging catheters are used. A typical OCT catheter is made of a single-mode optical fiber with gradient index lens and microprism or mirror at one extremity in order to guide the light to the sample (Prati et al., 2011). The catheter is housed within a torsion cable. It is simultaneously rotated to produce 2D cross-sectional images (Fig. 8.2b) and moved along the length of the vessel by an automated system of pullback to scan the segment of interest.
During the OCT exam the blood is cleared from the lumen because red blood cells cause significant signal attenuation (Bezerra et al., 2009). Two techniques

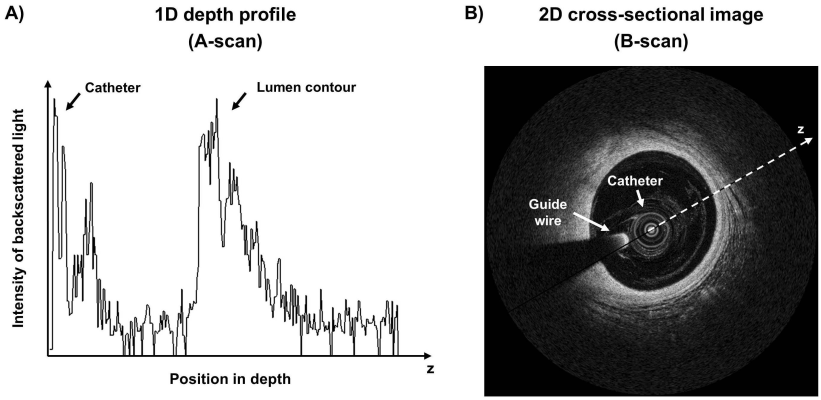

Figure 8.2: a) Example of one-dimensional (1D) depth profile (A-scan). z-axis represents the position in depth (axial position). b) Example of B-scan of a human coronary artery (B-scan). The B-scan is obtained by rotating the OCT catheter, thus scanning a 2D cross-sectional image of the vessel.

exist (Hamdan et al., 2012; Prati et al., 2010):

- *occlusive technique*, which consists in blood flow interruption by soft balloon inflation and flushing a crystalloid solution (usually Ringer's lactate) through the catheter;

- *non-occlusive technique*, which is performed by exclusively flushing an iso-osmolar fluid with a viscosity higher than the blood through the catheter. A commercially available contrast agent (Iodixanol 320, Visipaque^{TM}, GE Health Care, Ireland) is generally employed.

OCT systems can be classified in two categories, based on the different technologies that can be used to obtain the images (Prati et al., 2011):

- *time domain OCT (TD-OCT)*. It is the first generation of OCT. A scanning mirror is used in the reference arm (moving reference arm) to temporally observe the interference pattern a single point at a time allowing the scan of the whole sample.

- *Fourier domain OCT (FD-OCT)*. It represents the new generation of OCT. Two processing methods are used in FD-OCT (Fig. 8.3): spectral-domain OCT (SD-OCT) and swept-source OCT (SS-OCT). In SD-OCT the reference arm is static. The light of the detector arm is dispersed by a spectrometer onto a line scan camera. Each pixel of this camera detects a portion of the spectrum. In SS-OCT a swept light source is used to sequentially probe the sample with different optical frequencies. A single photodetector is then employed to collect portions of the spectrum as a function of time. The reference arm is static.

FD-OCT has shown advantages in image acquisition speed and signal-to-noise ratio with respect to TD-OCT (Choma et al., 2003; De Boer et al., 2003; Leitgeb et al., 2003). Moreover in FD-OCT the non-occlusive technique, which is easier and safer than the occlusive technique, is performed to clear the blood from the lumen (Hamdan et al., 2012). SS-OCT is the current setup that is used in intravascular imaging (Prati et al., 2011).
In Table 8.2 the main technical specifications of TD-OCT and SS-OCT are compared to IVUS which nowadays represents the gold standard intravascular technique. SS-OCT is characterized by a resolution about ten times higher than IVUS, higher frame rate and pull-back speed than IVUS. However, tissue penetration of OCT systems is limited if compared to IVUS (1-2 mm versus 10 mm, respectively for OCT systems and IVUS).

Table 8.2: Main technical specifications of TD-OCT, SS-OCT and IVUS.

	TD-OCT[a]	SS-OCT[b]	IVUS[c]
Energy source	Near-infrared light	Near-infrared light	Ultrasound (20-45 MHz)
Wave-length (μm)	1.3	1.3	-
Axial resolution (μm)	15-20	12-15	100-200
Lateral resolution (μm)	90	20-40	150-300
Frame rate (frame/s)	15-20	100	30
Pullback speed (mm/s)	1-1.5	20	0.5-1
Maximum scan diameter (mm)	6.8	10	15
Tissue penetration (mm)	1-2	1-2	10
Blood clearing	Occlusive technique	Non-occlusive technique	Not required

[a] Based on specifications of the Lightlab M2/M3 (St. Jude Medical Inc., St. Paul, MN, USA) TD-OCT system.
[b] Based on specifications of the Ilumien™ C7-XR™ (St. Jude Medical Inc.) SS-OCT system.
[c] Based on specifications of the Volcano (San Diego, CA, USA), Boston Scientific (Natick, MA, USA), and Terumo (Tokyo, Japan) IVUS systems.

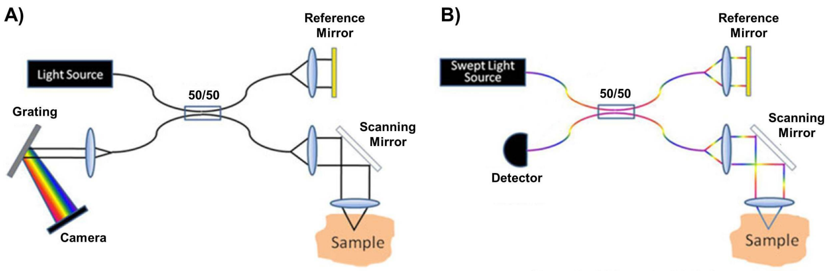

Figure 8.3: Schematic diagrams of the two existing setups of FD-OCT: a) spectral-domain OCT (SD-OCT). The light of the detector arm is dispersed by a spectrometer onto a line scan camera. Each pixel of this camera detects a portion of the spectrum; b) swept-source OCT (SS-OCT). A swept light source is used to sequentially probe the sample with different optical frequencies. A photodetector is then employed to collect portions of the spectrum over time. *Adapted with permission from The International Journal of Cardiovascular Imaging Vol.27 (2): 251-258. F. Prati et al. Intracoronary optical coherence tomography, basic theory and image acquisition techniques. ©(2011) Springer.*

8.2.2 OCT in coronary artery disease

OCT is used in several clinical diagnostic applications related to coronary artery disease (Ferrante et al., 2013). OCT is applied in the assessment of atherosclerotic plaques, allowing their visualization and the characterization of their structure and extension (Regar et al., 2011). The different components of a diseased coronary artery can be identified by OCT because they have different optical properties (Regar et al., 2011). In particular, the following components can be detected:

- *fibrous plaques*, which consist of homogeneous high back-scattering areas (Fig. 8.4a) (Jang et al., 2002, 2005; Kubo et al., 2007; Kume et al., 2006; Yabushita et al., 2002);

- *calcifications within plaques*, which are characterized by the presence of well-delineated, low back-scattering heterogeneous regions (Fig. 8.4b) (Jang et al., 2002, 2005; Kubo et al., 2007; Kume et al., 2006; Yabushita et al., 2002);

- *necrotic lipid pools*, which are less well-delineated than calcifications and appear as diffusely bordered signal poor regions with overlying signal-rich bands, corresponding to fibrous caps (Fig. 8.4c) (Jang et al., 2002, 2005; Kubo et al., 2007; Kume et al., 2006; Yabushita et al., 2002);

- *thrombi*, which are detected as masses protruding the vessel lumen partially separated from the inner surface of the artery (Fig. 8.4d). Red thrombi exhibit a marked signal attenuation with signal-free shadowing because they are mainly composed by red blood cells. White thrombi, which are principally composed by platelets and white blood cells, are characterized by a lower signal attenuation (Kume et al., 2006);

- *macrophages*, which appear as signal-rich, distinct, or confluent dots that exceed the intensity of background speckle noise (Tearney et al., 2003);

- *plaque dissections*, which are commonly associated to plaque rupture and appear as rims of tissue protruding into the lumen (Prati et al., 2007);

The limited tissue penetration of OCT (1-2 mm) makes this imaging technique not suitable to study the vessel remodeling as it is not possible to visualize the media in presence of an atherosclerotic plaque (Waksman et al., 2013).
OCT is successfully applied in PCI (Regar et al., 2011). Thanks to OCT high spatial resolution, stent struts are detectable. In particular, metallic stent struts

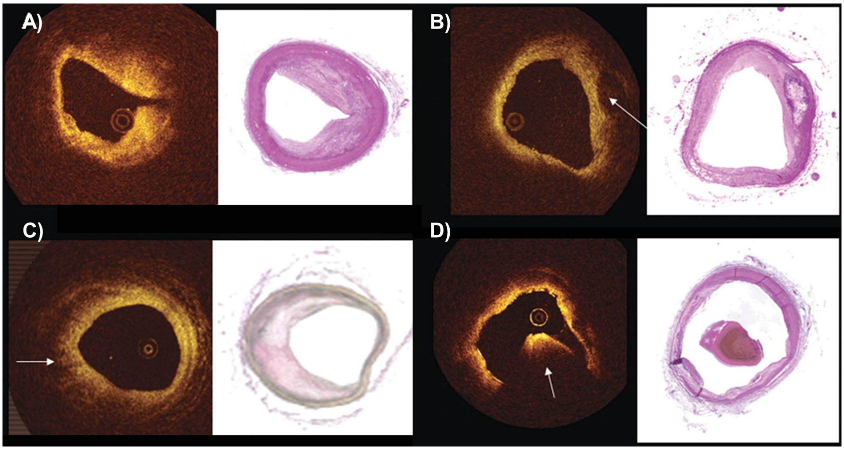

Figure 8.4: OCT examples of plaque composition (left panels) and corresponding histology (right panels): a) fibrous plaque; b) calcification (indicated by the arrow); c) lipid pool (indicated by the arrow); d) red thrombus (indicated by the arrow). *Adapted with permission from European Heart Journal Vol.31: 401-415. F. Prati et al. Expert review document on methodology, terminology, and clinical applications of optical coherence tomography: physical principles, methodology of image acquisition, and clinical application for assessment of coronary arteries and atherosclerosis.* ©*(2010) Oxford University Press.*

appear as signal-rich structures with dorsal shadowing which is due to the inability of light beam to pass through metal (Fig. 8.5) (Mehanna et al., 2011). OCT provides information on stent expansion and strut apposition. An example of well apposed and malapposed struts visible in OCT images is shown in Figs. 8.5a and 8.5b, respectively. OCT can also be used to identify the signs of vessel trauma, such as dissections or tissue prolapse, immediately after stent implantation (Fig. 8.6). In the end, OCT allows the evaluation of tissue coverage in follow-up analysis (Suzuki et al., 2008).

8.2.3 OCT image processing

Currently, the analysis of OCT images is conducted manually by an operator who contours and identifies relevant structures in order to measure clinically relevant information such as luminal area, stent strut to vessel wall distances and neointima coverage (Ughi et al., 2012). However, the manual analysis process is impractical for clinical routine because it is extremely time consuming and labor intensive when large datasets of images are investigated; furthermore, it is intrinsically operator-dependent (Ughi et al., 2012). In the recent years several automatic or semi-automatic algorithms have been proposed in the literature for the analysis of OCT images. These algorithms were developed for the following applications:

- *detection of the lumen contour* (Bourezak et al., 2010; Celi et al., 2013; Gurmeric et al., 2009; Lu et al., 2012; Sihan et al., 2009; Tsantis et al., 2012; Ughi et al., 2012, 2013; Unal et al., 2010)
- *detection of stent strut position* (Gurmeric et al., 2009; Lu et al., 2012; Tsantis et al., 2012; Ughi et al., 2012; Unal et al., 2010; Wang et al., 2013b; Xu et al., 2011);
- *quantification of stent strut malapposition* (Ughi et al., 2012; Unal et al., 2010);
- *quantification of stent strut coverage* (Ughi et al., 2012; Unal et al., 2010);
- *assessment of stent size cell and SB access* (Wang et al., 2013a)
- *characterization of atherosclerotic plaques* (Celi et al., 2013; Ughi et al., 2013)

Few works have been proposed for the reconstruction of 3D geometrical models of coronary arteries that might be used for fluid dynamic analyses. In these

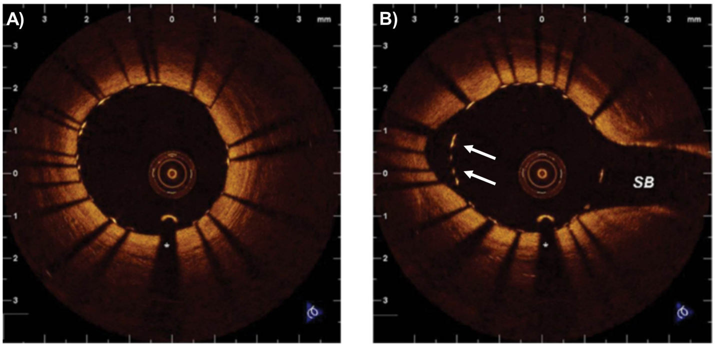

Figure 8.5: Examples of OCT images acquired immediately after stent deployment. Stent struts appear as signal-rich structures with dorsal shadowing. In a) all the struts are well apposed while in b) some struts, indicated by the arrows, are malapposed. *Adapted with permission from Herz Vol.36 (5): 417-429. E. Regar et al. The diagnostic value of intracoronary optical coherence tomography. ©(2011) Urban & Vogel, Muenchen.*

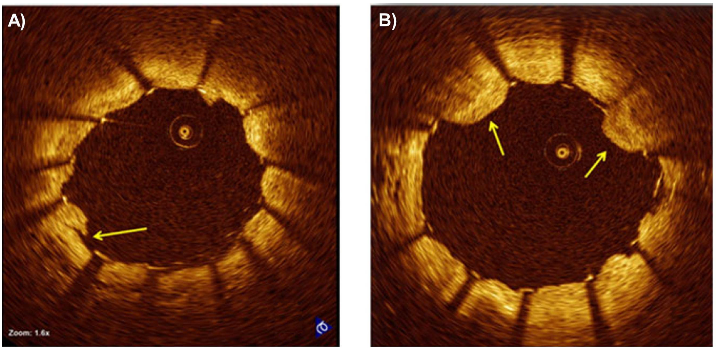

Figure 8.6: a) Dissection of luminal vessel surface between stent struts (yellow arrow). b) Tissue prolapse between struts (yellow arrows). *Reprinted with permission from International Journal of Cardiovascular Imaging Vol.27 (2): 259-269. E.A. Mehanna et al. Assessment of coronary stent by optical coherence tomography, methodology and definitions. ©(2011) Springer.*

works the reconstruction of the stent from imaging data was not performed. Indeed, Ellwein et al. (2011) developed a reconstruction method of patient-specific coronary arteries that combines OCT and CT images. Firstly, the vessel lumen border was detected in cross-sectional OCT images at 1-mm intervals. The integrated image analysis software of the OCT system was used. OCT images were then processed in MATLAB (MathWorks Inc., Natick, MA, USA) by removing measurement markers and applying an appropriate threshold in order to obtain binary images. The images were aligned vertically in succession and spaced by a distance calculated from the known pullback speed of the OCT exam. Secondly, since OCT images do not necessarily lie on the vessel centerline, the wire pullback pathway was determined in order to ensure accurate registration of the processed images. The wire adopts the straightest configuration within tortuous vessel, minimizing its total bending energy. Therefore, the wire pathway with minimum bending energy was determined using OCT and CT images by applying a shortest path algorithm to a graph representation of the artery. Thirdly, vessel lumen borders were registered orthogonal to the wire pathway (Fig. 8.7a). Lastly, the total collection of segments was lofted by means of a CAD software obtaining the fluid domain (Fig. 8.7b). The reconstruction method was applied to imaging data of a stented human LCX with its second obtuse marginal artery acquired immediately after stent implantation and at follow-up of 6 months. To include the bifurcation in the geometrical model, the distal region of the artery was reconstructed from CT data. The stent was not directly reconstructed from OCT images but was virtually positioned inside the artery using CAD operations, obtaining the final stented model (Fig. 8.7c) (Gundert et al., 2011). CFD simulations of the two cases (i.e. post-stenting and follow-up at 6 months) were performed. Major details about these analyses are reported in Section 3.3.3.

Bourantas et al. (2012) fused OCT with angiographic data in order to create a 3D geometrical model of a human RCA characterized by plaque rupture. The luminal surface of the vessel was reconstructed by adapting a methodology previously developed for the fusion of IVUS and angiographic images (Bourantas et al., 2005) to OCT and angiography. In particular, the 3D OCT catheter path was extracted from two end-diastolic angiographic images. The vessel lumen contours were detected from OCT images and they were placed perpendicularly onto the 3D path obtaining their absolute orientation. The outcome of this process was a point cloud that was used to create a non-uniform rational B-Spline (NURBS) surface representing the arterial lumen. A CFD simulation was subsequently performed to examine the association between hemodynamics and plaque rupture.

Athanasiou et al. (2012) also proposed a reconstruction method based on OCT and angiographic data. Their method considers the centerline of the vessel instead the catheter to correctly orientate the lumen borders in the space. The centerline of the vessel is semi-automatically extracted from two angiographic projections. The vessel lumen contours are automatically detected and they are placed perpendicularly onto the path using the centroid of each lumen border.

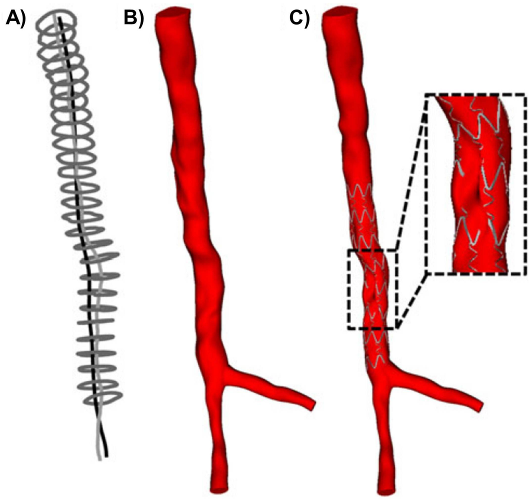

Figure 8.7: a) Registration of the vessel lumen borders (dark grey), which were obtained from OCT images, orthogonal to the wire pathway (black line). The centerline of the vessel is indicated in light grey. b) Fluid domain of the coronary bifurcation generated by lofting the lumen contours in a CAD software. c) Final fluid domain obtained by virtually positioning the stent inside the artery using CAD operations. In the magnification box, the thrombus area is depicted. *Reprinted with permission from Cardiovascular Engineering and Technology Vol.2 (3): 212-227. L.M. Ellwein et al. Optical Coherence Tomography for Patient-specific 3D Artery Reconstruction and Evaluation of Wall Shear Stress in a Left Circumflex Coronary Artery. ©(2011) Biomedical Engineering Society.*

Finally, the 3D geometrical model of the vessel is created starting from a point cloud containing the oriented vessel lumen contours.

8.3 3D reconstruction of an *in vitro* stented coronary bifurcation

8.3.1 Geometrical model reconstruction

An OCT exam was performed *in vitro* in an ideal silicone model of a stented coronary bifurcation. The artery model represents the LAD with its first diagonal branch. It is characterized by a bifurcation angle of 45° and by the following diameters: 3.5 mm for the proximal MB, 3 mm for the distal MB, and 2.6 for the SB. In this model a Multi-Link Vision® stent (Abbott Laboratories, Abbott Park, IL, USA) was deployed following the PSB stenting procedure. OCT images were acquired using the C7-XR^{TM} FD-OCT Intravascular Imaging System (St. Jude Medical, Inc.) at the Policlinico Gemelli hospital in Rome, Italy. A segment of the MB of the stented bifurcation model with a length of 54 mm was scanned using a pull-back speed of 20 mm/s. 271 cross-sectional images were acquired (frame-rate = 100 frame/s, distance between each frame = 0.2 mm). The images were stored in the DICOM medical imaging standard file and then they were processed in MATLAB R2010a.

In Fig. 8.8a an example of *in vitro* OCT frame which was acquired for the present work is shown. This image is slightly different if compared with an *in vivo* OCT frame (Fig. 8.8b). In fact, in the *in vivo* frame the vessel lumen contour and the dorsal shadows due to the presence of the stent struts are visible while in the *in vitro* frame the inner and outer borders of the silicone tube, and the position of the struts within the tube as well as their thickness are clearly recognizable.

The general workflow of the reconstruction method of the stented bifurcation model is schematized in Fig. 8.9. The first step of the method consists in the image pre-processing (Fig. 8.10): (1) images are converted to grayscale; (2) the lower part of each image, which contains the longitudinal section of the vessel, is cut because not necessary for the vessel reconstruction; (3) specific thresholds are applied to remove the noise, and (4) the images are converted into a logical matrix. After the pre-processing, the reconstruction method is characterized by two separated parts that allow the creation of the 3D stented artery geometry: the vessel and the stent reconstruction.

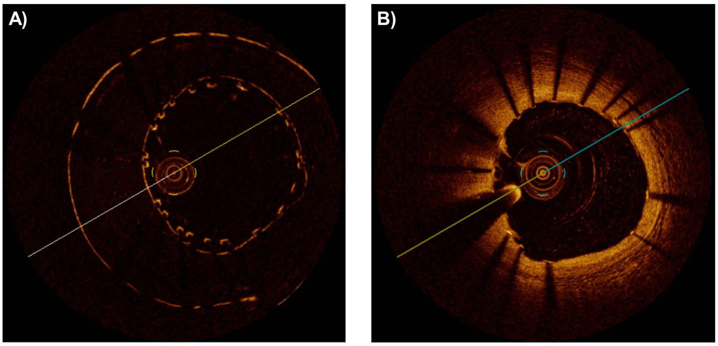

Figure 8.8: Example of (a) *in vitro* and (b) *in vivo* OCT images. In the *in vitro* image the inner and outer borders of the silicone tube, and the position and the thickness of the stent struts are clearly visible. In the *in vivo* image the vessel lumen contour, the dorsal shadows due to the presence of the struts, and the guide wire are recognizable.

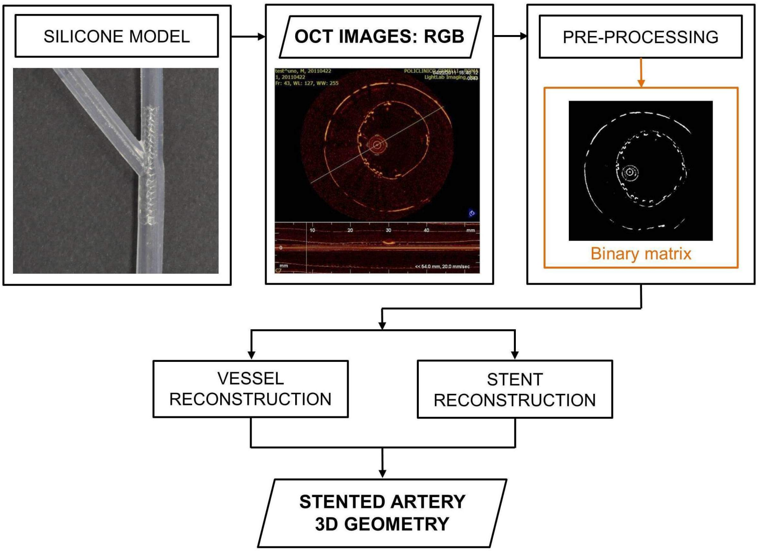

Figure 8.9: General workflow of the reconstruction method of an *in vitro* stented coronary bifurcation model from OCT images.

Vessel reconstruction

The reconstruction method of the vessel is schematized in Fig. 8.11. The first step of the algorithm consists in the stent strut removal. A series of automatic operations are performed in MATLAB for each frame. The algorithm starts with a raw identification of the struts combining ”opening” and ”closing” operations on a binary image characterized by a threshold that was set according to the measured noise level of the technique. In particular, ”opening” is a morphological operation of dilation followed by erosion that generally removes regions of an object, break thin connections, and removes thin protrusions (Gonzales et al., 2009); ”closing” is a morphological operation of erosion followed by dilation that joints narrow breaks, fills holes and long thin gulfs (Gonzales et al., 2009). Then, a subtraction is performed between the logical matrix, resulted from the pre-processing step, and the new matrix containing the struts (Fig. 8.12). The result is a matrix in which the vessel wall and the struts are separated, and the majority of the struts is eliminated. The outer border of the vessel is detected and removed by applying a dilation operation to each frame and then taking into account that the number of pixels of the outer border is higher than the inner

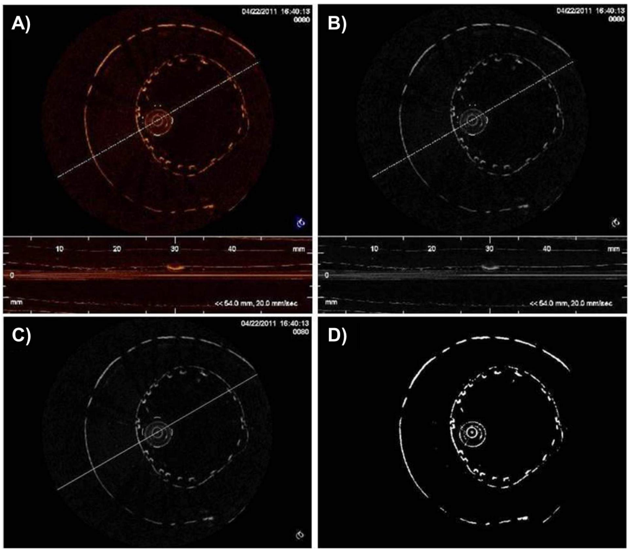

Figure 8.10: Pre-processing step of the reconstruction method of an *in vitro* stented coronary bifurcation model: a) original OCT image; b) conversion to grayscale; c) elimination of the lower part of the image, which contains the longitudinal section of the vessel; d) application of specific thresholds to remove the noise and the labels, and conversion of the image to a logical matrix.

one. The next step is the elimination of the catheter. Since its position is fixed in all the images, it is removed by assigning a value of zero to all the pixels of that region. Afterwards, the lumen border is fitted with an ellipse, which represents a good approximation for the inner contour of the ideal silicone coronary artery. Repeating the operations for all the frames, a point cloud representing the vessel is obtained.
The points are imported in the CAD software Rhinoceros v.4.0 (McNeel & Associates, Indianapolis, IN, USA) (Fig. 8.11). Hence, a surface mesh is created obtaining the geometry of the MB. The SB is created as an ideal cylinder since OCT was performed only in the MB. Its dimensions and orientation are known. In the end, the MB and the SB are combined, obtaining the geometrical model of the bifurcation (without stent).

Stent reconstruction

An algorithm that automatically identifies the position of the stent struts was developed in MATLAB (Fig. 8.13). In order to obtain images that contain only

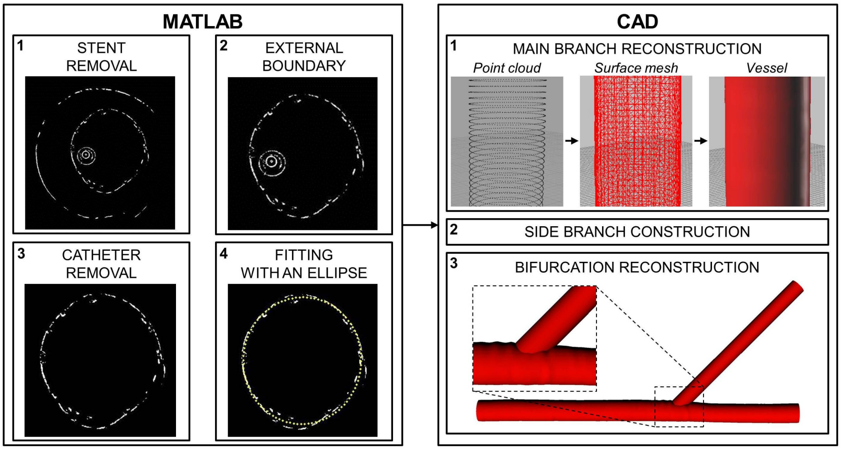

Figure 8.11: Diagram of the workflow used for the reconstruction of the vessel of an *in vitro* coronary bifurcation model starting from OCT images. *Reprinted from the Proceedings of the 13th IEEE International Conference on BioInformatics and BioEngineering, November, 10-13, 2013, Chania, Crete (Greece). C. Chiastra et al. Coronary stenting: from optical coherence tomography to fluid dynamic simulations. ©(2013) IEEE.*

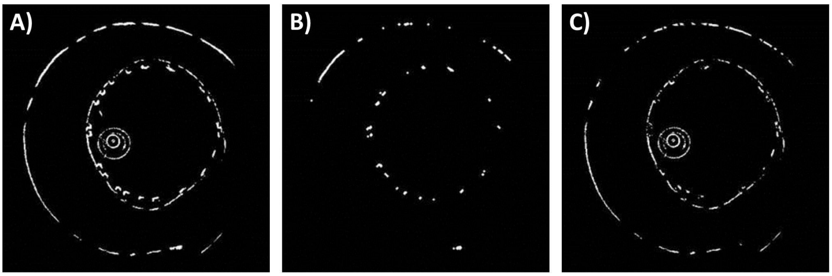

Figure 8.12: Removal of stent struts. A subtraction between (a) the binary image resulting from the pre-processing step and (b) the binary image containing the stent struts, which is obtained combining opening and closing operations, is done. The result is (c) a binary image, in which the majority of the struts are removed.

struts, each frame is segmented by applying a fuzzy c-means (FCM) clustering method in the inner zone of the fitted vessel. FCM clustering method performs the probability of one piece of data to belong to two or more clusters or seeds based on some features (Noordam et al., 2000). In this work these features are represented by the red, green, and blue (RGB) values of the native OCT image. FCM method is applied using three seeds which represent the vessels, the struts and the background. The method is initialized to the RGB values of these three labels. For each pixels of the image the probability to belong to each labels is calculated.
Subsequently, in order to correctly mark each pixel with only one of the three labels, a defuzzification step is performed. In this step the pixels are labeled according to the maximal probable mark. A logical matrix of the area containing the struts is then obtained. A rectangle is placed on each detected strut. This rectangle has the dimensions of the real strut cross-section of Multi-Link

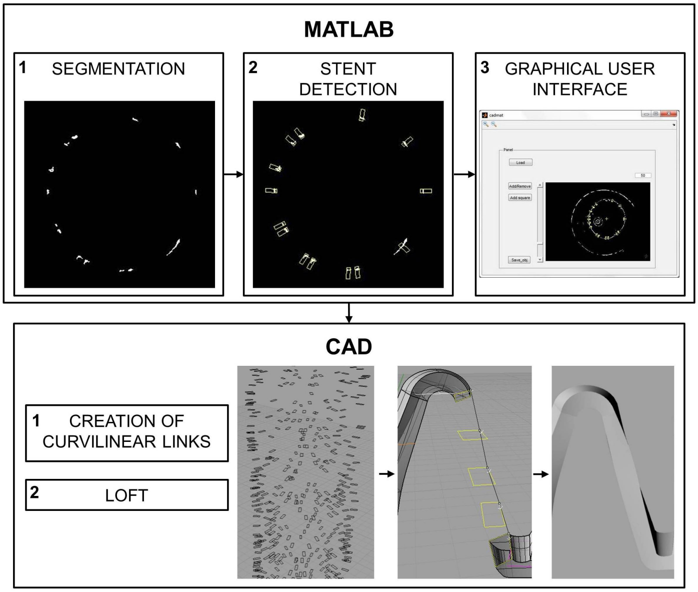

Figure 8.13: Diagram of the workflow used for the reconstruction of the stent of an *in vitro* coronary bifurcation model starting from OCT images. *Reprinted from the Proceedings of the 13th IEEE International Conference on BioInformatics and BioEngineering, November, 10-13, 2013, Chania, Crete (Greece). C. Chiastra et al. Coronary stenting: from optical coherence tomography to fluid dynamic simulations. ©(2013) IEEE.*

Vision® stent and is rotated so that the segment defined from the center of the ellipse and the shorter side of the rectangle is perpendicular to its shorter side. In the next step, the user, through a graphical user interface, can visualize all the slices, adding or removing rectangles if they are not correctly detected. When the creation of the rectangles is finished, the algorithm produces an object file that contains all the rectangles of the slices in the correct longitudinal position. In the final step, the object file is opened in the CAD software (Fig. 8.13), where all the rectangles are manually linked by loft operations, following the geometry of the Multi-Link Vision® stent and using curvilinear links extracted from a CAD model of the stent.

8.3.2 Fluid dynamic analysis

The 3D geometry obtained from OCT images applying the previously described reconstruction method was imported into ANSYS ICEM CFD v.14.0 (ANSYS Inc., Canonsburg, PA, USA) to create the computational grid. In order to assure accurate results in the stented region (ROI), the mesh size was chosen after a mesh independence study. Three tetrahedral meshes with increasing element number (4800565, 7923535 and 10751884 elements) were created to perform steady-state simulations. The second mesh was chosen as the percentage difference with the finest mesh in terms of WSS was lower than the chosen threshold (0.5 %). Then, in order to reduce the number of elements and to increase the computational speed, a hybrid discretization of the fluid domain was created, following the method exposed in Chapter 5. The number of elements of the hybrid mesh was 7,291,683, about 8 % lower than the full tetrahedral mesh, implying an increase of computational speed.
A feasibility transient fluid dynamic simulation was carried out by means of ANSYS FLUENT v.14.0 (ANSYS Inc., Canonsburg, PA, USA) in order to verify that the 3D reconstructed model was suitable for CFD analyses. Blood was assumed as an incompressible, non-Newtonian fluid with a density of 1060 kg/m^3 and the viscosity varying according to Carreau model (Section 5.2.2). At the inlet, a time-dependent blood flow was applied, referring to the work by Davies and colleagues (Davies et al., 2006). At the outlets, a flow split was imposed. The values of the flow split were calculated applying the relation between flow-rate and vessel diameter defined by van der Giessen et al. (2011). The arterial wall and the stent were assumed to be rigid and were defined with a no-slip condition. A coupled solver was used with a second-order upwind scheme for the momentum spatial discretization. Under-relaxation factors of 0.15 were used for pressure and momentum. Convergence criterion for con-

tinuity and velocity residual was set to 10^{-6}. The simulation was performed in parallel on one node of a cluster (2 quad-core Intel Xeon CPU E5620 @ 2.40GHz, 24 GB RAM for each node, InfiniBand Mellanox for the main cluster interconnections).

The results of the CFD simulation were analyzed in terms of velocity pattern, TAWSS, OSI, and RRT. TAWSS was investigated not only by means of contour maps but also with a quantitative analysis. The percentage area of the stented region exposed to TAWSS lower than 0.4 Pa was calculated. Moreover, the histogram of the area distribution of TAWSS was analyzed.

8.3.3 Results and discussion

The 3D geometrical model of the stented coronary bifurcation reconstructed from OCT images is shown in Fig. 8.14. Stent struts appear deformed because of the balloon expansion, and well apposed overall.

Fluid dynamic results are in agreement to those found in the literature, indicating that the geometrical model is suitable for CFD analyses. In particular, Fig. 8.15 shows the velocity magnitude contour map over a longitudinal plane at the peak flow rate (89.37 mL/min). In accordance to Foin et al. (2012b), it is possible to observe that the velocity profiles are skewed toward the carina,

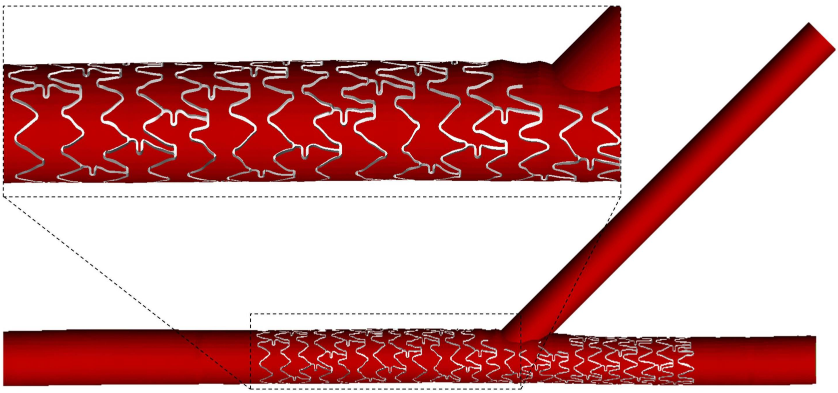

Figure 8.14: Final 3D geometrical model of an *in vitro* stented coronary bifurcation reconstructed from OCT images. *Reprinted from the Proceedings of the 13th IEEE International Conference on BioInformatics and BioEngineering, November, 10-13, 2013, Chania, Crete (Greece). C. Chiastra et al. Coronary stenting: from optical coherence tomography to fluid dynamic simulations. ©(2013) IEEE.*

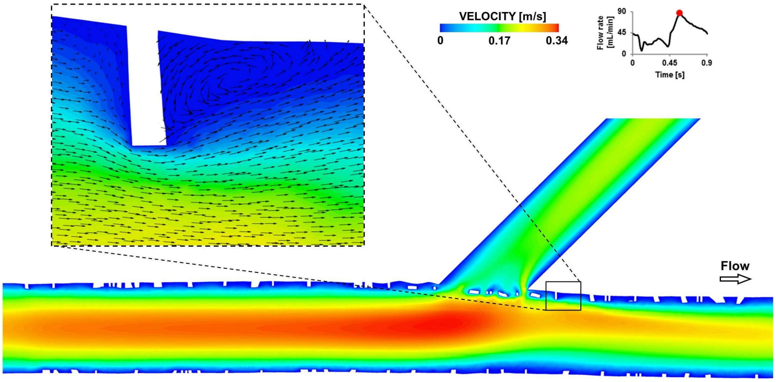

Figure 8.15: Contour map of velocity magnitude at peek flow rate (89.37 mL/min). In the magnification box, an example of recirculation zone that occurs in the vicinity of a stent strut is shown.

resulting in lower velocity in the region opposite to it. Moreover, there are recirculation zones near the stent struts, as found in Morlacchi et al. (2011a), and stagnation areas in the bifurcation region, where the struts alter the blood flow towards the SB. Figure 8.16 points out that low TAWSS (< 0.4 Pa) are located next to the struts and the bifurcation region, according with the results in Katritsis et al. (2012) and Chiastra et al. (2013). The quantitative analysis of TAWSS shows that the percentage area with TAWSS lower than 0.4 Pa was 72.8 %. This result is confirmed by the TAWSS distribution, which is characterized by a mean value of 0.32 Pa and positive values of skewness and kurtosis (6.1 and 72.5, respectively for skewness and kurtosis). These values of skewness and kurtosis indicate that the distribution of TAWSS is skewed to the right (wider area with TAWSS values lower than the mean) and more peaked if compared with the normal distribution. High values of OSI are found next to the carina, in the regions characterized by the lowest values of TAWSS. RRT values are high in the vicinity of stent struts (especially close to ”S-shaped connectors”) and the carina. These results are in accordance with the fluid dynamic studies by Chiastra et al. (2013) and Katritsis et al. (2012).

8.3.4 Conclusions

This work shows a method for the reconstruction of a stented coronary artery bifurcation model from OCT images. The geometry obtained through this method was investigated by means of a CFD simulation, in order to quantify near-wall quantities and to correlate them with ISR process. Although this is an ideal arterial vessel with a stent deployed, results confirmed that the highest risk of restenosis is located in the region near the bifurcation.

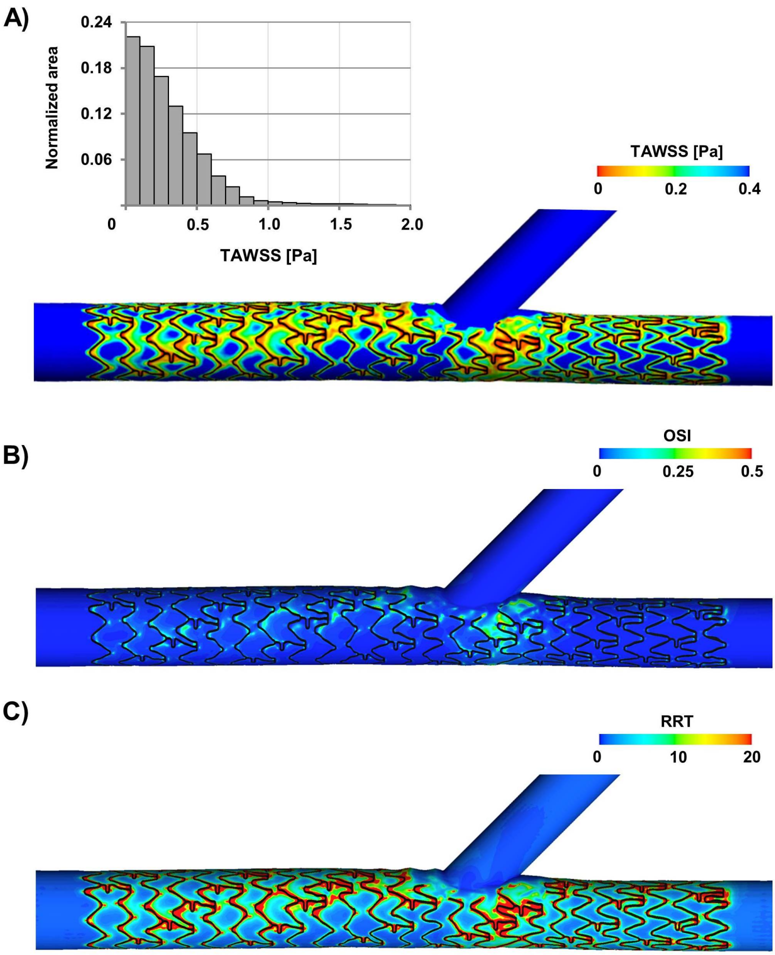

Figure 8.16: Contour maps of (a) TAWSS, (b) OSI, and (c) RRT. On the top left the TAWSS distribution is shown. Each bar of the histogram represents the amount of normalized area of the arterial wall with a defined range of TAWSS. Bar widths are 0.1 Pa.

8.4 3D reconstruction of an *in vivo* stented coronary artery

The reconstruction method described in Section 8.3, which was developed for an *in vitro* coronary bifurcation model, was adapted for the reconstruction of a 3D geometrical model for CFD simulations of an *in vivo* case. OCT gives information about the vessel lumen contour and the position of the stent struts in each cross-sectional image. However, the spatial orientation of the vessel and the stent is not provided by this imaging technique. Coronary angiography or CT can be used to obtain this information, as previously done in several works (Athanasiou et al., 2012; Bourantas et al., 2012; Ellwein et al., 2011). In other words, the angiographic or CT data can provide the spatial trajectory of the vessel, serving as stem on which the OCT cross-sectional images are positioned and orientated in the space. In this study, coronary angiography is considered.
Coronary angiography and OCT imaging were performed immediately after stent implantation in an adult patient with a LAD lesion treated with the Skylor™ stent (Medtronic Invatec, Roncadelle (BS), Italy) at the Policlinico Gemelli hospital in Rome, Italy. Coronary angiography was performed with the Allura Xper X-ray system (Philips, Amsterdam, The Netherlands). OCT images were acquired in the stented segment using the C7-XR™ FD-OCT Intravascular Imaging System (St. Jude Medical, Inc.) for a length of 54 mm. A pull-back speed of 20 mm/s and a frame-rate of 100 frame/s (distance between each frame 0.2 mm) were set. The images were stored in the DICOM medical imaging standard file in Cartesian coordinates and then they were processed in MATLAB R2010a. A schematic diagram of the reconstruction method developed for *in vivo* stented coronary arteries is shown in Fig. 8.17. The open-source software 3D IVUS ANGIO Tool 2.1 (Informatics and Telematics Institute, Thermi-Thessaloniki, Greece) was employed in order to obtain the 3D centerline of the vessel. This software allowed a semi-automatic reconstruction of the centerline combining two end-diastolic angiographic projections. The reconstruction method used by the software is described in detail in Giannoglou et al. (2006a,b) and Chatzizisis et al. (2006).
The OCT images were first pre-processed in MATLAB. In particular, the images were converted to grayscale and the lower part of each image containing the longitudinal section of the vessel was removed. Then, the algorithms for the detection of the lumen contour and the stent struts were applied. As previously explained in Section 8.3.1, *in vivo* OCT images are slightly different from *in vitro* images (Fig. 8.8). Therefore, new specific algorithms, which are in part different from those applied in the *in vitro* case, were developed in MATLAB.

The algorithm for the detection of the lumen contour of each OCT frame is based on the following steps (Fig. 8.18):

- *conversion of the image from Cartesian to polar coordinates*, by using the following relations:

$$r = \sqrt{i^2 + j^2}; \qquad \theta = tan^{-1}\frac{j}{i} \tag{8.1}$$

  where i and j are the Cartesian coordinates, and r (range dimension) and θ (acquisition angle) are the polar coordinates.

- *detection of the lumen border*. Firstly, the catheter is removed by considering its position which is fixed in the space. Secondly, ”opening” operations are performed in order to remove the image noise. Thirdly, each θ-coordinate of the image is scanned from the lowest to the highest value of r saving the first non-zero r-coordinate in order to find the

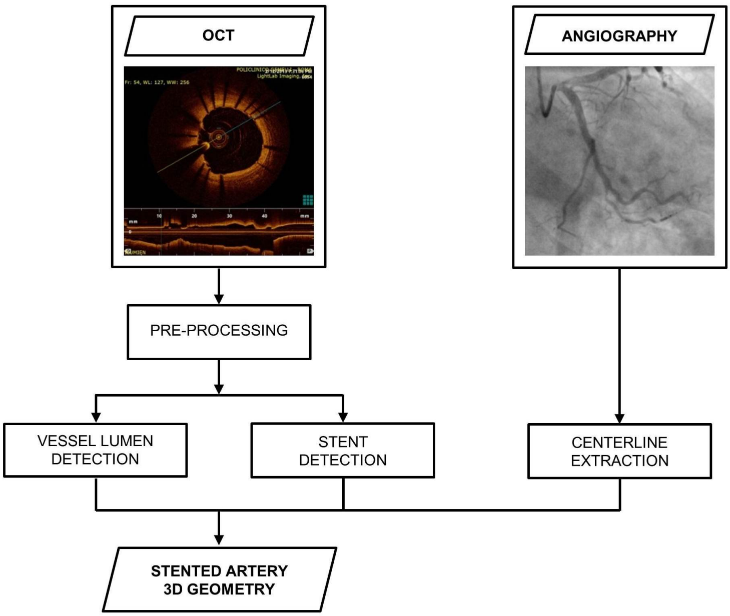

Figure 8.17: General workflow of the reconstruction method of an *in vivo* stented coronary artery from OCT and angiography images.

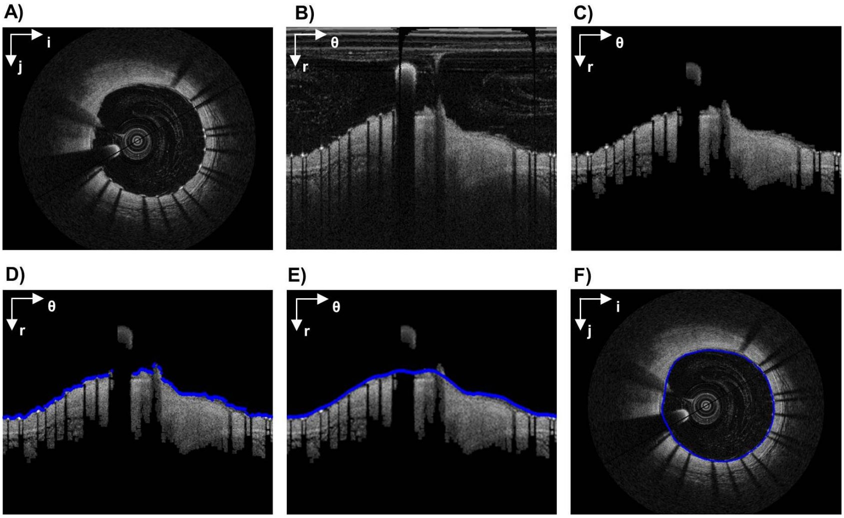

Figure 8.18: Main steps of the algorithm for the detection of the lumen contour of each OCT frame: a) OCT image after pre-processing; b) conversion to polar coordinates; c) removal of the catheter by considering its position which is fixed in the space; d) scanning of each θ-coordinate of the image from the lowest to the highest value of r in order to save the first non-zero r-coordinate representing the lumen border. The pixels that belong to the guide wire and not to the vessel lumen are removed; e) fitting of the lumen border; f) conversion to Cartesian coordinates. In each image the Cartesian coordinate system (i, j) or the polar coordinate system (r, θ) is indicated.

lumen border. Lastly, the detected coordinates (r, θ) that belong to the guide wire and not to the vessel lumen are removed. In particular, for each θ-coordinate of the image, the integral of the intensity profile over r is calculated as the sum of the grey value of each pixel. The θ-coordinates in which the guide wire is present are characterized by a lower integral value because of the wide shadow generated by the guide wire. Therefore, these coordinates are not considered for the lumen border detection.

- *fitting of the lumen border*. The pixels of the image detected as lumen contour are interpolated with the piecewise cubic Hermite interpolation. The result is smoothed with a local regression method that uses weighted linear least squares and a 2^{nd} degree polynomial model. The method assigns zero weight to data outside six mean absolute deviations.

- *conversion of the detected lumen contour from polar to Cartesian coordinates*. The trigometric functions sine and cosine are applied to transform the matrix $I(r, \theta)$ back to $I(i, j)$, as follows:

$$i = rcos\theta; \qquad j = rsin\theta \tag{8.2}$$

where the terms are defined as above.

This procedure is automatically repeated for each OCT frame. At the end of the process the user can visualize the vessel lumen borders by means of a graphical user interface and manually modify them if necessary.
The algorithm for the detection of the stent struts was applied to the OCT images previously converted into polar coordinates (r, θ). This algorithm works under the assumptions that there is only one strut for each θ-coordinate (as a consequence, overlapping stents are excluded) and that the struts are well apposed. In order to find the strut position along the θ-axis, the algorithm uses the dorsal shadows that are visible behind the struts. For each θ-coordinate of the image the integral of the intensity profile over r is calculated as the sum of the grey value of each pixel. Considering all the θ-coordinates of the image, the profile of the integral values along the θ-axis is then created (Fig. 8.19a). The relative minima of this profile correspond to the strut position along the θ-axis. In order to define the strut position along the r-axis, the struts are placed on the vessel lumen border (Fig. 8.19b). At the end of the strut detection process, the images are converted back to Cartesian coordinates. A rectangle with the dimensions of the real strut cross-section of the Skylor^{TM} stent is placed on each detected strut. This rectangle is rotated so that the segment defined from the

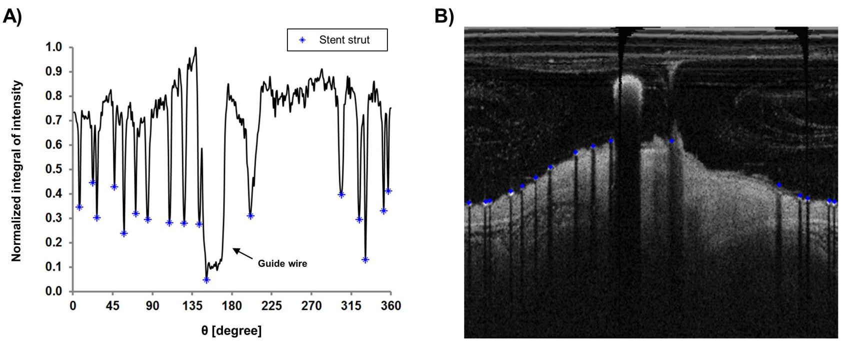

Figure 8.19: a) Normalized integral over r of the grey intensity calculated for each θ-coordinate of the image as the sum of the grey value of each pixel. The relative minima of this profile correspond to the strut position along the θ-axis. b) OCT frame in polar coordinates. The position of the detected stent struts is indicated in blue. The struts are not placed on the guide wire.

centroid of the vessel contour and the shorter side of the rectangle is perpendicular to its shorter side. In the end, the user can visualize all the frames using a graphical user interface, adding or removing rectangles if they are not correctly positioned (Fig. 8.20).
The next step for the creation of the 3D model of the stented artery consisted in the registration of all the detected vessel contours and stent struts orthogonal to the vessel centerline using the centroid of each lumen contour (Fig. 8.21a), as previously done by Athanasiou et al. (2012).
In the final step of the reconstruction method, the lumen contours and the struts were imported as a point cloud in the CAD software Rhinoceros v.4.0 for the creation of the final 3D geometrical model of the stented coronary artery. Figure 8.21b shows a preliminary model of the coronary artery without the stent that was obtained by lofting the lumen contours. The black rectangles represent the strut cross-section that were detected in each OCT image.

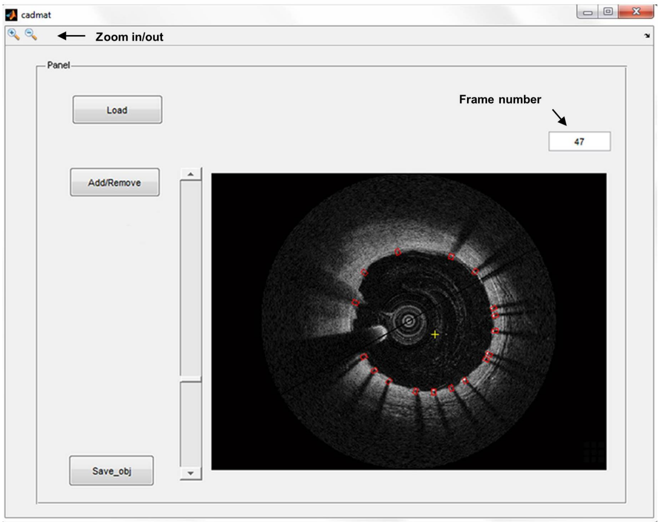

Figure 8.20: Graphical user interface that allow to visualize all the OCT frames adding or removing stent struts if they are not correctly positioned. The ”Load” button imports all the OCT frames in the interface. The user can choose the frame to visualize with the sliding bar that is positioned on the left of the image. In each frame the rectangles that represent the strut cross-sections are shown in red while the centroid of the vessel lumen appears in yellow. The user can add or remove the rectangles by clicking the ”Add/Remove” button and then selecting the pixel of interest in the image. Once the user is satisfied, the position of the rectangles of all the frames can be saved in a object file by clicking the ”Save_obj” button.

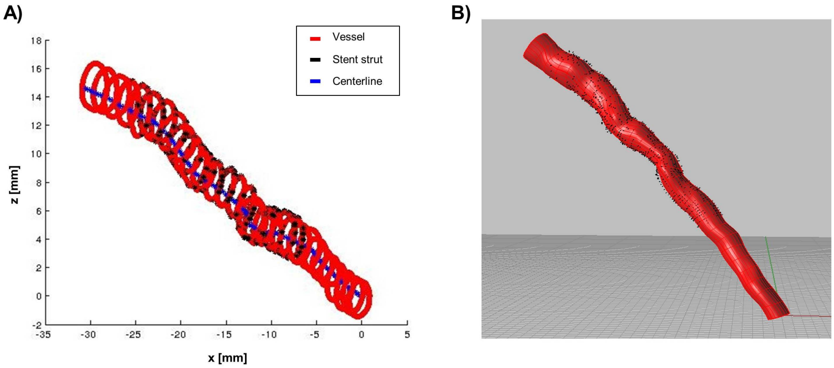

Figure 8.21: a) Registration in MATLAB of all the detected vessel contours and stent struts orthogonal to the vessel centerline using the centroid of each lumen contour. Only one frame every five is shown for clarity. b) Preliminary 3D model of the coronary artery without the stent that was obtained by lofting the lumen contours in the CAD software. The black rectangles represent the strut cross-section that are detected in each OCT image.

8.5 Limitations and future works

The studies presented in this chapter are preliminary. The reconstruction methods were only applied on single *in vitro* and *in vivo* cases. Therefore, the robustness of the implemented algorithms should be tested considering more cases. Moreover, the reconstruction methods were not validated. The *in vitro* case could be used for this purpose, following an approach similar to the one adopted by Wang et al. (2013a). In particular, a micro-CT scan of the stented coronary bifurcation model could be performed, providing a resolution more than 10 times higher than OCT in the longitudinal direction. Assuming the 3D geometrical model obtained from micro-CT as the reference, validation could be performed by comparing the vessel and the position of the stent struts of 3D model reconstructed from OCT images with the ones from micro-CT. *In vivo* cases are not suitable for validation because, at present, apart from OCT there are no other imaging technique that allow the reconstruction of the stented vessel.

The main limitation of the studies presented in this chapter is the reconstruction of the stent. Specific algorithms were developed in MATLAB to automatically detect the struts and place rectangles representing the strut cross-section on them. However, the loft operations requested in the CAD software to obtain the final 3D model of the stent are manual, implying elevated reconstruction

time and operator-dependet results. In order to make the reconstruction process automatic, an algorithm for registering an ideal CAD stent geometry to the struts detected from OCT could be implemented. As an alternative, a method of fast virtual deployment of the stent inside the artery model, similar to the one developed by Larrabide et al. (2012a,b) for intracranial aneurysm, could be used. This method is based on a constrained deformable model of the stent. The stent is represented by a moving mesh that deforms under the effect of internal and external forces until it reaches the final configuration. In this specific case, the constrains could be represented by stent design, the vessel geometry, and the cross-section of the detected struts.
In the vessel reconstruction method of the *in vitro* case an elliptical fitting was used for the lumen border. This is a good approximation for the inner contour of the ideal silicone coronary artery. However, this fitting is not applicable to *in vivo* cases in which the vessel is deformed and not elliptical. In these cases, the lumen border can be fitted with a high order polynomial or a spline, or interpolated, using for example the piecewise cubic Hermite interpolation as done in the *in vivo* case (Section 8.4). Another limitation is related to the algorithm for the detection of the stent struts developed for the *in vivo* case that is not able to detect either malapposed or overlapped struts.
A drawback of the approach proposed in this chapter is that post-operative OCT can be only used to achieve a verification but not a prediction. However, the approaches of Chapters 7 and 8 could be combined. In fact, the pre-operative scan of a patient could be used to predict the stented geometry using structural finite element analyses and the geometry reconstructed from post-operative OCT of the same patient could be used to validate such prediction.
In conclusion, although the reconstruction methods proposed in this chapter are preliminary and not validated, they represent a first step towards the semi-automatic creation of image-based stented coronary artery models for CFD simulations.

Chapter 9

Final remarks

9.1 Conclusions

THE present thesis is focused on the numerical modeling of hemodynamics in stented coronary artery models. Indeed, the altered hemodynamics generated by the stent presence in a diseased coronary artery is considered an important stimulus to ISR (Wentzel et al., 2008), one of the main complications of PCI with stenting. Fluid dynamic analyses are a useful tool to study the local fluid dynamics within stented coronary arteries because they allow the calculation of quantities involved in the ISR process at a level of detail not always accessible with experimental techniques. The following specific conclusions can be drawn for the three main topics of the present thesis:

- *the study of the effect of wall compliance of stented coronary artery models on hemodynamic quantities.* The results of FSI models of a straight stented coronary artery were compared to the corresponding rigid-wall models (Chapter 4). Two different materials were considered for the stents, i.e. CoCr and PLLA. Similar results were found in terms of TAWSS and instantaneous WSS between compliant and rigid-wall cases. These results indicate that, at least for idealized models of stented coronary artery, rigid-wall assumption for fluid dynamic simulations is adequate when the aim of the study is the study of near-wall quantities like WSS.

- *the comparison, from the fluid dynamic perspective, of different stenting procedures for the treatment of bifurcation lesions.* Rigid-wall fluid dynamic simulations were performed on idealized stented coronary bifurcation models (Chapter 6). A hybrid meshing strategy (Chapter 5), which uses both tetrahedral and hexahedral elements, was applied for the creation of the computational grids in order to reduce the computational costs.
  Firstly, FKB inflation within PSB approach, which nowadays is the preferred bifurcation stenting strategy, was investigated. Results of CFD simulations highlighted the advantages of FKB inflation in terms of flow pattern and access to the SB, but also its drawbacks in terms of overexpansion of the proximal part of the MB (wider region characterized by low and oscillating WSS). This study showed also that the use of a tapered balloon deployed in the SB during FKB might reduce the main drawbacks of this procedure.
  Secondly, the different hemodynamic scenarios provoked by PSB performed with a proximal or a distal access to SB were compared. Results

in terms of WSS distribution, velocity and helicity fields were superior for the distal access, giving a quantitative support to the clinical experience that suggests to perform the distal access instead of the proximal one within PSB approach.
Lastly, the double stenting culotte technique was studied, comparing the behavior of a conventional stent with the dedicated stent (Tryton^{TM} stent), which is characterized by fewer struts in its proximal part. The use of this dedicated device reduced the amount of double metallic layers in the proximal part of the MB (lower metal-to-artery ratio), which represents a critical point of the culotte technique. Moreover, fluid dynamic results were found improved in the Tryton-based model. In fact, the particular design of the dedicated device markedly decreased the areas with low TAWSS and high RRT.

- *the study of the hemodynamics of image-based stented coronaries.* Two cases of pathologic LAD with their bifurcations reconstructed from CTA and CCA were studied (Chapter 7), investigating both near-wall and bulk flow quantities. Results of WSS and RRT showed that the regions prone to the risk of restenosis are located next to stent struts, to the bifurcations and to the stent overlapping zone. Looking at the bulk flow, helical flow structures were generated by the shape of the vessel upstream from the stented segment and by the bifurcation. Helical recirculating microstructures were also visible downstream of the stent struts.
Moreover, reconstruction methods of stented coronary artery models for CFD simulations were developed starting from OCT images (Chapter 8). Although the methodology illustrated in this thesis is preliminary and not validated, it represents a first step towards the semi-automatic creation of image-based stented coronary artery models for CFD simulations.

Summarizing, the main achievements of the present work are: (1) the implementation of a FSI model of a stented coronary artery; (2) the development of a hybrid meshing strategy for reducing computational costs of fluid dynamic simulations; (3) the fluid dynamic assessment of different stenting procedures for the treatment of coronary bifurcations; (4) the hemodynamic analysis of image-based models of stented coronary artery models which replicate a real stenting procedure; (5) the development of reconstruction methods of *in vitro* and *in vivo* stented coronary artery models from OCT images.

9.2 Future perspectives

The methods developed in this thesis can be used as a starting point for further research works. In particular, additional studies might be performed for the assessment, from the fluid dynamic perspective, of stenting procedures for the treatment of challenging lesions (e.g. bifurcation lesions or LMCA lesions), giving general guidelines to interventional cardiologists. Further studies might be also performed to investigate the hemodynamic alterations induced by the stent deployment in patient-specific coronary arteries, identifying, from a merely fluid dynamic point of view, the regions that are more prone to the risk of restenosis. More in detail, a study considering a large number of patient-specific cases would be desired in order to better understand the role of the hemodynamic alterations in the ISR process. Two possible methodological approaches might be employed for the creation of the CFD models: (1) the reconstruction of the vessel from patient-specific images followed by structural simulations of stent deployment replicating the real complete stenting procedure, as done in Chapter 7; (2) the reconstruction of the entire geometrical model (i.e. vessel and stent) using patient-specific OCT images, as performed in Chapter 8. The latter approach represents the most innovative solution because it allows to obtain the real geometry of the stented artery without performing simulations. The work presented in Chapter 8, although preliminary, shows promising results for the creation of this kind of models. However, great efforts are required for the validation of the reconstruction methods and for their improvement in order to make them reliable.

In order to screen the main parameters that could induce hemodynamics alterations after coronary stenting, a sensitivity analysis might be performed using design of experiments. Important parameters to be investigated are the elastic properties of the arterial wall and the plaque composition (e.g. presence of calcifications), which may affect the initial geometry used for the CFD study when a sequential structural and fluid dynamic approach is followed.

The indications obtained from the fluid dynamic simulations should be carefully evaluated because the altered fluid dynamics provoked by the presence of stents in the coronary arteries is not the only factor involved in ISR process. The vascular injury caused by device implantation, the stent design (e.g. bare-metal stent or DES) and hypoxia should be also taken into account. Several works focused on structural simulations of stent implantation have been proposed in the literature (Martin and Boyle, 2011; Morlacchi and Migliavacca, 2013). The results of these kind of simulations provide better insight on the changes of the mechanical environment due to the stent expansion. Virtual models that simultaneously take into account the fluid dynamics and the drug release would be also useful to better predict ISR regions, making models more predictive. Some multiphysics works have been already proposed in the literature coupling fluid dynamics and drug release analysis (O'Connell et al., 2010). However, these works consider simplified vessel geometries (Kolachalama et al., 2009) or approximate the stent as a line and not as a 3D structure (Cutrì et al., 2013; D'Angelo et al., 2011), with the impossibility of an accurate study of the local fluid dynamics. In the end, the correlation between ISR and hypoxia is another important aspect to be considered. Recent indications of this correlation have been elucidated through *in vivo* (Sanada et al., 1998; Santilli et al., 2000) and computational (Caputo et al., 2013; Coppola and Caro, 2009) studies.

Bibliography

Anderson, J., Rodriguez, A., and Chang, D. (2008). Foreign body reaction to biomaterials. *Seminars in Immunology*, 20(2):86–100.

Antman, E., Selwyn, A., Braunwald, E., and Loscalzo, J. (2008). Ischemic heart disease. In Fauci, A., Kasper, D., Longo, D., Braunwald, E., Hauser, S., Jameson, J., and Loscalzo, J., editors, *Harrisons Principles of Internal Medicine*. McGraw-Hill Publ. Comp. 17^{th} ed., part 9, section 237.

Aoki, J., Abizaid, A., Serruys, P., Ong, A., Boersma, E., Sousa, J., and Bruining, N. (2005a). Evaluation of four-year coronary artery response after sirolimus-eluting stent implantation using serial quantitative intravascular ultrasound and computer-assisted grayscale value analysis for plaque composition in event-free patients. *Journal of the American College of Cardiology*, 46(9):1670–1676.

Aoki, J., Colombo, A., Dudek, D., Banning, A., Drzewiecki, J., Zmudka, K., Schiele, F., Russell, M., Koglin, J., and Serruys, P. (2005b). Peristent remodeling and neointimal suppression 2 years after polymer-based, paclitaxel-eluting stent implantation: Insights from serial intravascular ultrasound analysis in the TAXUS II study. *Circulation*, 112(25):3876–3883.

Arbab-Zadeh, A., Texter, J., Ostbye, K., Kitagawa, K., Brinker, J., George, R., Miller, J., Trost, J., Lange, R., Lima, J., and Lardo, A. (2010). Quantification of lumen stenoses with known dimensions by conventional angiography and computed tomography: Implications of using conventional angiography as gold standard. *Heart*, 96(17):1358–1363.

Archie Jr., J., Hyun, S., Kleinstreuer, C., Longest, P., Truskey, G., and Buchanan, J. (2001). Hemodynamic parameters and early intimal thickening in branching blood vessels. *Critical Reviews in Biomedical Engineering*, 29(1):1–64.

Asakura, T. and Karino, T. (1990). Flow patterns and spatial distributions of atherosclerotic lesions in human coronary arteries. *Circulation Research*, 66(4):1045–1066.

Asanuma, T., Higashikuni, Y., Yamashita, H., Nagai, R., Hisada, T., and Sugiura, S. (2013). Discordance of the areas of peak wall shear stress and tissue stress in coronary artery plaques as revealed by fluid-structure interaction finite element analysis: A case study. *International Heart Journal*, 54(1):54–58.

Athanasiou, L., Bourantas, C., Siogkas, P., Sakellarios, A., Exarchos, T., Naka, K., Papafaklis, M., Michalis, L., Prati, F., and Fotiadis, D. (2012). 3D reconstruction of coronary arteries using frequency domain optical coherence tomography images and biplane angiography. *Proceedings of the Annual International Conference of the IEEE Engineering in Medicine and Biology Society, San Diego, CA, USA*, pages 2647–2650.

Baim, D. (2008). Percutaneous coronary intervention. In Fauci, A., Kasper, D., Longo, D., Braunwald, E., Hauser, S., Jameson, J., and Loscalzo, J., editors, *Harrisons Principles of Internal Medicine*. McGraw-Hill Publ. Comp. 17th ed., part 9, section 240.

Balossino, R., Gervaso, F., Migliavacca, F., and Dubini, G. (2008). Effects of different stent designs on local hemodynamics in stented arteries. *Journal of Biomechanics*, 41(5):1053–1061.

Balossino, R., Pennati, G., Migliavacca, F., Formaggia, L., Veneziani, A., Tuveri, M., and Dubini, G. (2009). Computational models to predict stenosis growth in carotid arteries: Which is the role of boundary conditions? *Computer Methods in Biomechanics and Biomedical Engineering*, 12(1):113–123.

Bathe, K. (2006a). *Theory and Modeling guide, vol. I: ADINA Solids & Structures*. ADINA R&D, Inc., Watertown, MA, USA.

Bathe, K. (2006b). *Theory and Modeling guide, vol. II: ADINA CFD & FSI*. ADINA R&D, Inc., Watertown, MA, USA.

Bathe, K.-J. and Zhang, H. (2004). Finite element developments for general fluid flows with structural interactions. *International Journal for Numerical Methods in Engineering*, 60(1):213–232.

Bathe, K.-J., Zhang, H., and Ji, S. (1999). Finite element analysis of fluid flows fully coupled with structural interactions. *Computers and Structures*, 72(1):1–16.

Behan, M., Holm, N., Curzen, N., Erglis, A., Stables, R., De Belder, A., Niemel, M., Cooter, N., Chew, D., Steigen, T., Oldroyd, K., Jensen, J., Lassen, J., Thuesen, L., and Hildick-Smith, D. (2011). Simple or complex stenting for bifurcation coronary lesions: A patient-level pooled-analysis of the nordic bifurcation study and the british bifurcation coronary study. *Circulation: Cardiovascular Interventions*, 4(1):57–64.

Belzacq, T., Avril, S., Leriche, E., and Delache, A. (2012). A numerical parametric study of the mechanical action of pulsatile blood flow onto axisymmetric stenosed arteries. *Medical Engineering and Physics*, 34(10):1483–1495.

Berne, R. and Levy, M. (1967). *Cardiovascular physiology*. Mosby, St. Louis, MO, U.S.A.

Berry, J., Santamarina, A., Moore Jr., J., Roychowdhury, S., and Routh, W. (2000). Experimental and computational flow evaluation of coronary stents. *Annals of Biomedical Engineering*, 28(4):386–398.

Bezerra, H., Costa, M., Guagliumi, G., Rollins, A., and Simon, D. (2009). Intracoronary optical coherence tomography: A comprehensive review. Clinical and research applications. *JACC: Cardiovascular Interventions*, 2(11):1035–1046.

Bourantas, C., Kourtis, I., Plissiti, M., Fotiadis, D., Katsouras, C., Papafaklis, M., and Michalis, L. (2005). A method for 3D reconstruction of coronary arteries using biplane angiography and intravascular ultrasound images. *Computerized Medical Imaging and Graphics*, 29(8):597–606.

Bourantas, C., Papafaklis, M., Naka, K., Tsakanikas, V., Lysitsas, D., Alamgir, F., Fotiadis, D., and Michalis, L. (2012). Fusion of optical coherence tomography and coronary angiography - in vivo assessment of shear stress in plaque rupture. *International Journal of Cardiology*, 155(2):e24–e26.

Bourezak, R., Lamouche, G., and Cheriet, F. (2010). Automatic lumen segmentation from intravascular OCT images. *Proceedings of SPIE Medical Imaging 2010: Computer-Aided Diagnosis, San Diego, CA, USA*, 76242R.

Brar, S., Gray, W., Dangas, G., Leon, M., Aharonian, V., Brar, S., and Moses, J. (2009). Bifurcation stenting with drug-eluting stents: A systematic review and meta-analysis of randomised trials. *EuroIntervention*, 5(4):475–484.

Brezinski, M., Tearney, G., Bouma, B., Izatt, J., Hee, M., Swanson, E., Southern, J., and Fujimoto, J. (1996). Optical coherence tomography for optical biopsy: Properties and demonstration of vascular pathology. *Circulation*, 93(6):1206–1213.

Cannon, C. and Braunwald, E. (2008). Unstable angina and non-ST-elevation myocardial infarction. In Fauci, A., Kasper, D., Longo, D., Braunwald, E., Hauser, S., Jameson, J., and Loscalzo, J., editors, *Harrisons Principles of Internal Medicine*. McGraw-Hill Publ. Comp. 17th ed., part 9, section 238.

Caputo, M., Chiastra, C., Cianciolo, C., Cutrì, E., Dubini, G., Gunn, J., Keller, B., Migliavacca, F., and Zunino, P. (2013). Simulation of oxygen transfer in stented arteries and correlation with in-stent restenosis. *International Journal for Numerical Methods in Biomedical Engineering*. In press.

Cárdenes, R., Díez, J., Duchateau, N., Pashaei, A., and Frangi, A. (2013). Model generation of coronary artery bifurcations from CTA and single plane angiography. *Medical Physics*, 40(1). art.no. 013701.

Cárdenes, R., Díez, J., Larrabide, I., Bogunović, H., and Frangi, A. (2011). 3D modeling of coronary artery bifurcations from CTA and conventional coronary angiography. *Lecture Notes in Computer Science (including subseries Lecture Notes in Artificial Intelligence and Lecture Notes in Bioinformatics)*, 6893 LNCS(PART 3):395–402.

Carmines, D., McElhaney, J., and Stack, R. (1991). A piece-wise non-linear elastic stress expression of human and pig coronary arteries tested in vitro. *Journal of Biomechanics*, 24(10):899–906.

Celi, S., Vaghetti, M., Palmieri, C., and Berti, S. (2013). Superficial coronary calcium analysis by OCT: Looking forward an imaging algorithm for an automatic 3D quantification. *International Journal of Cardiology*, 168(3):2958–2960.

Charonko, J., Karri, S., Schmieg, J., Prabhu, S., and Vlachos, P. (2009). In vitro, time-resolved PIV comparison of the effect of stent design on wall shear stress. *Annals of Biomedical Engineering*, 37(7):1310–1321.

Chatzizisis, Y., Coskun, A., Jonas, M., Edelman, E., Feldman, C., and Stone, P. (2007). Role of endothelial shear stress in the natural history of coronary atherosclerosis and vascular remodeling. Molecular, cellular, and vascular behavior. *Journal of the American College of Cardiology*, 49(25):2379–2393.

Chatzizisis, Y., Giannoglou, G., Matakos, A., Basdekidou, C., Sianos, G., Panagiotou, A., Dimakis, C., Parcharidis, G., and Louridas, G. (2006). In-vivo accuracy of geometrically correct three-dimensional reconstruction of human coronary arteries: Is it influenced by certain parameters? *Coronary Artery Disease*, 17(6):545–551.

Chen, H., Moussa, I., Davidson, C., and Kassab, G. (2012). Impact of main branch stenting on endothelial shear stress: Role of side branch diameter, angle and lesion. *Journal of the Royal Society Interface*, 9(71):1187–1193.

Chen, S., Zhang, J., Ye, F., Chen, Y., Patel, T., Kawajiri, K., Lee, M., Kwan, T., Mintz, G., and Tan, H. (2008). Study comparing the double kissing (DK) crush with classical crush for the treatment of coronary bifurcation lesions: The DKCRUSH-1 bifurcation study with drug-eluting stents. *European Journal of Clinical Investigation*, 38(6):361–371.

Chen, Z., Fan, Y., Deng, X., and Xu, Z. (2011a). A new way to reduce flow disturbance in endovascular stents: A numerical study. *Artificial Organs*, 35(4):392–397.

Chen, Z., Fan, Y., Deng, X., and Xu, Z. (2011b). A new way to reduce flow disturbance in endovascular stents: A numerical study. *Artificial Organs*, 35(4):392–397.

Chiastra, C., Morlacchi, S., Gallo, D., Morbiducci, U., Cárdenes, R., Larrabide, I., and Migliavacca, F. (2013). Computational fluid dynamic simulations of image-based stented coronary bifurcation models. *Journal of the Royal Society Interface*, 10(84). art.no. 20130193.

Chiastra, C., Morlacchi, S., Pereira, S., Dubini, G., and Migliavacca, F. (2012). Computational fluid dynamics of stented coronary bifurcations studied with a hybrid discretization method. *European Journal of Mechanics, B/Fluids*, 35:76–84.

Chiu, J.-J. and Chien, S. (2011). Effects of disturbed flow on vascular endothelium: Pathophysiological basis and clinical perspectives. *Physiological Reviews*, 91(1):327–387.

Choma, M., Sarunic, M., Yang, C., and Izatt, J. (2003). Sensitivity advantage of swept source and Fourier domain optical coherence tomography. *Optics Express*, 11(18):2183–2189.

Collet, C., Costa, R., and Abizaid, A. (2011). Dedicated bifurcation analysis: dedicated devices. *The international journal of cardiovascular imaging*, 27(2):181–188.

Colombo, F., Biondi-Zoccai, G., Infantino, V., Omed, P., Moretti, C., Sciuto, F., Siliquini, R., Chiad, S., Trevi, G., and Sheiban, I. (2009). A long-term comparison of drug-eluting versus bare metal stents for the percutaneous treatment of coronary bifurcation lesions. *Acta cardiologica*, 64(5):583–588.

Coppola, G. and Caro, C. (2009). Arterial geometry, flow pattern, wall shear and mass transport: Potential physiological significance. *Journal of the Royal Society Interface*, 6(35):519–528.

Costa, R. and Moussa, I. (2006). Percutaneous treatment of coronary bifurcation lesions in the era of drug-eluting stents. *Minerva Cardioangiologica*, 54(5):577–589.

Cutrì, E., Zunino, P., Morlacchi, S., Chiastra, C., and Migliavacca, F. (2013). Drug delivery patterns for different stenting techniques in coronary bifurcations: A comparative computational study. *Biomechanics and Modeling in Mechanobiology*, 12(4):657–669.

Dai, G., Kaazempur-Mofrad, M., Natarajan, S., Zhang, Y., Vaughn, S., Blackman, B., Kamm, R., Garca-Cardea, G., and Gimbrone Jr., M. (2004). Distinct endothelial phenotypes evoked by arterial waveforms derived from atherosclerosis-susceptible and -resistant regions of human vasculature. *Proceedings of the National Academy of Sciences of the United States of America*, 101(41):14871–14876.

Dangas, G., Claessen, B., Caixeta, A., Sanidas, E., Mintz, G., and Mehran, R. (2010). In-stent restenosis in the drug-eluting stent era. *Journal of the American College of Cardiology*, 56(23):1897–1907.

D'Angelo, C., Zunino, P., Porpora, A., Morlacchi, S., and Migliavacca, F. (2011). Model reduction strategies enable computational analysis of controlled drug release from cardiovascular stents? *SIAM Journal on Applied Mathematics*, 71(6):2312–2333.

Dardik, A., Chen, L., Frattini, J., Asada, H., Aziz, F., Kudo, F., and Sumpio, B. (2005). Differential effects of orbital and laminar shear stress on endothelial cells. *Journal of Vascular Surgery*, 41(5):869–880.

Davies, J., Whinnett, Z., Francis, D., Manisty, C., Aguado-Sierra, J., Willson, K., Foale, R., Malik, I., Hughes, A., Parker, K., and Mayet, J. (2006). Evidence of a dominant backward-propagating "suction" wave responsible for diastolic coronary filling in humans, attenuated in left ventricular hypertrophy. *Circulation*, 113(14):1768–1778.

Davis, N. (2005). Atherosclerosis - an inflammatory process. *Journal of insurance medicine (New York, N.Y.)*, 37(1):72–75.

De Boer, J., Cense, B., Park, B., Pierce, M., Tearney, G., and Bouma, B. (2003). Improved signal-to-noise ratio in spectral-domain compared with time-domain optical coherence tomography. *Optics Letters*, 28(21):2067–2069.

De Bruyne, B., Bartunek, J., Sys, S., Pijls, N., Heyndrickx, G., and Wijns, W. (1996). Simultaneous coronary pressure and flow velocity measurements in humans: Feasibility, reproducibility, and hemodynamic dependence of coronary flow velocity reserve, hyperemic flow versus pressure slope index, and fractional flow reserve. *Circulation*, 94(8):1842–1849.

Delfino, A., Stergiopulos, N., Moore Jr., J., and Meister, J.-J. (1997). Residual strain effects on the stress field in a thick wall finite element model of the human carotid bifurcation. *Journal of Biomechanics*, 30(8):777–786.

Demiray, H. (1972). A note on the elasticity of soft biological tissues. *Journal of Biomechanics*, 5(3):309–311.

DePaola, N., Gimbrone Jr., M., Davies, P., and Dewey Jr., C. (1992). Vascular endothelium responds to fluid shear stress gradients. *Arteriosclerosis and Thrombosis*, 12(11):1254–1257.

Deplano, V., Bertolotti, C., and Barragan, P. (2004). Three-dimensional numerical simulations of physiological flows in a stented coronary bifurcation. *Medical and Biological Engineering and Computing*, 42(5):650–659.

Dodge Jr., J., Brown, B., Bolson, E., and Dodge, H. (1992). Lumen diameter of normal human coronary arteries: Influence of age, sex, anatomic variation, and left ventricular hypertrophy or dilation. *Circulation*, 86(1):232–246.

Donea, J., Giuliani, S., and Halleux, J. (1982). An arbitrary lagrangian-eulerian finite element method for transient dynamic fluid-structure interactions. *Computer Methods in Applied Mechanics and Engineering*, 33(1-3):689–723.

Doriot, P.-A., Dorsaz, P.-A., Dorsaz, L., De Benedetti, E., Chatelain, P., and Delafontaine, P. (2000). In-vivo measurements of wall shear stress in human coronary arteries. *Coronary Artery Disease*, 11(6):495–502.

Drake, R., Vogl, W., and Mitchell, A. (2012). *Gray's basic anatomy*. Churchill Livingstone, Elsevier Inc.

Duraiswamy, N., Cesar, J., Schoephoerster, R., and Moore Jr., J. (2008). Effects of stent geometry on local flow dynamics and resulting platelet deposition in an in vitro model. *Biorheology*, 45(5):547–561.

Duraiswamy, N., Schoephoerster, R., and Moore Jr., J. (2009). Comparison of near-wall hemodynamic parameters in stented artery models. *Journal of Biomechanical Engineering*, 131(6).

Edelman, E. and Rogers, C. (1998). Pathobiologic responses to stenting. *American Journal of Cardiology*, 81(7 A):4E–6E.

Ellwein, L., Otake, H., Gundert, T., Koo, B.-K., Shinke, T., Honda, Y., Shite, J., and LaDisa Jr., J. (2011). Optical coherence tomography for patient-specific 3D artery reconstruction and evaluation of wall shear stress in a left circumflex coronary artery. *Cardiovascular Engineering and Technology*, 2(3):212–227.

Farooq, M., Khasnis, A., Majid, A., and Kassab, M. (2009). The role of optical coherence tomography in vascular medicine. *Vascular Medicine*, 14(1):63–71.

Fercher, A., Hitzenberger, C., Drexler, W., Kamp, G., and Sattmann, H. (1993). In vivo optical coherence tomography. *American Journal of Ophthalmology*, 116(1):113–114.

Ferrante, G., Presbitero, P., Whitbourn, R., and Barlis, P. (2013). Current applications of optical coherence tomography for coronary intervention. *International Journal of Cardiology*, 165(1):7–16.

Figueroa, C., Vignon-Clementel, I., Jansen, K., Hughes, T., and Taylor, C. (2006). A coupled momentum method for modeling blood flow in three-dimensional deformable arteries. *Computer Methods in Applied Mechanics and Engineering*, 195(41-43):5685–5706.

Filipovic, N., Teng, Z., Radovic, M., Saveljic, I., Fotiadis, D., and Parodi, O. (2013). Computer simulation of three-dimensional plaque formation and progression in the carotid artery. *Medical and Biological Engineering and Computing*, 51(6):607–616.

Finet, G., Gilard, M., Perrenot, B., Rloufol, G., Motreff, P., Gavit, L., and Prost, R. (2007). Fractal geometry of arterial coronary bifurcations: a quantitative coronary angiography and intravascular ultrasound analysis. *EuroIntervention*, 3:490–498.

Finet, G., Huo, Y., Rioufol, G., Ohayon, J., Guerin, P., and Kassab, G. (2010). Structure-function relation in the coronary artery tree: From fluid dynamics to arterial bifurcations. *EuroIntervention*, 6(SUPPL. J):J10–J15.

Foin, N., Alegria-Barrero, E., Torii, R., Chan, P., Viceconte, N., Davies, J., and C., D. M. (2012a). Crush, culotte, T and protrusion: which 2-stent technique for treatment of true bifurcation lesions? - insights from in vitro experiments and micro-computed tomography. *Circulation Journal*, 77:73–80.

Foin, N., Torii, R., Mortier, P., De Beule, M., Viceconte, N., Chan, P., Davies, J., Xu, X., Krams, R., and Di Mario, C. (2012b). Kissing balloon or sequential dilation of the side branch and main vessel for provisional stenting of bifurcations: Lessons from micro-computed tomography and computational simulations. *JACC: Cardiovascular Interventions*, 5(1):47–56.

Fox, B., James, K., Morgan, B., and Seed, A. (1982). Distribution of fatty and fibrous plaques in young human coronary arteries. *Atherosclerosis*, 41(2-3):337–347.

Frazin, L., Vonesh, M., Chandran, K., Shipkowitz, T., Yaacoub, A., and Mcpherson, D. (1996). Confirmation and initial documentation of thoracic and abdominal aortic helical flow: An ultrasound study. *ASAIO Journal*, 42(6):951–956.

Frye, R., Alderman, E., Andrews, K., Bost, J., Bourassa, M., Chaitman, B., Detre, K., Faxon, D., Follmann, D., Hlatky, M., Jones, R., Kelsey, S., Rogers, W., Rosen, A., Schaff, H., Sellers, M., Sopko, G., Tyrrell, K., and Williams,

D. (1996). Comparison of coronary bypass surgery with angioplasty in patients with multivessel disease: The Bypass Angioplasty Revascularization Investigation (BARI) investigators. *New England Journal of Medicine*, 335(4):217–225.

Fujimoto, J. (2001). Optical coherence tomography. *Comptes Rendus de l'Academie des Sciences - Series IV: Physics, Astrophysics*, 2(8):1099–1111.

Gabriele, M., Wollstein, G., Ishikawa, H., Xu, J., Kim, J., Kagemann, L., Folio, L., and Schuman, J. (2010). Three dimensional optical coherence tomography imaging: Advantages and advances. *Progress in Retinal and Eye Research*, 29(6):556–579.

Gallo, D., Steinman, D., Bijari, P., and Morbiducci, U. (2012). Helical flow in carotid bifurcation as surrogate marker of exposure to disturbed shear. *Journal of Biomechanics*, 45(14):2398–2404.

Gao, H., Long, Q., Graves, M., Gillard, J., and Li, Z. (2009). Carotid arterial plaque stress analysis using fluid-structure interactive simulation based on in-vivo magnetic resonance images of four patients. *Journal of Biomechanics*, 42(10):1416–1423.

Gasser, T., Ogden, R., and Holzapfel, G. (2006). Hyperelastic modelling of arterial layers with distributed collagen fibre orientations. *Journal of the Royal Society Interface*, 3(6):15–35.

Gastaldi, D., Morlacchi, S., Nichetti, R., Capelli, C., Dubini, G., Petrini, L., and Migliavacca, F. (2010). Modelling of the provisional side-branch stenting approach for the treatment of atherosclerotic coronary bifurcations: Effects of stent positioning. *Biomechanics and Modeling in Mechanobiology*, 9(5):551–561.

Gerbeau, J.-F., Vidrascu, M., and Frey, P. (2005). Fluid-structure interaction in blood flows on geometries based on medical imaging. *Computers and Structures*, 83(2-3):155–165.

Gerlach, H., Esposito, C., and Stern, D. (1990). Modulation of endothelial hemostatic properties: An active role in the host response. *Annual Review of Medicine*, 41:15–24.

Giannoglou, G., Chatzizisis, Y., Sianos, G., Tsikaderis, D., Matakos, A., Koutkias, V., Diamantopoulos, P., Maglaveras, N., Parcharidis, G., and

Louridas, G. (2006a). In-vivo validation of spatially correct three-dimensional reconstruction of human coronary arteries by integrating intravascular ultrasound and biplane angiography. *Coronary Artery Disease*, 17(6):533–543.

Giannoglou, G., Chatzizisis, Y., Sianos, G., Tsikaderis, D., Matakos, A., Koutkias, V., Diamantopoulos, P., Maglaveras, N., Parcharidis, G., and Louridas, G. (2006b). Integration of multi-modality imaging for accurate 3d reconstruction of human coronary arteries in vivo. *Nuclear Instruments and Methods in Physics Research, Section A: Accelerators, Spectrometers, Detectors and Associated Equipment*, 569(2 SPEC. ISS.):310–313.

Go, A., Mozaffarian, D., Roger, V., Benjamin, E., Berry, J., Borden, W., Bravata, D., Dai, S., Ford, E., Fox, C., Franco, S., Fullerton, H., Gillespie, C., Hailpern, S., Heit, J., Howard, V., Huffman, M., Kissela, B., Kittner, S., Lackland, D., Lichtman, J., Lisabeth, L., Magid, D., Marcus, G., Marelli, A., Matchar, D., McGuire, D., Mohler, E., Moy, C., Mussolino, M., Nichol, G., Paynter, N., Schreiner, P., Sorlie, P., Stein, J., Turan, T., Virani, S., Wong, N., Woo, D., and Turner, M. (2013). Heart disease and stroke statistics-2013 update: A report from the American Heart Association. *Circulation*, 127(1):e6–e245.

Gonzales, R., Woods, R., and Eddins, S. (2009). *Digital Image Processing using MATLAB*. Gatesmark Publishing. 2nd ed.

Gradus-Pizlo, I., Bigelow, B., Mahomed, Y., Sawada, S., Rieger, K., and Feigenbaum, H. (2003). Left anterior descending coronary artery wall thickness measured by high-frequency transthoracic and epicardial echocardiography includes adventitia. *American Journal of Cardiology*, 91(1):27–32.

Grottum, P., Svindland, A., and Walloe, L. (1983). Localization of atherosclerotic lesions in the bifurcation of the main left coronary artery. *Atherosclerosis*, 47(1):55–62.

Grube, E., Dawkins, K., Guagliumi, G., Banning, A., Zmudka, K., Colombo, A., Thuesen, L., Hauptman, K., Marco, J., Wijns, W., Joshi, A., and Mascioli, S. (2009). TAXUS VI final 5-year results: A multicentre, randomised trial comparing polymer-based moderate-release paclitaxel-eluting stent with a bare metal stent for treatment of long, complex coronary artery lesions. *EuroIntervention*, 4(5):572–577.

Gülan, U., Lüthi, B., Holzner, M., Liberzon, A., Tsinober, A., and Kinzelbach, W. (2012). Experimental study of aortic flow in the ascending aorta via particle tracking velocimetry. *Experiments in Fluids*, 53(5):1469–1485.

Gundert, T., Dholakia, R., McMahon, D., and LaDisa, J. (2013). Computational fluid dynamics evaluation of equivalency in hemodynamic alterations between driver, integrity, and similar stents implanted into an idealized coronary artery. *Journal of Medical Devices, Transactions of the ASME*, 7(1). art.no. 011004.

Gundert, T., Marsden, A., Yang, W., and Ladisa, J. (2012). Optimization of cardiovascular stent design using computational fluid dynamics. *Journal of Biomechanical Engineering*, 134(1).

Gundert, T., Shadden, S., Williams, A., Koo, B.-K., Feinstein, J., and Ladisa Jr., J. (2011). A rapid and computationally inexpensive method to virtually implant current and next-generation stents into subject-specific computational fluid dynamics models. *Annals of Biomedical Engineering*, 39(5):1423–1437.

Gurmeric, S., Isguder, G., Carlier, S., and Unal, G. (2009). A new 3D automated computational method to evaluate in-stent neointimal hyperplasia in in-vivo intravascular optical coherence tomography pullbacks. *Proceedings of the International Conference on Medical Image Computing and Computer-Assisted Intervention (MICCAI)*, 12(Pt 2):776–785.

Guyton, A. and Hall, J. (2006). *Textbook of Medical Physiology*. Elsevier Inc. 17$^{\text{th}}$ ed., chapter 21.

Haluska, B., Jeffriess, L., Mottram, P., Carlier, S., and Marwick, T. (2007). A new technique for assessing arterial pressure wave forms and central pressure with tissue Doppler. *Cardiovascular Ultrasound*, 5. art.no. 6.

Hamdan, R., Gonzalez, R., Ghostine, S., and Caussin, C. (2012). Optical coherence tomography: From physical principles to clinical applications. *Archives of Cardiovascular Diseases*, 105(10):529–534.

Hasan, M., Rubenstein, D., and Yin, W. (2013). Effects of cyclic motion on coronary blood flow. *Journal of Biomechanical Engineering*, 135(12). art.no. 121002.

He, Y., Duraiswamy, N., Frank, A., and Moore Jr., J. (2005). Blood flow in stented arteries: A parametric comparison of strut design patterns in three dimensions. *Journal of Biomechanical Engineering*, 127(4):637–647.

Himburg, H., Grzybowski, D., Hazel, A., LaMack, J., Li, X.-M., and Friedman, M. (2004). Spatial comparison between wall shear stress measures and porcine arterial endothelial permeability. *American Journal of Physiology - Heart and Circulatory Physiology*, 286(5 55-5):H1916–H1922.

Hofer, M., Rappitsch, G., Perktold, K., Trubel, W., and Schima, H. (1996). Numerical study of wall mechanics and fluid dynamics in end-to-side anastomoses and correlation to intimal hyperplasia. *Journal of Biomechanics*, 29(10):1297–1308.

Hoi, Y., Zhou, Y.-Q., Zhang, X., Henkelman, R., and Steinman, D. (2011). Correlation between local hemodynamics and lesion distribution in a novel aortic regurgitation murine model of atherosclerosis. *Annals of Biomedical Engineering*, 39(5):1414–1422.

Holzapfel, G., Sommer, G., Gasser, C., and Regitnig, P. (2005). Determination of layer-specific mechanical properties of human coronary arteries with nonatherosclerotic intimal thickening and related constitutive modeling. *American Journal of Physiology - Heart and Circulatory Physiology*, 289(5 58-5):H2048–H2058.

Huang, D., Swanson, E., Lin, C., Schuman, J., Stinson, W., Chang, W., Hee, M., Flotte, T., Gregory, K., Puliafito, C., and Fujimoto, J. (1991). Optical coherence tomography. *Science*, 254(5035):1178–1181.

Huo, Y., Choy, J., Svendsen, M., Sinha, A., and Kassab, G. (2009). Effects of vessel compliance on flow pattern in porcine epicardial right coronary arterial tree. *Journal of Biomechanics*, 42(5):594–602.

Huo, Y. and Kassab, G. (2009). A scaling law of vascular volume. *Biophysical Journal*, 96(2):347–353.

Jang, I.-K., Bouma, B., Kang, D.-H., Park, S.-J., Park, S.-W., Seung, K.-B., Choi, K.-B., Shishkov, M., Schlendorf, K., Pomerantsev, E., Houser, S., Aretz, H., and Tearney, G. (2002). Visualization of coronary atherosclerotic plaques in patients using optical coherence tomography: Comparison with intravascular ultrasound. *Journal of the American College of Cardiology*, 39(4):604–609.

Jang, I.-K., Tearney, G., MacNeill, B., Takano, M., Moselewski, F., Iftima, N., Shishkov, M., Houser, S., Aretz, H., Halpern, E., and Bouma, B. (2005). In vivo characterization of coronary atherosclerotic plaque by use of optical coherence tomography. *Circulation*, 111(12):1551–1555.

Kassab, G. (2007). Design of coronary circulation: A minimum energy hypothesis. *Computer Methods in Applied Mechanics and Engineering*, 196(31-32):3033–3042.

Katritsis, D., Theodorakakos, A., Pantos, I., Gavaises, M., Karcanias, N., and Efstathopoulos, E. (2012). Flow patterns at stented coronary bifurcations: Computational fluid dynamics analysis. *Circulation: Cardiovascular Interventions*, 5(4):530–539.

Katritsis, G., Siontis, G., and Ioannidis, J. (2009). Double versus single stenting for coronary bifurcation lesions a meta-analysis. *Circulation: Cardiovascular Interventions*, 2(5):409–415.

Kelle, S., Hays, A., Hirsch, G., Gerstenblith, G., Miller, J., Steinberg, A., Schr, M., Texter, J., Wellnhofer, E., Weiss, R., and Stuber, M. (2011). Coronary artery distensibility assessed by 3.0 Tesla coronary magnetic resonance imaging in subjects with and without coronary artery disease. *American Journal of Cardiology*, 108(4):491–497.

Kessler, W., Moshage, W., Galland, A., Zink, D., Achenbach, S., Nitz, W., Laub, G., and Bachmann, K. (1998). Assessment of coronary blood flow in humans using phase difference MR imaging: Comparison with intracoronary Doppler flow measurement. *International Journal of Cardiac Imaging*, 14(3):179–186.

Kilner, P., Yang, G., Mohiaddin, R., Firmin, D., and Longmore, D. (1993). Helical and retrograde secondary flow patterns in the aortic arch studied by three-directional magnetic resonance velocity mapping. *Circulation*, 88(5 I):2235–2247.

Kolachalama, V., Levine, E., and Edelman, E. (2009). Luminal flow amplifies stent-based drug deposition in arterial bifurcations. *PLoS ONE*, 4(12).

Koshiba, N., Ando, J., Chen, X., and Hisada, T. (2007). Multiphysics simulation of blood flow and LDL transport in a porohyperelastic arterial wall model. *Journal of Biomechanical Engineering*, 129(3):374–385.

Ku, D. (2007). Blood flow in arterues. *Annual Review of Fluid Mechanics*, 29:399–434.

Ku, D., Giddens, D., Zarins, C., and Glagov, S. (1985). Pulsatile flow and atherosclerosis in the human carotid bifurcation. positive correlation between plaque location and low and oscillating shear stress. *Arteriosclerosis*, 5(3):293–302.

Kubo, T., Imanishi, T., Takarada, S., Kuroi, A., Ueno, S., Yamano, T., Tanimoto, T., Matsuo, Y., Masho, T., Kitabata, H., Tsuda, K., Tomobuchi, Y., and Akasaka, T. (2007). Assessment of culprit lesion morphology in acute myocardial infarction. Ability of optical coherence tomography compared with intravascular ultrasound and coronary angioscopy. *Journal of the American College of Cardiology*, 50(10):933–939.

Kume, T., Akasaka, T., Kawamoto, T., Ogasawara, Y., Watanabe, N., Toyota, E., Neishi, Y., Sukmawan, R., Sadahira, Y., and Yoshida, K. (2006). Assessment of coronary arterial thrombus by optical coherence tomography. *American Journal of Cardiology*, 97(12):1713–1717.

LaDisa Jr., J., Olson, L., Molthen, R., Hettrick, D., Pratt, P., Hardel, M., Kersten, J., Warltier, D., and Pagel, P. (2005). Alterations in wall shear stress predict sites of neointimal hyperplasia after stent implantation in rabbit iliac arteries. *American Journal of Physiology - Heart and Circulatory Physiology*, 288(5 57-5):H2465–H2475.

Lantz, J. and Karlsson, M. (2012). Large eddy simulation of LDL surface concentration in a subject specific human aorta. *Journal of Biomechanics*, 45(3):537–542.

Larrabide, I., Kim, M., Augsburger, L., Villa-Uriol, M., Rüfenacht, D., and Frangi, A. (2012a). Fast virtual deployment of self-expandable stents: Method and in vitro evaluation for intracranial aneurysmal stenting. *Medical Image Analysis*, 16(3):721–730.

Larrabide, I., Villa-Uriol, M.-C., Cárdenes, R., Barbarito, V., Carotenuto, L., Geers, A., Morales, H., Pozo, J., Mazzeo, M., Bogunović, H., Omedas, P., Riccobene, C., Macho, J., and Frangi, A. (2012b). AngioLab-A software tool for morphological analysis and endovascular treatment planning of intracranial aneurysms. *Computer Methods and Programs in Biomedicine*, 108(2):806–819.

Latib, A. and Colombo, A. (2008). Bifurcation disease. What do we know, what should we do? *JACC: Cardiovascular Interventions*, 1(3):218–226.

Law, A. and McComas, M. (2001). How to build valid and credible simulation models. *Proceedings of the Winter Simulation Conference, Arlington, VA, USA*, 1:22–29.

Lee, S., Kang, S., Hur, N., and Jeong, S.-K. (2012). A fluid-structure interaction analysis on hemodynamics in carotid artery based on patient-specific clinical data. *Journal of Mechanical Science and Technology*, 26(12):3821–3831.

Lefèvre, T., Chevalier, B., and Louvard, Y. (2010a). Is there a need for dedicated bifurcation devices? *EuroIntervention*, 6(SUPPL. J):J123–J129.

Lefèvre, T., Darremont, O., and Albiero, R. (2010b). Provisional side branch stenting for the treatment of bifurcation lesions. *EuroIntervention*, 6(SUPPL. J):J65–J71.

Lefèvre, T., Louvard, Y., Morice, M.-C., Dumas, P., Loubeyre, C., Benslimane, A., Premchand, R., Guillard, N., and Piéchaud, J.-F. (2000). Stenting of bifurcation lesions: Classification, treatments, and results. *Catheterization and Cardiovascular Interventions*, 49(3):274–283.

Lei, M., Kleinstreuer, C., and Truskey, G. (1996). A focal stress gradient-dependent mass transfer mechanism for atherogenesis in branching arteries. *Medical Engineering and Physics*, 18(4):326–332.

Leitgeb, R., Hitzenberger, C., and Fercher, A. (2003). Performance of fourier domain vs. time domain optical coherence tomography. *Optics Express*, 11(8):889–894.

Lemos, P., Serruys, P., Van Domburg, R., Saia, F., Arampatzis, C., Hoye, A., Degertekin, M., Tanabe, K., Daemen, J., Liu, T., McFadden, E., Sianos, G., Hofma, S., Smits, P., Van Der Giessen, W., and De Feyter, P. (2004). Unrestricted utilization of sirolimus-eluting stents compared with conventional bare stent implantation in the ”real world”: The Rapamycin-Eluting Stent Evaluated at Rotterdam Cardiology Hospital (RESEARCH) registry. *Circulation*, 109(2):190–195.

Leung, J., Wright, A., Cheshire, N., Crane, J., Thom, S., Hughes, A., and Xu, Y. (2006). Fluid structure interaction of patient specific abdominal aortic aneurisms: A comparison with solid stress models. *BioMedical Engineering Online*, 5. art.no. 33.

Leuprecht, A., Perktold, K., Prosi, M., Berk, T., Trubel, W., and Schima, H. (2002). Numerical study of hemodynamics and wall mechanics in distal end-to-side anastomoses of bypass grafts. *Journal of Biomechanics*, 35(2):225–236.

Libby, P. (2002). Inflammation in atherosclerosis. *Nature*, 420(6917):868–874.

Libby, P. (2008). The pathogenesis, prevention, and treatment of atherosclerosis. In Fauci, A., Kasper, D., Longo, D., Braunwald, E., Hauser, S., Jameson, J., and Loscalzo, J., editors, *Harrisons Principles of Internal Medicine*. McGraw-Hill Publ. Comp. 17^{th} ed., part 9, section 235.

Liu, X., Fan, Y., and Deng, X. (2010). Effect of spiral flow on the transport of oxygen in the aorta: A numerical study. *Annals of Biomedical Engineering*, 38(3):917–926.

Lonyai, A., Dubin, A., Feinstein, J., Taylor, C., and Shadden, S. (2010). New insights into pacemaker lead-induced venous occlusion: Simulation-based investigation of alterations in venous biomechanics. *Cardiovascular Engineering*, 10(2):84–90.

Louvard, Y., Medina, A., and Stankovic, G. (2010). Definition and classification of bifurcation lesions and treatments. *EuroIntervention*, 6(SUPPL. J):J31–J35.

Louvard, Y., Thomas, M., Dzavik, V., Hildick-Smith, D., Galassi, A., Pan, M., Burzotta, F., Zelizko, M., Dudek, D., Ludman, P., Sheiban, I., Lassen, J., Darremont, O., Kastrati, A., Ludwig, J., Iakovou, I., Brunel, P., Lansky, A., Meerkin, D., Legrand, V., Medina, A., and Lefvre, T. (2008). Classification of coronary artery bifurcation lesions and treatments: Time for a consensus! *Catheterization and Cardiovascular Interventions*, 71(2):175–183.

Lu, H., Gargesha, M., Wang, Z., Chamie, D., Attizzani, G., Kanaya, T., Ray, S., Costa, M., Rollins, A., Bezerra, H., and Wilson, D. (2012). Automatic stent detection in intravascular OCT images using bagged decision trees. *Biomedical Optics Express*, 3(11):2809–2824.

Malek, A., Alper, S., and Izumo, S. (1999). Hemodynamic shear stress and its role in atherosclerosis. *Journal of the American Medical Association*, 282(21):2035–2042.

Malek, A. and Izumo, S. (1992). Physiological fluid shear stress causes downregulation of endothelin-1 mRNA in bovine aortic endothelium. *American Journal of Physiology - Cell Physiology*, 263(2 32-2):C389–C396.

Malvè, M., Chandra, S., Garca, A., Mena, A., Martnez, M., Finol, E., and Doblar, M. (2013). Impedance-based outflow boundary conditions for human carotid haemodynamics. *Computer Methods in Biomechanics and Biomedical Engineering*, In press.

Malvè, M., García, A., Ohayon, J., and Martínez, M. (2012). Unsteady blood flow and mass transfer of a human left coronary artery bifurcation:FSI vs. CFD. *International Communications in Heat and Mass Transfer*, 39(6):745–751.

Martin, D. and Boyle, F. (2011). Computational structural modelling of coronary stent deployment: A review. *Computer Methods in Biomechanics and Biomedical Engineering*, 14(4):331–348.

Massai, D., Soloperto, G., Gallo, D., Xu, X., and Morbiducci, U. (2012). Shear-induced platelet activation and its relationship with blood flow topology in a numerical model of stenosed carotid bifurcation. *European Journal of Mechanics, B/Fluids*, 35:92–101.

Mauri, L., Silbaugh, T., Wolf, R., Zelevinsky, K., Lovett, A., Zhou, Z., Resnic, F., and Normand, S.-L. (2008). Long-term clinical outcomes after drug-eluting and bare-metal stenting in Massachusetts. *Circulation*, 118(18):1817–1827.

McLaren, M. and Kennedy, G. (2005). Endothelium II: inflammatory response. *Surgery*, 23(1):1–6.

Medina, A., Surez de Lezo, J., and Pan, M. (2006). A new classification of coronary bifurcation lesions. *Revista Espanola de Cardiologia*, 59(2):183.

Mehanna, E., Attizzani, G., Kyono, H., Hake, M., and Bezerra, H. (2011). Assessment of coronary stent by optical coherence tomography, methodology and definitions. *The international journal of cardiovascular imaging*, 27(2):259–269.

Moffatt, H. and Tsinober, A. (1992). Helicity in laminar and turbulent flow. *Annual Review of Fluid Mechanics*, 24(1):281–312.

Morbiducci, U., Diego, G., Ponzini, R., Diana, M., Antiga, L., Montevecchi, F., and Redaelli, A. (2010). Quantitative analysis of bulk flow in image-based hemodynamic models of the carotid bifurcation: The influence of outflow conditions as test case. *Annals of Biomedical Engineering*, 38(12):3688–3705.

Morbiducci, U., Ponzini, R., Grigioni, M., and Redaelli, A. (2007). Helical flow as fluid dynamic signature for atherogenesis risk in aortocoronary bypass. A numeric study. *Journal of Biomechanics*, 40(3):519–534.

Morbiducci, U., Ponzini, R., Rizzo, G., Cadioli, M., Esposito, A., Montevecchi, F., and Redaelli, A. (2011). Mechanistic insight into the physiological relevance of helical blood flow in the human aorta: An in vivo study. *Biomechanics and Modeling in Mechanobiology*, 10(3):339–355.

Morlacchi, S. (2013). *Structural and fluid dynamic assessment of stenting procedures for coronary bifurcations*. PhD thesis. Politecnico di Milano, Italy.

Morlacchi, S., Chiastra, C., Gastaldi, D., Pennati, G., Dubini, G., and Migliavacca, F. (2011a). Sequential structural and fluid dynamic numerical simulations of a stented bifurcated coronary artery. *Journal of Biomechanical Engineering*, 133(12). art.no. 121010.

Morlacchi, S., Colleoni, S., Cárdenes, R., Chiastra, C., Díez, J., Larrabide, I., and Migliavacca, F. (2013). Patient-specific simulations of stenting procedures in coronary bifurcations: Two clinical cases. *Medical Engineering and Physics*, 35(9):1272–1281.

Morlacchi, S., Keller, B., Arcangeli, P., Balzan, M., Migliavacca, F., Dubini, G., Gunn, J., Arnold, N., Narracott, A., Evans, D., and Lawford, P. (2011b). Hemodynamics and in-stent restenosis: Micro-CT images, histology, and computer simulations. *Annals of Biomedical Engineering*, 39(10):2615–2626.

Morlacchi, S. and Migliavacca, F. (2013). Modeling stented coronary arteries: Where we are, where to go. *Annals of Biomedical Engineering*, 41(7):1428–1444.

Murphy, E. and Boyle, F. (2012). Reducing in-stent restenosis through novel stent flow field augmentation. *Cardiovascular Engineering and Technology*, 3(4):353–373.

Murphy, J. and Boyle, F. (2010a). A numerical methodology to fully elucidate the altered wall shear stress in a stented coronary artery. *Cardiovascular Engineering and Technology*, 1(4):256–268.

Murphy, J. and Boyle, F. (2010b). Predicting neointimal hyperplasia in stented arteries using time-dependant computational fluid dynamics: A review. *Computers in Biology and Medicine*, 40(4):408–418.

Murray, C. (1926). The physiological principle of minimum work: I. The vascular system and the cost of blood volume. *Proceedings of the National Academy of Sciences of United States of America*, 12:207–214.

Mylotte, D., Routledge, H., Harb, T., Garot, P., Hovasse, T., Benamer, H., Unterseeh, T., Chevalier, B., Morice, M.-C., Louvard, Y., and Lefèvre, T. (2013). Provisional side branch-stenting for coronary bifurcation lesions: Evidence of improving procedural and clinical outcomes with contemporary techniques. *Catheterization and Cardiovascular Interventions*, 82(4):E437–E445.

Nakazawa, G., Finn, A., Vorpahl, M., Ladich, E., Kolodgie, F., and Virmani, R. (2011). Coronary responses and differential mechanisms of late stent thrombosis attributed to first-generation sirolimus- and paclitaxel-eluting stents. *Journal of the American College of Cardiology*, 57(4):390–398.

Nakazawa, G., Yazdani, S., Finn, A., Vorpahl, M., Kolodgie, F., and Virmani, R. (2010). Pathological findings at bifurcation lesions. The impact of flow distribution on atherosclerosis and arterial healing after stent implantation. *Journal of the American College of Cardiology*, 55(16):1679–1687.

Noordam, J., van den Broek, W., and Buydens, L. (2000). Geometrically guided fuzzy C-means clustering for multivariate image segmentation. *Proceedings of the International Conference on Pattern Recognition*, 1:462–465.

O'Connell, B., McGloughlin, T., and Walsh, M. (2010). Factors that affect mass transport from drug eluting stents into the artery wall. *BioMedical Engineering Online*, 9.

Ojha, M. (1993). Spatial and temporal variations of wall shear stress within an end-to-side arterial anastomosis model. *Journal of Biomechanics*, 26(12):1377–1388.

Okano, M. and Yoshida, Y. (1993). Influence of shear stress on endothelial cell shapes and junction complexes at flow dividers of aortic bifurcations in cholesterol-fed rabbits. *Frontiers of medical and biological engineering: the international journal of the Japan Society of Medical Electronics and Biological Engineering*, 5(2):95–120.

Ormiston, J., Webster, M., Ruygrok, P., Stewart, J., White, H., and Scott, D. (1999). Stent deformation following simulated side-branch dilatation: A comparison of five stent designs. *Catheterization and Cardiovascular Interventions*, 47(2):258–264.

Pant, S., Bressloff, N., Forrester, A., and Curzen, N. (2010). The influence of strut-connectors in stented vessels: A comparison of pulsatile flow through five coronary stents. *Annals of Biomedical Engineering*, 38(5):1893–1907.

Park, S.-J., Kang, S.-J., Virmani, R., Nakano, M., and Ueda, Y. (2012). In-stent neoatherosclerosis: A final common pathway of late stent failure. *Journal of the American College of Cardiology*, 59(23):2051–2057.

Perktold, K., Hofer, M., Rappitsch, G., Loew, M., Kuban, B., and Friedman, M. (1998). Validated computation of physiologic flow in a realistic coronary artery branch. *Journal of Biomechanics*, 31(3):217–228.

Perktold, K. and Rappitsch, G. (1995). Computer simulation of local blood flow and vessel mechanics in a compliant carotid artery bifurcation model. *Journal of Biomechanics*, 28(7):845–856.

Peters, R., Kok, W., Rijsterborgh, H., Van Dijk, M., Koch, K., Piek, J., David, G., and Visser, C. (1996). Reproducibility of quantitative measurements from intracoronary ultrasound images. beat-to-beat variability and influence of the cardiac cycle. *European Heart Journal*, 17(10):1593–1599.

Pflederer, T., Ludwig, J., Ropers, D., Daniel, W., and Achenbach, S. (2006). Measurement of coronary artery bifurcation angles by multidetector computed tomography. *Investigative Radiology*, 41(11):793–798.

Pietrabissa, R., Mantero, S., Marotta, T., and Menicanti, L. (1996). A lumped parameter model to evaluate the fluid dynamics of different coronary bypasses. *Medical Engineering and Physics*, 18(6):477–484.

Prati, F., Cera, M., Ramazzotti, V., Imola, F., Giudice, R., and Albertucci, M. (2007). Safety and feasibility of a new non-occlusive technique for facilitated intracoronary optical coherence tomography (OCT) acquisition in various clinical and anatomical scenarios. *EuroIntervention*, 3(3):365–370.

Prati, F., Jenkins, M., Di Giorgio, A., and Rollins, A. (2011). Intracoronary optical coherence tomography, basic theory and image acquisition techniques. *The international journal of cardiovascular imaging*, 27(2):251–258.

Prati, F., Regar, E., Mintz, G., Arbustini, E., Di Mario, C., Jang, I.-K., Akasaka, T., Costa, M., Guagliumi, G., Grube, E., Ozaki, Y., Pinto, F., and Serruys, P. (2010). Expert review document on methodology, terminology, and clinical applications of optical coherence tomography: Physical principles, methodology of image acquisition, and clinical application for assessment of coronary arteries and atherosclerosis. *European Heart Journal*, 31(4):401–415.

Prosi, M., Perktold, K., Ding, Z., and Friedman, M. (2004). Influence of curvature dynamics on pulsatile coronary artery flow in a realistic bifurcation model. *Journal of Biomechanics*, 37(11):1767–1775.

Quarteroni, A. and Veneziani, A. (2003). Analysis of a geometrical multiscale model based on the coupling of ODEs and PDEs for blood flow simulations. *Multiscale Modeling & Simulation*, 1(2):173–195.

Ramanathan, T. and Skinner, H. (2005). Coronary blood flow. *Continuing Education in Anaesthesia, Critical Care & Pain*, 5(2):61–64.

Ramaswamy, S., Vigmostad, S., Wahle, A., Lai, Y.-G., Olszeski, M., Braddy, K., Brennan, T., Rossen, J., Sonka, M., and Chandran, K. (2004). Fluid dynamic analysis in a human left anterior descending coronary artery with arterial motion. *Annals of Biomedical Engineering*, 32(12):1628–1641.

Regar, E., Ligthart, J., Bruining, N., and Van Soest, G. (2011). The diagnostic value of intracoronary optical coherence tomography. *Herz*, 36(5):417–429.

Rikhtegar, F., Pacheco, F., Wyss, C., Stok, K., Ge, H., Choo, R., Ferrari, A., Poulikakos, D., Mller, R., and Kurtcuoglu, V. (2013a). Compound ex vivo and in silico method for hemodynamic analysis of stented arteries. *PLoS ONE*, 8(3). art.no. e58147.

Rikhtegar, F., Wyss, C., Stok, K., Poulikakos, D., M üller, R., and Kurtcuoglu, V. (2013b). Hemodynamics in coronary arteries with overlapping stents. *Journal of Biomechanics*. In press.

Rodríguez, J., Ruiz, C., Doblaré, M., and Holzapfel, G. (2008). Mechanical stresses in abdominal aortic aneurysms: Influence of diameter, asymmetry, and material anisotropy. *Journal of Biomechanical Engineering*, 130(2).

Sakuma, H., Kawada, N., Takeda, K., and Higgins, C. (1999). MR measurement of coronary blood flow. *Journal of Magnetic Resonance Imaging*, 10(5):728–733.

Sammel, A., Chen, D., and Jepson, N. (2013). New generation coronary stent technology-is the future biodegradable? *Heart Lung and Circulation*, 22(7):495–506.

Sanada, J.-I., Matsui, O., Yoshikawa, J., and Matsuoka, T. (1998). An experimental study of endovascular stenting with special reference to the effects on the aortic vasa vasorum. *CardioVascular and Interventional Radiology*, 21(1):45–49.

Santilli, S., Tretinyak, A., and Lee, E. (2000). Transarterial wall oxygen gradients at the deployment site of an intra-arterial stent in the rabbit. *American Journal of Physiology - Heart and Circulatory Physiology*, 279(4 48-4):H1518–H1525.

Schaar, J., De Korte, C., Mastik, F., Van Damme, L., Krams, R., Serruys, P., and Van Der Steen, A. (2005). Three-dimensional palpography of human coronary arteries: Ex vivo validation and in-patient evaluation. *Herz*, 30(2):125–133.

Schmitt, J., Kolstad, D., and Petersen, C. (2005). Intravascular optical coherence tomography - opening a window into coronary artery disease. *European Cardiology Review*, 1(1):1–5.

Scotti, C. and Finol, E. (2007). Compliant biomechanics of abdominal aortic aneurysms: A fluid-structure interaction study. *Computers and Structures*, 85(11-14):1097–1113.

Scotti, C., Jimenez, J., Muluk, S., and Finol, E. (2008). Wall stress and flow dynamics in abdominal aortic aneurysms: Finite element analysis vs. fluid-structure interaction. *Computer Methods in Biomechanics and Biomedical Engineering*, 11(3):301–322.

Secco, G. and Di Mario, C. (2013). Bifurcational lesions: Do we really need dedicated devices? *International Journal of Cardiology*, 169:155–156.

Seo, T., Schachter, L., and Barakat, A. (2005). Computational study of fluid mechanical disturbance induced by endovascular stents. *Annals of Biomedical Engineering*, 33(4):444–456.

Sharma, S., Sweeny, J., and Kini, A. (2010). Coronary bifurcation lesions: A current update. *Cardiology Clinics*, 28(1):55–70.

Sheiban, I., Omed, P., Biondi-Zoccai, G., Moretti, C., Sciuto, F., and Trevi, G. (2009). Update on dedicated bifurcation stents. *Journal of Interventional Cardiology*, 22(2):150–155.

Sigwart, U., Puel, J., Mirkovitch, V., Joffre, F., and Kappenberger, L. (1987). Intravascular stents to prevent occlusion and restenosis after transluminal angioplasty. *New England Journal of Medicine*, 316(12):701–706.

Sihan, K., Botha, C., Post, F., De Winter, S., Gonzalo, N., Regar, E., Serruys, P., Hamers, R., and Bruining, N. (2009). Fully automatic three-dimensional quantitative analysis of intracoronary optical coherence tomography: Method and validation. *Catheterization and Cardiovascular Interventions*, 74(7):1058–1065.

Spaan, J. (1991). *Coronary blood flow*. Kluwer Academic Publishers.

Spurk, J. and Aksel, N. (2008). *Fluid mechanics*. Springer Verlag.

Stonebridge, P., Hoskins, P., Allan, P., and Belch, J. (1996). Spiral laminar flow in vivo. *Clinical Science*, 91(1):17–21.

Sun, A., Fan, Y., and Deng, X. (2012). Intentionally induced swirling flow may improve the hemodynamic performance of coronary bifurcation stenting. *Catheterization and Cardiovascular Interventions*, 79(3):371–377.

Sun, D., Zheng, Y., Yin, T., Tang, C., Yu, Q., and Wang, G. (2013). Coronary drug-eluting stents: From design optimization to newer strategies. *Journal of Biomedical Materials Research - Part A*. Published online.

Suzuki, Y., Ikeno, F., Koizumi, T., Tio, F., Yeung, A., Yock, P., Fitzgerald, P., and Fearon, W. (2008). In vivo comparison between optical coherence tomography and intravascular ultrasound for detecting small degrees of in-stent neointima after stent implantation. *JACC: Cardiovascular Interventions*, 1(2):168–173.

Swanson, E., Izatt, J., Hee, M., Huang, D., Lin, C., Schuman, J., Puliafito, C., and Fujimoto, J. (1993). In vivo retinal imaging by optical coherence tomography. *Optics Letters*, 18(21):1864–1869.

Tada, S. and Tarbell, J. (2005). A computational study of flow in a compliant carotid bifurcation-stress phase angle correlation with shear stress. *Annals of Biomedical Engineering*, 33(9):1202–1212.

Takizawa, K., Brummer, T., Tezduyar, T., and Chen, P. (2012). A comparative study based on patient-specific fluid-structure interaction modeling of cerebral aneurysms. *Journal of Applied Mechanics, Transactions ASME*, 79(1). art.no. 010908.

Takizawa, K., Moorman, C., Wright, S., Purdue, J., McPhail, T., Chen, P., Warren, J., and Tezduyar, T. (2011). Patient-specific arterial fluid-structure interaction modeling of cerebral aneurysms. *International Journal for Numerical Methods in Fluids*, 65(1-3):308–323.

Tang, D., Yang, C., Kobayashi, S., and Ku, D. (2001). Steady flow and wall compression in stenotic arteries: A three-dimensional thick-wall model with fluid-wall interactions. *Journal of Biomechanical Engineering*, 123(6):548–557.

Tang, D., Yang, C., Kobayashi, S., and Ku, D. (2004). Effect of a lipid pool on stress/strain distributions in stenotic arteries: 3D fluid-structure interactions (FSI) models. *Journal of Biomechanical Engineering*, 126(3):363–370.

Tang, D., Yang, C., and Ku, D. (1999). 3D thin-wall model with fluid-structure interactions for blood flow in carotid arteries with symmetric and asymmetric stenoses. *Computers and Structures*, 72(1):357–377.

Tang, D., Yang, C., Mondal, S., Liu, F., Canton, G., Hatsukami, T., and Yuan, C. (2008). A negative correlation between human carotid atherosclerotic plaque progression and plaque wall stress: In vivo MRI-based 2D/3D FSI models. *Journal of Biomechanics*, 41(4):727–736.

Tearney, G., Yabushita, H., Houser, S., Aretz, H., Jang, I.-K., Schlendorf, K., Kauffman, C., Shishkov, M., Halpern, E., and Bouma, B. (2003). Quantification of macrophage content in atherosclerotic plaques by optical coherence tomography. *Circulation*, 107(1):113–119.

Teng, Z., Canton, G., Yuan, C., Ferguson, M., Yang, C., Huang, X., Zheng, J., Woodard, P., and Tang, D. (2010). 3D critical plaque wall stress is a better predictor of carotid plaque rupture sites than flow shear stress: An in vivo MRI-based 3D FSI study. *Journal of Biomechanical Engineering*, 132(3).

Tezduyar, T., Sathe, S., Cragin, T., Nanna, B., Conklin, B., Pausewang, J., and Schwaab, M. (2007). Modelling of fluid-structure interactions with the space-time finite elements: Arterial fluid mechanics. *International Journal for Numerical Methods in Fluids*, 54(6-8):901–922.

Theodorakakos, A., Gavaises, M., Andriotis, A., Zifan, A., Liatsis, P., Pantos, I., Efstathopoulos, E., and Katritsis, D. (2008). Simulation of cardiac motion on non-Newtonian, pulsating flow development in the human left anterior descending coronary artery. *Physics in Medicine and Biology*, 53(18):4875–4892.

Thuesen, L., Kelbk, H., Klvgaard, L., Helqvist, S., Jrgensen, E., Aljabbari, S., Krusell, L., Jensen, G., Btker, H., Saunamki, K., Lassen, J., and van Weert, A. (2006). Comparison of sirolimus-eluting and bare metal stents in coronary bifurcation lesions: Subgroup analysis of the Stenting Coronary Arteries in Non-Stress/Benestent Disease Trial (SCANDSTENT). *American Heart Journal*, 152(6):1140–1145.

Torii, R., Oshima, M., Kobayashi, T., Takagi, K., and Tezduyar, T. (2006). Fluid-structure interaction modeling of aneurysmal conditions with high and normal blood pressures. *Computational Mechanics*, 38(4-5):482–490.

Torii, R., Oshima, M., Kobayashi, T., Takagi, K., and Tezduyar, T. (2010). Role of 0D peripheral vasculature model in fluid-structure interaction modeling of aneurysms. *Computational Mechanics*, 46(1):43–52.

Torii, R., Wood, N., Hadjiloizou, N., Dowsey, A., Wright, A., Hughes, A., Davies, J., Francis, D., Mayet, J., Yang, G.-Z., Thom, S., and Xu, X. (2009). Fluid-structure interaction analysis of a patient-specific right coronary artery with physiological velocity and pressure waveforms. *Communications in Numerical Methods in Engineering*, 25(5):565–580.

Truskey, G., Barber, K., Robey, T., Olivier, L., and Combs, M. (1995). Characterization of a sudden expansion flow chamber to study the response of endothelium to flow recirculation. *Journal of Biomechanical Engineering*, 117(2):203–210.

Tsantis, S., Kagadis, G., Katsanos, K., Karnabatidis, D., Bourantas, G., and Nikiforidis, G. (2012). Automatic vessel lumen segmentation and stent strut detection in intravascular optical coherence tomography. *Medical Physics*, 39(1):503–513.

Ughi, G., Adriaenssens, T., Onsea, K., Kayaert, P., Dubois, C., Sinnaeve, P., Coosemans, M., Desmet, W., and D'hooge, J. (2012). Automatic segmentation of in-vivo intra-coronary optical coherence tomography images to assess stent strut apposition and coverage. *International Journal of Cardiovascular Imaging*, 28(2):229–241.

Ughi, G., Adriaenssens, T., Sinnaeve, P., Desmet, W., and D'hooge, J. (2013). Automated tissue characterization of in vivo atherosclerotic plaques by intravascular optical coherence tomography images. *Biomedical Optics Express*, 4(7):1014–1030.

Unal, G., Gurmeric, S., and Carlier, S. (2010). Stent implant follow-up in intravascular optical coherence tomography images. *International Journal of Cardiovascular Imaging*, 26(7):809–816.

Van Dem-Mieras, M. and Muller, A. (1986). Blood coagulation as a part of the haemostatic system. In Zwaal, R. and Hemker, H., editors, *Blood coagulation*. Elsevier Science Publisher B.V. chapter 1, pages 1-14.

van der Giessen, A., Groen, H., Doriot, P.-A., de Feyter, P., van der Steen, A., van de Vosse, F., Wentzel, J., and Gijsen, F. (2011). The influence of boundary conditions on wall shear stress distribution in patients specific coronary trees. *Journal of Biomechanics*, 44(6):1089–1095.

Vignon-Clementel, I., Alberto Figueroa, C., Jansen, K., and Taylor, C. (2006). Outflow boundary conditions for three-dimensional finite element modeling of blood flow and pressure in arteries. *Computer Methods in Applied Mechanics and Engineering*, 195(29-32):3776–3796.

Waksman, R., Kitabata, H., Prati, F., Albertucci, M., and Mintz, G. (2013). Intravascular ultrasound versus optical coherence tomography guidance. *Journal of the American College of Cardiology*, 62(17 SUPPL):S32–S40.

Wang, A., Eggermont, J., Dekker, N., de Koning, P., Reiber, J., and Dijkstra, J. (2013a). 3D assessment of stent cell size and side branch access in intravascular optical coherence tomographic pullback runs. *Computerized Medical Imaging and Graphics*.

Wang, A., Eggermont, J., Dekker, N., Garcia-Garcia, H., Pawar, R., Reiber, J., and Dijkstra, J. (2013b). Automatic stent strut detection in intravascular optical coherence tomographic pullback runs. *International Journal of Cardiovascular Imaging*, 29(1):29–38.

Weissman, N., Palacios, I., and Weyman, A. (1995). Dynamic expansion of the coronary arteries: Implications for intravascular ultrasound measurements. *American Heart Journal*, 130(1):46–51.

Wentzel, J., Gijsen, F., Schuurbiers, J., van der Steen, A., and Serruys, P. (2008). The influence of shear stress on in-stent restenosis and thrombosis. *EuroIntervention*, 4 Suppl C:C27–32.

Williams, A., Koo, B.-K., Gundert, T., Fitzgerald, P., and LaDisa Jr., J. (2010). Local hemodynamic changes caused by main branch stent implantation and subsequent virtual side branch balloon angioplasty in a representative coronary bifurcation. *Journal of Applied Physiology*, 109(2):532–540.

Wolters, B., Rutten, M., Schurink, G., Kose, U., De Hart, J., and Van De Vosse, F. (2005). A patient-specific computational model of fluid-structure interaction in abdominal aortic aneurysms. *Medical Engineering and Physics*, 27(10):871–883.

Xu, C., Schmitt, J., Akasaka, T., Kubo, T., and Huang, K. (2011). Automatic detection of stent struts with thick neointimal growth in intravascular optical coherence tomography image sequences. *Physics in Medicine and Biology*, 56(20):6665–6675.

Yabushita, H., Bouma, B., Houser, S., Aretz, H., Jang, I.-K., Schlendorf, K., Kauffman, C., Shishkov, M., Kang, D.-H., Halpern, E., and Tearney, G. (2002). Characterization of human atherosclerosis by optical coherence tomography. *Circulation*, 106(13):1640–1645.

Yang, C., Bach, R., Zheng, J., Naqa, I., Woodard, P., Teng, Z., Billiar, K., and Tang, D. (2009). In vivo IVUS-based 3D fluid-structure interaction models with cyclic bending and anisotropic vessel properties for human atherosclerotic coronary plaque mechanical analysis. *IEEE transactions on bio-medical engineering*, 56(10):2420–2428.

Yang, C., Canton, G., Yuan, C., Ferguson, M., Hatsukami, T., and Tang, D. (2010). Advanced human carotid plaque progression correlates positively with flow shear stress using follow-up scan data: An in vivo MRI multi-patient 3D FSI study. *Journal of Biomechanics*, 43(13):2530–2538.

Yang, C., Canton, G., Yuan, C., Ferguson, M., Hatsukami, T., and Tang, D. (2011). Impact of flow rates in a cardiac cycle on correlations between advanced human carotid plaque progression and mechanical flow shear stress and plaque wall stress. *BioMedical Engineering Online*, 10.

Yazdani, S., Nakano, M., Otsuka, F., Kolodgie, F., and Virmani, R. (2010). Atheroma and coronary bifurcations: Before and after stenting. *EuroIntervention*, 6(SUPPL. J):J24–J30.

Yin, W., Shanmugavelayudam, S., and Rubenstein, D. (2011). The effect of physiologically relevant dynamic shear stress on platelet and endothelial cell activation. *Thrombosis Research*, 127(3):235–241.

Zahn, R., Hamm, C., Schneider, S., Zeymer, U., Nienaber, C., Richardt, G., Kelm, M., Levenson, B., Bonzel, T., Tebbe, U., Sabin, G., and Senges, J. (2005). Incidence and predictors of target vessel revascularization and clinical event rates of the sirolimus-eluting coronary stent (results from the prospective multicenter German Cypher Stent Registry). *American Journal of Cardiology*, 95(11):1302–1308.

Zamir, M. (1999). On fractal properties of arterial trees. *Journal of Theoretical Biology*, 197(4):517–526.

Zamir, M. (2001). Fractal dimensions and multifractility in vascular branching. *Journal of Theoretical Biology*, 212(2):183–190.

Zarins, C., Giddens, D., Bharadvaj, B., Sottiurai, V., Mabon, R., and Glagov, S. (1983). Carotid bifurcation atherosclerosis. Quantitative correlation of plaque localization with flow velocity profiles and wall shear stress. *Circulation Research*, 53(4):502–514.

Zeng, D., Ding, Z., Friedman, M., and Ross Ethier, C. (2003). Effects of cardiac motion on right coronary artery hemodynamics. *Annals of Biomedical Engineering*, 31(4):420–429.

Zhang, F., Dong, L., and Ge, J. (2009). Simple versus complex stenting strategy for coronary artery bifurcation lesions in the drug-eluting stent era: A meta-analysis of randomised trials. *Heart*, 95(20):1676–1681.

Zheng, T., Wen, J., Diang, W., Deng, X., and Fan, Y. (2012). Numerical investigation of oxygen mass transfer in a helical-type artery bypass graft. *Computer methods in biomechanics and biomedical engineering*. In press.

Zhou, Y., Kassab, G., and Molloi, S. (1999). On the design of the coronary arterial tree: A generalization of Murray's law. *Physics in Medicine and Biology*, 44(12):2929–2945.

Zhou, Y., Kassab, G., and Molloi, S. (2002). In vivo validation of the design rules of the coronary arteries and their application in the assessment of diffuse disease. *Physics in Medicine and Biology*, 47(6):977–993.

Zimmerman, S. and Vacek, J. (2011). Imaging techniques in acute coronary syndromes: a review. *ISRN Cardiology*, 2011. art.no. 359127.

Publications

Papers

Chiastra, C., Migliavacca, F., Martínez, M.A., and Malvè, M. (2014). On the necessity of modelling fluid-structure interaction for stented coronary arteries. *Journal of the Mechanical Behavior of Biomedical Materials* (accepted for publication).

Morlacchi, S., **Chiastra, C.**, Cutrì, E., Zunino, P., Burzotta, F., Dubini, G., and Migliavacca, F. (2014). Stent deformation, physical stress and drug elution obtained with provisional stenting, conventional culotte and tryton-based culotte to treat bifurcations: a virtual simulation study. *EuroIntervention* (accepted for publication).

Caputo, M., **Chiastra, C.**, Cianciolo, C., Cutr, E., Dubini, G., Gunn, J., Keller, B., Migliavacca, F., and Zunino, P. (2013). Simulation of oxygen transfer in stented arteries and correlation with in-stent restenosis. *International Journal for Numerical Methods in Biomedical Engineering*, 29(12): 1373-1387.

Chiastra, C., Morlacchi, S., Gallo, D., Morbiducci, U., Cárdenes, R., Larrabide, I., and Migliavacca, F. (2013). Computational fluid dynamic simulations of image-based stented coronary bifurcation models. *Journal of the Royal Society Interface*, 10(84), art.no. 20130193.

Morlacchi, S., Colleoni, S.G., Cárdenes, R., **Chiastra, C.**, Díez, J.L., Larrabide, I., and Migliavacca, F. (2013). Patient-specific simulations of stenting procedures in coronary bifurcations: two clinical cases. *Medical Engineering & Physics*, 35: 1272-1281.

Cutrì, E., Zunino, P., Morlacchi, S., **Chiastra, C.**, and Migliavacca, F. (2013).

Drug delivery patterns for different stenting techniques in coronary bifurcations: a comparative computational study. *Biomechanics and Modeling in Mechanobiology*, 12(4): 657-669

Chiastra, C., Morlacchi, S., Pereira, S., Dubini, G., and Migliavacca, F. (2012). Computational fluid dynamics of stented coronary bifurcations studied with a hybrid discretization method. *European Journal of Mechanics - B/Fluids*, 35: 76-84.

Morlacchi, S., **Chiastra, C.**, Gastaldi, D., Pennati, G., Dubini, G., and Migliavacca, F. (2011). Sequential structural and fluid dynamic numerical simulation of a stented bifurcated coronary artery. *Journal of Biomechanical Engineering*, 133, art.no. 121010.

Dubini, G., Ambrosi, D., Bagnoli, P., Boschetti, F., Caiani, G.C., **Chiastra, C.**, Conti, C.A., Corsini, C., Costantino, M.L., D'angelo, C., Formaggia, L., Fumero, R., Gastaldi, D., Migliavacca, F., Morlacchi, S., Nobile, F., Pennati, G., Petrini, L., Quarteroni, A., Redaelli, A., Stevanella, M., Veneziani, A., Vergara, C., Votta, E., Wu, W., and Zunino, P. (2011) Trends in biomedical engineering: focus on Patient Specific modeling and life support systems. *Journal of Applied Biomaterials & Biomechanics*, 9, 109-117.

Book chapters

Chiastra, C. and Migliavacca, F. (2014). Modelling of blood flow in stented coronary arteries. In Kuznetsov, A. and Becker, S., editors, *Heat transfer and fluid flow in biological processes*. Elsevier (accepted for publication).

Proceedings

Chiastra, C., Montin, E., Burzotta, F., Mainardi, L., and Migliavacca, F. (2013). Coronary stenting: from optical coherence tomography to fluid dynamic simulations. *Proceedings of 13th IEEE International Conference on BioInformatics and BioEngineering*, Chaina, Crete (Greece), November 10th-13th, 2013.

Chiastra, C., Morlacchi, S., Gallo, D., Morbiducci, U., Cárdenes, R., Larrabide, I., Frangi, A.F., Dubini, G., and Migliavacca, F. (2013). Patient-specific stented coronary bifurcations: numerical analysis of near-wall quantities and the bulk flow. *Proceedings of ASME Summer Bioengineering Conference*, Sunriver, Oregon (USA), June 26th-29th, 2013.

Malvè, M., **Chiastra, C.**, Morlacchi, S., Martínez, M.A., and Migliavacca, F. (2012). Comparison between fluid-structure interaction and fluid dynamic simulations of stented coronary arteries. *Proceedings of ICTAM - 23rd International Congress of Theoretical and Applied Mechanics*, Beijing (China), August 19th-24th, 2012.

Chiastra, C., Morlacchi, S., Dubini, G., and Migliavacca, F. (2012). A comparison between standard and dedicated stents for coronary bifurcations: structural and fluid dynamic numerical simulations. *Proceedings of CMBBE 2012 - 10th International Symposium on Biomechanics and Biomedical Engineering*, Berlin (Germany), April 11th-14th, 2012.

Cutrì, E., Zunino, P., Morlacchi, S., **Chiastra, C.**, and Migliavacca, F. (2012). Drug release in coronary bifurcation stenting. *Proceedings of CMBBE 2012 - 10th International Symposium on Biomechanics and Biomedical Engineering*, Berlin (Germany), April 11th-14th, 2012.

Cattaneo, L., **Chiastra, C.**, Cutrì, E., Migliavacca, F., Morlacchi, S., and Zunino P. (2011). An immersed boundary method for drug release applied to drug eluting stents dedicated to arterial bifurcations. *Proceedings of Enumath - European Conference on Numerical Mathematics and Advanced Applications*, Leicester (Great Britain), September 5th-9th, 2011.

Morlacchi, S., **Chiastra, C.**, Dubini, G., and Migliavacca, F. (2011). Numerical modeling of stenting procedures in coronary bifurcations: a structural and fluid dynamic combined approach. *Proceedings of ASME Summer Bioengineering Conference*, Farmington, Pennsylvania (USA). June 22nd-25th, 2011.

Chiastra, C., Morlacchi, S., Dubini, G., and Migliavacca, F. (2011). A structural and fluid dynamic approach to investigate a new angioplasty balloon dedicated to bifurcation lesions. *Proceedings of SCATh*, Graz (Austria), July 11th-13th, 2011.

Morlacchi, S., **Chiastra, C.**, Dubini, G., and Migliavacca, F. (2011). Numerical analysis of the culotte stenting technique: comparison between a standard and a dedicated device. *Proceedings of SCATh*, Graz (Austria), July 11th-13th, 2011.

Chiastra, C., Morlacchi, S., Dubini, G., Zunino, P., and Migliavacca, F. (2011). A structural and fluid dynamic approach to design a new tapered balloon dedicated to stenting procedure in coronary bifurcations. *Proceedings of EUROMECH 529: Cardiovascular Fluid Mechanics*, Cagliari (Italy), June 27th-29th, 2011.